SELF-ASSEMBLING PEPTIDES: FROM FUNDAMENTAL DESIGN TO THERAPEUTIC APPLICATIONS

by

WEIKE CHEN

Presented to the Faculty of the Graduate School of

The University of Texas at Arlington in Partial Fulfillment

of the Requirements

for the Degree of

DOCTOR of PHILOSOPHY

THE UNIVERSITY OF TEXAS AT ARLINGTON

August 2022

Abstract

Supramolecular peptide-based biomaterials have attracted much attention from researchers in various science and engineering fields because of the ease of synthesis and precise control over structures and physicochemical properties on multiple length levels. Self-assembled peptides have shown great potential as functional biomaterials for both diagnosis and treatment of various diseases. In **Chapter 1**, I will introduce several self-assembled peptide systems in terms of molecular design, structure characterization, and their biological applications. In particular, I will discuss new peptide self-assemblies with trigger-responsive properties for targeted molecular imaging and therapy.

In **Chapter 2**, I will focus on peptide self-assembly that can target the reductive tumor microenvironment for selective imaging of tumor cells. The *in vitro* fluorescence cell imaging demonstrated that assembling peptide precursors can undergo chemical and physical transformation to peptide nanofibers with multivalent display of tumor targeting ligands at the reductive tumor sites. These nanofibers show selective binding to U87mg tumor cells that have overexpression of integrin receptors, showing their potentials as tumor targeting probes.

In **Chapter 3**, I will discuss the design and application of self-assembled peptides toward safe and effective antimicrobial therapy development. Natural antimicrobial peptides (AMPs) are potent to kill pathogenic bacteria, however it suffers from severe cytotoxicity against mammalian cells. To overcome the intrinsic limitation of natural AMPs, we incorporated them in a self-assembled antimicrobial nanofiber (SAANs) that our group developed previously. The integration of natural AMPs on SAANs greatly reduced the cytotoxicity against healthy cells but retained potent antimicrobial activity. The mechanism was elucidated through a combined biophysical and biochemical assay using lipid vesicles as a model membrane system.

In **Chapter 4**, I further advanced our design to develop novel self-assembled peptide nanofibers with bacterial targeting capability. A series of responsive peptide nanofibers were generated that showed acid-triggered antimicrobial activity. The *in vitro* antimicrobial and hemocompatibility assay suggested that these nanofibers were nearly nontoxic toward human blood cells at neural physiological conditions but can selectively kill both Gram-positive and Gram-negative bacteria at acidic conditions.

In **Chapter 5,** I will discuss the most recent results on the design of peptide self-assembly with alkaline-responsive antimicrobial activity. Given the urgent need to combat bacterial infections in diseases with an elevated pH, we synthesized a new type of alkaline-responsive antimicrobial hydrogel based on polydiacetylene-peptide (PDA-Pep). Upon pH elevation, the peptide domain is deprotonated and triggers the conformational change of the PDA domain, leading to a colorimetric transition from blue to purple. Simultaneously, the deprotonation induces a gel-to-sol macroscopic phase transition of the fiber network formed in PDA-Pep hydrogels, which causes a selective release of the antimicrobial agents that are encapsulated in the gels into the infection site to kill bacteria. The translational potential of PDA-Pep hydrogels for pH-sensing and on-demand alkaline-triggered antibiotic delivery were demonstrated on inoculated pig skins. The work lays the foundation for the development of multifunctional alkaline-responsive materials in which multiple small molecule or macromolecular therapeutics can be encapsulated to achieve synergistic biological functions against a wide range of multidrug-resistant pathogens.

Acknowledgments

I would like to first thank my PhD advisor, Professor He Dong, for her inspiration, guidance, and patience during my PhD study. I will never forget the valuable education and skills I learned working under her mentorship.

I extend my warmest gratitude to my committee members, Professor Kayunta Johnson-Winters, Professor Jongyun Heo, and Professor Saiful Chowdhury. Thanks for your precious time and expertise.

Thanks to our collaborators Dr. Shuxin Li and Dr. Paul Renick in Professor Tang's lab, Professor Peter Kroll and Dr. John C Lang in Chemistry department, Shan Hazoor and Ryan Madigan in Professor Frank W. Foss Jr's lab, Dr. Paul Renick, Dr. Nikhil Pandy, Dr. Uday K. Chintapula in Professor Kytai T. Nguyen's lab, Dr. Yan Chang in Professor Zui Pan's lab, Professor Xiankai Sun in University of Texas Southwestern Medical Center, and Professor Chuanbin Mao in University of Oklahoma for thoughtful discussions and great companionship.

A special gratitude to my current and former lab mates, Su Yang, Haritha Asokan Sheeja, Ashley A. Adones, Dr. Dawei Xu, Dr. Xiushuang Yuan, Dr. Jun Wang for your encouragement and experimental discussions.

I would also like to thank my parents for standing and supporting me to pursue an academic career.

Contents

List of Figures

List of Tables

Abbreviation

AFM	Atomic force microscope
ALP	Alkaline phosphatase
AMP	Antimicrobial peptide
ACN	Acetonitrile
CD	Circular dichroism
CLSM	Confocal laser scanning microscope
CAC	Critical aggregation concentration
CR	Congo red
CuI	Copper (I) iodide
DIPEA	N, N-Diisopropylethylamine
DMF	Dimethylformamide
DMSO	Dimethyl sulfoxide
DCM	Dichloromethane
DLS	Dynamic light scattering
DTT	DL-Dithiothreitol
DA	Diacetylene
ESI/MS	Electrospray ionization/mass spectrometry
EtOH	Ethanol

EtOAc	Ethyl acetate
equiv	Equivalent
Fmoc	Fluorenylmethyloxycarbonyl
GSH	Glutathione
HPLC	High-performance liquid chromatography
HBTU	*N,N,N′,N′*-Tetramethyl-*O*-(1*H*-benzotriazol-1-yl)uronium hexafluorophosphate
H_2O	Deionized water
h	Hour
HCl	Hydrochloric acid
K_2CO_3	Potassium carbonate
MDP	Multidomain peptide
MES	2-(N-morpholino)ethanesulfonic acid
MMP	Matrix metalloproteinase
MHB	Mueller Hinton Broth
MALDI	Matrix assisted laser desorption ionization
MIC	Minimum inhibitory concentration
MeOH	Methanol
mmol	Milli mole
min	Minute
M	Molar

N_2	Nitrogen
NaOH	Sodium hydroxide
°C	Degree Celsius
PBS	Phosphate-buffered saline
PA	Peptide amphiphile
$Pd(PPh3)_4$	Tetrakis(triphenylphosphine)palladium(0)
Py	Pyridine
ROS	Reactive oxygen species
RBF	Round bottom flask
SEM	Scanning electron microscopy
SDS	Sodium dodecyl sulfate
TEM	Transmission electron microscopy
TFA	Trifluoroacetic acid
THF	Tetrahydrofuran
TMS	Trimethylsilyl
TIS	Triisopropylsilane

Chapter 1: Chemistry and Biology of Peptide Self-assembly

1.1 Self-assembled Peptides as Functional Biomaterials

Molecular self-assembly utilizes non-covalent interactions such as hydrogen bonding, hydrophobic interactions, π-π interactions, metal chelation, and van der Waals interactions to synthesize functional materials.[1] By precisely tailoring molecular motifs used in the self-assembly, one can generate materials with dynamic behaviors that can respond to disease-specific endogenous stimuli such as pH, enzymatic degradation, and reductive environment. Biological functionals can be achieved to suit various needs in biomedical applications such as controlled drug delivery,[2] biosensing,[3] tissue engineering,[4] and self-adjuvanting vaccines.[5]

Peptides and peptide derivatives have been recognized as attractive building blocks for the construction of supramolecular biomaterials due to their chemical versatility, biocompatibility, and biodegradability.[6] Synthetic peptides are designed to adopt various supramolecular structures including α-helix, β-sheet, coiled-coil and collagens, which in turn affect the nanostructures of peptide assembly.[7] Unlike traditional polymeric materials, the modularity of supramolecular peptide biomaterials allows them can be compartmentalized into functional motifs including targeting ligands, self-assembling domains, stimuli-responsive linkers, therapeutic drugs, and contrast agents to favor the simplicity and precision of chemical design of peptide assembly.[8] Moreover, due to the reversible non-covalent driving forces, the assembly/disassembly process of supramolecular peptides can be controlled depending on the disease's associated microenvironment to achieve desired biomedical applications.[9]

1.2 Aliphatic Peptide Amphiphiles

Peptide amphiphiles (PAs) are small molecules that consist of a short peptide sequence linked to an aliphatic tail and were developed Stupp group.[10] The general chemical structure of PA is shown in **Figure 1.1A**.[11] Domain I contains a long hydrophobic alkyl tail with tunable length and composition that can be changed to modify PA mechanical property. Domain II is comprised of a β-sheet forming peptide sequence capable of forming intermolecular hydrogen bonding. The amino acid residues in the peptide sequence can be adjusted to tune the PA mechanical property and gelation kinetics. Domain III typically consists of charged amino acids in order to enhance water solubility as well as design pH-responsive peptide assembly. Domain IV incorporates a bioactive signaling epitope displaying on the nanostructure surface to interact with cells or proteins to achieve desired biological functions. In an aqueous solution, PAs can self-assemble into high-aspect-ratio nanofibers through three major inter/intramolecular interactions, including the hydrophobic interactions of alkyl tails, hydrogen bonding among β-sheet forming peptides, and electrostatic repulsion between charged amino acids (**Figure 1.1B**). The first two are attractive interactions that tend to promote the assembly of PA molecules, whereas the electrostatic repulsion from either positively charged or negatively charged amino acid in the terminus favors the disassembly of PA molecules. The final PA assemblies with tunable nanostructure size, morphology, physical and mechanical property reflect a delicate balance of these inter/intramolecular driving forces.

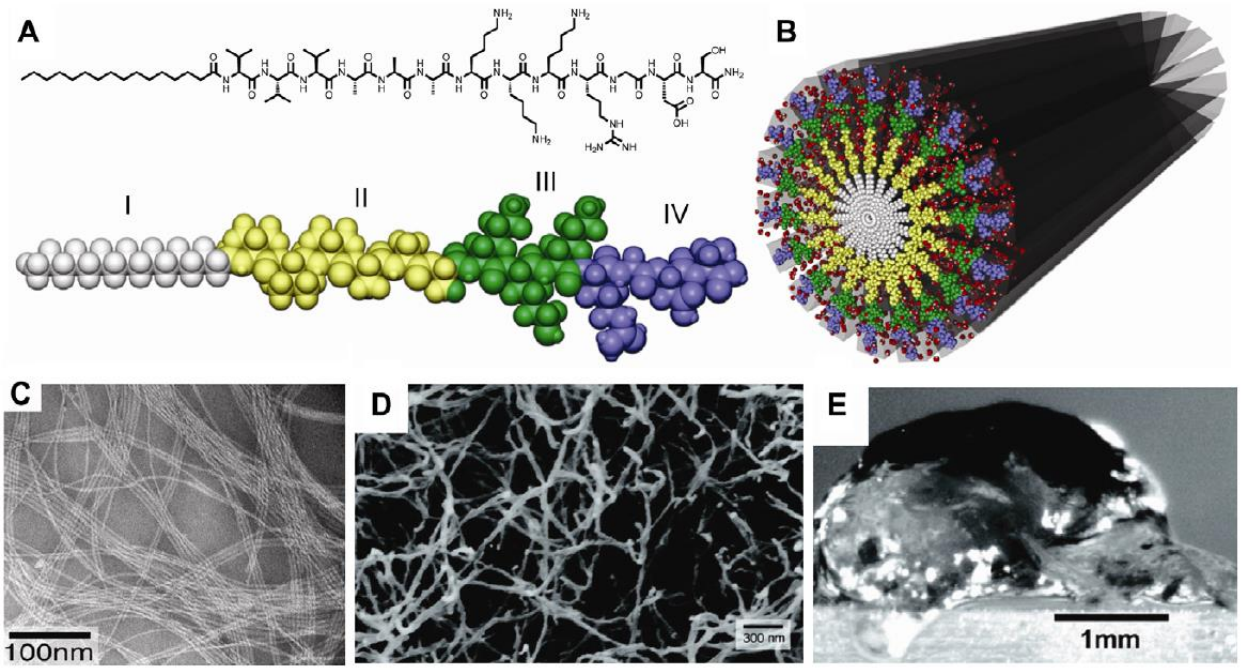

Figure 1.1. (A) Chemical structure of RGDS-bearing PA molecule, highlighting the four structure domains (I-IV). **(B)** The proposed self-assembly model of PA molecules with red spheres representing water molecules. **(C)** TEM image of PA nanofibers in aqueous solution. **(D)** SEM image of a PA fibrillar network formed by mixing cell culture media with a PA solution. **(E)** Image of a PA gel after *in vivo* gelation. Figure adapted from reference 11.

The nanostructures of self-assembling PAs were typically characterized by transmission electron microscopy (TEM) and scanning electron microscopy (SEM). With the chemical design above, the PA molecules can self-assemble into nanofibers that are 6-12 nm in width and up to several microns in length (**Figure 1.1C** and **1.1D**). By addition of salts or a change in solution pH, the electrostatic repulsion of charged amino acids can be relieved allowing the elongation of nanofiber and formation of a fibrillar network, ultimately generating a three-dimensional hydrogel at the appropriate concentration and solvent composition (**Figure 1.1E**).

1.3 Aromatic Peptide Amphiphiles

Aromatic peptide amphiphiles that are composed of a short sequence-typically a dipeptide or even a single amino acid capped at the N-terminus with a synthetic aromatic moiety are gaining

popularity as building blocks for the construction of supramolecular peptide materials.[12] The chemical structure of aromatic peptide amphiphiles consist of four key motifs including N-terminal aromatic, linker, peptide sequence, and the C-termini (**Figure 1.2A**). The N-terminal aromatic moiety is a key design that provides a driving force to induce the self-assembly of aromatic peptide amphiphiles. The Fmoc group commonly serves as N-terminal aromatic moiety because of its nonpolar benzene ring. It has been reported that Fmoc can promote the peptide assembly process and facilitate gelation via the π-π stack packing of the benzene ring.[13] Moreover, various aromatic moieties have been synthesized and utilized at N-terminus including phenyl, naphthalene, azobenzene, and pyrene derivatives for various applications.[12] The selection of linker between N-terminal aromatic group and peptide component is also important for the peptide amphiphile assembly. It has been found that linkers with relative linear geometry allow more effective intermolecular interactions in both aromatic and peptide assembly domains. For example, the previous study demonstrated that carbamate moiety of Fmoc group provides more rigid fluorenyl conformation promoting robust aromatic stacking and H-bonding interactions compared to equivalent ethylcarbonyl linker.[14] The peptide sequence also plays an important role in peptide assembly. Twenty natural amino acids are existing in living systems, but only hydrophobic amino acid residues such as alanine (A), valine (V), leucine (L), isoleucine (I), methionine (M), and three aromatic residues such as phenylalanine (F), tyrosine (Y), and tryptophan (W) are used as assembling domains to induce peptide assembly (**Figure 1.2B**). The most commonly explored assembling domain is diphenylalanine (FF) due to its aromatic π-π stacking, which dominates the peptide assembly process. The C-terminus usually is free carboxyl group that is vital for achieving pH-dependent peptide assembly and gelation. For example, the typical pKa for C-terminal carboxylic acid is approximately 3.5, at high pH, the carboxylic is deprotonated and the Fmoc-FF

is unfolded due to the electrostatic repulsion among negatively charged carboxylic acids. Once the buffer pH is below pKa, the peptide assembly can be triggered because of the protonation of carboxyl acid that relieves the electrostatic interaction, leading to the nanofiber formation and hydrogelation.[15]

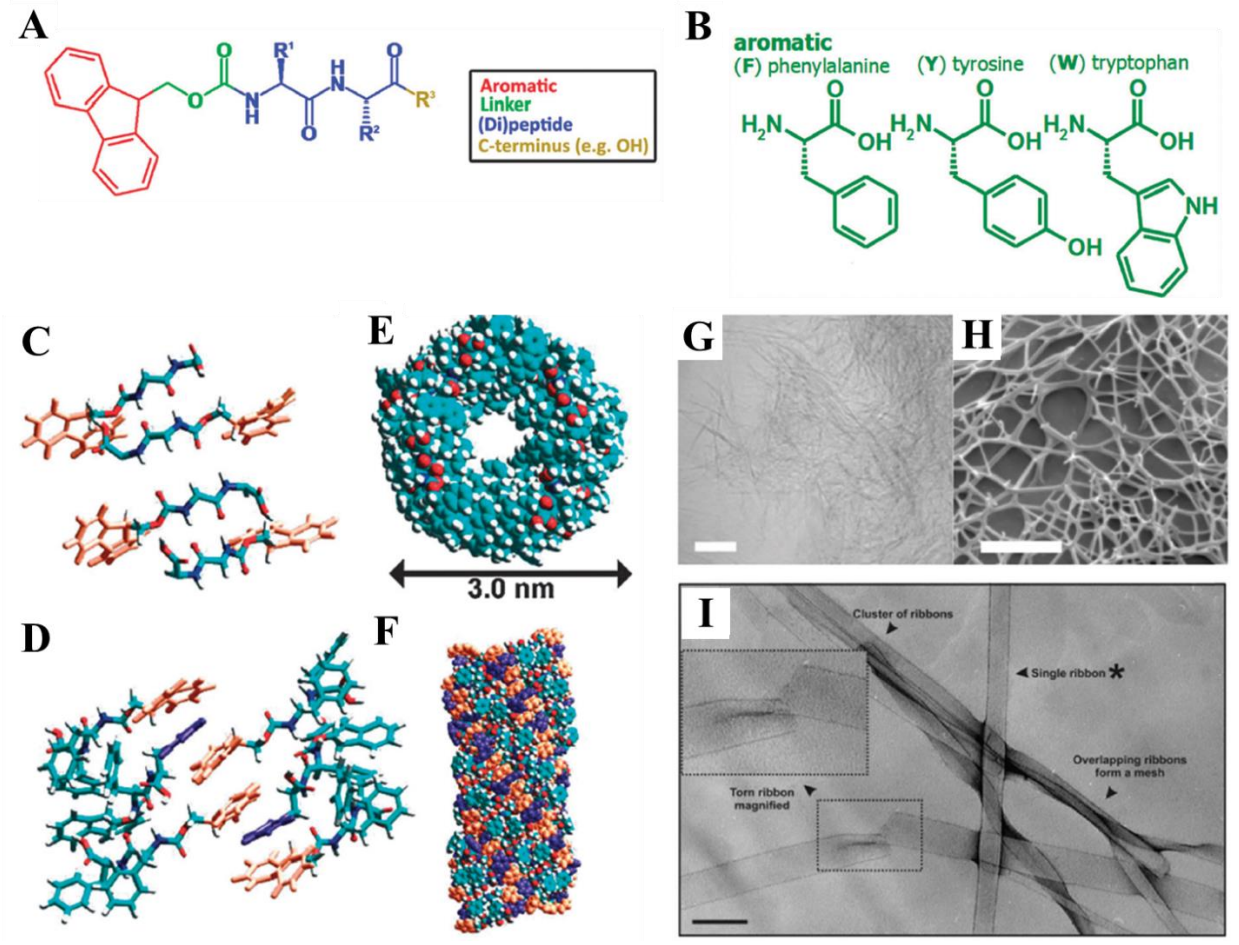

Figure 1.2. (A) Chemical structure of aromatic peptide amphiphile. Fmoc dipeptide is utilized as a typical example. **(B)** Natural aromatic amino acids include phenylalanine (F), tyrosine (Y) and tryptophan (W). **(C)** and **(D)** present the self-assembly model of Fmoc-FF: the packing model assumes that the Fmoc-FF peptides arrange in an anti-parallel β-sheet pattern. In this representation, the Fmoc groups are colored in orange and the Phe side chains are colored in violet. Due to the twist of the β-sheets, a cylindrical structure is created **(E)**. Its side views are shown in **(F)**. **(G)** Light microscopy image shows fibrillar structures (scale bar = 10 mm). **(H)** Cryo-SEM shows the presence of flat bundles of fibers (scale bars = 500 nm). **(I)** TEM images of Fmoc-FF showing an overlapping mesh of extended ribbons (scale bar = 500 Å). Figure adapted from reference 12 and 16.

The self-assembly of Fmoc-FF via major three inter/intramolecular interactions. Hydrophobic interaction and π-π stack packing between the N-terminal Fmoc group and the benzene ring of side chain of diphenylalanine. Intermolecular hydrogen bonding of peptide backbone and electrostatic interaction of C-terminal carboxyl group. The most commonly stacking model of Fmoc-FF has been proposed is interlocked antiparallel stacking conformation where stacks of hydrogen-bonded peptide components are interlocked via antiparallel stacking between adjacent N-terminal groups (**Figure 1.2C, 1.2D, 1.2E,** and **1.2F**).[16] Under specific pH conditions, Fmoc-FF can self-assemble to form large flat ribbons. Images collected by light microscopy, scanning and transmission electron microscopies (SEM and TEM) are reported in **Figure 1.2G, H, I** respectively, confirming this theoretical model.

1.4 β-hairpin Peptides

Self-assembling β-hairpin peptide, MAX1, which comprised of two β-strands was designed by Schneider group.[17] The general peptide sequence of MAX1 was shown in **Figure 1.3A**. MAX1 consists of two β-strand sequences of alternating hydrophobic and hydrophilic residues (Lys and Val) flanking a tetrapeptide (-V^{D}PPT-) sequence (where P is proline, T is threonine, and V^{D} is the D form of valine) that adopt a type II' turn structure. MAX1 remains unfolded in low ionic strength buffer at pH 7.4 due to the electrostatic repulsion of positively charged lysine residues. By the addition of mono- and divalent inorganic salts or an increase in pH, the electrostatic repulsion between charged lysine can be relieved, resulting in the intramolecular folding and peptide assembly to form a non-covalently cross-linked network of short fibrils rich in β-sheet structure, forming mechanically rigid and self-supporting hydrogel (**Figure 1.3B** and **1.3E**). In the folded state, the nonpolar valine residues tend to aggregate to form a hydrophobic pocket whereas the hydrophilic lysine residues are exposed to water molecules. The

folded β-hairpin peptide can self-assemble through both facial and lateral association. The facial association occurs via the burial of the hydrophobic face of distinct hairpins and lateral association happens through the formation of intermolecular hydrogen bonds and van der Waals contacts.

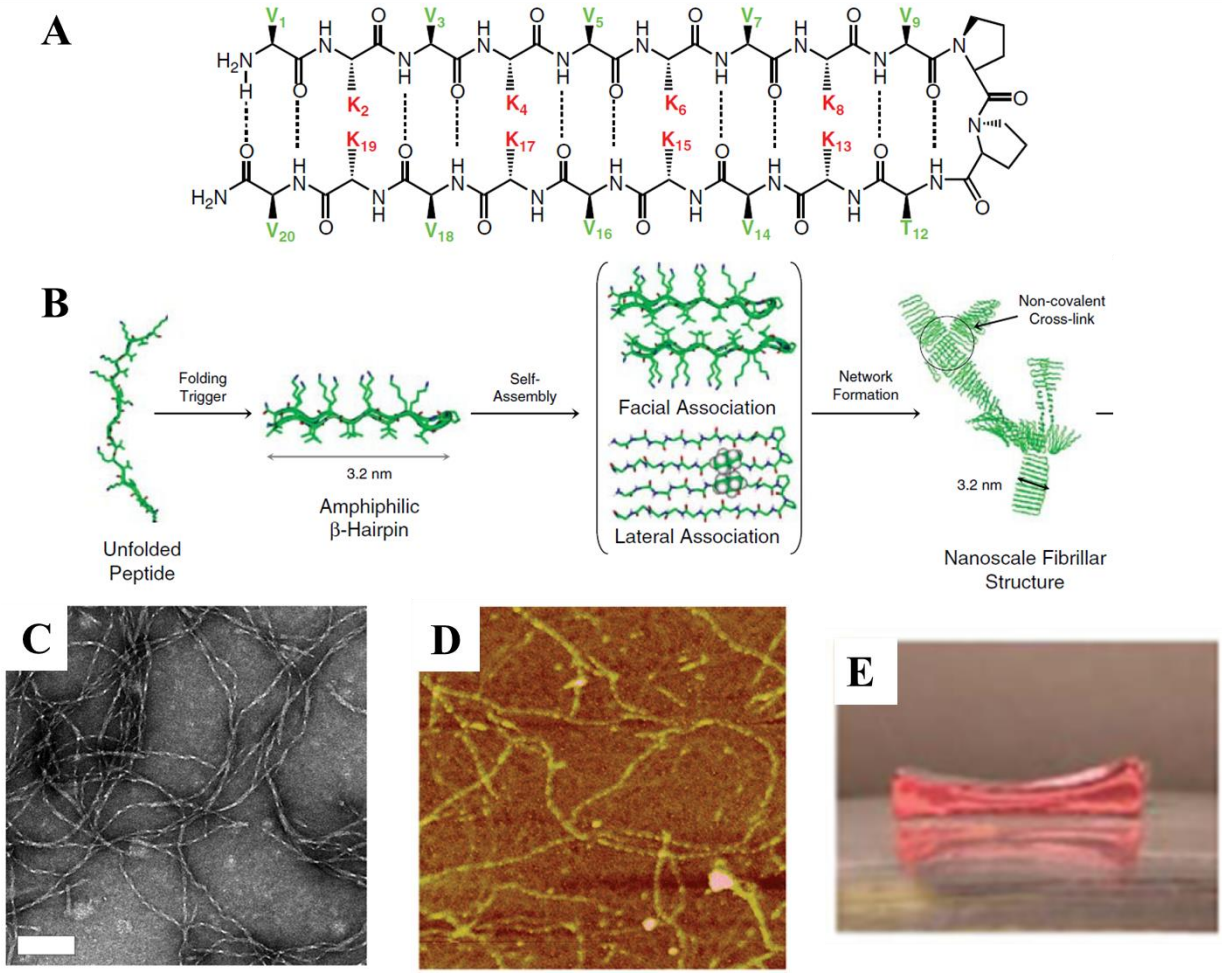

Figure 1.3. (A) Chemical structure of MAX1 comprised of two β-strands of alternating valine (green) and lysine (red) residues connected via a type II′ β-turn. **(B)** Environmentally triggered folding, self-assembly, and non-covalent fibril cross-linking lead to hydrogelation. **(C)** TEM displays the twisted fibril nanostructure of MAX1. **(D)** AFM measurements of the fibrils in topology mode. **(E)** MAX1 hydrogel. Figure adapted from reference 17 and 18.

The nanostructure of MAX1 was characterized by TEM and atomic force microscopy (AFM) (**Figure 1.3C** and **1.3D**). MAX1 formed monodispersed long nanofibers that are 6 nm in

width and up to several microns in length. The resulting nanofibers can be elongated to form hydrogel with bundling fibrillar network.[18]

1.5 Multidomain Peptides (MDPs)

The multidomain peptides (MDPs) were first designed and synthesized by Dong *et al* from Dr. Hartgerink's lab.[19] As shown in **Figure 1.4A and 1.4B**, The general chemical structure of MDPs includes assembling motif consisting of alternating hydrophilic and hydrophobic amino acids that induce peptide assembly and N- and C-terminus peptide sequences containing charged amino acids to improve water solubility (C represents N- or C-terminal amino acids, X represents hydrophilic amino acids, Y represents hydrophobic amino acids, n is the number of terminal amino acids, m is the number of alternating hydrophilic-hydrophobic repeating units). By utilizing twenty natural amino acids, the amino acid residues in functional motifs including assembling motifs and N-/C-terminal motifs can be adjusted to fabricate peptide assembly with tunable nanostructure size, morphology, and mechanical property for achieving desired biofunctions. The N-/C- terminal peptides typically are made up of negatively (Glutamic acid, E) or positively (Lysine, K) charged amino acids, which can improve solubility in aqueous buffers. The hydrophilic residues usually include glutamine (Gln), serine (Ser), threonine (Thr), and cysteine (Cys) while the hydrophobic residues consist of aliphatic and aromatic amino acids such as leucine (Leu), phenylalanine (Phe), tyrosine (Tyr) and tryptophan (Trp). With the above modular motifs, the MDPs can adopt a β-sheet secondary structure with hydrophobic amino acids interacting with each other on one face of the peptide backbone and hydrophilic amino acids on the other face exposing to water molecules (**Figure 1.4C**). In this "hydrophobic sandwich" structure, hydrophobic faces of the MDPs pack against one another to minimize contact with surrounding water molecules. When aligned,

hydrogen bonding between adjacent peptide backbones can occur, inducing peptide assembly and formation of nanofibers (**Figure 1.4D**).

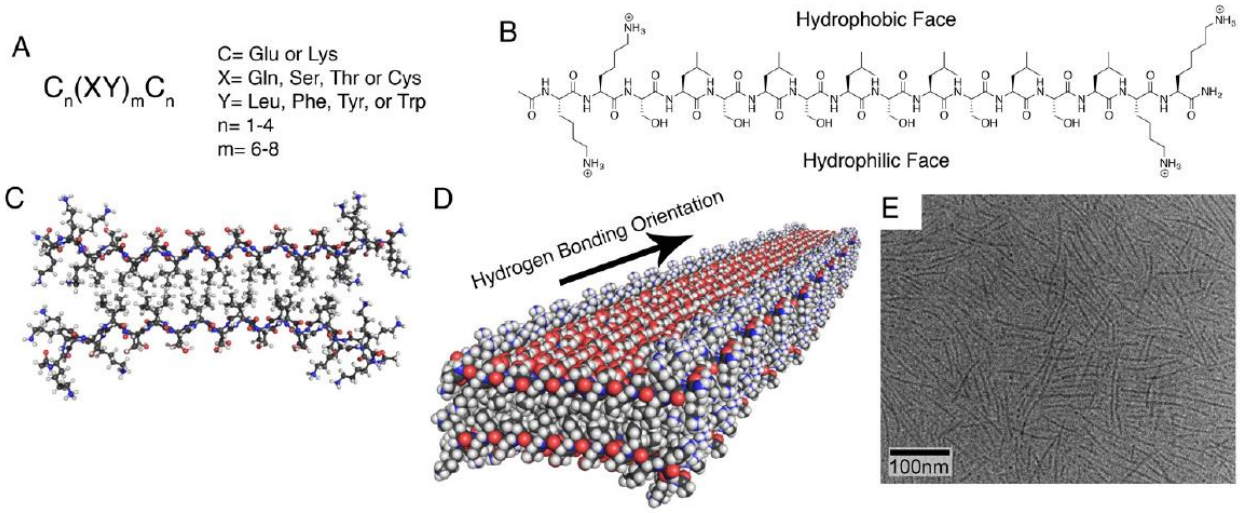

Figure 1.4. Self-assembly of MDPs. **(A)** General composition of multidomain peptides **(B)** the primary sequence of an example MDP, $K_2(SL)_6K_2$. **(C)** The repeating unit of the MDP nanofiber **(D)** Depiction of an MDP nanofiber **(E)** cryo-TEM image of self-assembled MDP, $K_2(QL)_6K_2$. Figure adapted from reference 19.

The characterization of secondary structures and nanostructures of MDPs by using circular dichroism (CD) that provides the secondary structure information and TEM, AFM and SEM that visualize the nanostructure.[20] For example, the CD spectra showed that the MDP with peptide sequence of $K_2(QL)_6K_2$ adopts the antiparallel β-sheet secondary structure and can self-assemble into nanofibers with 5 nm in width and up to 200 nm length as shown in TEM images (**Figure 1.4E**).

1.6 Trigger-responsive Peptide Self-assembly for Targeted Cancer Therapy

Supramolecular peptide biomaterials have been recognized as attractive and promising carriers for targeted tumor imaging and therapy.[21] To enhance tumor targeting specificity, the tumor microenvironment (TME)-responsive self-assembling peptide systems have the potential to

provide effective tumor treatment through targeting tumor cells and accumulating or releasing drugs at the desired sites to minimize the side effects. Various stimuli-responsive self-assembling peptide systems have been developed that respond to tumor-associated pathological stimuli, such as alkaline phosphatase (ALP),[22] matrix metalloproteinase,[23] acidic pH,[24] reactive oxygen species (ROS),[25] and hypoxia conditions.[26] In these processes, small molecules or oligopeptides are designed to undergo chemical transformation under tumor-associated physiological conditions and subsequently induce supramolecular assembly at the tumor sites to achieve tumor imaging and on-demand drug release for enhancing tumor targeting specificity and sensitivity. In this section, the recent research of tumor-triggered self-assembling peptides was summarized with an emphasis of their modular design and corresponding bio-functionalities.

Enzyme-responsive peptide assembly. Besides converting natural substrates, many intracellular/extracellular enzymes have also been exploited as bio-stimulus to trigger the in-situ peptide assemblies. For this purpose, enzyme-specific recognition motifs can be incorporated into the molecular design of the peptide precursors to tailor their bio-responsiveness towards a certain enzyme within the cell.

ALP-responsive peptide assembly. Wang et al developed an enzyme-responsive diphenylalanine (FF)-based peptide assembly with the integration of enzyme-instructed tumor cell targeting and mitochondria targeting to selectively kill cancer cells without acquired drug resistance.[27] As shown in **Figure 1.5A**, the peptide precursor consists of four functional motifs, including (i) a tetrapeptide, FF_pYK (F represents phenylalanine, Y represents Tyrosine, and K represents lysine) functions as a self-assembling building block; (ii) an enzymatic trigger, tyrosine phosphate ($_pY$), whose phosphate group can be hydrolyzed by the tumor cell-overexpressing ALP; (iii) an environment-sensitive fluorophore (4-nitro-2,1,3-benzoxadiazole (NBD)), which can

monitor the dynamic peptide assembly in intracellular environment; (iv) a mitochondria targeting motif, triphenylphosphonium (TPP). The peptide precursor was designed to be hydrolyzed by ALP located on the tumor cell membrane and subsequently underwent chemical and physical transformation to form peptide assembly or aggregates on the tumor cell membrane. Further, the peptide assembly can be internalized by cancer cells through the caveolae/lipid raft-mediated endocytosis and then escape from late endosome/lysosome, inducing dysfunction of mitochondria to release cytochrome c and resulting in cancer cell death. The cytotoxicity data showed that peptide precursors can selectively kill over 90% of Saos2 cells (human osteosarcoma cells which express a high level of ALP) while being nontoxic toward HS5 (normal human bone marrow stromal cells that express a low level of ALP on the cell surface). Moreover, the peptide precursors did not induce the acquired drug resistance of Saos 2 cells as demonstrated by the comparable IC_{50} towards Saos 2 before and after being repeatedly stimulation. The development of highly sensitive and accurate detection systems for cancer diagnosis is highly demanding. Wu et al constructed an ALP-activatable self-assembling peptide-based probe for the enhanced photoacoustic imaging of tumors.[28] As shown in **Figure 1.5B**, the peptide precursor, 1P, is made up of two building blocks, a NIR dye IT775, serving as an exogenous contrast agent; and a well-studied assembling module, Phe-Phe-Tyr (H_2PO_3)-OH, which can be dephosphorylated by tumor-secreted ALP to induce the peptide assembly. The 1P can self-assemble into nanoparticles via the catalyzation by the extracellular high expression of ALP with the self-quenching of NIR fluorescence while enhancement of photoacoustic (PA) signal for tumor imaging. The *in vivo* PA imaging showed that in the ALP-overexpression Hela cell mice model, PA signal of 1P was 2.3 folds higher than that of a control group with an ALP inhibitor at 4 h after 1P injection (**Figure 1.5B**), implying its high detection sensitivity for the cancer diagnosis. In another study, by employing the same ALP-

responsive assembling domain, FF_PY, a dual enzyme and reduction-triggered FFY-based peptide assembly was developed by Yang group to achieve selective killing of liver cancer cells.[29] As shown in **Figure 1.5D**, The peptide precursor, compound 1, was designed to self-assemble into nanoparticles through the extracellular ALP-mediated dephosphorylation and subsequently be taken up by liver cancer cells through integrin receptor-mediated endocytosis. The disulfide bond in the internalized nanoparticle further can be reduced and cleaved by the intracellular overexpressed glutathione, resulting in the chemical and physical transformation to form intracellular nanofibers. The *in vitro* cytotoxicity showed that tandem self-assembly of compound 1 induces selective cancer cell uptake and killing due to the intracellular nanofibers might change the viscosity or interact with functional proteins, leading to cancer cell death.

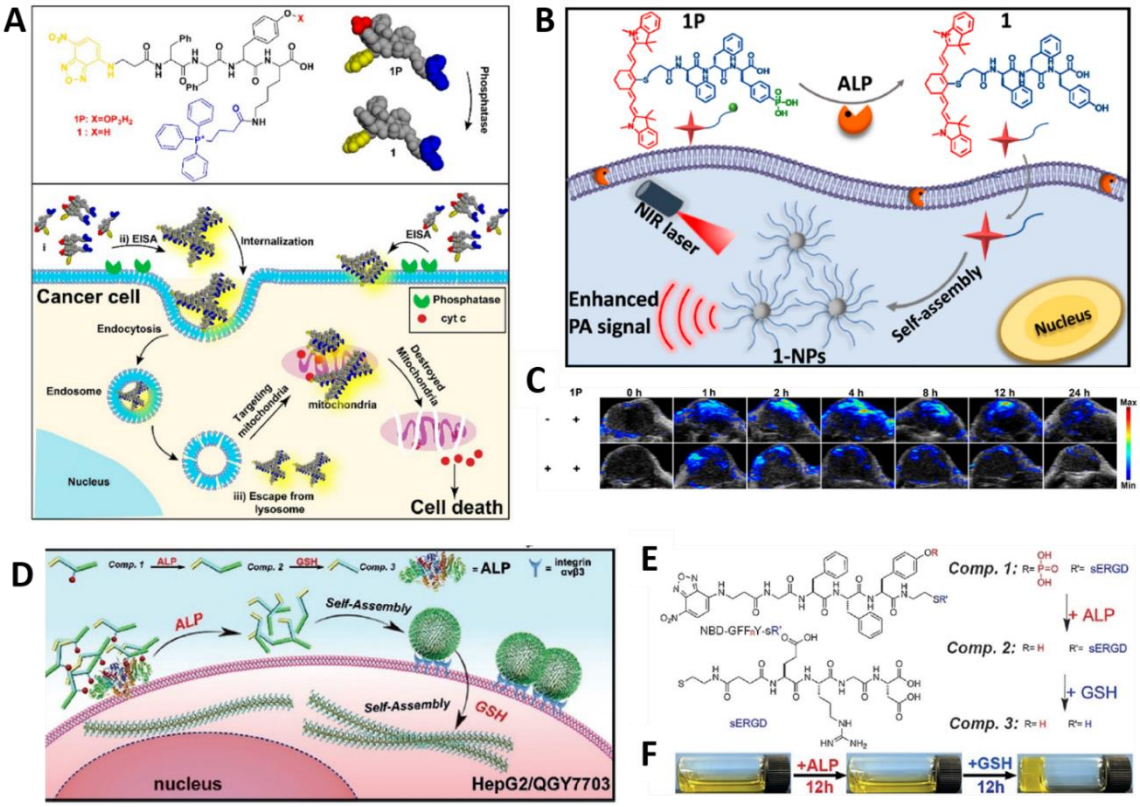

Figure 1.5. (A) Schematic illustration of ALP-instructed self-assembly for targeting mitochondria and inducing death of cancer cells. **(B)** Schematic illustration of ALP-triggered self-assembly of

near-infrared nanoparticles for the enhanced photoacoustic imaging of tumors. **(C)** Time-course PA images of tumors after injections of 1P with (bottom row) or without (top row) the pretreatment of an ALP inhibitor. **(D)** Schematic illustration of the tandem molecular self-assembly in the extra- and intracellular environment of liver cancer cells. **(E)** Chemical structures and schematic illustration of the conversion of 1 into 2 by ALP and then of 2 into 3 by glutathione (GSH). **(F)** Optical images of conversion of solution 1 to solution 2 by ALP and gelation of compound 3 by adding GSH. Figure adapted from reference 27, 28, and 29.

MMP-responsive peptide assembly. A matrix MMP-7-triggered self-assembling peptide precursor that exhibited remarkable cytotoxicity to cancer cells while being non-toxic to normal cells was developed by Maruyama group (**Figure 1.6A**).[30] As shown in **Figure 1.6B**, the peptide precursor, ER-C16, contains four distinct motifs: (i) a 16-carbon alkyl chain that promotes peptide assembly through the hydrophobic interaction; (ii) a tetrapeptide, GGGH (Gly-Gly-Gly-His), serves as a major building block that acts as both an acceptor and a donor of hydrogen bonds; (iii) an enzyme-responsive linker, PLGL (Pro-Leu-Gly-Leu), which can be cleaved by MMP-7 overexpressed by tumor cells; (iv) a cationic dipeptide, RK (Arg-Lys), which prevents the self-assembly of ER-C16 due to its electrostatic repulsion. ER-C16 formed micelle-like nanostructures exhibiting low cytotoxicity towards normal cells at physiological conditions. At the tumor microenvironment, the ER-C16 micelles can be internalized by tumor cells, following the cleavage of enzyme-sensitive linker by tumor-associated MMP-7 initiates the formation of intracellular nanofibers that can cause cancer cell death by the induced high intracellular viscosity. The *in vitro* cytotoxicity showed that ER-C16 exhibited selective killing of MMP-7 overexpressing cancer cells such as Hela, MIAPaCall, SKBR3, MCF-7, and A431while maintaining low cytotoxicity towards normal human dermal microvascular endothelial cells. Moreover, it was found that the expression level of MMP-7 in various cancer cell lines was correlated with cytotoxicity as demonstrated by the higher concentration of intracellular MMP-7 leading to the higher cancer cell killing efficiency of ER-C16. In another study, Kalafatovic et al a developed MMP-9-responsive peptide assembly with encapsulation of doxorubicin (DOX) that can selectively inhibit cancer cell growth with

synergistic effects (**Figure 1.6C**).[31] As shown in **Figure 1.6D**, the peptide precursor consists of two building blocks, including (i) an assembling domain with peptide sequence of PhAc-FF that promotes peptide assembly through hydrophobic interaction and π-π stacking pack; (ii) MMP-9-responsive linker with peptide sequence of AGLDD (Ala-Gly-Leu-Asp-Asp), which can be hydrolyzed and cleaved by cancer cell-secreted MMP-9. Within the encapsulation of anticancer drug, DOX, peptide precursor formed spherical nanoparticles in the normal tissues and underwent a micelle-to-nanofiber transformation in the presence of tumor microenvironment with high levels of MMP-9. The fibrillar network was designed to tightly bind with the cancer cell membrane because of its amphiphilic property and entrapped DOX can accumulate at the tumor microenvironment exhibiting potent anticancer activity. The *in vitro* cytotoxicity and *in vivo* tumor treatment results showed that the combination of peptide precursor and DOX showed a synergistic effect to inhibit cancer cell growth as demonstrated by lower tumor cell viability treated by peptide precursor/DOX combination compared to DOX alone. Recently, MMP-2-triggered supramolecular ionic peptide assembly was introduced by Dr. Dong lab.[32] As shown in **Figure 1.6E**, the peptide precursor termed CS-MDP is made up of three domains consisting of (i) a membrane-active self-assembling domain, $K_{10}(QW)_6E_3$ (K: lysine, Q: glutamine, W: tryptophan, E: glutamic acid, and 10, 6, 3 represent the number of amino acids), which alone can self-assemble into nanofibers; (ii) MMP-2-sensitive linker, PLGLAG, which can be hydrolyzed and cleaved by MMP-2 overexpressed by most cancer cells; (iii) a cationic capping domain, K_5, whose electrostatic interaction can hinder peptide assembly. The CS-MDP formed spherical nanoparticles with low cell membrane activity at physiological conditions. At the tumor microenvironment, the cleavage of enzyme-responsive linker by MMP-2 caused the removal of cationic capping domain and subsequently increased hydrophobicity of fragment of CS-MDP, resulting in the peptide

assembly of CS-MDP fragment to form nanofibers (**Figure 1.6F**). The resulting supramolecular cationic nanofibers can selectively bind with tumor cells and deliver anticancer drugs to inhibit tumor cell growth.

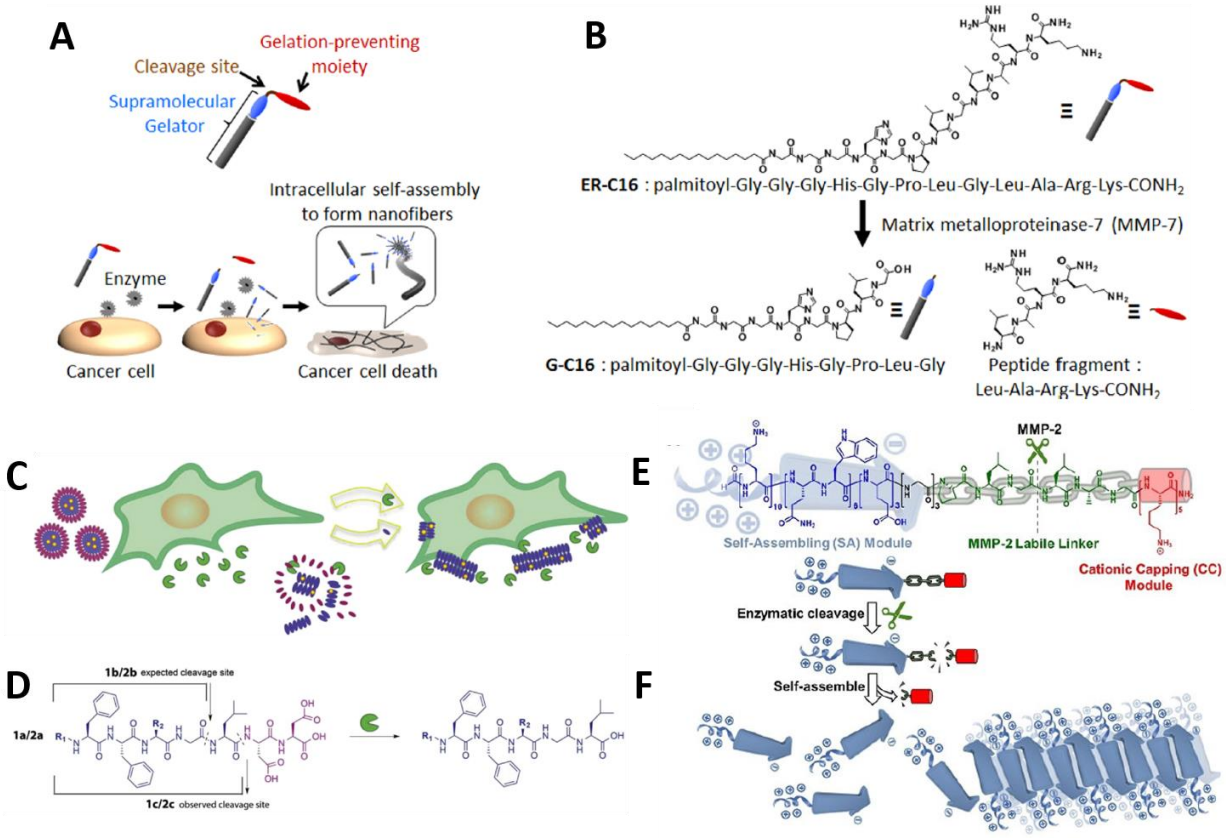

Figure 1.6. (A) Schematic illustration of the self-assembly of MMP7-responsive peptide gelator induces cancer cell death. **(B)** Molecular structures of ER-C16 and fragments upon MMP-7 cleavage. **(C)** Schematic representation of micelle-to-nanofiber transition of MMP-9-responsive peptide amphiphiles in the presence of MMP-9 expressing cancer cells. **(D)** Chemical structure of the MMP-9 responsive peptide amphiphiles. **(E)** Chemical structure of CS-MDP. **(F)** MMP-2-triggered self-assembly of CS-MDP. Figure adapted from reference 30, 31, and 32.

Cathepsin B (CtsB)-responsive peptide assembly. A CtsB-sensitive self-assembling peptide-based prodrug was synthesized by Wang group.[33] The peptide-based prodrug, CPT-LFPR, contains five functional modules (i) a hydrophobic chemodrug camptothecin (CPT) that serves as an anticancer drug; (ii) an assembling scaffold, LVFF, which can self-assemble into β-sheet forming nanofibers; (iii) an existing enzyme-cleavable linker, GFLG, which can be hydrolyzed by

CtsB that is a lysosomal protease in tumor cells; (iv) a hydrophilic poly(ethyleneglycol) (PEG) to increase solubility in physiological condition; (v) a tumor targeting ligand, RGD, which can specifically bind with integrin receptors overexpressed on most tumor cell membrane. The circular dichroism (CD) and transmission electron microscopy (TEM) demonstrated that CPT-LFPR formed spherical nanostructures in the absence of CtsB while undergoing chemical and physical transformation to form β-sheet forming nanofibers in the presence of CtsB. The high-performance liquid chromatography (HPLC) data confirmed that micelles-to-nanofiber transition is induced by the CtsB-mediated hydrolysis of an enzyme-responsive linker. Moreover, the *in vivo* data showed that CPT-LFPR prodrug can form intracellular nanofibers with an effective accumulation of prodrugs, leading to inhibition of tumor growth.

Caspase-3/7-responsive peptide assembly. A tumor-selective cascade activatable self-detained system (TCASS) was developed by Zhao group for drug delivery and cancer imaging.[34] The TCASS is constructed based on an enzyme-triggered self-assembling drug-peptide conjugate precursor, which contains four motifs (i) a tumor specific recognition ligand (AVPIAQK) that can specifically recognize X-linked inhibitor of apoptosis protein (XIAP) that is overexpressed by cancer cells; (ii) an enzyme cleavable linker (DEVD) that can be cleaved by intracellular caspase-3/7; (iv) a self-assembling motif (KLVFFAEGG) that promote peptide assembly; (iv) a functional molecule (fluorescence probe, Cy or anticancer drug, DOX). At physiological conditions, TCASS precursor exhibited good tumor tissue penetrating capability due to its monomeric molecular diffusion. Once internalized by tumor cells, the TCASS can specifically bind with intracellular XIAP and following molecular cleavage of enzyme-responsive linker by active caspase-3/7, triggering the in situ self-assembly of TCASS fragment to form intracellular fibril network with the enhanced accumulation and retention of anticancer drugs. The encapsulated DOX further can

be released via hydrolysis of acid-sensitive hydrazone bond by intracellular acidic conditions and the free DOX can enter the cell nucleus and bind with DNA to inhibit tumor cell growth. The *in vivo* results demonstrated that TCASS exhibited high-efficiency molecular accumulation and retention in tumor tissue compared to identical SiO2 nanoparticles and liposomes. Meanwhile, by the integration of chemodrug (DOX), the therapeutic efficiency of TCASS was enhanced while systemic toxicity was negligible. Moreover, with the conjugation of a contrast agent, TCASS can effectively detect bladder cancer in an isolated human intact bladder with enhanced specificity and sensitivity.

ROS-responsive peptide assembly. ROS primarily consists of hydrogen peroxide (H_2O_2), singlet oxygen ($^1O_2$), hydroxyl radical ($^{\cdot}OH$), superoxide (O^{2-}), and peroxynitrite ($ONOO^-$) are mainly generated in mitochondria.[35] ROS plays an important role in physiological processes such as cell proliferation and apoptosis.[36] Unlike normal cells, tumor cells typically have an overproduction of ROS leading to oxidative stress, which causes abnormal cell growth.[37] The overexpression of ROS has been explored to design oxidation-sensitive motifs that can be modified to create ROS-responsive self-assembling peptides with desired bioactivities.

A ROS-responsive peptide assembly system was developed by Yu group.[38] As shown in **Figure 1.7A**, the peptide precursor had a sequence of EIMIME (Glu-IIe-Met-IIe-Met-Glu), whose hydrophobic amino acids (IMIM) function as peptide assembling domain, which was designed to self-assemble into nanofibers and N-/C-terminal hydrophilic amino acids (E) increase solubility in aqueous solution. The benefits of utilization of methionine (M) are not only its hydrophobic property which can promote peptide assembly, but also it can undergo reliable oxidation-induced conversion between hydrophobic thioether and hydrophilic sulfoxide or sulfone groups, which has been utilized in the construction of other ROS-responsive nanomaterials. To achieve anticancer

therapeutic efficiency and targeted tumor imaging, the anticancer drug (Camptothecin, CPT) and photosensitizer (Chlorin 6, Ce6 produce ROS under laser irradiation) were incorporated into EIMIME via a co-assembly strategy. The EIMIME can self-assemble into nanofibers at physiological conditions. When reaching tumor tissue, the thioether group of Met can be oxidized by *in situ* generated ROS upon laser irradiation, resulting in a shift of amphiphilicity from hydrophobicity to hydrophilicity of Met as accompanied by nanostructure transition from nanofibers to spherical nanoparticles. Once EIMIME nanoparticles were uptake by tumor cells, the intracellular reductive condition can reduce and cleave the disulfide bond which links with CPT and EIMIME, resulting in the controlled release of CPT to inhibit tumor cell growth. In another study, ROS-responsive polymer-peptide conjugates (PPCs) were constructed by Wang group.[39] As shown in **Figure 1.7B**, The polymer-peptide conjugates contained five functional modules (i) a β-sheet forming peptide KLVFF; (ii) a ROS-cleavable linker; (iii) a hydrophilic poly(ethylene glycol) (mPEG) that can increase water solubility; (iv) a mitochondria-targeting ligand, $CG_3(KLAKLAK)_2$; (v) a poly(vinylalcohol) (PVA). The PPCs were designed to self-assemble into nanoparticles at physiological conditions. Upon internalization by tumor cells, the PPCs nanoparticle with multivalent mitochondria targeting ligand can recognize and bind with mitochondria. The ROS-sensitive linker was cleaved by intracellular overexpressed ROS, resulting in the removal of hydrophilic mPEG and inducing nanoparticle-to-nanofiber nanostructure transition. PPCs nanofiber with KLAK targeting ligand can disrupt mitochondria and induce apoptosis, resulting in tumor cell death. The *in vivo* data showed that PPC nanofiber exhibited higher accumulation in the tumor sites compared to control groups including PPC without β-sheet forming peptide and nonresponsive PPC. Moreover, PPC exhibited prolonged retention in the tumor sites with 96 hrs due to the aggregation-induced-retention (AIR) effect. The multivalent

KLAK ligands displaying on the nanofiber surface can greatly inhibit tumor growth. In another approach, a ROS-responsive platinum (II)-containing tripeptide was constructed by Weil group.[40] As shown in **Figure 1.7D**, the metallo-*iso*tripeptide 1·TAT is composed of four functionalities: (i) a pro-assembling isopeptide, ISA (IIe-Ser-Ala), which had a propensity to form nanofibers; (ii) an endogenous ROS-cleavable immolative boronic acid group; (iii) a transporter peptide (TAT), YGRKKRRQRRR, that carries an acid-salicylhydroxamate (SHA) group that binds to a boronic acid via an acid-responsive dynamic covalent bond and enable cellular uptake and endosomal escape; (iv) a platinum (II) terpyridine (Pt-tpy) complex coordinated to the alkynyl group on the N-terminus of *iso*-ISA peptide. The 1·TAT was internalized by tumor cells via TAT-mediated endocytosis and following an intracellular endosomal escape. Once reaching the cytosol, the weak acidic condition and endogenous over-generated H_2O_2 induced the cleavage of acid and reduction-sensitive linkers, leading to the removal of TAT and in situ self-assembly of Pt-ISA fragment 2_{NF}, which can block metabolic functions including aerobic glycolysis and oxidative phosphorylation, thereby shutting down ATP production, resulting in tumor cell death (**Figure 1.7C**). By using A549 and MDA-MB-231 as tumor cell models, the cellular metabolism effects of 2_{NF} on tumor cells were unraveled. The results showed that intracellular transformation of 1·TAT to 2_{NF} interferes with both oxidative phosphorylation (OxPhos) and aerobic glycolysis (AGlyc) pathways preventing metabolic adaption, resulting in early apoptosis and death of tumor cells.

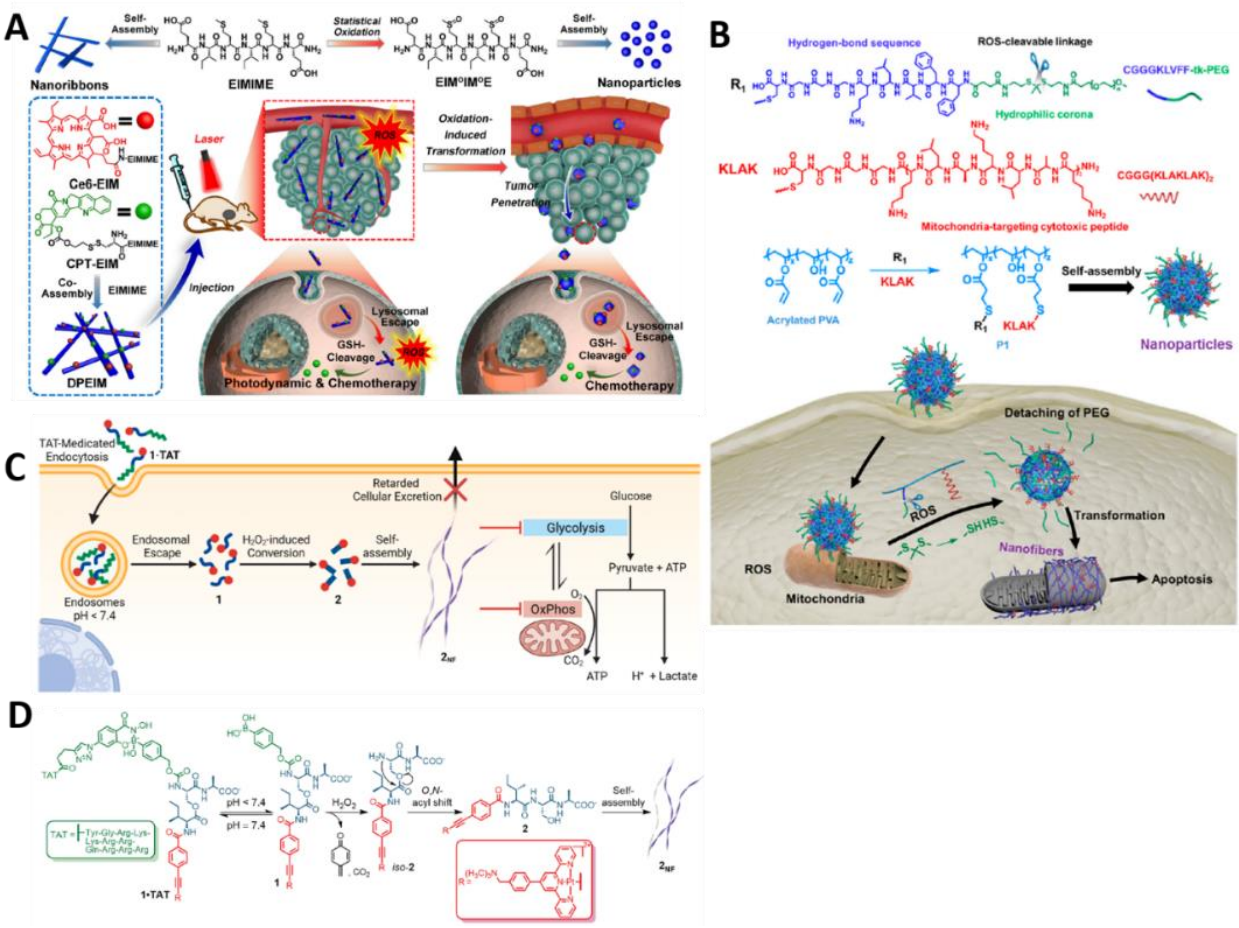

Figure 1.7. (A) Molecular structure of ROS-responsive EIMIME and schematic illustration of EIMIME with co-assembly of Ce6 and CPT undergo morphological transition by in situ ROS generation, resulting in the enhanced combinatorial photodynamic and chemo-therapeutic efficacy. **(B)** Synthetic route of ROS-sensitive PPCs and mitochondria locational morphology transformation. **(C)** Schematic illustration of the intracellular H_2O_2-induced formation of linear platinum (II) complexes that self-assemble into platinum (II)-containing nanofibers, which affects energy homeostasis and disrupts cellular metabolism. **(D)** Chemical design and reaction scheme for all chemical transformations of the ISA-platinum (II) complex 1·TAT into nanofibers 2_{NF}. Figure adapted from reference 38, 39, and 40.

pH-responsive peptide assembly. The physiological pH in tissue and inside cellular organelles has a large impact on biological processes. The local pH of tumor tissue is characterized by a slightly acidic pH (6.7-7.1) due to the enhanced glycolytic rate of cancer cells. The pH of early and late endosomes is even more acidic, which typically is around 4.7-6.3.[9] Because of the different local pH of tumor tissues compared to normal tissues, functional groups that are

susceptible to protonation or deprotonation under acidic tumor microenvironments have been utilized to construct acid-responsive peptide assembly for tumor therapeutics and imaging.

An acid-activatable self-assembling peptide-porphyrin conjugate was constructed by Hest group for photodynamic therapy (PDT) with prolonged tumor retention times.[41] The peptide-porphyrin conjugate (PWG) was designed by coupling the pH-responsive dipeptide tryptophan-glycine (WG) to hydrophobic porphyrin (P) core via amidation (**Figure 1.8A**). The function of tryptophan is to provide delocalized π electrons for fluorescence, and the carboxy group of glycine is to serve as the acid-sensitive unit. At physiological pH, peptide-porphyrin conjugate forms spherical nanoparticles because of the electrostatic repulsion among the deprotonated carboxyl group. When reaching tumor tissue, the acidic tumor microenvironment triggered the protonation of carboxyl group of PWG and consequently promoted the formation of intermolecular hydrogen bonds, inducing the transformation of nanoparticles into nanofibers, which exhibited enhanced accumulation and retention effects. The *in vitro* cellular uptake and intracellular localization assay show that PWG entered tumor cells through endocytosis and most of them were trapped in the lysosome. Under laser irradiation, the $^1O_2$ was generated by the porphyrin, showing potent cytotoxicity to MCF-7 breast tumor cells as demonstrated that 80% of tumor cells were killed by PWG compared to that under dark. The *in vivo* tumor-bearing mice model showed that the fluorescence signal of PWG reached strongest at 72 hrs and even could be detected at 360 hrs post-injection. Moreover, the PWG exhibited potent therapeutic efficiency which can completely eradicate mice tumors after 21 days. The *in vitro* and *in vivo* results demonstrates that PWG can be a novel fluorescence probe for long-time tumor imaging and ensure high therapeutic PDT efficiency. In another similar approach, an acid-adaptable pentapeptide was introduced by Yu lab.[42] As shown in **Figure 1.8B**, the functional modules of the pentapeptide, FF-Amp-FF (AmpF)

contains an acid-responsive noncanonical (*S, R*)-4-amino proline (Amp) that exhibits cis/trans-amide isomerization sensitive to acidic pH and a two diphenylalanine segments that provide driving forces for peptide assembly via π-π stacking. AmpF self-assembled into superhelices in blood vessels with pH 7.4. When reaching tumor tissues with typical slightly acidic pH of 6.5, the Amp underwent an isomerization transition from cis-amide to trans-amide, resulting in the morphological transformation from nanofibers to nanoparticles, which can be effectively internalized by tumor cells via endocytosis and following endo/lysosome escape to accumulate in the cytoplasm. The nearly neutral pH of cytoplasm the reversible transformation of AmpF from nanoparticles to nanofibers with enhanced tumor accumulation and retention times. To achieve the photodynamic therapy, the Ce6 was integrated into AmpF through peptide co-assembly method. The *in vitro* cytotoxicity results showed that the intracellular nanoparticle to nanofiber transformation allowed AmpF to exhibit the highest cellular uptake, generation of $^1O_2$ and breast cancer killing efficiency under laser irradiation compared to non-responsive AmpF and free Ce6. The *in vivo* mice data demonstrated that under laser irradiation, AmpF nanofibers can completely eradicate tumor cells up to 14 days with improved accumulation and retention at tumor sites. In another study, a pH-responsive self-assembling peptide (PSP) was developed by Hou group.[43] As shown in **Figure 1.8C**, PSP consisted of four functional motifs (i) a N-terminal hydrophobic motif, VVVVV, which promotes peptide assembly via hydrophobic interaction and intermolecular hydrogen bonding; (ii) a pH-sensitive linker, HH, which can be protonated under acidic conditions while remaining neutral under physiological conditions; (iii) a tumor targeting ligand, RGDC, which can specifically recognize and bind with integrin receptors on the tumor cell membrane; (iv) a C-terminal p53 activator, $^{D}T^{D}A^{D}W^{D}Y^{D}A^{D}N^{D}F^{D}E^{D}A^{D}L^{D}L^{D}R$ (^{D}PMI), which can activate p53 to inhibit tumor cell growth. ^{D}PMI self-assembled into spherical nanoparticles at physiological pH.

In the tumor acidic microenvironment, the protonation of histidine increased the electrostatic repulsion of nanoparticles, resulting in peptide disassembly to form nanoparticles with reduced size. The resultant nanoparticles entered tumor cells through integrin-mediated endocytosis and following the release of p53 activator to the cytoplasm via enzymatic hydrolysis. The released p53 can induce cell apoptosis to suppress tumor cell growth.

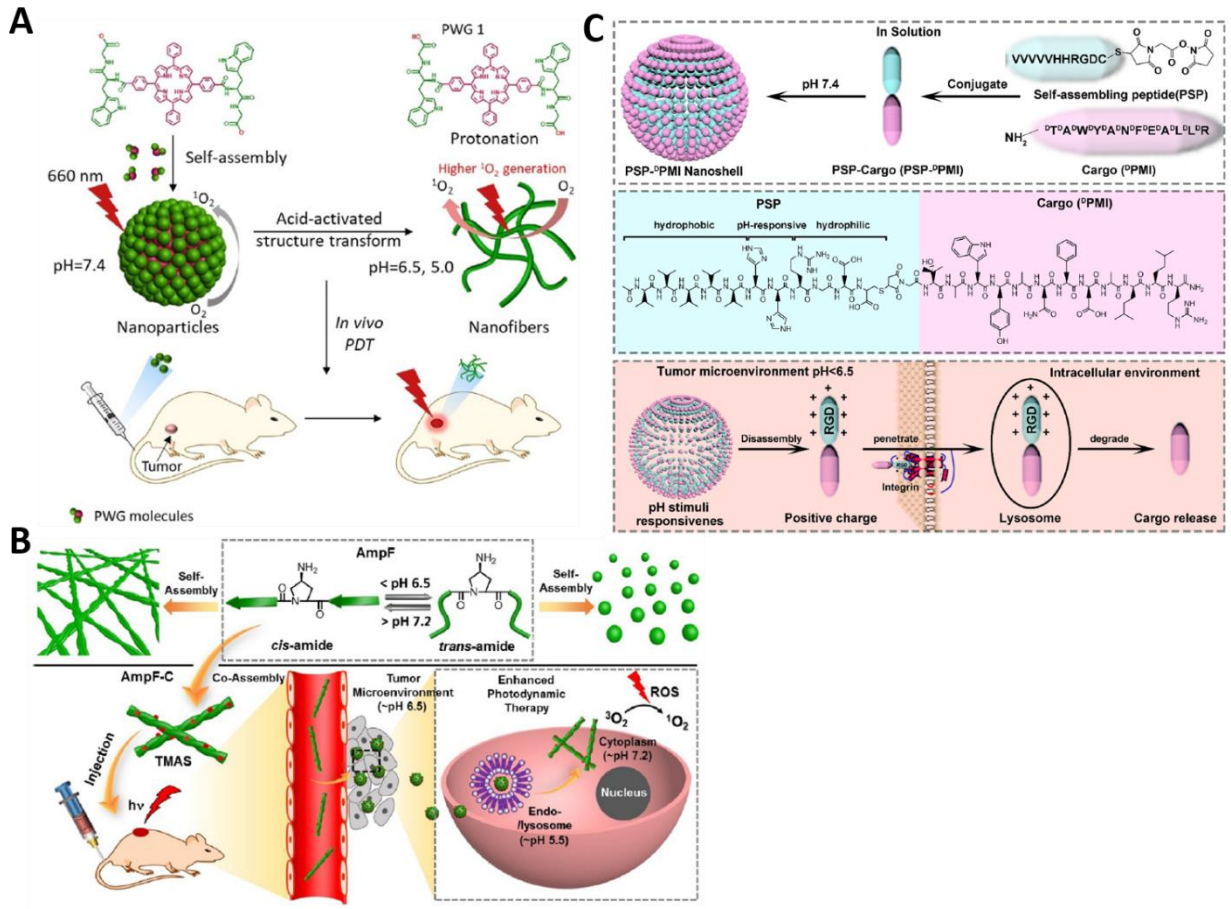

Figure 1.8. (A) Schematic illustration of acid-activatable self-assembly of PWG nanoparticles and their application in PDT. Protonation of PWG (PWG 1) in the acidic microenvironment of tumor tissue and lysosomes induces the nanoparticle-to-nanofiber transformation, inducing generation of singlet oxygen. **(B)** (Top) Pentapeptide AmpF undergoes a morphological transition between superhelices and nanoparticles promoted by the cis/trans-isomerization of Amp amide bonds. (Bottom) Creation of TMAS nanomedicines via co-assembly of AmpF and AmpF-C is capable of prolonging body circulation, facilitating tumor penetration and accumulation, and eventually increasing intracellular retention. **(C)** Schematic illustration of synthetic procedure and chemical structure of pH-responsive PSP-^{D}PMI. Figure adapted from reference 41, 42, and 43.

1.7 Trigger-responsive Peptide Self-assembly for Targeted Antimicrobial Therapy

The emergence of antibiotic resistance in bacteria has resulted in multidrug-resistant (MDR) bacterial infections. Particularly, the ESKAPE pathogens, including *Enterococcus faecium*, *S. aureus*, *Klebsiella pneumoniae*, *Acinetobacter baumannii*, *P. aeruginosa*, and *Enterobacter species*. These bacteria are responsible for most hospital-acquired infections, which requires the development of targeted bacterial therapy and is a challenge to health care worldwide. Recently, supramolecular peptide-based nanomaterials with the bottom-up structure design and versatile biological functions have received attention in the development of diagnosis and therapy for various diseases. Aromatic dipeptides and amphiphilic peptides serve as molecular building blocks that can self-assemble into well-defined supramolecular nanostructures via noncovalent interactions. It is also possible to endow the supramolecular peptide-based nanomaterials with a responsive property to external stimuli, promoting the development of targeted therapy for combating bacterial infections.

Peptide-antibiotic assembly. Vancomycin is a glycopeptide antibiotic widely used in the treatment of Gram-positive bacterial infections.[44] Through binding with the D-Ala-D-Ala dipeptide present in Gram-positive bacteria, vancomycin will inhibit cell wall biosynthesis and cause bacterial death.[45] Inspired by the specific targeting of vancomycin towards Gram-positive bacteria, the construction of self-assembling peptide-vancomycin conjugates that can selectively detect and eliminate Gram-positive bacteria has attracted attention in the field of targeted bacterial therapy.

Ren et al. constructed a diphenylalanine (FF)-based NBD-Vancomycin (Van) conjugate composed of an aromatic FF with self-assembling ability, in addition to Van with Gram-positive bacterial targeting capability and an environment-sensitive fluorescence probe, NBD. This

combination was used for detecting Gram-positive bacteria (**Figure 1.9A**).[46] By using a "surface-induced self-assembly" strategy, NBD-Van conjugates can self-assemble into nanoparticles on the bacterial surface through hydrogen bonding interactions of vancomycin towards the D-Ala-D-Ala dipeptide on Gram-positive bacteria. The resultant nanoparticles can enhance the fluorescence signal of NBD for simultaneous bacterial detection and inhibition.

In another approach, Yang et al. developed an AIEgen-peptide nanoprobe with aggregation-induced emission (AIE) effects.[47] As shown in **Figure 1.9B**, AIEgen-peptides have a general formula of TPE-Br-$^{D}F^{D}F^{D}Y^{D}E_{n}G^{D}K$-Vancomycin (Van) (n = 1, 2, 3). The AIE effect of the nanoprobe was contributed to 4,4'-(2-(4-bromophenyl)-2-phenylethene-1,1-diyl)bis(methoxybenzene) (TPE-Br). The presence of $^{D}F^{D}F^{D}Y^{D}$ provided self-assembling ability while vancomycin conferred Gram-positive bacterial targeting property. AIEgen-peptide conjugates can self-assemble to nanoaggregates in situ on the Gram-positive bacterial surface, inducing the fluorescence switching from "off" to "on". Under light irradiation, the production of reactive oxygen species (ROS) by AIEgens can inhibit bacterial growth. It should be noted that the bacterial sensitivity of AIEgen-peptide conjugates was demonstrated *in vitro* by using bioluminescent pathogenic bacteria, *S. aureus Xen 36* as a model strain. The limit of fluorescence detection of AIEgen-peptide conjugate was 2.4 x 10^3 CFU/mL, a 1000-fold reduction compared with bioluminescent signals.

To overcome the existing challenges in radio-nuclide-related imaging-based techniques for the detection of bacterial infections, which was sensitive to inflammatory reactions rather than specific bacterial pathogens, Yang et al. constructed a dual fluorescent- and isotopic-labeled self-assembling vancomycin, ^{125}I-Rho-FF-Vancomycin (Van), for precise imaging of methicillin-resistant *staphylococcus aureus* (*MRSA*) infection (**Figure 1.9C**).[48] This peptide-van conjugate-

based probe can self-assemble to nanoaggregates on the surface of *MRSA* through the multivalent binding of vancomycin and D-Ala-D-Ala on the bacterial wall. the *In* vivo fluorescence signal of Rho-FF-Van on the *MRSA*-induced infection site was 8.7-fold higher than that on the Gram-negative bacteria. Moreover, in *MRSA*-pneumonia mice, ^{125}I-Rho-FF-Van exhibited 8.9- to 13.3-fold higher isotope signals than non-assembling and healthy control groups.

Triclosan (TCS) is a synthetic antibiotic with broad-spectrum antimicrobial activities.[49] TCS can target and inhibit the synthesis of fatty acid in bacterial cell walls and disrupt the bacterial membrane, leading to bacterial death.[50] However, the low water solubility of triclosan limits its clinical use. To enhance the water solubility and antimicrobial efficiency of TCS, Yang et al. designed a "nanoantibiotic" composed of a self-assembling peptide, GFFY, and an antibiotic, TCS (**Figure 1.9D**).[51] This nanoantibiotic can self-assemble into nanofibers with bacterial membrane-disrupting property and slowly release the TCS to inhibit the synthesis of fatty acid at weakly acid bacterial infection sites. Nanoantibiotic via self-assembly of the antibiotic-peptide conjugate can increase TCS solubility by 850-fold and showed potent antimicrobial activities against both Gram-negative and Gram-positive bacteria.

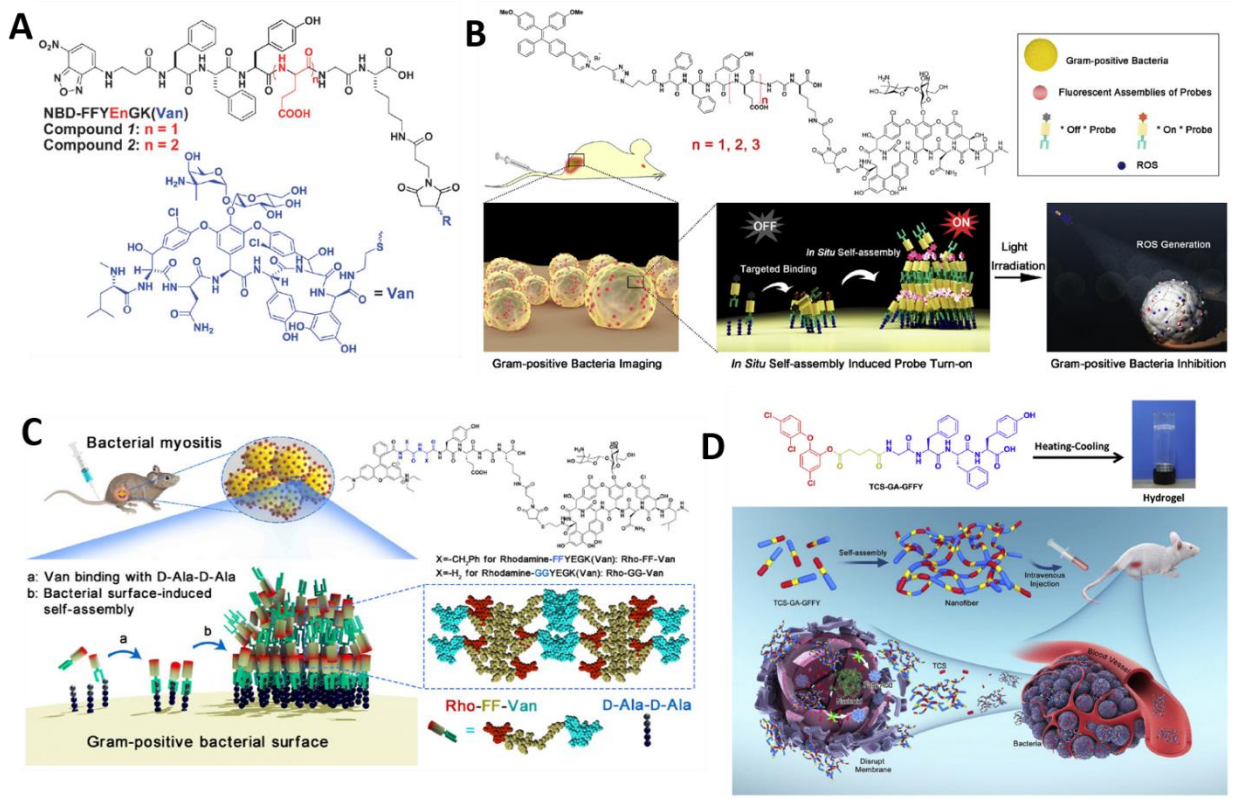

Figure 1.9. (A) Chemical structures of NBD-Van conjugates (1: NBD–FFYEGK(Van) and 2: NBD–FFYEEGK(Van)). **(B)** Chemical structures of AIEgen-peptide conjugates and schematic illustration of in situ self-assembled AIEgen-peptide conjugates for gram-positive bacteria diagnosis and therapy. **(C)** Molecular structures of Rho-FF-Van and Rho-GG-Van and illustration of bacterial surface-induced self-assembly of Rho-FF-Van. **(D)** Chemical structure of TCS-GA-GFFY and schematic illustration of the formation of the TCS-GA-GFFY hydrogel nanoantibiotic for the treatment of bacterial infections. Figure adapted from reference 46, 47, 48, and 49.

Self-assembled peptides. Pre-assembled peptides are also important for enhancing the sensitivity and specificity of targeted bacterial therapy.

P. aeruginosa, a Gram-negative bacteria, is responsible for pneumonia in cystic fibrosis sufferers.[52] Recently it has been reported that molecule c-di-GMP, bis-(3'-5')-cyclic dimeric guanosine monophosphate plays an important role in biofilm formation of Gram-negative bacteria.[53] To develop a targeted treatment of *P. aeruginosa*, Castelletto et al. designed a series of self-assembling arginine-based tripeptides, RXR (X = W, F, or non-natural residue 2-napthylalanine (2NAI)) that can selectively kill *P. aeruginosa* through targeting of c-di-GMP

(**Figure 1.10A**).[54] RXR can self-assemble to irregular fractal-like structures in an aqueous solution. Upon the interaction with c-di-GMP, the nanostructure transitions of RFR and RWR from irregular nanostructures to extended nanotape structures. In contrast, R2NAlR turned to large nanosheets. This morphology transition is due both to the electrostatic and π-stack interactions between RXR and c-di-GMP. The i*n vitro* bacterial killing and anti-biofilms assay showed RFR and RWR with higher binding ability with c-di-GMP exhibited selective antimicrobial activity against *P. aeruginosa*, compared to R2NAlR (**Figure 1.10B**).

Inspired by the unique antimicrobial mechanism of human defensin-6 (HD6), which can self-assemble into fibrous networks, trap microbial pathogens and block bacterial invasion, Fan et al. rationally constructed an HD6 mimic peptide (HDMP) for inhibition of Gram-positive bacterial invasion.[55] As shown in **Figure 1.10C**, the HDMP consisted of three functional motifs: (i) A peptide targeting ligand (RLYLRIGRR) that can specifically bind with lipoteichoic acid (LTA) on Gram-positive bacterial membranes; (ii) A self-assembling scaffold (KLVFF); (iii) Aromatic bis-pyrenes (BP) which provides the potential for transport of HDMP through intravenous administration. The HDMP first self-assembled into nanoparticles in aqueous solutions before being recognized by Gram-positive bacteria (*S. aureus*), and transformed into nanofibers, forming a fibrous network. Both *in vitro* and *in vivo* experiments show that these in situ self-assembled fibrous networks can trap *S. aureus,* inducing bacterial agglutination and inhibiting bacterial invasion.

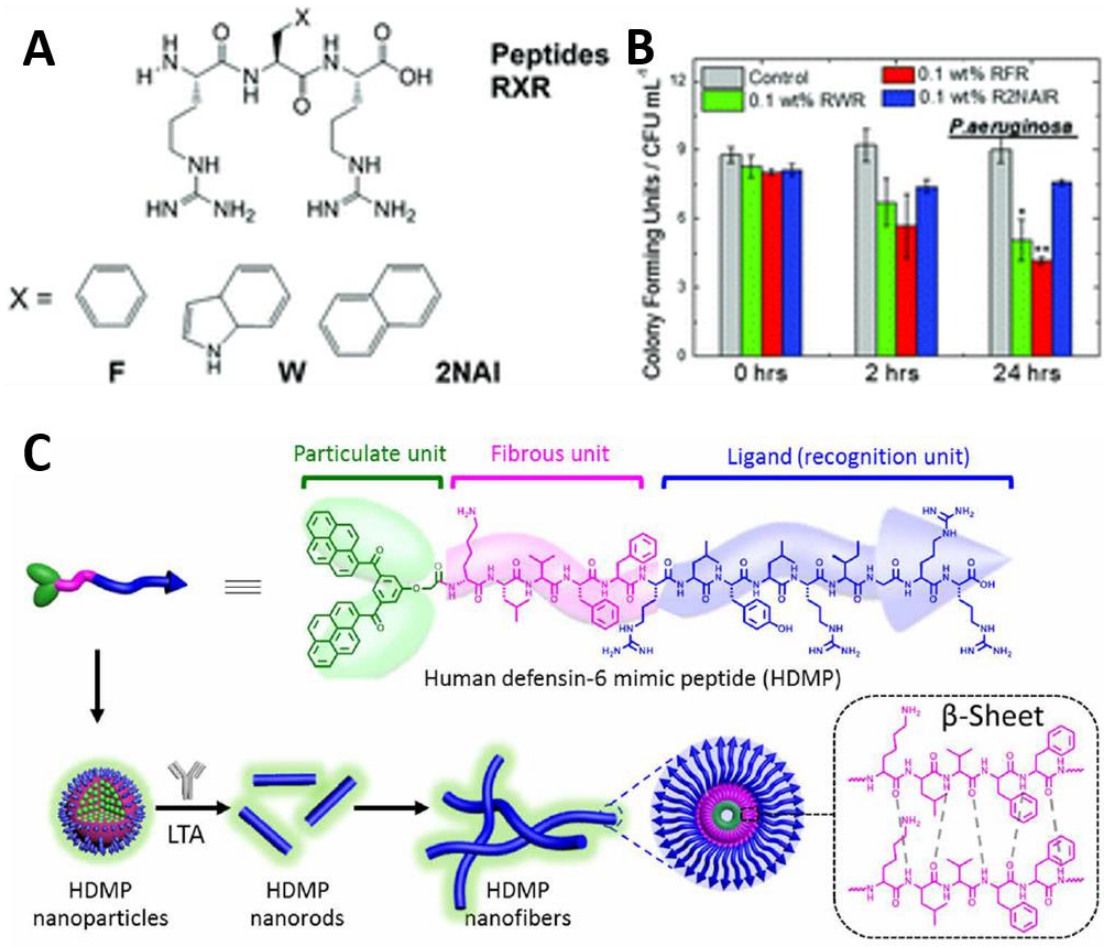

Figure 1.10. (A) Chemical structure of tripeptides RXR and **(B)** Antimicrobial activity against *P. aeruginosa* of RXR. **(C)** Molecular structures of HDMP and schematic illustration of HDMP assembly into NPs, transforming into nanorods and nanofibers (NFs) upon the incubation of lipoteichoic acid (LTA). Figure adapted from reference 54 and 55.

Bacterial microenvironment-triggered peptide assembly/disassembly. The local environments in bacteria-infected tissues are completely different from those of healthy cells.[56-58] By utilizing the unique infectious microenvironment caused by bacteria, the enhancement of antimicrobial activity and selectivity of supramolecular peptide based-nanomaterials can be achieved through peptide assembly/disassembly in response to external stimuli.

Yang et al. developed the first example of intracellular enzyme-responsive supramolecular assemblies that inhibited bacterial growth (**Figure 1.11A**).[59] The precursor of hydrogel with a

general formula $C_{10}H_7CH_2C(O)$-L-Phe-L-Phe-Tyr-$(PO(OH)_2)$. This precursor will penetrate bacteria through passive diffusion, and then be hydrolyzed by overexpressed ALP present in *E.coli*, cleaving the phosphate group and leading to the self-assembly of hydrogel, which can change the viscosity of the cytoplasm and stress the bacteria.

The survival of *S.aureus* inside phagocytic cells is one of the causes of the treatment failure of antibiotics.[60,61] Delivering antibiotics to eliminate *S. aureus* inside the macrophage remains a challenge, owing to its limited cell-penetrating ability and active exportation by the host cells.[62,63] To target intracellular bacteria, Cai et al. developed a chlorophyll-peptide based photoacoustic agent (MPC) for detection of intracellular *S.aureus*.[64] As shown in **Figure 1.11B**, the MPC consists of three motifs, a targeting ligand (mannose) that can specifically recognize macrophages, a caspase-1 responsive peptide linker, and a photoacoustic agent (PA). Mannose functionalization of MPC allowed mannose receptor-mediated cell uptake of the nanostructures into the macrophages. Overexpressed caspase-1 cleaved the responsive peptide linker, leading to the detachment of PA. The resultant fragment of PA self-assembled into aggregates and enhanced the photoacoustic signal allowing for the detection of *S. aureus* infection. In addition, *in vivo S. aureus* studies showed the PA intensity of MPC increased more than 2-fold over that of control agent, suggesting enhanced sensitivity and specificity to intracellular infected macrophages.

In another approach, Li et al. developed an enzyme-activated chlorophyll-peptide-vancomycin (Van)-based nanoprobe for specific and sensitive imaging of Gram-positive bacterial infection.[57] As shown in **Figure 1.11C**, this chlorophyll-peptide-van conjugate, Ppa-PLGVRG-Van, contained a photoacoustic contrast agent, a gelatinase responsive linker, and vancomycin. It was shown that it can specifically target the Gram-positive bacterial cell walls through hydrogen binding of vancomycin. Following this interaction, gelatinase overexpressed by Gram-positive

bacteria can selectively cleave the responsive linker, leading to the formation of twisted nanofibers on the bacterial membrane with an enhanced photoacoustic signal. Important to note is that *in vivo* *S. aureus* studies using an infected mouse model showed that Ppa-PLGVRG-Van can reduce the detection limits to 10^3 CFU/mL, much lower than that in previous reported,[65] suggesting its better sensitivity for the detection of Gram-positive bacterial infections.

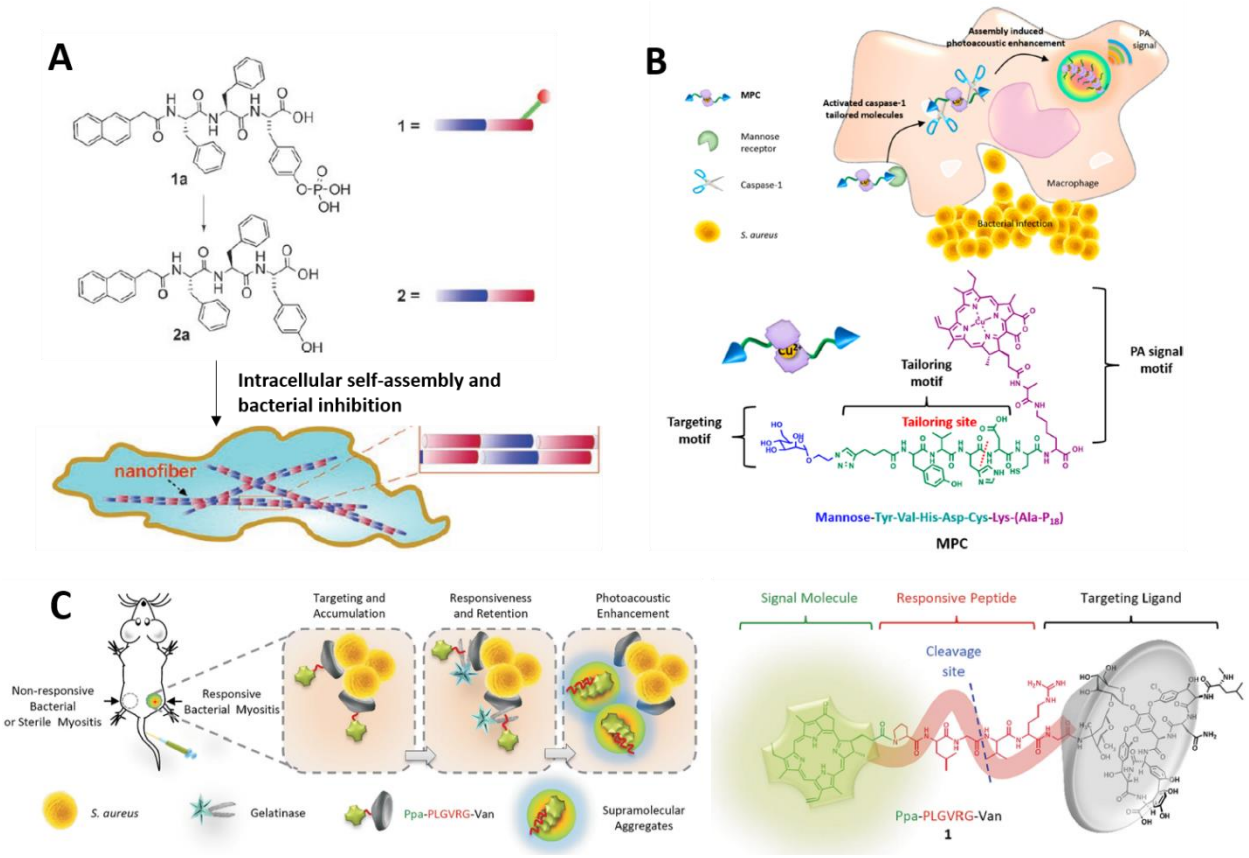

Figure 1.11. (A) Chemical structures of ALP-responsive peptide precursor (1a) and the corresponding gelator (2a) and schematic representation of intracellular nanofiber formation leading to the inhibition of bacterial growth. **(B)** Schematic representation of intracellular *S. aureus* infection detection *in vivo* and the molecular structure of MPC. **(C)** Illustration of bacterial infection imaging based on an *in vivo* aggregation strategy and molecular structure of Ppa-PLGVRG-Van. Figure adapted from reference 57, 59, and 64.

1.8 References

(1) Savyasachi, A. J.; Kotova, O.; Shanmugaraju, S.; Bradberry, S. J.; Ó'Máille, G. M.; Gunnlaugsson, T. Supramolecular chemistry: a toolkit for soft functional materials and organic particles. *Chem* **2017**, *3*, 764-811.

(2) Eskandari, S.; Guerin, T.; Toth, I.; Stephenson, R. J. Recent advances in self-assembled peptides: Implications for targeted drug delivery and vaccine engineering. *Adv. Drug Deliv. Rev.* **2017**, *110*, 169-187.
(3) Duan, X.; Rajan, N. K.; Routenberg, D. A.; Huskens, J.; Reed, M. A. Regenerative electronic biosensors using supramolecular approaches. *ACS nano* **2013**, *7*, 4014-4021.
(4) Tatman, P. D.; Muhonen, E. G.; Wickers, S. T.; Gee, A. O.; Kim, E.-S.; Kim, D.-H. Self-assembling peptides for stem cell and tissue engineering. *Biomater. Sci.* **2016**, *4*, 543-554.
(5) Hudalla, G. A.; Modica, J. A.; Tian, Y. F.; Rudra, J. S.; Chong, A. S.; Sun, T.; Mrksich, M.; Collier, J. H. A self-adjuvanting supramolecular vaccine carrying a folded protein antigen. *Adv. Healthc. Mater.* **2013**, *2*.
(6) Varanko, A.; Saha, S.; Chilkoti, A. Recent trends in protein and peptide-based biomaterials for advanced drug delivery. *Adv. Drug Deliv. Rev.* **2020**, *156*, 133-187.
(7) Lou, S.; Wang, X.; Yu, Z.; Shi, L. Peptide tectonics: encoded structural complementarity dictates programmable self-assembly. *Adv. Sci.* **2019**, *6*, 1802043.
(8) Chen, W.; Li, S.; Renick, P.; Yang, S.; Pandy, N.; Boutte, C.; Nguyen, K. T.; Tang, L.; Dong, H. Bacterial acidity-triggered antimicrobial activity of self-assembling peptide nanofibers. *J. Mater. Chem. B* **2019**, *7*, 2915-2919.
(9) Chagri, S.; Ng, D. Y.; Weil, T. Designing bioresponsive nanomaterials for intracellular self-assembly. *Nat. Rev. Chem.* **2022**, *6*, 320-338.
(10) Cui, H.; Webber, M. J.; Stupp, S. I. Self-assembly of peptide amphiphiles: From molecules to nanostructures to biomaterials. *Peptide Science: Original Research on Biomolecules* **2010**, *94*, 1-18.
(11) Matson, J. B.; Zha, R. H.; Stupp, S. I. Peptide self-assembly for crafting functional biological materials. *Curr. Opin. Solid State Mater. Sci.* **2011**, *15*, 225-235.
(12) Fleming, S.; Ulijn, R. V. Design of nanostructures based on aromatic peptide amphiphiles. *Chem. Soc. Rev.* **2014**, *43*, 8150-8177.
(13) McCloskey, A. P.; Draper, E. R.; Gilmore, B. F.; Laverty, G. Ultrashort self-assembling Fmoc-peptide gelators for anti-infective biomaterial applications. *J. Pept. Sci.* **2017**, *23*, 131-140.
(14) Fleming, S.; Debnath, S.; Frederix, P. W.; Tuttle, T.; Ulijn, R. V. Aromatic peptide amphiphiles: significance of the Fmoc moiety. *Chem. Commun.* **2013**, *49*, 10587-10589.
(15) Tang, C.; Smith, A. M.; Collins, R. F.; Ulijn, R. V.; Saiani, A. Fmoc-diphenylalanine self-assembly mechanism induces apparent p K a shifts. *Langmuir* **2009**, *25*, 9447-9453.
(16) Diaferia, C.; Morelli, G.; Accardo, A. Fmoc-diphenylalanine as a suitable building block for the preparation of hybrid materials and their potential applications. *J. Mater. Chem. B* **2019**, *7*, 5142-5155.
(17) Rughani, R. V.; Schneider, J. P. Molecular design of β-hairpin peptides for material construction. *MRS Bull.* **2008**, *33*, 530-535.
(18) Nagarkar, R. P.; Hule, R. A.; Pochan, D. J.; Schneider, J. P. De novo design of strand-swapped β-hairpin hydrogels. *J. Am. Chem. Soc.* **2008**, *130*, 4466-4474.
(19) Dong, H.; Paramonov, S. E.; Aulisa, L.; Bakota, E. L.; Hartgerink, J. D. Self-assembly of multidomain peptides: balancing molecular frustration controls conformation and nanostructure. *J. Am. Chem. Soc.* **2007**, *129*, 12468-12472.
(20) Moore, A. N.; Hartgerink, J. D. Self-assembling multidomain peptide nanofibers for delivery of bioactive molecules and tissue regeneration. *Acc. Chem. Res.* **2017**, *50*, 714-722.

(21) Wang, Y.; Zhang, X.; Wan, K.; Zhou, N.; Wei, G.; Su, Z. Supramolecular peptide nano-assemblies for cancer diagnosis and therapy: from molecular design to material synthesis and function-specific applications. *J. Nanobiotechnology* **2021**, *19*, 1-31.
(22) Shi, J.; Schneider, J. P. De novo design of selective membrane-active peptides by enzymatic control of their conformational bias on the cell surface. *Angew. Chem., Int. Ed. Engl.* **2019**, *58*, 13706-13710.
(23) Han, Q. J.; Lan, X. T.; Wen, Y.; Zhang, C. Z.; Cleary, M.; Sayyed, Y.; Huang, G.; Tuo, X.; Yi, L.; Xi, Z. Matrix metalloproteinase-9-responsive surface charge-reversible nanocarrier to enhance endocytosis as efficient targeted delivery system for cancer diagnosis and therapy. *Adv. Healthc. Mater.* **2021**, *10*, 2002143.
(24) Cheng, Z.; Cheng, Y.; Chen, Q.; Li, M.; Wang, J.; Liu, H.; Li, M.; Ning, Y.; Yu, Z.; Wang, Y. Self-assembly of pentapeptides into morphology-adaptable nanomedicines for enhanced combinatorial chemo-photodynamic therapy. *Nano Today* **2020**, *33*, 100878.
(25) Hu, B.; Lian, Z.; Zhou, Z.; Shi, L.; Yu, Z. Reactive oxygen species-responsive adaptable self-assembly of peptides toward advanced biomaterials. *ACS Appl. Bio Mater.* **2020**, *3*, 5529-5551.
(26) Hu, B.; Song, N.; Cao, Y.; Li, M.; Liu, X.; Zhou, Z.; Shi, L.; Yu, Z. Noncanonical amino acids for hypoxia-responsive peptide self-assembly and fluorescence. *J. Am. Chem. Soc.* **2021**, *143*, 13854-13864.
(27) Wang, H.; Feng, Z.; Wang, Y.; Zhou, R.; Yang, Z.; Xu, B. Integrating enzymatic self-assembly and mitochondria targeting for selectively killing cancer cells without acquired drug resistance. *J. Am. Chem. Soc.* **2016**, *138*, 16046-16055.
(28) Wu, C.; Zhang, R.; Du, W.; Cheng, L.; Liang, G. Alkaline phosphatase-triggered self-assembly of near-infrared nanoparticles for the enhanced photoacoustic imaging of tumors. *Nano Lett.* **2018**, *18*, 7749-7754.
(29) Zhan, J.; Cai, Y.; He, S.; Wang, L.; Yang, Z. Tandem molecular self-assembly in liver cancer cells. *Angew. Chem., Int. Ed. Engl.* **2018**, *130*, 1831-1834.
(30) Tanaka, A.; Fukuoka, Y.; Morimoto, Y.; Honjo, T.; Koda, D.; Goto, M.; Maruyama, T. Cancer cell death induced by the intracellular self-assembly of an enzyme-responsive supramolecular gelator. *J. Am. Chem. Soc.* **2015**, *137*, 770-775.
(31) Kalafatovic, D.; Nobis, M.; Son, J.; Anderson, K. I.; Ulijn, R. V. MMP-9 triggered self-assembly of doxorubicin nanofiber depots halts tumor growth. *Biomaterials* **2016**, *98*, 192-202.
(32) Yang, S.; Chang, Y.; Hazoor, S.; Brautigam, C.; Foss Jr, F. W.; Pan, Z.; Dong, H. Modular design of supramolecular ionic peptides with cell-selective membrane activity. *ChemBioChem* **2021**, *22*, 3164-3168.
(33) Cheng, D.-B.; Wang, D.; Gao, Y.-J.; Wang, L.; Qiao, Z.-Y.; Wang, H. Autocatalytic morphology transformation platform for targeted drug accumulation. *J. Am. Chem. Soc.* **2019**, *141*, 4406-4411.
(34) An, H.-W.; Li, L.-L.; Wang, Y.; Wang, Z.; Hou, D.; Lin, Y.-X.; Qiao, S.-L.; Wang, M.-D.; Yang, C.; Cong, Y. A tumour-selective cascade activatable self-detained system for drug delivery and cancer imaging. *Nat. Commun.* **2019**, *10*, 1-15.
(35) Nita, M.; Grzybowski, A. The role of the reactive oxygen species and oxidative stress in the pathomechanism of the age-related ocular diseases and other pathologies of the anterior and posterior eye segments in adults. *Oxid. Med. Cell. Longev.* **2016**, *2016*.
(36) Checa, J.; Aran, J. M. Reactive oxygen species: drivers of physiological and pathological processes. *J. Inflamm. Res.* **2020**, *13*, 1057.

(37) Shi, D.-y.; Xie, F.-z.; Zhai, C.; Stern, J. S.; Liu, Y.; Liu, S.-l. The role of cellular oxidative stress in regulating glycolysis energy metabolism in hepatoma cells. *Mol. Cancer* **2009**, *8*, 1-15.
(38) Song, N.; Zhou, Z.; Song, Y.; Li, M.; Yu, X.; Hu, B.; Yu, Z. In situ oxidation-regulated self-assembly of peptides into transformable scaffolds for cascade therapy. *Nano Today* **2021**, *38*, 101198.
(39) Cheng, D.-B.; Zhang, X.-H.; Gao, Y.-J.; Ji, L.; Hou, D.; Wang, Z.; Xu, W.; Qiao, Z.-Y.; Wang, H. Endogenous reactive oxygen species-triggered morphology transformation for enhanced cooperative interaction with mitochondria. *J. Am. Chem. Soc.* **2019**, *141*, 7235-7239.
(40) Zhou, Z.; Maxeiner, K.; Moscariello, P.; Xiang, S.; Wu, Y.; Ren, Y.; Whitfield, C. J.; Xu, L.; Kaltbeitzel, A.; Han, S. In situ assembly of Platinum (II)-metallopeptide nanostructures disrupts energy homeostasis and cellular metabolism. *J. Am. Chem. Soc.* **2022**.
(41) Sun, B.; Chang, R.; Cao, S.; Yuan, C.; Zhao, L.; Yang, H.; Li, J.; Yan, X.; van Hest, J. C. Acid-activatable transmorphic peptide-based nanomaterials for photodynamic therapy. *Angew. Chem., Int. Ed. Engl.* **2020**, *132*, 20763-20769.
(42) Li, M.; Ning, Y.; Chen, J.; Duan, X.; Song, N.; Ding, D.; Su, X.; Yu, Z. Proline isomerization-regulated tumor microenvironment-adaptable self-assembly of peptides for enhanced therapeutic efficacy. *Nano Lett.* **2019**, *19*, 7965-7976.
(43) He, W.; Yan, J.; Jiang, W.; Li, S.; Qu, Y.; Niu, F.; Yan, Y.; Sui, F.; Wang, S.; Zhou, Y. Peptide-induced self-assembly of therapeutics into a well-defined nanoshell with tumor-triggered shape and charge switch. *Chem. Mater.* **2018**, *30*, 7034-7046.
(44) Nagarajan, R. Antibacterial activities and modes of action of vancomycin and related glycopeptides. *Antimicrob. Agents Chemother.* **1991**, *35*, 605-609.
(45) Wang, F.; Zhou, H.; Olademehin, O. P.; Kim, S. J.; Tao, P. Insights into Key Interactions between Vancomycin and Bacterial Cell Wall Structures. *ACS Omega* **2018**, *3*, 37-45.
(46) Ren, C.; Wang, H.; Zhang, X.; Ding, D.; Wang, L.; Yang, Z. Interfacial self-assembly leads to formation of fluorescent nanoparticles for simultaneous bacterial detection and inhibition. *Chem. Commun.* **2014**, *50*, 3473-3475.
(47) Yang, C.; Hu, F.; Zhang, X.; Ren, C.; Huang, F.; Liu, J.; Zhang, Y.; Yang, L.; Gao, Y.; Liu, B. Combating bacterial infection by in situ self-assembly of AIEgen-peptide conjugate. *Biomaterials* **2020**, 119972.
(48) Yang, C.; Ren, C.; Zhou, J.; Liu, J.; Zhang, Y.; Huang, F.; Ding, D.; Xu, B.; Liu, J. Dual fluorescent- and isotopic-labelled self-assembling vancomycin for in vivo imaging of bacterial infections. *Angew. Chem., Int. Ed. Engl.* **2017**, *56*, 2356-2360.
(49) Machado, A. H. S.; Garcia, I. M.; Motta, A. d. S. d.; Leitune, V. C. B.; Collares, F. M. Triclosan-loaded chitosan as antibacterial agent for adhesive resin. *J. Dent.* **2019**, *83*, 33-39.
(50) Howse, G. L.; Bovill, R. A.; Stephens, P. J.; Osborn, H. M. I. Synthesis and antibacterial profiles of targeted triclosan derivatives. *Eur. J. Med. Chem.* **2019**, *162*, 51-58.
(51) Yang, L.; Zhang, C.; Huang, F.; Liu, J.; Zhang, Y.; Yang, C.; Ren, C.; Chu, L.; Liu, B.; Liu, J. Triclosan-based supramolecular hydrogels as nanoantibiotics for enhanced antibacterial activity. *J. Control. Release* **2020**, *324*, 354-365.
(52) Doring, G.; Conway, S.; Heijerman, H.; Hodson, M.; Hoiby, N.; Smyth, A.; Touw, D. Antibiotic therapy against Pseudomonas aeruginosa in cystic fibrosis: a European consensus. *Eur. Respir. J.* **2000**, *16*, 749-767.
(53) Hengge, R. Principles of c-di-GMP signalling in bacteria. *Nat. Rev. Microbiol.* **2009**, *7*, 263-273.

(54) Castelletto, V.; Edwards-Gayle, C. J.; Hamley, I. W.; Barrett, G.; Seitsonen, J.; Ruokolainen, J.; de Mello, L. R.; da Silva, E. R. Model self-assembling arginine-based tripeptides show selective activity against Pseudomonas bacteria. *Chem. Commun.* **2020**, *56*, 615-618.
(55) Fan, Y.; Li, X.-D.; He, P.-P.; Hu, X.-X.; Zhang, K.; Fan, J.-Q.; Yang, P.-P.; Zheng, H.-Y.; Tian, W.; Chen, Z.-M. A biomimetic peptide recognizes and traps bacteria in vivo as human defensin-6. *Sci. Adv.* **2020**, *6*, eaaz4767.
(56) Zhang, X.; Ren, C.; Hu, F.; Gao, Y.; Wang, Z.; Li, H.; Liu, J.; Liu, B.; Yang, C. Detection of bacterial alkaline phosphatase activity by enzymatic in situ self-assembly of the AIEgen-peptide conjugate. *Anal. Chem.* **2020**, *92*, 5185-5190.
(57) Li, L. L.; Ma, H. L.; Qi, G. B.; Zhang, D.; Yu, F.; Hu, Z.; Wang, H. Pathological-condition-driven construction of supramolecular nanoassemblies for bacterial infection detection. *Adv. Mater.* **2016**, *28*, 254-262.
(58) Azzopardi, E. A.; Ferguson, E. L.; Thomas, D. W. The enhanced permeability retention effect: a new paradigm for drug targeting in infection. *J. Antimicrob. Chemother.* **2013**, *68*, 257-274.
(59) Yang, Z.; Liang, G.; Guo, Z.; Guo, Z.; Xu, B. Intracellular hydrogelation of small molecules inhibits bacterial growth. *Angew. Chem., Int. Ed. Engl.* **2007**, *46*, 8216-8219.
(60) Lehar, S. M.; Pillow, T.; Xu, M.; Staben, L.; Kajihara, K. K.; Vandlen, R.; DePalatis, L.; Raab, H.; Hazenbos, W. L.; Hiroshi Morisaki, J. Novel antibody–antibiotic conjugate eliminates intracellular S. aureus. *Nature* **2015**, *527*, 323-328.
(61) Gresham, H. D.; Lowrance, J. H.; Caver, T. E.; Wilson, B. S.; Cheung, A. L.; Lindberg, F. P. Survival of Staphylococcus aureus inside neutrophils contributes to infection. *J. Immunol.* **2000**, *164*, 3713-3722.
(62) Kamaruzzaman, N. F.; Kendall, S.; Good, L. Targeting the hard to reach: challenges and novel strategies in the treatment of intracellular bacterial infections. *Br. J. Pharmacol.* **2017**, *174*, 2225-2236.
(63) Ibarra, J. A.; Steele-Mortimer, O. Salmonella–the ultimate insider. Salmonella virulence factors that modulate intracellular survival. *Cell. Microbiol.* **2009**, *11*, 1579-1586.
(64) Cai, Q.; Fei, Y.; Hu, L.; Huang, Z.; Li, L.-L.; Wang, H. Chemotaxis-instructed intracellular Staphylococcus aureus infection detection by a targeting and self-assembly signal-enhanced photoacoustic probe. *Nano Lett.* **2018**, *18*, 6229-6236.
(65) Qi, G.; Li, L.; Yu, F.; Wang, H. Vancomycin-modified mesoporous silica nanoparticles for selective recognition and killing of pathogenic gram-positive bacteria over macrophage-like cells. *ACS Appl. Mater. Interfaces* **2013**, *5*, 10874-10881.

Chapter 2: Design of Peptide Self-assembly for Targeted Cancer Cell Imaging*

2.1 Introduction

Designing nanomaterials with a comprehensive understanding of the role of targeting ligand density and geometry in governing of tumor-targeting efficiency is still underway. Construction of multivalent targeting ligands covalently bonded with polymetric scaffolds has been considered as an effective strategy to enhance tumor targeting efficiency for the delivery of contrast agents and therapeutic drugs to targeted diseased tissues.[1-9] An optimal targeting system should have little affinity for healthy cells but a high affinity for pathologic cells in order to maximize both biological safety and therapeutic efficacy. Currently, the main strategies to generate multivalent ligands rely on covalent synthesis of low molecular weight dendrimers or macromolecular scaffolds which contain multiple copies of ligands capable of binding cell surface receptors existing on cell membranes. However, dendrimers-based targeting ligands typically have short blood circulation and quick clearance, resulting in low tumor targeting efficiency.[10-12] On the other hand, while synthetic ligands localized on a macromolecular scaffold have been successful in targeting tumor tissues, their large size represents a major challenge for both deep penetration of solid tumors and excretion of the nonspecifically bound molecules.[13,14] Incorporating small molecule ligands into polymers or nanoparticles can be an effective strategy for improving targeting efficiency, but surface modification may lead to an increase in bulk, which limits access to diseased tissue and prevents or retards clearance from healthy organs.[15]

* This chapter is based on Weike Chen, Shuxin Li, John C. Lang, Yan Chang, Zui Pan, Peter Kroll, Xiankai Sun, Liping Tang, He Dong. Combined tumor environment triggered self‐assembling peptide nanofibers and inducible multivalent ligand display for cancer cell targeting with enhanced sensitivity and specificity. *Small*, **2020**, *16*, 2002780. Some sections were rearranged for continuity.

Recently, there have been remarkable advances in the development of trigger-responsive *in situ* self-assembly for directing tumor specificity.[16-25] In this strategy, small molecules or oligopeptides are designed to undergo chemical transformation under tumor-associated physiological conditions and subsequently induce supramolecular assembly at the tumor site in order to perform desired functions. Enzyme-instructed peptide self-assembly has attracted great attention for targeted cancer therapy due to the overexpression of certain enzymes in diseased tissues. Among many noteworthy examples, the Xu and Uljin group have developed a range of intracellular and extracellular enzyme-triggered self-assembly for selectively killing cancer cells, such as alkaline phosphatase (ALP), carboxylesterase and matrix metalloproteinase (MMP) responsive design.[19,20,26-29] The Maruyama reported a novel mechanism for cancer cell targeting and killing through MMP-7 triggered supramolecular hydrogels that can induce intracellular stress on cancer cells.[21] Tandem molecular self-assembly was recently demonstrated by the Yang group to kill liver cancer cells selectively.[30] The Wang group designed and synthesized a series of tumor microenvironment-induced peptide and peptide-polymer self-assemblies for targeted *in vivo* cancer imaging and therapy.[31-34] The Schneider group studied the conformational landscape of self-assembled peptides under enzymatic control and provided important insights into supramolecular assembly activity by controlling peptide conformation.[35] The Nilsson group demonstrated a powerful method for controlling self-assembly using reduction as triggers.[36] The above studies illustrate that *in situ* triggered self-assembly has the potential for overcoming constraints of poor tissue penetration of bulk assemblies while maximizing retention time for low molecular weight therapeutics which only self-assemble at the site of tumor tissues for enhanced tumor accumulation. Most recently the Yang group reported on the selective formation of supramolecular peptide nanofiber hydrogels with combined features of tumor-triggered self-

assembly and multivalent presentation of ligands for the cell membrane receptor (CCK2R) to inhibit cancer cells.[24] This approach provided additional benefits to further improve cancer cell targeting specificity by targeting both tumor microenvironment and cell surface receptors although the sensitivity remains largely unexplored because a relatively high peptide concentration is often needed to induce hydrogel formation *in situ*.

Inspired by the above studies, in an attempt to improve both tumor cell targeting specificity and sensitivity, we developed a new tumor microenvironment-responsive supramolecular peptide-based scaffold and use it to direct multivalent ligand presentation for tumor cell targeting. The strategy involves the design of a ligand conjugated self-assembling monomer precursor (SAM-P). SAM-P consists of a β-sheet forming peptide as the self-assembling domain, which is linked to a sheddable cationic domain *via* a tumor-responsive element at the C-terminus. The targeting ligand is attached at the N-terminus of the β-sheet forming peptide (**Figure 2.1**). The hypothesis is that in the presence of a cationic capping domain with considerable electrostatic repulsion, the SAM-P does not have the ability to self-assemble, and therefore can display only a monovalent ligand. However, in a tumor mimicking microenvironment, with the capping domain selectively cleaved by a reducing agent, such as glutathione which is often elevated in the tumor microenvironment, chemical transformation of the SAM-P to the SAM active building blocks occurs, which is followed by self-assembly of the SAMs to form supramolecular assemblies with induced multivalent ligand presentations. These β-sheet forming peptides can be modularly designed to form either supramolecular nanofibers with different lengths or spherical particles displaying multivalent ligands towards cell surface receptors. The effect of supramolecular structures and resulted multivalent ligand presentation on cancer cell targeting specificity and sensitivity has been investigated through combined biophysical characterization and *in vitro* fluorescence assay.

Through these preliminary findings, we have established a phenomenological rationale for a self-assembly mechanism by which supramolecular assemblies with multivalent ligand presentation can be *in situ* generated at diseased sites capable of enhancing both targeting specificity and sensitivity.

2.2 Results and Discussion

2.2.1 Peptide Design

Figure 2.1 shows the design and chemical structure of SAM-P used in this study and the mechanism of action in response to a tumor-specific stimulus. A general design strategy involves covalent attachment of a cationic domain, such as oligo-lysine through a tumor-specific linker at the C-terminus of a β-sheet forming peptide that can self-assemble when standing alone. The N-terminus of the peptide is appended with a targeting ligand through a flexible triglycine linker. The hypothesis is that with the oligo-lysine domain, the precursor SAM-P does not have the ability to self-assemble due to strong electrostatic repulsion. Rather it forms unimers that have monovalent ligand presentation and therefore weak targeting ability. In a tumor microenvironment, an environment-specific trigger cleaves the highly charged oligo-lysine domain to increase the self-assembling capacity of the retained β-sheet peptide on the SAM, thus leading to supramolecular assemblies with multivalent ligand presentation for enhanced tumor targeting. For proof-of-concept, we synthesized SAM-P with a disulfide bond linker capable of responding to a reductive tumor-mimicking microenvironment in which higher levels of glutathione are found than normal tissues.[37] The synthesis of the disulfide bond linker follows a previous procedure by the Yang group and we have recently used it for the synthesis of a range of reduction-sensitive cell

penetrating peptides.[38,39] We used a linear Arg-Gly-Asp-Ser (RGDS) peptide as a model targeting ligand toward $\alpha_v\beta_3$ integrin receptor overexpressed on some tumor cells.[40-42]

The key component of SAM-P is the self-assembling peptide domain which is based on *de novo* designed multidomain peptides (MDPs). In the past decade, we and several other groups studied self-assembled MDPs and showed their therapeutic efficacy and excellent biocompatibility as tissue scaffolds,[43-46] drug and gene delivery vehicles,[38,47-50] and recently antimicrobial agents.[51-54] As demonstrated previously, the MDP was designed to have a general sequence of $K_x(QL)_yK_x$ in which x and y represent the numbers of lysine (K) residues and the numbers of glutamine (Q) and leucine (L) pairs of repeating units. The alternating hydrophilic-hydrophobic (QL) domain drives the self-assembly to form "sandwich"-like β-sheet nanofibers while the terminal domains drive disassembly due to electrostatic repulsion among the lysine residues. The end products reflect a balance between the attractive forces provided by the (QL) repeating units, the repulsive forces among the lysine residues and entropic disordering. A wide range of supramolecular nanostructures can be synthesized by adjusting the length ratio between the central and terminal blocks to control both the thermodynamics and kinetics of the self-assembly process.

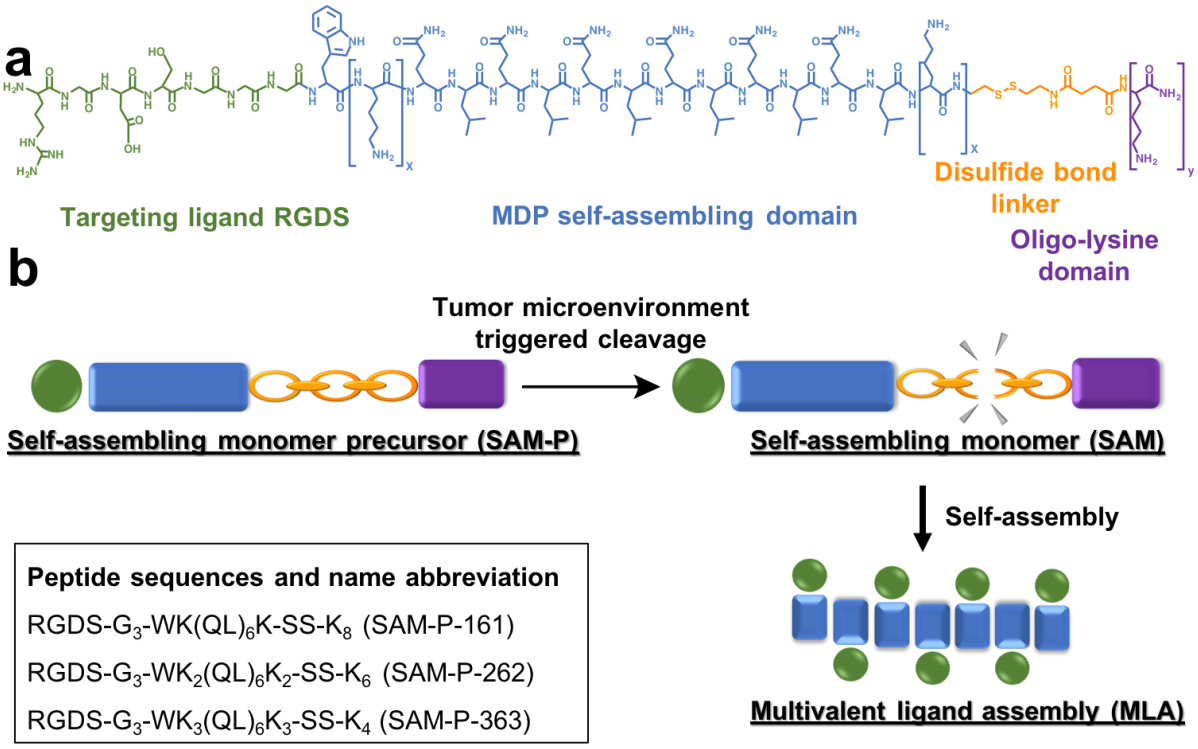

Figure 2.1. Illustration of the chemical design of the assembling precursor that undergoes reduction-triggered self-assembly to form supramolecular assemblies with multivalent ligand presentation for tumor targeting. a) Color-coded representation of the assembling precursor containing (i) targeting ligand such as RGDS; (ii) self-assembling MDP domain; (iii) disulfide bond linker and (iv) sheddable oligo-lysine domain. b) Illustration of the tumor microenvironment triggered cleavage of SAM-P and the self-assembly of the cleavage product, SAM, to form supramolecular assemblies with multivalent ligand presentation.

In this study, we have synthesized SAM-P based on three MDP sequences which have the same number of (QL) repeating units, at six, but varying numbers of lysine residues from 1 to 3. Based on our previous work,[55] the selection of these MDPs is expected to generate supramolecular assemblies of different morphologies with multivalent ligand presentation. As mentioned above, we appended RGDS at the N-terminus of the MDPs and a sheddable oligo-lysine block at the C-terminus through a disulfide bond linker (labeled as SS) to allow trigger-responsive self-assembly. **Figure 2.1** shows the sequences of all the precursors and their name abbreviations. For example, the SAM-P with the sequence of RGDS-G_3-$WK(QL)_6K$-(SS)-K_8 is abbreviated as SAM-P-161 in which the numbers define the balance within the MDP, i.e., #1 refers to the number of internal

lysine residues flanking both ends of the (QL) domain and #6 is the number of (QL) repeating units. Similarly, SAM-P-262 represents the sequence of RGDS-G_3-$WK_2(QL)_6K_2$-(SS)-K_6 and SAM-P-363 refers to the sequence of RGDS-G_3-$WK_3(QL)_6K_3$-(SS)-K_4. Tryptophan was included for accurate determination of peptides' concentration by UV spectroscopy. Note the total number of lysine on all SAM-P is conserved and set at 10 to allow sufficient charge repulsion to prevent spontaneous self-assembly before their exposure to the reductive microenvironment.

2.2.2 Structural Characterization

To explore the vulnerability of the SAM-P to cleavage by a reductive microenvironment, we incubated them with dithiothreitol (DTT) in Tris buffer (pH 7.4, 20 mM) for 2 hrs and monitored the cleavage reaction by high-performance liquid chromatography (HPLC) and matrix-assisted laser desorption/ionization (MALDI) mass spectrometry. Both HPLC (**Figure 2.2**) and MALDI (**Figure 2.3A-C**) confirmed the completion of the cleavage reaction for all precursors upon treatment with DTT. The mass of the cleavage products corresponds to the molecular weights of peptide fragments upon disulfide bond cleavage. For example, for SAM-P-161, the molecular ion peak was found to be at 3751.19 in the absence of DTT (**Figure 2.3A**). Upon the addition of DTT, the peak shifted to a lower m/z value at 2552.95 corresponding to the mass of the peptide which was specifically cleaved at the disulfide bond. As shown by the reverse-phase HPLC results (**Figure 2.2**), the increase of retention time upon DTT treatment suggests the cleavage products are more hydrophobic than the precursors which consist of a larger fraction of hydrophilic lysine residues. To investigate whether self-assembly can occur under the reducing condition, we performed critical assembly concentration (CAC) measurements. CACs were determined using a previously established fluorescence self-quenching method.[53] Previously, we used tryptophan as the fluorophore for monitoring the fluorescence intensity as a function of peptide intensity. In the

current work, we used nitrobenzoxadiazole (NBD) as a more sensitive fluorescence probe for CAC determination. At the CAC, fluorescence quenching occurs leading to a deviation of the linearity of fluorescence increase with concentration. As shown in **Figure 2.3D-F**, a non-linear relationship was observed for all three precursors after DTT treatment suggesting higher-ordered assemblies were formed as concentrations were increased. The CAC values were determined at 6.4 μM, 8.4 μM and 8.9 μM for SAM-P-161, SAM-P-262 and SAM-P-363, respectively. CACs have been commonly used to evaluate the thermodynamic stability of amphiphilic assemblies. The trend of CAC values observed here is consistent with the design in which the equilibrium favors self-assembly as the length of the retained lysine domain was reduced on the MDPs. It is also worth noting the red shift in fluorescence spectra as the concentration of peptides increased to induce self-assembly in the presence of DTT. It is also worth noting the red shift in fluorescence spectra as the concentration of peptides increased to induce self-assembly in the presence of DTT (**Figure 2.4**). Based on literature studies,[56] the degree of red shift in fluorescence emission correlates with the degree of solvent exposure of the NBD moiety and possibly the numbers of self-assembling species and the structural flexibility of the NBD moiety on these nanostructures. For all other physical characterization and *in vitro* cell-based experiments, the experimental concentration of all precursors is above their respective CAC to favor the equilibrium toward self-assembly.

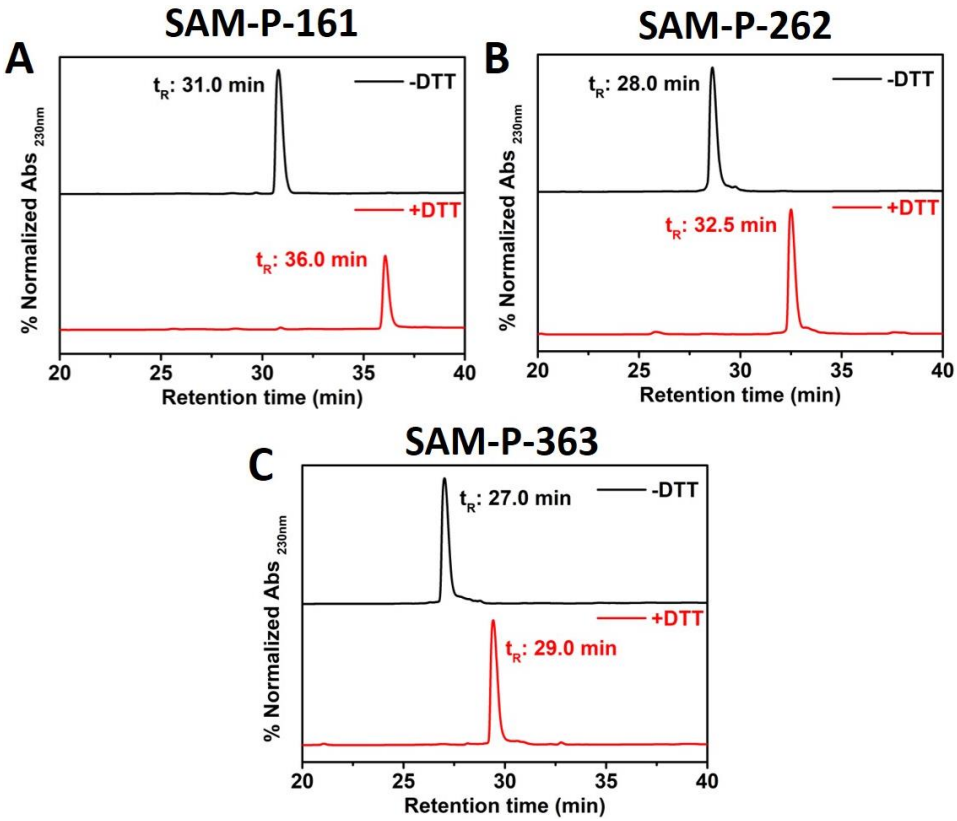

Figure 2.2. HPLC analysis of **(A)** SAM-P-161 **(B)** SAM-P-262 and **(C)** SAM-P-363 in the absence/presence of DTT (1 mM) in Tris buffer (pH 7.4, 20 mM). Peptide concentration: 50 μM. Incubation time: 2 hrs.

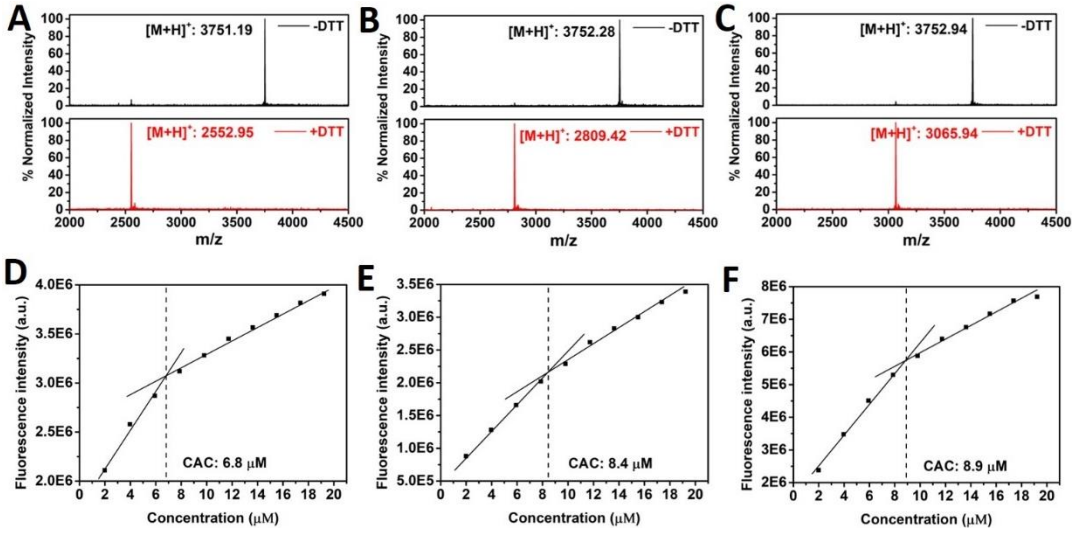

Figure 2.3. MALDI mass spectrometry characterization of **(A)** SAM-P-161, **(B)** SAM-P-262 and **(C)** SAM-P-363 with and without DTT in Tirs buffer (pH = 7.4, 20 mM). CAC determination of **(D)** SAM-P-161, **(E)** SAM-P-262, and **(F)** SAM-P-363 with pre-treatment with DTT (10 mM) for 2 hrs to induce self-assembly.

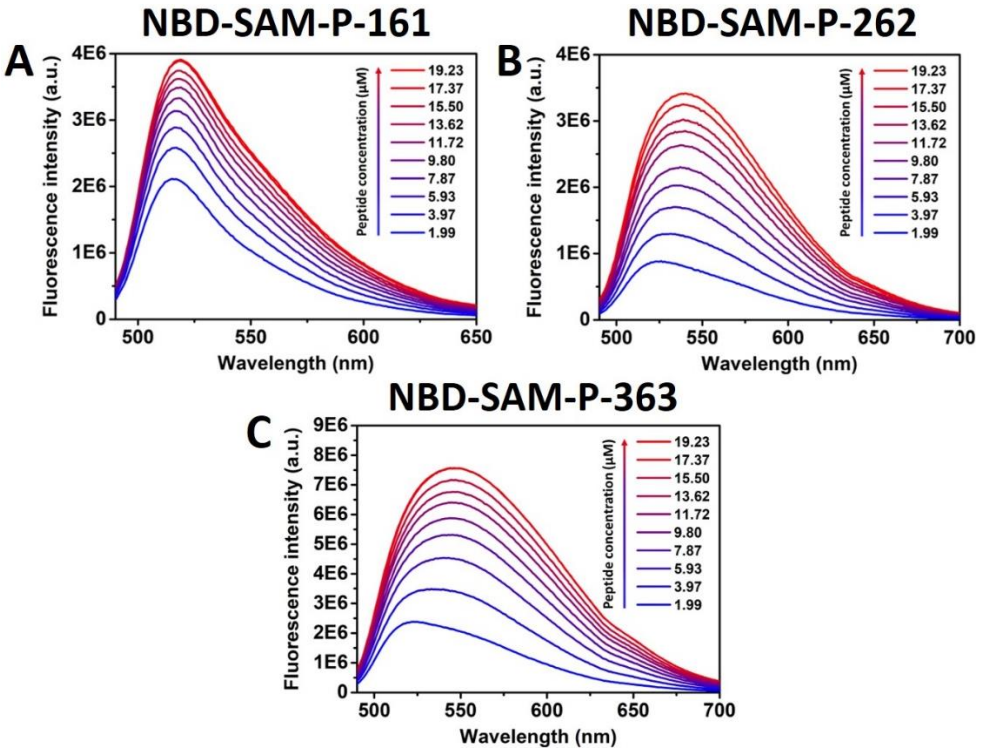

Figure 2.4. Fluorescence emission spectra of **(A)** NBD-SAM-P-161 **(B)** NBD-SAM-P-262 and **(C)** NBD-SAM-P-363 as a function of peptide concentration in Tris buffer (pH 7.4, 20 mM) upon pre-incubation with DTT for 2 hrs. Concentrated NBD labeled peptide solutions (500 μM) were pre-incubated with DTT (10 mM) for 2 hrs and used for incremental addition of peptide solution to Tris buffer.

Reduction-triggered self-assembly was investigated by circular dichroism (CD) spectroscopy and negatively stained transmission electron microscopy (TEM). CD spectroscopy provided information about molecular secondary structures and TEM revealed how molecules are packed into a supramolecular structure and their morphologies. As shown in **Figure 2.5**, in the absence of DTT, all three precursors formed predominantly α-helical structures indicated by the presence of the two characteristic minima at 208 nm and 222 nm in the CD spectra. TEM showed spherical aggregates under the non-reductive condition without DTT (**Figure 2.6A-C**). Dynamic light scattering (DLS) suggested a particle with a hydrodynamic diameter at ~ 5.4 nm (**Figure 2.6J-L**), likely composed of SAM-P in the form of small oligomers having a low density of targeting ligands. Upon incubation with DTT to remove the oligo-lysine domain at the C-terminus,

the SAM-P-161 and SAM-P-262 precursors revealed a structural transition from α-helices to β-sheets (**Figure 2.5A** and **2.5B**), which was accompanied by supramolecular nanofiber formation (**Figure 2.6D-E** and **2.6G-H**) as monitored by TEM. DLS was also used to monitor DTT-triggered self-assembly and possible structural change in the solution state. It should be noted that the hydrodynamic diameter obtained from the DLS measurements may not provide the actual size of non-spherical nanostructures, such as nanofibers, but gives an evaluation of a rotationally averaged particle dimension as a semi-quantitative measure. DLS showed an increase of "averaged" hydrodynamic diameters for both SAM-P-161 and SAM-P-262 upon the addition of DTT, further supporting reduction-triggered supramolecular assembly to form a larger scale nanostructure. Based on the time-dependent CD and TEM studies, it was found that SAM-P-262 required longer incubation time to be converted to β-sheets and form nanofibers than SAM-P-161. In addition, nanofibers formed by SAM-P-262 upon DTT cleavage tend to be longer, but lower in concentration than those formed by SAM-P-161 (**Figure 2.6G** and **2.6H**). The trend of "averaged" hydrodynamic diameter changes as evaluated by DLS is consistent with the TEM results showing a time-dependent reduction triggered supramolecular nanofiber assembly (**Figure 2.6J** and **2.6K**). For example, after 2 hrs of incubation with DTT, the diameter of the SAM-P-161 assembly is 39 nm compared to 109 nm for the SAM-P-262 assembly. After 8 hrs, although the size of both assemblies increased, the diameter of SAM-P-161 (d = 52 nm) was still smaller than that of SAM-P-262 (d = 170 nm). Although the detailed mechanism for different fiber morphology is not fully understood, the structural polymorphism observed for protein nanofibers is not uncommon in nature, especially for amyloid-like β-sheet peptide assembly. As parts of our continuing research interests, we will focus on understanding the molecular mechanisms responsible for the different fiber morphologies, which are likely attributed to their sequence-dependent nucleation and

assembly kinetics, as commonly reported for amyloid-like mimetic assemblies.[57] While a significant structural change was induced on SAM-P-161 and SAM-P-262, the molecular structure of SAM-P-363 did not change upon DTT treatment (**Figure 2.5C**). TEM showed spherical particles of 10-20 nm in diameter for SAM-P-363 after DTT treatment (**Figure 2.6F** and **2.6I**) although larger nanoparticles with diameters of 50-70 nm were occasionally observed. Some of the particles seem to have a hollow interior likely due to structural collapse. It is worth noting that the reduction of particle size due to structural collapse is not uncommon for nanostructures, such as liposomes that are susceptible to the drying condition during negatively stained TEM sample preparation.[58,59] As such, we performed DLS measurement which represents a more accurate method to determine the size of SAM-P-363 with and without DTT in the solution state. DLS revealed a much larger hydrodynamic diameter for SAM-P-363 upon DTT treatment than peptide without DTT (**Figure 2.6L**), suggesting SAM-P-363 can also undergo DTT-triggered self-assembly to form supramolecular structures consisting of multivalent ligands.

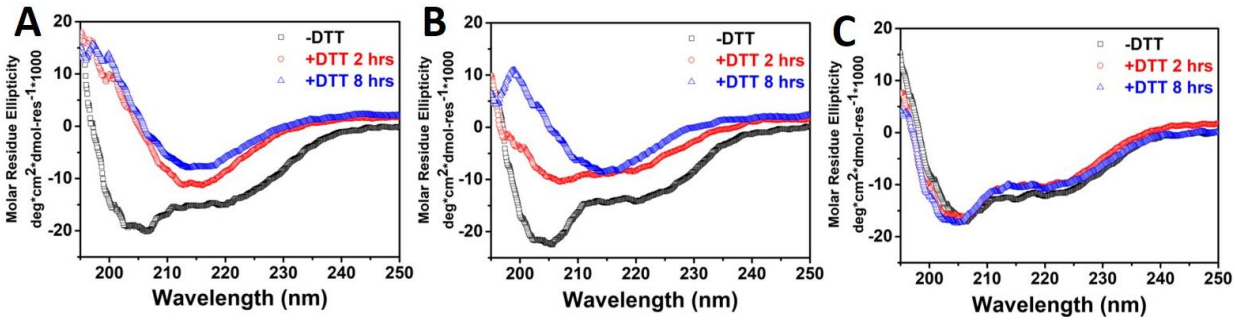

Figure 2.5. CD spectroscopy of **(A)** SAM-P-161, **(B)** SAM-P-262 and **(C)** SAM-P-363 in the absence and presence of DTT (1 mM) in Tirs buffer (pH = 7.4, 20 mM) as monitored by time-dependent CD spectroscopy. Peptide concentration: 50 μM.

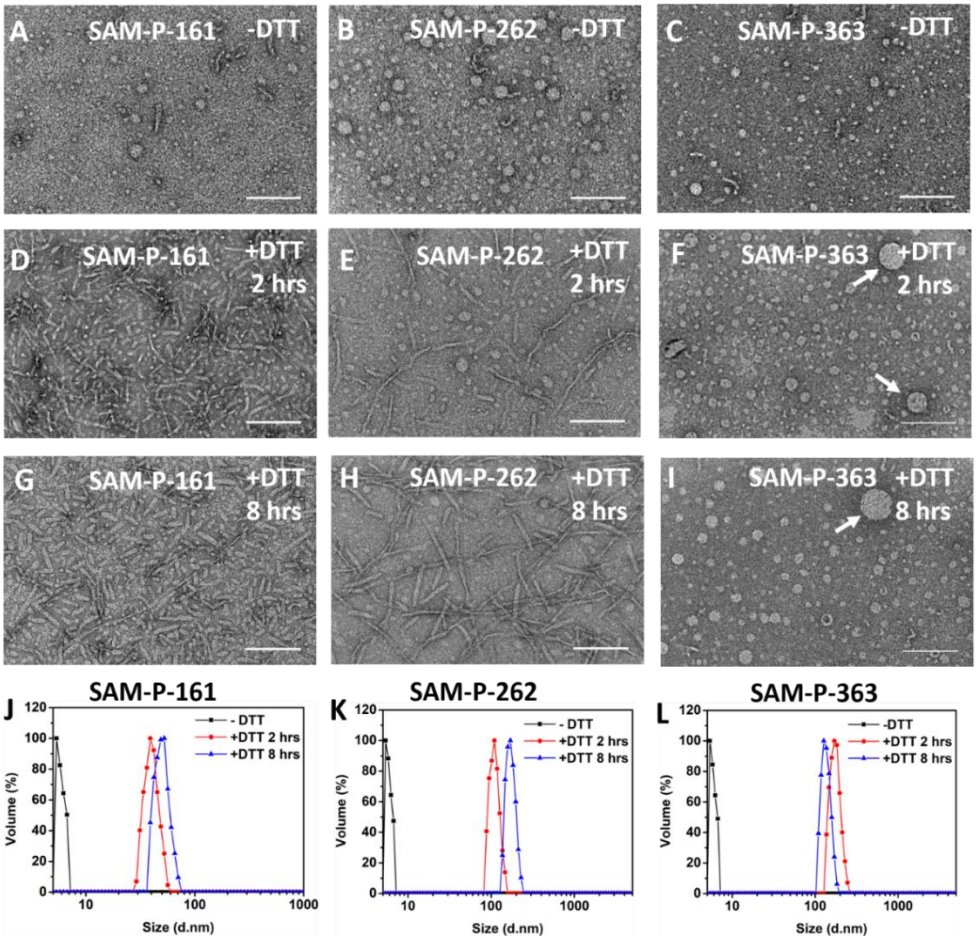

Figure 2.6. TEM images of **(A)** SAM-P-161, **(B)** SAM-P-262, **(C)** SAM-P-363 in the absence of DTT. TEM images of **(D)** SAM-P-161, **(E)** SAM-P-262 and **(F)** SAM-P-363 upon DTT treatment for 2 hrs. TEM images of **(G)** SAM-P-161, **(H)** SAM-P-262 and **(I)** SAM-P-363 upon DTT treatment for 8 hrs. Peptide concentration: 50 μM. Scale bar: 100 nm. DLS measurements of **(J)** SAM-P-161, **(K)** SAM-P-262, and **(L)** SAM-P-363 with/without DTT. Peptide concentration: 20 μM, DTT concentration: 1 mM.

Self-assembling β-sheet nanofibers in solution were further confirmed by the Congo Red (CR) binding experiment. CR is a diazo dye that is widely used to characterize and identify amyloid-like β-sheet fibers.[60,61] It has been reported that the binding between CR and β-sheet peptides can induce a hyperchromic effect (increase in absorbance) with a bathochromic effect (red shift of maximum absorbance) as well as an increase of the fluorescence emission intensity.[62-65] Based on our spectroscopic analysis, the self-assembly behavior of SAM-P-161, SAM-P-262 and SAM-P-363 at non-reducing and reducing conditions were elucidated. As shown in **Figure**

2.7A and **2.7B**, upon incubation with DTT, SAM-P-161 and SAM-P-262 exhibited a significant increase in the UV-vis absorbance and a red shift of the absorbance maximum from 498 nm to 510 nm, indicating the formation of β-sheet nanofibers.[66] Self-assembly of β-sheet nanofibers was also confirmed by the enhancement of the fluorescence emission of SAM-P-161 and SAM-P-262 at ~ 600 nm upon the addition of DTT **(Figure 2.7D** and **2.7E)**. In contrast, minimum spectroscopic changes were observed for SAM-P-363 upon the addition of DTT (**Figure 2.7C** and **2.7F**), which is consistent with previous characterizations indicating the cleavage product of SAM-P-363 was incapable of self-assembling into β-sheet nanostructures under the reducing condition. Based on the solution-phase based CR binding assay, we understand that although all three precursors undergo reduction-triggered self-assembly, the resulting assemblies exhibited different molecular packing and supramolecular morphology. These considerations are expected to have a strong influence on the multivalent ligand presentation within the assembly and potentially their tumor cell targeting specificity and sensitivity.

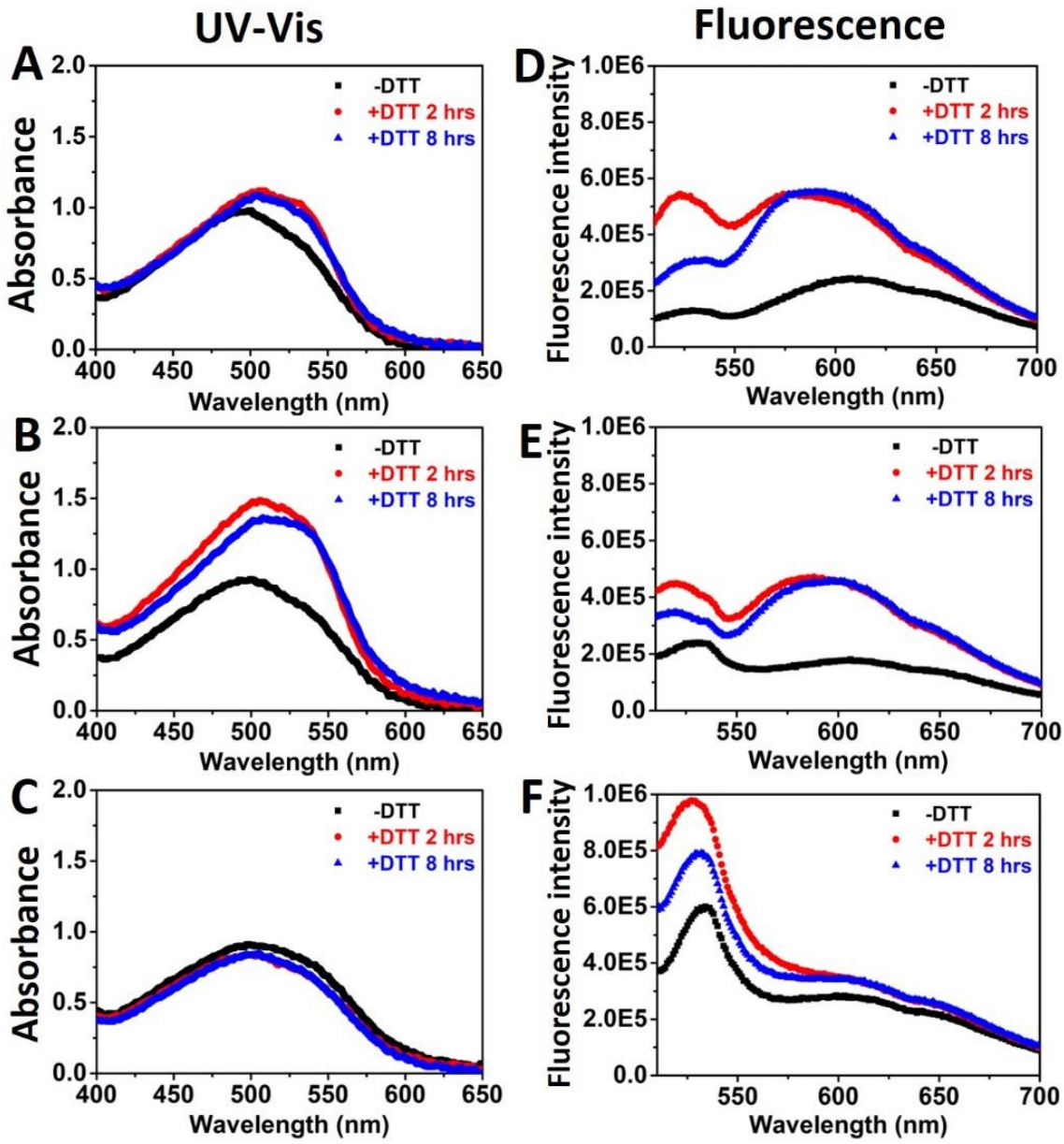

Figure 2.7. UV-Vis spectra of Congo red upon incubation with **(A)** SAM-P-161, **(B)** SAM-P-262 and **(C)** SAM-P-363 with and without DTT (1 mM). Fluorescence spectra of Congo red upon incubation with **(D)** SAM-P-161, **(E)** SAM-P-262 and **(F)** SAM-P-363 with and without DTT. Peptide concentration: 50 μM. Congo red concentration: 50 μM.

2.2.3 *In vitro* Biological Assay for Tumor Cell Targeting

The ability of reduction-triggered self-assembly for tumor cell targeting was investigated by *in vitro* cell-based fluorescence imaging and flow cytometry methods. NBD labeled precursors

were synthesized and incubated with human primary glioblastoma U87MG cells which are known to express high levels of the integrin receptor, $\alpha_v\beta_3$ for RGDS ligand targeting.[40,41] In addition, it was reported that higher levels of glutathione were found in the extracellular tumor microenvironment compared to normal tissues and intracellular environment. In most tumor tissues, the concentration of glutathione is in the range of 1 mM ~10 mM,[67] making it a highly reductive microenvironment. To mimic the tumor reductive microenvironment, we added 1 mM of glutathione in the U87MG cell culture to facilitate cleavage of the precursors and their self-assembly process. **Figure 2.8** and **2.9** showed confocal laser scanning microscopic (CLSM) images of U87MG cells upon incubation with different precursors for 2 hrs and **Figure 2.10** showed the imaging results after 8 hrs of incubation. It was found that SAM-P-262 treated cells exhibited the strongest fluorescence among all groups (**Figure 2.8B**), followed by cells treated with SAM-P-161 (**Figure 2.8A**). Much less fluorescence was observed for U87MG cells upon incubation with SAM-P-363 which formed spherical supramolecular assemblies instead of nanofibers (**Figure 2.8C**). Flow cytometry analysis provided quantitative results of different precursors for the targeting of U87MG cells (**Figure 2.8D**), which are consistent with what was determined by the confocal microscopic analysis. Although SAM-P-161, SAM-P-262 and SAM-P-363 can all undergo trigger-responsive self-assembly to form supramolecular nanostructures with multivalent ligand presentation, cell targeting sensitivity varied dramatically. Based on the CLMS imaging results, supramolecular nanofibers seemed to offer much better sensitivity than spherical aggregates. Elongation of nanofiber further enhanced the sensitivity, presumably due to a larger quantity of ligands presented at the fiber-solvent interface for more effective receptor interactions and tumor cell targeting (**Figure 2.8E**). The detained molecular and cellular mechanism for supramolecular structure-dependent targeting activity is of great interest to us. With

modularly designed SAM-P, we expect to establish a library of supramolecular nanofibers with tunable chemical functionality, molecular and supramolecular structures to further optimize the targeting sensitivity toward a range of cancer cells.

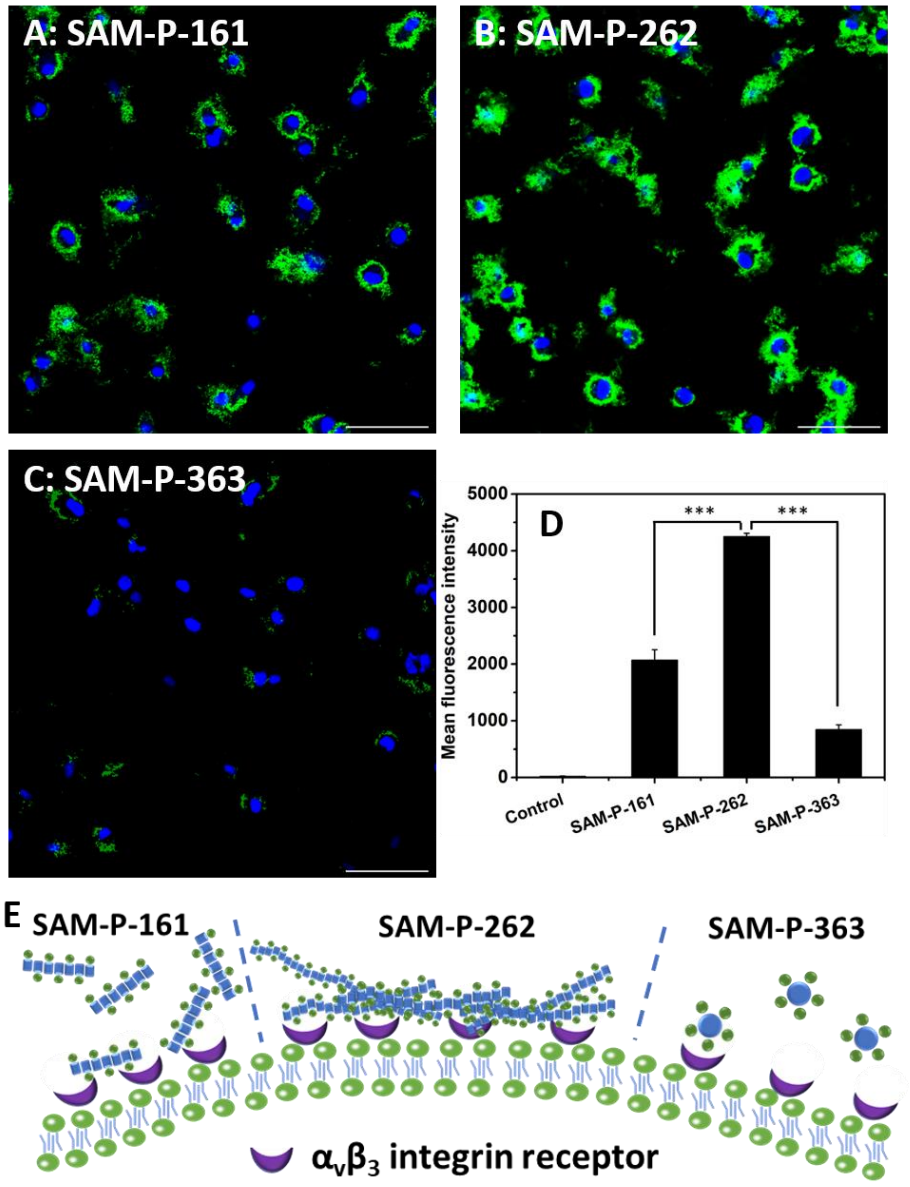

Figure 2.8. Fluorescence microscopic images of U87MG cells incubated with NBD labeled **(A)** SAM-P-161, **(B)** SAM-P-262, **(C)** SAM-P-363 for 2 hrs. **(D)** Fluorescence intensity of U87MG cells incubated with different peptide precursors for 2 hrs as quantified by flow cytometry. (E) Schematic cartoon shows supramolecular structure-dependent receptor targeting with elongated nanofibers formed by SAM-P-262 offering a higher sensitivity than short nanofibers and spherical aggregates. Peptide concentration: 20 μM. Scale bar: 50 μm. Statistic significant difference is indicated by ***$p < 0.001$.

To investigate tumor cell specificity, we selected SAM-P-262, the most sensitive precursor and incubated it with NIH/3T3 mouse fibroblasts which do not have the $\alpha_v\beta_3$ integrin receptor upon incubation with SAM-P-262. As shown in **Figure 2.9D**, much lower fluorescence was observed for NIH/3T3 cells after 2 hrs of incubation with SAM-P-262 than U87MG cells (**Figure 2.9A**). To illustrate the combined effect of supramolecular nanofibers and multivalent ligand presentation on tumor targeting specificity and sensitivity, two additional peptides were synthesized as controls. As shown in **Figure 2.1**, SAM-P-262 (-RGDS) is expected to self-assemble into supramolecular nanofibers but without the active RGDS targeting segment. Similarly, another control peptide was synthesized by removing the disulfide bond linker on SAM-P-262, termed as SAM-P-262 (-SS). SAM-P-262 (-SS) retains the RGDS ligand but does not have the ability to self-assemble or self-assemble into non-fibrous structures. CD and TEM showed that SAM-P-262 (-RGDS) underwent reduction-triggered secondary structural transition and supramolecular nanofiber formation (**Figure 2.11**). SAM-P-262 (-SS) does not have the reduction-sensitive linker and existed as predominantly α-helices with and without DTT (**Figure 2.11D**). TEM revealed irregular spherical aggregates likely due to non-specific aggregation of peptide monomers (**Figure 2.11E-F**). Both peptides were incubated with U87MG cells for 2 hrs followed by washing with PBS buffer and CLSM imaging. As shown in **Figure 2.9B** and **2.9C**, negligible fluorescence was observed upon incubating U87MG cells with these two peptides, further supporting the important roles of both supramolecular nanofibers and multivalent ligand presentation to endow tumor cell targeting capability. In order to demonstrate and confirm the receptor-mediated tumor cell targeting, we conducted an RGD competition assay by pre- and co-incubating a free RGD peptide along with SAM-P-262 in U87MG cell culture. Upon incubation for 2 hrs or 8 hrs, peptides were removed, and cells were washed with PBS buffer for CLMS

imaging. As shown in **Figure 2.12**, a significant reduction of the fluorescence signal occurred upon incubating the U87MG cells with SAM-P-262 in the presence of free RGD peptides, confirming the specific binding between RGDS ligand with the $\alpha_v\beta_3$ integrin receptor on the cell membrane.

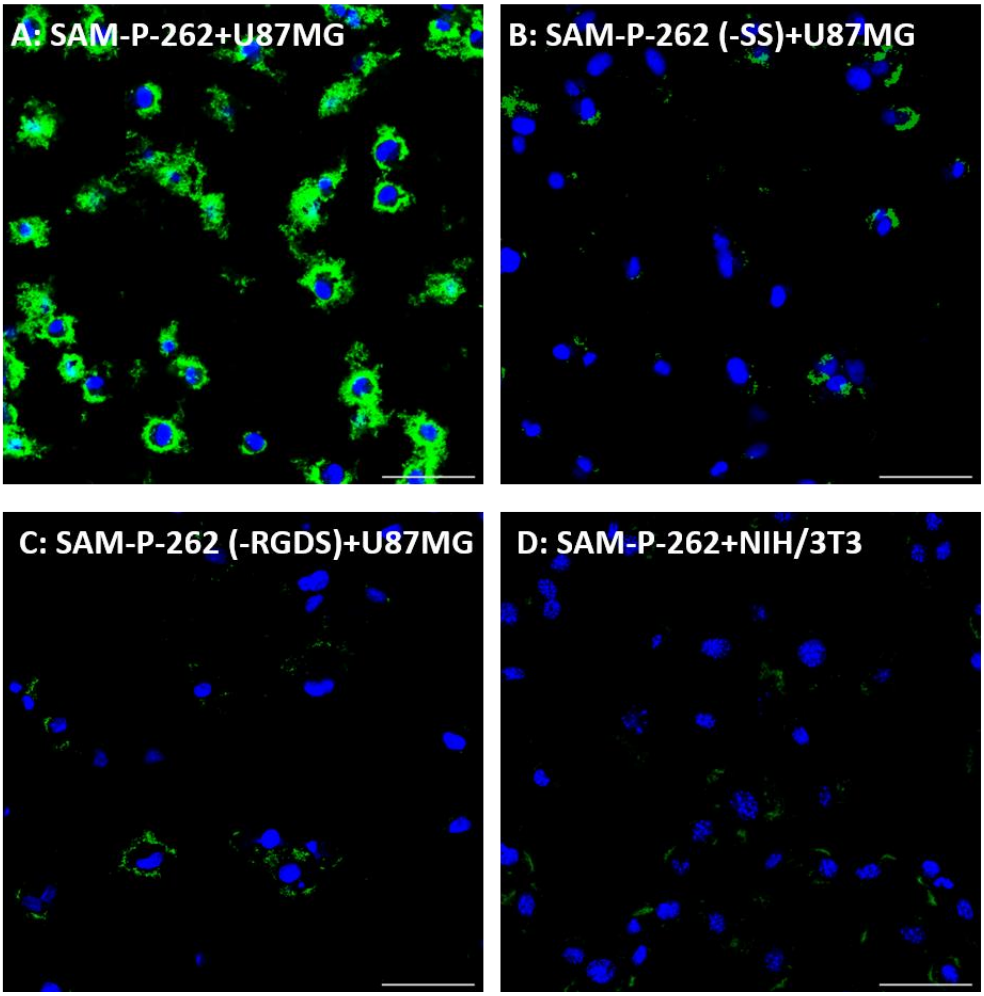

Figure 2.9. Fluorescence microscopic images of U87MG cells incubated with NBD labeled **(A)** SAM-P-262, **(B)** SAM-P-262 (-SS) and **(C)** SAM-P-363 (-RGDS) for 2 hrs. **(D)** Fluorescence microscopic images of NIH/3T3 cells incubated with NBD labeled SAM-P-262 for 2 hrs. Peptide concentration: 20 μM. Scale bar: 50 μm.

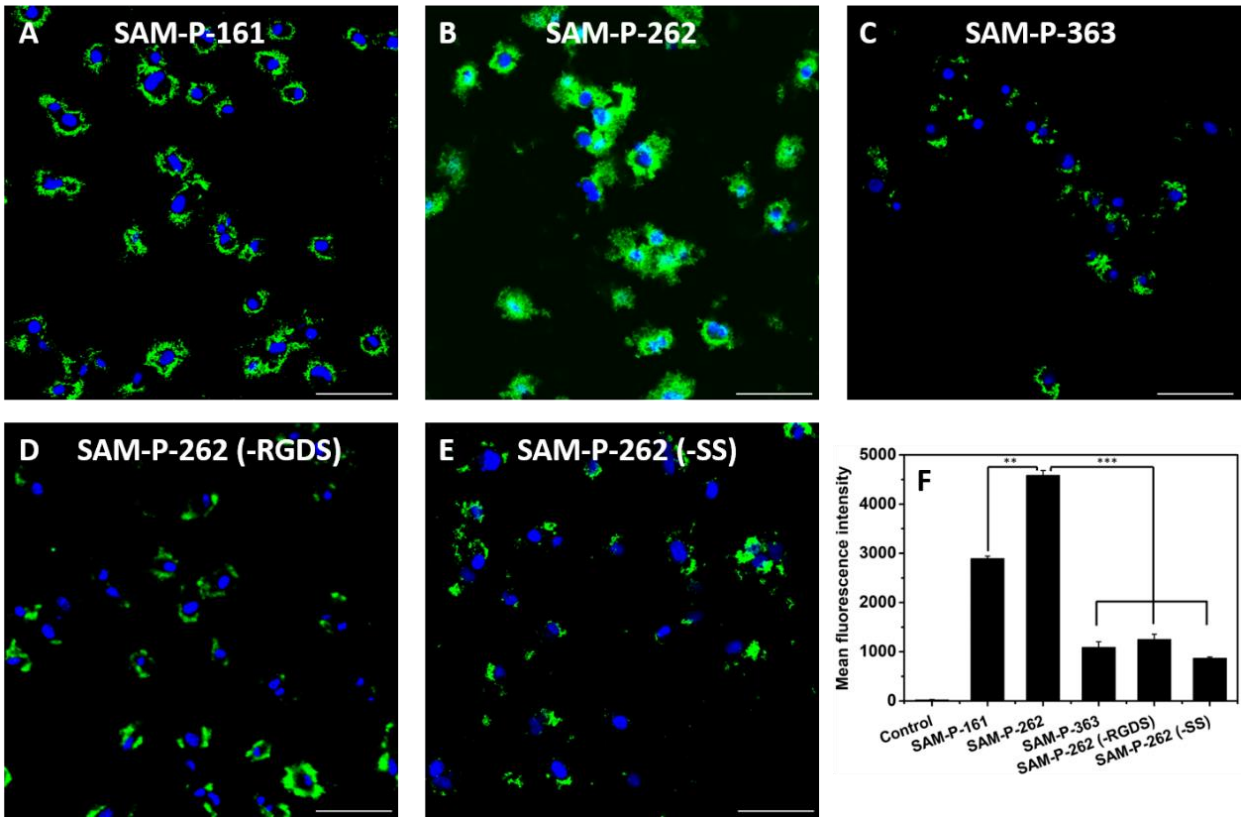

Figure 2.10. CLSM images of U87MG cells incubated with NBD labeled **(A)** SAM-P-161, **(B)** SAM-P-262, **(C)** SAM-P-363, **(D)** SAM-P-262 (-RGDS), and **(E)** SAM-P-262 (-SS) for 8 hrs. **(F)** Fluorescence intensity of U87MG cells incubated with different peptide precursors for 8 hrs as quantified by flow cytometry. Peptide concentration: 20 μM. Scale bar: 50 μm. Statistic significant difference are indicated by $^{**}p < 0.01$ and $^{***}p < 0.001$.

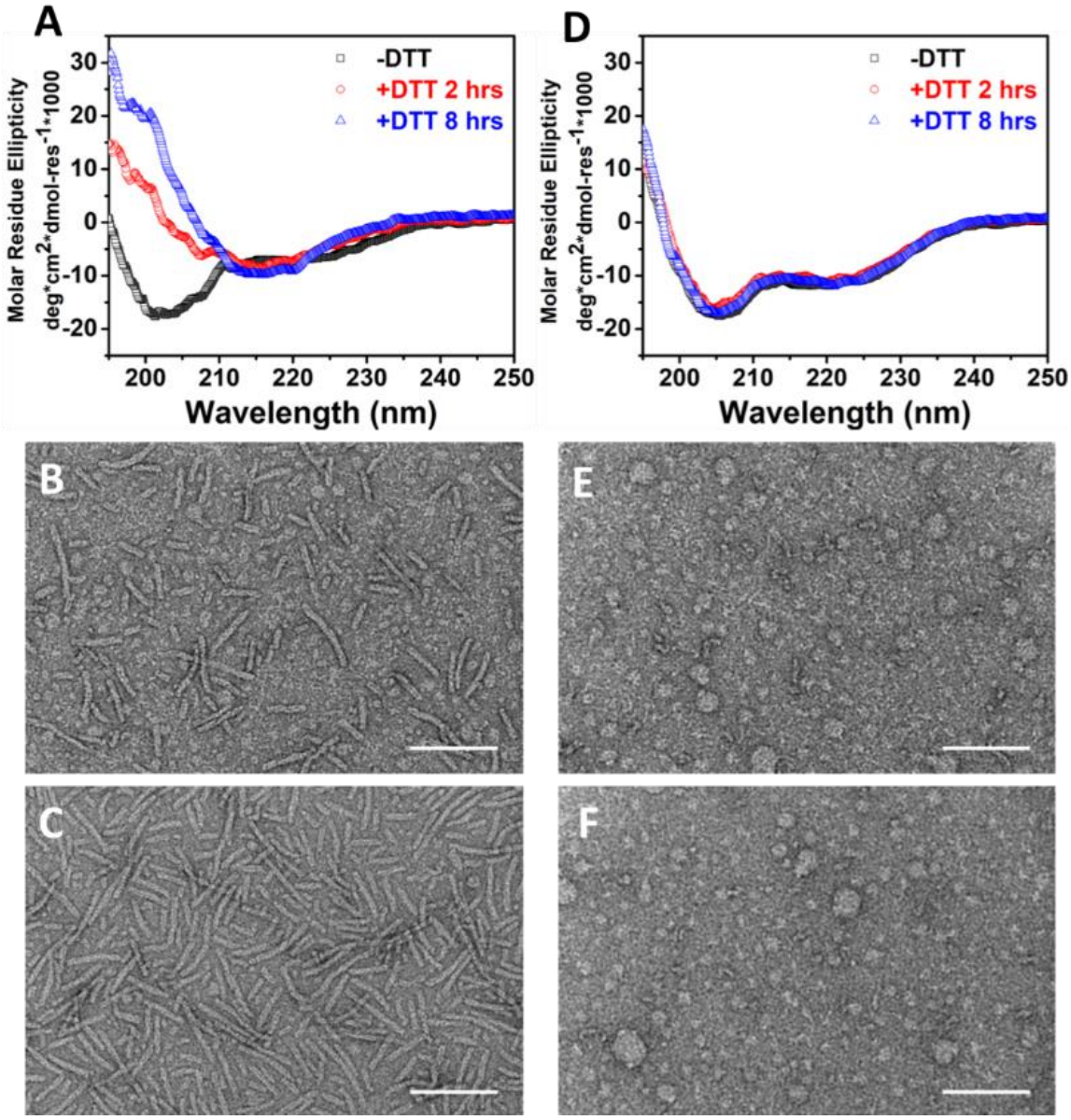

Figure 2.11. Time-dependent CD spectroscopy of (**A**) SAM-P-262 (-RGDS) and (**D**) SAM-P-262 (-SS) upon DTT treatment (1 mM). TEM images of SAM-P-262 (-RGDS) upon DTT treatment for (**B**) 2 hrs and (**C**) 8 hrs, confirming reduction-induced nanofiber formation. TEM images of SAM-P-262 (-SS) upon DTT treatment for (**E**) 2 hrs and (**F**) 8 hrs confirming its non-responsiveness. Scale bar: 100 nm.

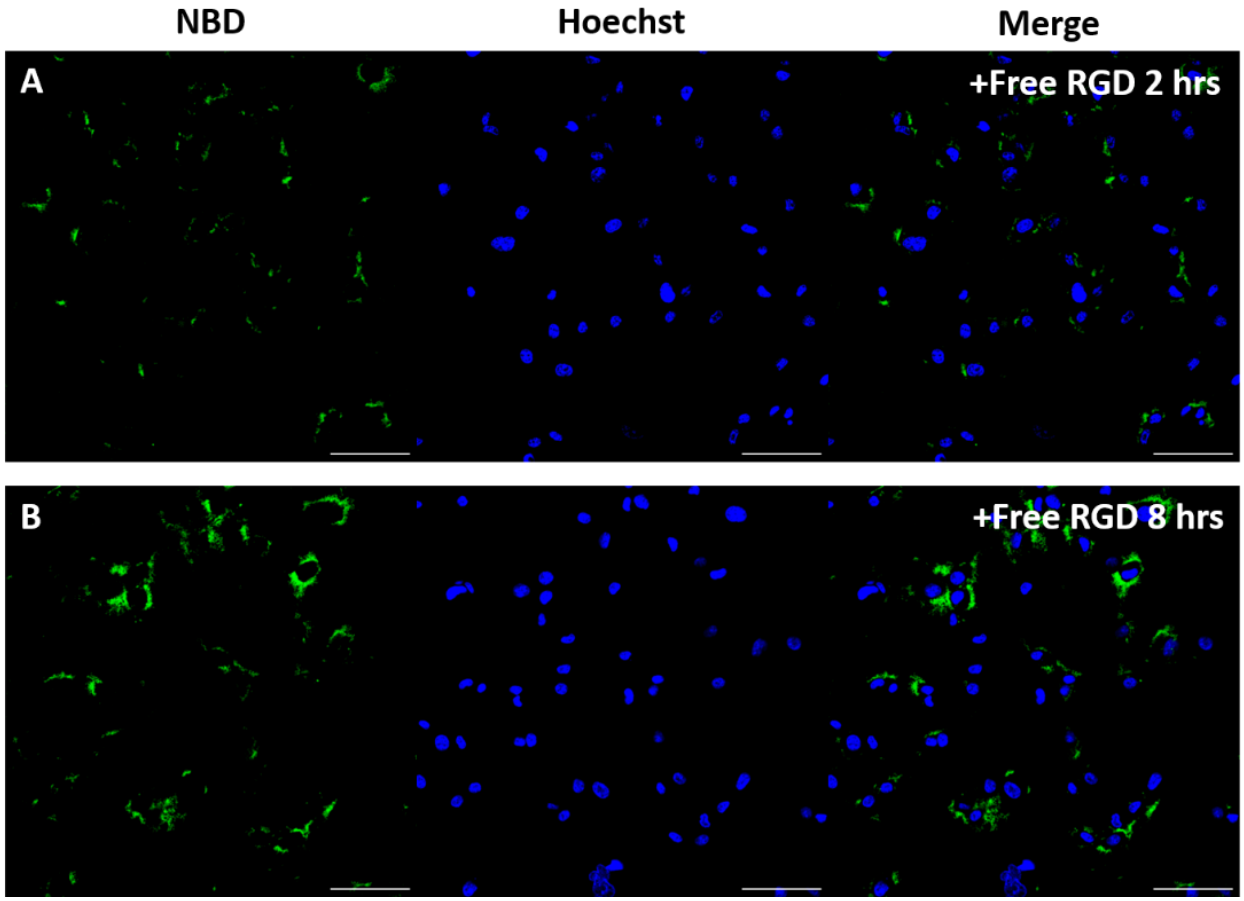

Figure 2.12. CLSM images of U87MG cells co-incubated with NBD labeled SAM-P-262 and free RGD peptide for **(A)** 2 hrs and **(B)** 8 hrs. Cells were pre-treated with free RGD for 24 hrs before the addition of NBD labeled SAM-P-262 and RGD peptide. NBD labeled SAM-P-262 concentration: 20 μM. RGD concentration: 800 μM. Scale bar: 50 μm.

While SAM-P-161 and SAM-P-262 are effective for tumor cell targeting, their cellular localization is obscure based on the fluorescent images shown in **Figure 2.8**. These images suggest significant fractions of peptides were localized on the cell membrane. Although molecular imaging does not necessarily require the imaging agents to reach the cytoplasm, for therapeutic applications, it is essential to have parts if not all of the therapeutic components to be transported across the cell membrane. To track the cellular localization of the assemblies, we incubated U87MG cells with NBD labeled precursors for 2 hrs, followed by CR staining. CR can effectively quench the green fluorescence from NBD-labeled peptides, as confirmed by the fluorescence resonance energy

transfer (FRET) assay performed in the aqueous solution (**Figure 2.13**). As a result, by staining U87MG cells with CR, only the intracellular assemblies labeled by NBD emit fluorescence (excited at ~490 nm) while those that are attached to the cell membrane undergo FRET and therefore become invisible by fluorescence detection in the FITC channel. Consistent with the experimental design and expectation, **Figure 2.14A** and **2.14B** revealed the punctate green fluorescence pattern within the cells treated with SAM-P-161 and SAM-P-262 and red fluorescence from CR on the cell membrane. While we continue working toward a quantitative measurement for cell localization, we believe parts of the assemblies can be taken up inside cells. While we are primarily focusing on the targeted cell imaging in this work, additionally chemical modification to enhance their cytosolic delivery and endosome escaping capability will make them promising candidates for the development of targeted theranostic agents. In addition, we believe these assemblies are relatively stable as β-sheet nanofibers which are responsible for CR binding on the cell membrane. The binding between CR and these β-sheet assemblies is highly specific as demonstrated by the negligible red fluorescence for cells treated with SAM-P-363 (**Figure 2.14C**), or for cells without any treatment (data not shown). The cytotoxicity of different precursors was evaluated in NIH/3T3 mouse fibroblast culture and the cell viability was quantified by the MTT assay after 24 hrs of incubation with each precursor. As shown in **Figure 2.15**, these precursors showed cell viability at > 50% up to 80 μM. Although the cytotoxicity can be further improved through suitable chemical modification, such as PEGylation,[68] we believe the current design can be used as a basis for further structural and activity optimization.

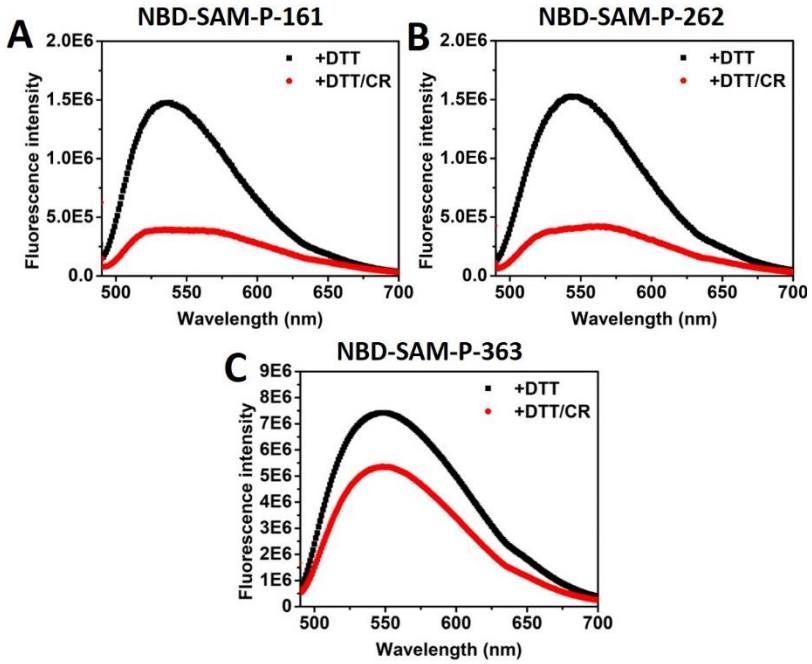

Figure 2.13. Fluorescence emission spectra of **(A)** NBD labeled SAM-P-161, **(B)** NBD labeled SAM-P-262 and **(C)** NBD labeled SAM-P-363 in the presence of DTT (1 mM) with and without Congo red showing the FRET effect between NBD and Congo red. Peptide concentration: 20 µM. Congo red concentration: 20 µM.

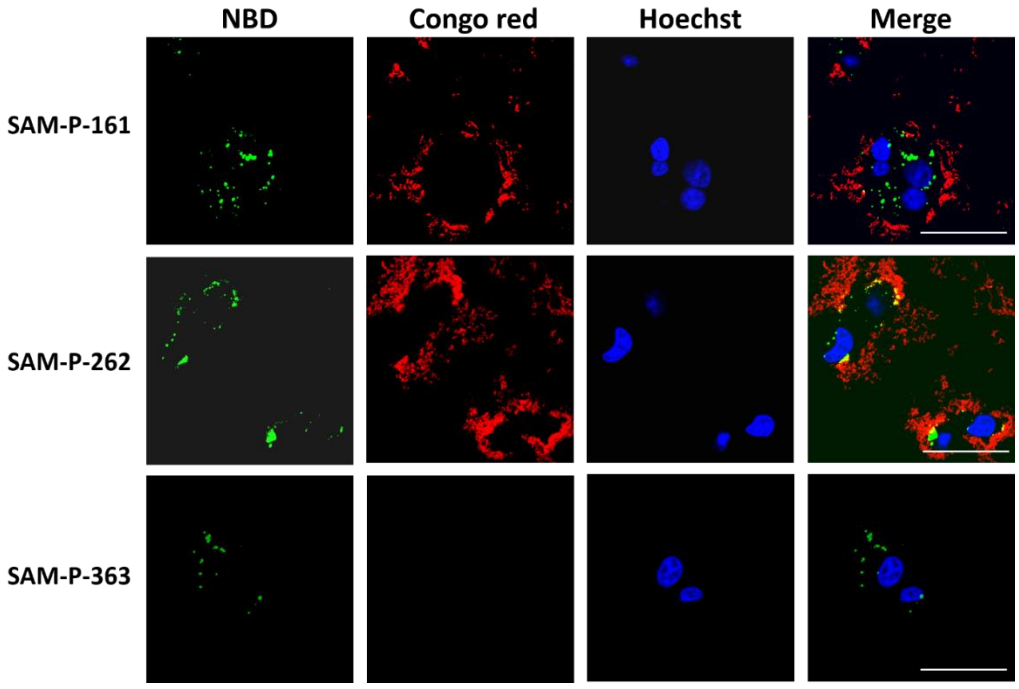

Figure 2.14. Fluorescence images of U87MG cells after incubation with NBD labeled **(A)** SAM-P-161, **(B)** SAM-P-262 and **(C)** SAM-P-363 followed by Congo red staining. Peptide concentration: 20 µM. Congo red concentration: 20 µM. Scale bar: 50 µm.

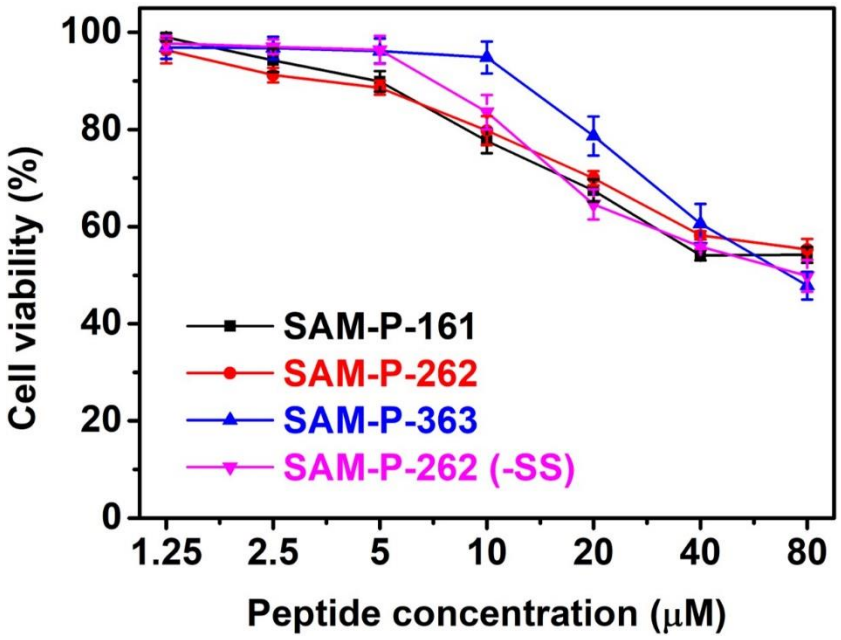

Figure 2.15. Cell viability assay of NIH/3T3 mouse fibroblasts upon incubation with SAM-P-161, SAM-P-262, SAM-P-363, and SAM-P-262 (-SS). The assay was performed after 24 hrs of incubation of cells with peptides with a total peptide concentration ranging from 1.25 μM to 80 μM.

2.3 Conclusions

We demonstrated that tumor microenvironment-triggered peptide self-assembly can be used as an effective method to induce multivalent ligand presentation for tumor cell targeting. Using modularly designed peptide monomer precursors capable of self-assembly into different supramolecular morphologies, we studied the combined effect of supramolecular assembly and multivalent ligand presentation on tumor cell targeting specificity and sensitivity. Through combined biophysical characterizations and *in vitro* fluorescence assay, we showed that anisotropic nanofibers are more effective to organize multivalent ligands for enhanced cell targeting specificity and sensitivity than supramolecular spherical nanoparticles. Elongation of nanofibers further promoted ligand-receptor interactions and targeting sensitivity. This proof-of-concept study laid the foundation for the generation of supramolecular nanofibers containing various ligands, including some of the "weak" ligands, such as the linear RGDS for improved

tumor cell targeting. The modular nature of the SAM-P design and synthesis offers great advantages for the construction of supramolecular nanofibers with various other trigger-responsive domains in response to the physiological and pathological conditions of a variety of diseases, not limited to cancer, for targeted molecular imaging and therapy.

2.4 Experimental Section

Materials. Fmoc-protected amino acids, *N,N,N′,N′*-Tetramethyl-*O*-(1*H*-benzotriazol-1-yl)uronium hexafluorophosphate (HBTU), and MBHA rink amide resin, were purchased from Novabiochem. Piperidine, diisopropylethylamine (DIPEA), 6-(7-Nitrobenzofurazan-4-ylamino) hexanoic acid (NBD-hexanoic acid), MTT assay kit, Congo red, and DL-Dithiothreitol (DTT) were purchased from Sigma-Aldrich. Solvents for peptide synthesis and purification including dimethyl formamide (DMF), acetonitrile, trifluoroacetic acid (TFA), Eagle's Minimum Essential Medium (EMEM), Dulbecco's modified Eagle medium (DMEM) culture medium and Hoechst 33342 nucleus staining dye, glutathione (reduced) were purchased from Fisher Scientific. Fetal Bovine Serum (FBS) was purchased from VWR. TEM staining reagent, uranium acetate dihydrate and TEM grid were purchased from TED PELLA, INC. U87 MG cell line was provided by Dr. Xiankai Sun lab at UT Southwestern Medical Center.

Synthesis and purification of peptides. Peptides were synthesized on a *Prelude*® peptide synthesizer using standard FMOC-solid phase peptide synthesis procedures. Fmoc groups were deprotected in 20% (V/V) piperidine in N, N-dimethylformamide (DMF) for 5 min and repeated 2 times. HBTU was used as the coupling reagent and reacted with Fmoc-protected amino acids in the presence of DIPEA with a molar ratio of 1:1:2.5 (amino acid: HBTU: DIPEA). The Fmoc-terminated disulfide bond linker was synthesized according to previous procedures[38,39] and used in the same manner as other Fmoc-amino acid protected amino acid for the coupling reaction.

Nitrobenzoxadiazole (NBD)-terminated peptides were synthesized as follows. After final deprotection of the peptide, the N-terminus was coupled with 4 equivalents of NBD-hexanoic acid using a combination of 4 equivalents of HBTU and 8 equivalents of DIPEA in DMF. The reaction mixture was stirred overnight. The completion of the coupling reaction was confirmed by the Kaiser test. A mixture of trifluoroacetic acid (TFA) / triisopropanolsilane (TIS) / H_2O (95/2.5/2.5 by volume) was used to cleavage the peptides from resin for 3 hrs. The cleavage solution was filtered, and filtrates were collected. The resin was washed three times with neat TFA, and all filtrate solutions were combined and evaporated under airflow. The residual peptide solution was precipitated in cold diethyl ether, followed by centrifugation and washing with cold diethyl ether for three times. The crude peptide was dried under vacuum overnight for HPLC purification. The peptide was purified using a preparative reversed phase C4 column with a linear gradient of water/acetonitrile (5% to 95% of acetonitrile in 30 mins) containing 0.05% TFA. Elution was monitored at 230 nm and 280 nm. The cleavage and purification procedure followed the same procedure as described for the nonlabelled peptides. The molecular mass was confirmed by MALDI-TOF mass spectrometry.

Critical aggregation concentration (CAC) determination. Concentrated NBD labelled peptide solutions (500 μM) were pre-incubated with DTT (10 mM) for 2 hrs. Increments of 2 μL of this solution were added incrementally to 500 μL Tris buffer (pH 7.4, 20 mM). Fluorescence spectra were acquired after each peptide addition by monitoring fluorescence emission from 485 nm to 700 nm using an excitation wavelength at 480 nm. Fluorescence intensity at λ_{max} was plotted as a function of peptides concentrations. The CAC was determined to be the concentration at which nonlinearity started to develop.

Circular dichroism (CD) spectroscopy. CD spectroscopy was performed on a Jasco 710 CD spectrometer. Samples were prepared by dilution of the peptide stock solution to a concentration at 50 μM in Tris buffer (pH 7.4, 20 mM). DTT was added to samples to reach a final concentration at 1 mM and mixed for 2 hrs and 8 hrs. The CD spectra were collected from 250 nm to 190 nm at room temperature (RT) using a 1 mm cuvette, a bandwidth at 0.1 nm, scan rate at 100 nm/min and a response time of 2 sec. Each spectrum was averaged from three scans. The mDeg of rotation was converted to molar residual ellipticity via the formula $\theta = \frac{1000 \times mDeg}{c * n * l}$ where c is the concentration of the peptide solution expressed in μM, n is the number of amino acids in the peptide sequence and l is the path length of the cell used in the unit of millimeter.

Transmission electron microscopy (TEM). Sample preparation was the same as that used in the CD experiment. Samples at the reducing condition were prepared by incubating peptides with DTT (1 mM) for 2 hrs and 8 hrs. 10 μL of peptide solution was pipetted onto a lacey carbon grid (TED PELLA 01824). After 2 minutes, excess solution was carefully removed with filter paper. 10 μL of 2 wt % uranyl acetate aqueous solution was pipetted onto the grid for negative staining. After 2 minutes, excess staining solution was removed and the TEM samples were dried for overnight before imaging on a Hitachi H-9500 high-resolution TEM.

Dynamic light scattering measurement (DLS). The light scattering measurements were made using a BI-200SM Research Goniometer System (Brookhaven Instruments Corporation, Holtsville, NY, a Nova Instruments LLC company, Wakefield, MA) and data processed using their Particle Explorer software. This instrument is capable of doing angle and temperature dependent static and dynamic light scattering (DLS) evaluations. Measurements were made on solutions studied in 12 mm diameter glass cells, primarily at 90°. These solutions were equilibrated at room temperature, 23 °C. Typically, the autocorrelation functions for the DLS measurements were acquired over a

period of 2 or more minutes, at photon count rates greater than 100 kc/s. Size distributions were inferred from decay rates of the correlation function and evaluated using both intensity and volume weightings.

Congo red (CR) binding study. Peptide solutions were prepared in Tris buffer (pH 7.4, 20 mM) with a final concentration of 50 μM and DTT (1 mM) was added and mixed for different time periods at 2 hrs or 8 hrs. After respective mixing time, a stock solution of CR (3 mM) was added to the peptide solution to reach a final CR concentration of 50 μM. UV absorbance was measured in the spectral range 400–650 nm using a Thermo Nanodrop UV-Vis Spectrometer (Thermo Scientific™). Fluorescence emission was measured in the spectral range 490-700 nm using a Horiba Jobin Yvon FluoroMax-3 bench-top fluorometer.

Cell uptake. U87MG cells were seeded in a confocal dish with a cell density at ~10^5 and incubated at 37 ^oC for 24 hrs. Cell suspensions were removed and washed three times with PBS buffers to remove any non-adherent cell. 20 μL of 200 μM NBD labelled peptide solutions (in Tris buffer) was mixed with 180 μL of fresh cell culture EMEM medium containing 1 mM of glutathione. After incubation at 37 ^oC for 2 hrs or 8 hrs, the culture medium was removed and washed extensively three times with PBS buffer. For groups with CR staining, the CR stock solution was added to the cell culture to reach a final concentration at 20 μM and incubated for 1 hr. After removing CR solution and washing three times with PBS buffer, cells were stained Hoechst 33342 at room temperature for 15 min and followed by washing three times with PBS buffer. Cells were analyzed by an A1R HD25 confocal laser scanning microscope (Nikon) and fluorescence images were processed using ImageJ.

RGD competition assay. Free RGD peptides were added to cell culture medium with a final concentration of 800 μM. After 24 hrs of incubation with U87MG cells, glutathione was added to

the cell culture to reach a final concentration at 1 mM followed by the addtion of NBD-labelled peptides to reach a total peptide concentration at 20 μM. After 2 hrs or 8 hrs of incubation, cells were washed with PBS buffer to remove any non-specific bound peptides. Cells were stained with nuclear-specific dye, Hoechst 33342 at room temperature for 15 min followed by PBS buffer washing for three times. Cells were analyzed by an A1R HD25 confocal laser scanning microscope (Nikon) and fluorescence images were processed using ImageJ.

Flow cytometry. U87MG cells were seeded onto a 24-well plate at a density of 10^5 cells/well and incubated for 24 hrs 37 °C. Culture medium was replaced with 450 μL fresh EMEM medium (containing 1 mM of glutathione) and 50 μL of NBD-labeled peptide solutions (200 μM) were added. After incubation with NBD-labeled peptides for 2 hrs or 8 hrs, cells were washed with PBS buffer for three times. Cells were digested with trypsin and washed twice with PBS buffer. Cell uptake of the NBD-labeled peptide was quantified using a BD LSR II flow cytometer. A minimum of 10,000 events per sample was analyzed and data were processed using FlowJo software.

Cytotoxicity measurement. NIH/3T3 mouse fibroblasts were seeded onto a 96-well plate at a density of ~10^4 cells/well and incubated for 24 hrs at 37 °C. After 24 hrs, DMEM culture medium was removed. 10 μL of peptide solution in Tris buffer (20 mM, pH 7.4) at various concentrations (800, 400, 200, 100, 50, 25, 12.5 μM) was mixed with 90 μL cell culture medium in a 96-well plate. After 24 hrs of incubation, the MTT assay was performed to quantify the cell viability by monitoring UV absorbance at 450 nm. Cells without peptides were used as a control. All experiments were performed in four replicates.

Statistical analysis. The data for flow cytometry measurement were expressed as means ± standard deviation (SD). The statistical analysis was performed using Student's T-test and one-way analysis of variance (ANOVA) at confidence levels of 95% and above.

2.5 References

(1) Tjandra, K. C.; Thordarson, P. Multivalency in drug delivery–when is it too much of a good thing? *Bioconjug. Chem.* **2019**, *30*, 503-514.

(2) Jayaraman, N. Multivalent ligand presentation as a central concept to study intricate carbohydrate–protein interactions. *Chem. Soc. Rev.* **2009**, *38*, 3463-3483.

(3) Wang, J.; Tian, S.; Petros, R. A.; Napier, M. E.; DeSimone, J. M. The complex role of multivalency in nanoparticles targeting the transferrin receptor for cancer therapies. *J. Am. Chem. Soc.* **2010**, *132*, 11306-11313.

(4) Lee, J.; Bai, Y.; Chembazhi, U. V.; Peng, S.; Yum, K.; Luu, L. M.; Hagler, L. D.; Serrano, J. F.; Chan, H. Y. E.; Kalsotra, A.; Zimmerman, S. C. Intrinsically cell-penetrating multivalent and multitargeting ligands for myotonic dystrophy type 1. *Proc. Natl. Acad. Sci. U. S. A.* **2019**, *116*, 8709.

(5) Curk, T.; Dobnikar, J.; Frenkel, D. Optimal multivalent targeting of membranes with many distinct receptors. *Proc. Natl. Acad. Sci. U. S. A.* **2017**, *114*, 7210.

(6) Dirksen, A.; Langereis, S.; de Waal, B. F.; van Genderen, M. H.; Hackeng, T. M.; Meijer, E. A supramolecular approach to multivalent target-specific MRI contrast agents for angiogenesis. *Chem. Comm.* **2005**, 2811-2813.

(7) Weissleder, R.; Kelly, K.; Sun, E. Y.; Shtatland, T.; Josephson, L. Cell-specific targeting of nanoparticles by multivalent attachment of small molecules. *Nat. Biotechnol.* **2005**, *23*, 1418-1423.

(8) Shokeen, M.; Pressly, E. D.; Hagooly, A.; Zheleznyak, A.; Ramos, N.; Fiamengo, A. L.; Welch, M. J.; Hawker, C. J.; Anderson, C. J. Evaluation of multivalent, functional polymeric nanoparticles for imaging applications. *ACS nano* **2011**, *5*, 738-747.

(9) Liu, W.; Hao, G.; Long, M. A.; Anthony, T.; Hsieh, J.-T.; Sun, X. Imparting multivalency to a bifunctional chelator: a scaffold design for targeted PET imaging probes. *Angew. Chem. Int. Ed. Engl.* **2009**, *48*, 7346-7349.

(10) Winnard, J. P.; Raman, V. Real time non-invasive imaging of receptor–ligand interactions in vivo. *J. Cell. Biochem.* **2003**, *90*, 454-463.

(11) Orcutt, K. D.; Rhoden, J. J.; Ruiz-Yi, B.; Frangioni, J. V.; Wittrup, K. D. Effect of small-molecule–binding affinity on tumor uptake in vivo: a systematic study using a pretargeted bispecific antibody. *Mol. Cancer Ther.* **2012**, *11*, 1365-1372.

(12) Humblet, V.; Misra, P.; Bhushan, K. R.; Nasr, K.; Ko, Y.-S.; Tsukamoto, T.; Pannier, N.; Frangioni, J. V.; Maison, W. Multivalent scaffolds for affinity maturation of small molecule cell surface binders and their application to prostate tumor targeting. *J. Med. Chem.* **2009**, *52*, 544-550.

(13) Huang, K.; Ma, H.; Liu, J.; Huo, S.; Kumar, A.; Wei, T.; Zhang, X.; Jin, S.; Gan, Y.; Wang, P. C.; He, S.; Zhang, X.; Liang, X.-J. Size-dependent localization and penetration of ultrasmall gold nanoparticles in cancer cells, multicellular spheroids, and tumors in vivo. *ACS nano* **2012**, *6*, 4483-4493.

(14) Blanco, E.; Shen, H.; Ferrari, M. Principles of nanoparticle design for overcoming biological barriers to drug delivery. *Nat. Biotechnol.* **2015**, *33*, 941-951.

(15) Alkilany, A. M.; Zhu, L.; Weller, H.; Mews, A.; Parak, W. J.; Barz, M.; Feliu, N. Ligand density on nanoparticles: A parameter with critical impact on nanomedicine. *Adv. Drug Deliv. Rev.* **2019**, *143*, 22-36.

(16) Versluis, F.; van Esch, J. H.; Eelkema, R. Synthetic self-assembled materials in biological environments. *Adv. Mater.* **2016**, *28*, 4576-4592.

(17) Zhang, D.; Qi, G.-B.; Zhao, Y.-X.; Qiao, S.-L.; Yang, C.; Wang, H. In situ formation of nanofibers from purpurin18-peptide conjugates and the assembly induced retention effect in tumor sites. *Adv. Mater.* **2015**, *27*, 6125-6130.
(18) Kim, B. J.; Xu, B. Enzyme-instructed self-assembly for cancer therapy and imaging. *Bioconjug. Chem.* **2020**, *31*, 492-500.
(19) Kalafatovic, D.; Nobis, M.; Son, J.; Anderson, K. I.; Ulijn, R. V. MMP-9 triggered self-assembly of doxorubicin nanofiber depots halts tumor growth. *Biomaterials* **2016**, *98*, 192-202.
(20) Pires, R. A.; Abul-Haija, Y. M.; Costa, D. S.; Novoa-Carballal, R.; Reis, R. L.; Ulijn, R. V.; Pashkuleva, I. Controlling cancer cell fate using localized biocatalytic self-assembly of an aromatic carbohydrate amphiphile. *J. Am. Chem. Soc.* **2015**, *137*, 576-579.
(21) Tanaka, A.; Fukuoka, Y.; Morimoto, Y.; Honjo, T.; Koda, D.; Goto, M.; Maruyama, T. Cancer cell death induced by the intracellular self-assembly of an enzyme-responsive supramolecular gelator. *J. Am. Chem. Soc.* **2015**, *137*, 770-775.
(22) Wang, H.; Feng, Z.; Wang, Y.; Zhou, R.; Yang, Z.; Xu, B. Integrating enzymatic self-assembly and mitochondria targeting for selectively killing cancer cells without acquired drug resistance. *J. Am. Chem. Soc.* **2016**, *138*, 16046-16055.
(23) Wu, C.; Zhang, R.; Du, W.; Cheng, L.; Liang, G. Alkaline phosphatase-triggered self-assembly of near-infrared nanoparticles for the enhanced photoacoustic imaging of tumors. *Nano Lett.* **2018**, *18*, 7749-7754.
(24) Wang, Y.; Zhan, J.; Chen, Y.; Ai, S.; Li, L.; Wang, L.; Shi, Y.; Zheng, J.; Yang, Z. Selective pericellular hydrogelation by the overexpression of an enzyme and a membrane receptor. *Nanoscale* **2019**, *11*, 13714-13719.
(25) An, H.-W.; Li, L.-L.; Wang, Y.; Wang, Z.; Hou, D.; Lin, Y.-X.; Qiao, S.-L.; Wang, M.-D.; Yang, C.; Cong, Y.; Ma, Y.; Zhao, X.-X.; Cai, Q.; Chen, W.-T.; Lu, C.-Q.; Xu, W.; Wang, H.; Zhao, Y. A tumour-selective cascade activatable self-detained system for drug delivery and cancer imaging. *Nat. Commun.* **2019**, *10*, 4861.
(26) Li, J.; Kuang, Y.; Shi, J.; Zhou, J.; Medina, J. E.; Zhou, R.; Yuan, D.; Yang, C.; Wang, H.; Yang, Z.; Liu, J.; Dinulescu, D. M.; Xu, B. Enzyme-instructed intracellular molecular self-assembly to boost activity of cisplatin against drug-resistant ovarian cancer cells. *Angew. Chem. Int. Ed. Engl.* **2015**, *54*, 13307-13311.
(27) Zhou, J.; Xu, B. Enzyme-instructed self-assembly: a multistep process for potential cancer therapy. *Bioconjug. Chem.* **2015**, *26*, 987-999.
(28) Feng, Z.; Wang, H.; Chen, X.; Xu, B. Self-assembling ability determines the activity of enzyme-instructed self-assembly for inhibiting cancer cells. *J. Am. Chem. Soc.* **2017**, *139*, 15377-15384.
(29) Zhou, J.; Du, X.; Yamagata, N.; Xu, B. Enzyme-instructed self-assembly of small D-peptides as a multiple-step process for selectively killing cancer cells. *J. Am. Chem. Soc.* **2016**, *138*, 3813-3823.
(30) Zhan, J.; Cai, Y.; He, S.; Wang, L.; Yang, Z. Tandem molecular self-assembly in liver cancer cells. *Angew. Chem. Int. Ed. Engl.* **2018**, *57*, 1813-1816.
(31) An, H.-W.; Hou, D.; Zheng, R.; Wang, M.-D.; Zeng, X.-Z.; Xiao, W.-Y.; Yan, T.-D.; Wang, J.-Q.; Zhao, C.-H.; Cheng, L.-M.; Zhang, J.-M.; Wang, L.; Wang, Z.-Q.; Wang, H.; Xu, W. A near-infrared peptide probe with tumor-specific excretion-retarded effect for image-guided surgery of renal cell carcinoma. *ACS nano* **2020**, *14*, 927-936.

(32) Cong, Y.; Ji, L.; Gao, Y.-J.; Liu, F.-H.; Cheng, D.-B.; Hu, Z.; Qiao, Z.-Y.; Wang, H. Microenvironment-induced in situ self-assembly of polymer–peptide conjugates that attack solid tumors deeply. *Angew. Chem. Int. Ed. Engl.* **2019**, *58*, 4632-4637.
(33) Zhao, X. X.; Li, L. L.; Zhao, Y.; An, H. W.; Cai, Q.; Lang, J. Y.; Han, X. X.; Peng, B.; Fei, Y.; Liu, H.; Qin, H.; Nie, G.; Wang, H. In situ self-assembled nanofibers precisely target cancer-associated fibroblasts for improved tumor imaging. *Angew. Chem. Int. Ed. Engl.* **2019**, *131*, 15431-15438.
(34) Liu, F.-H.; Cong, Y.; Qi, G.-B.; Ji, L.; Qiao, Z.-Y.; Wang, H. Near-infrared laser-driven in situ self-assembly as a general strategy for deep tumor therapy. *Nano Lett.* **2018**, *18*, 6577-6584.
(35) Shi, J.; Fichman, G.; Schneider, J. P. Enzymatic control of the conformational landscape of self-assembling peptides. *Angew. Chem. Int. Ed. Engl.* **2018**, *57*, 11188-11192.
(36) Bowerman, C. J.; Nilsson, B. L. A Reductive Trigger for peptide self-assembly and hydrogelation. *J. Am. Chem. Soc.* **2010**, *132*, 9526-9527.
(37) Guo, X.; Cheng, Y.; Zhao, X.; Luo, Y.; Chen, J.; Yuan, W.-E. Advances in redox-responsive drug delivery systems of tumor microenvironment. *J. Nanobiotechnology* **2018**, *16*, 74.
(38) Yang, S.; Xu, D.; Dong, H. Design and fabrication of reduction-sensitive cell penetrating nanofibers for enhanced drug efficacy. *J. Mater. Chem. B* **2018**, *6*, 7179-7184.
(39) Ren, C.; Song, Z.; Zheng, W.; Chen, X.; Wang, L.; Kong, D.; Yang, Z. Disulfide bond as a cleavable linker for molecular self-assembly and hydrogelation. *Chem. Comm.* **2011**, *47*, 1619-1621.
(40) Garlich, J. R.; De, P.; Dey, N.; Su, J. D.; Peng, X.; Miller, A.; Murali, R.; Lu, Y.; Mills, G. B.; Kundra, V.; Shu, H.-K.; Peng, Q.; Durden, D. L. A vascular targeted pan phosphoinositide 3-kinase inhibitor prodrug, SF1126, with antitumor and antiangiogenic activity. *Cancer Res.* **2008**, *68*, 206-215.
(41) Wu, P.-H.; Opadele, A. E.; Onodera, Y.; Nam, J.-M. Targeting integrins in cancer nanomedicine: applications in cancer diagnosis and therapy. *Cancers* **2019**, *11*, 1783.
(42) Cheng, Y.-J.; Cheng, H.; Zhao, X.; Xu, X.-D.; Zhuo, R.-X.; He, F. Self-assembled micelles of a multi-functional amphiphilic fusion (MFAF) peptide for targeted cancer therapy. *Polymer Chemistry* **2015**, *6*, 3512-3520.
(43) Nguyen, P. K.; Gao, W.; Patel, S. D.; Siddiqui, Z.; Weiner, S.; Shimizu, E.; Sarkar, B.; Kumar, V. A. Self-assembly of a dentinogenic peptide hydrogel. *ACS Omega* **2018**, *3*, 5980-5987.
(44) Moore, A. N.; Hartgerink, J. D. Self-assembling multidomain peptide nanofibers for delivery of bioactive molecules and tissue regeneration. *Acc. Chem. Res.* **2017**, *50*, 714-722.
(45) Kumar, V. A.; Liu, Q.; Wickremasinghe, N. C.; Shi, S.; Cornwright, T. T.; Deng, Y.; Azares, A.; Moore, A. N.; Acevedo-Jake, A. M.; Agudo, N. R.; Pan, S.; Woodside, D. G.; Vanderslice, P.; Willerson, J. T.; Dixon, R. A.; Hartgerink, J. D. Treatment of hind limb ischemia using angiogenic peptide nanofibers. *Biomaterials* **2016**, *98*, 113-119.
(46) Kumar, V. A.; Taylor, N. L.; Shi, S.; Wickremasinghe, N. C.; D'Souza, R. N.; Hartgerink, J. D. Self-assembling multidomain peptides tailor biological responses through biphasic release. *Biomaterials* **2015**, *52*, 71-78.
(47) Xu, D.; Samways, D. S. K.; Dong, H. Fabrication of self-assembling nanofibers with optimal cell uptake and therapeutic delivery efficacy. *Bioact. Mater.* **2017**, *2*, 260-268.
(48) Xu, D.; Jiang, L.; DeRidder, L.; Elmore, B.; Bukhari, M.; Wei, Q.; Samways, D. S. K.; Dong, H. Membrane activity of a supramolecular peptide-based chemotherapeutic enhancer. *Mol. Biosyst.* **2016**, *12*, 2695-2699.

(49) Xu, D.; Dustin, D.; Jiang, L.; Samways, D. S. K.; Dong, H. Designed filamentous cell penetrating peptides: probing supramolecular structure-dependent membrane activity and transfection efficiency. *Chem. Comm.* **2015**, *51*, 11757-11760.
(50) Yang, M.; Xu, D.; Jiang, L.; Zhang, L.; Dustin, D.; Lund, R.; Liu, L.; Dong, H. Filamentous supramolecular peptide–drug conjugates as highly efficient drug delivery vehicles. *Chem. Comm.* **2014**, *50*, 4827-4830.
(51) Cheng, D.-B.; Zhang, X.-H.; Gao, Y.-J.; Ji, L.; Hou, D.; Wang, Z.; Xu, W.; Qiao, Z.-Y.; Wang, H. Endogenous reactive oxygen species-triggered morphology transformation for enhanced cooperative interaction with mitochondria. *J. Am. Chem. Soc.* **2019**, *141*, 7235-7239.
(52) Li, M.; Ning, Y.; Chen, J.; Duan, X.; Song, N.; Ding, D.; Su, X.; Yu, Z. Proline isomerization-regulated tumor microenvironment-adaptable self-assembly of peptides for enhanced therapeutic efficacy. *Nano Lett.* **2019**, *19*, 7965-7976.
(53) Xu, D.; Chen, W.; Tobin-Miyaji, Y. J.; Sturge, C. R.; Yang, S.; Elmore, B.; Singh, A.; Pybus, C.; Greenberg, D. E.; Sellati, T. J.; Qiang, W.; Dong, H. Fabrication and microscopic and spectroscopic characterization of cytocompatible self-assembling antimicrobial nanofibers. *ACS Infect. Dis.* **2018**, *4*, 1327-1335.
(54) Xu, D.; Jiang, L.; Singh, A.; Dustin, D.; Yang, M.; Liu, L.; Lund, R.; Sellati, T. J.; Dong, H. Designed supramolecular filamentous peptides: balance of nanostructure, cytotoxicity and antimicrobial activity. *Chem. Comm.* **2015**, *51*, 1289-1292.
(55) Dong, H.; Paramonov, S. E.; Aulisa, L.; Bakota, E. L.; Hartgerink, J. D. Self-assembly of multidomain peptides: balancing molecular frustration controls conformation and nanostructure. *J. Am. Chem. Soc.* **2007**, *129*, 12468-12472.
(56) Amaro, M.; Filipe, H. A. L.; Prates Ramalho, J. P.; Hof, M.; Loura, L. M. S. Fluorescence of nitrobenzoxadiazole (NBD)-labeled lipids in model membranes is connected not to lipid mobility but to probe location. *Phys. Chem. Chem. Phys.* **2016**, *18*, 7042-7054.
(57) Wang, S.-T.; Lin, Y.; Spencer, R. K.; Thomas, M. R.; Nguyen, A. I.; Amdursky, N.; Pashuck, E. T.; Skaalure, S. C.; Song, C. Y.; Parmar, P. A.; Morgan, R. M.; Ercius, P.; Aloni, S.; Zuckermann, R. N.; Stevens, M. M. Sequence-dependent self-assembly and structural diversity of islet amyloid polypeptide-derived β-sheet fibrils. *ACS nano* **2017**, *11*, 8579-8589.
(58) Kitamura, A.; Kiyota, T.; Tomohiro, M.; Umeda, A.; Lee, S.; Inoue, T.; Sugihara, G. Morphological behavior of acidic and neutral liposomes induced by basic amphiphilic α-helical peptides with systematically varied hydrophobic-hydrophilic balance. *Biophys. J.* **1999**, *76*, 1457-1468.
(59) Ruozi, B.; Belletti, D.; Tombesi, A.; Tosi, G.; Bondioli, L.; Forni, F.; Vandelli, M. A. AFM, ESEM, TEM, and CLSM in liposomal characterization: a comparative study. *Int J Nanomedicine* **2011**, *6*, 557-563.
(60) Grzegorz, Z.; Anna, J.; Katarzyna, C.; Barbara, P.; Barbara, S. Congo red fluorescence upon binding to macromolecules – a possible explanation for the enhanced intensity. *Bio-Algorithms and Med-Systems* **2017**, *13*, 69-78.
(61) Klunk, W. E.; Pettegrew, J. W.; Abraham, D. J. Quantitative evaluation of congo red binding to amyloid-like proteins with a beta-pleated sheet conformation. *J. Histochem. Cytochem.* **1989**, *37*, 1273-1281.
(62) Klunk, W. E.; Jacob, R. F.; Mason, R. P.: [19] Quantifying amyloid by congo red spectral shift assay. In *Methods in Enzymology*; Academic Press, 1999; Vol. 309; pp 285-305.
(63) Pepe, A.; Bochicchio, B. An elastin-derived self-assembling polypeptide. *J. Soft Matter* **2013**, *2013*.

(64) Girych, M.; Gorbenko, G.; Maliyov, I.; Trusova, V.; Mizuguchi, C.; Saito, H.; Kinnunen, P. Combined thioflavin T–Congo red fluorescence assay for amyloid fibril detection. *Methods Appl. Fluoresc.* **2016**, *4*, 034010.
(65) Kan, A.; Birnbaum, D. P.; Praveschotinunt, P.; Joshi, N. S. Congo red fluorescence for rapid *in situ* characterization of synthetic curli systems. *Appl. Environ. Microbiol.* **2019**, *85*, e00434-00419.
(66) Shahi, P.; Sharma, R.; Sanger, S.; Kumar, I.; Jolly, R. S. Formation of amyloid fibrils via longitudinal growth of oligomers. *Biochemistry* **2007**, *46*, 7365-7373.
(67) Tew, K. D. Glutathione-associated enzymes in anticancer drug resistance. *Cancer Res.* **1994**, *54*, 4313-4320.
(68) Somani, S.; Laskar, P.; Altwaijry, N.; Kewcharoenvong, P.; Irving, C.; Robb, G.; Pickard, B. S.; Dufès, C. PEGylation of polypropylenimine dendrimers: effects on cytotoxicity, DNA condensation, gene delivery and expression in cancer cells. *Sci. Rep.* **2018**, *8*, 9410.

Chapter 3: Design of Peptide Self-assembly for Antimicrobial Therapy*

One of the major hurdles in the development of antimicrobial peptide (AMP)-based materials is their poor capacity to selectively kill bacteria without harming nearby mammalian cells. Namely, they are antimicrobial but cytotoxic. Current methods of nanoparticle-encapsulated AMPs to target bacteria selectively still have not yet overcome this hurdle. Here we demonstrate a simple yet effective method to address this daunting challenge by associating a natural AMP with a β-sheet-forming synthetic peptide. The integrated peptides self-assembled to form a supramolecular nanofiber, resulting in the presentation of the AMP at the nanofiber-solvent interface in a precisely controlled manner. Using melittin as a model natural AMP, we found that the conformation of melittin changed dramatically when presented on the nanofiber surface, which in turn modulated the induced membrane permeability of the bacterial and mammalian cell membranes. Specifically, the presentation of melittin on the nanofiber restricted its hydrophobic residues, leading to a reduction of the hydrophobic interaction with lipids in the cell membranes. Compellingly, the reduced hydrophobic interaction led to a considerable decrease of melittin's induced permeability of the mammalian cell membrane than that of the bacterial cell membrane. As a result, the AMP-displaying nanofiber preferentially permeabilized and disrupted the membrane of the bacteria without compromising the mammalian cells. Such improved membrane selectivity and cytocompatibility were confirmed in cell-based membrane localization and live-dead assay. Our new strategy holds great promise for fabricating cytocompatible antimicrobial assemblies that offer safer and more effective administration of therapeutic AMPs. These assemblies, with intrinsic antimicrobial activity and cytocompatibility, can also serve as building

* This chapter is based on Weike Chen, Su Yang, Shuxin Li, John C. Lang, Chuanbin Mao, Peter Kroll, Liping Tang, He Dong. " Self-assembled peptide nanofibers display natural antimicrobial peptides to selectively kill bacteria without compromising cytocompatibility. *ACS Appl. Mater. Interfaces*, **2019**, *11*, 28681-28689. Some sections were rearranged for continuity.

blocks for the construction of higher-ordered scaffolds for other biomedical applications such as tissue engineering and regenerative medicine.

3.1 Introduction

The increased bacterial drug resistance to conventional antibiotics has been considered one of the greatest threats to public health. Antimicrobial peptides (AMPs) are short and generally positive peptides that have brought tremendous opportunity and promise to overcome the prevalence of bacterial resistance by direct disruption of bacterial membranes via electrostatic and hydrophobic interactions, which is less likely to induce drug resistance.[1-4] In the past three decades, substantial efforts have been made for the development of high-throughput sources for AMP discovery, however, most AMPs acting on cell membranes are not completely selective to bacterial cells but are also toxic to mammalian and blood cells, which has limited their clinical applications.[5-7] To minimize the intrinsic hemolytic and cytotoxic effects of AMPs, nanoparticles have been developed as nanocarriers to deliver AMPs to the site of infections.[8,9] However, unlike lower molecular weight antibiotics and anticancer drugs, the encapsulation of AMPs within a designated nanoparticulate compartment and the control over subsequent release can be challenging, since the formation and stability of secondary structure of AMPs are based on weak non-covalent interactions that are sensitive to environmental factors such pH, ionic strength, metal ions, and non-aqueous solvents present in common manufacturing processes. Disruption of any of these interactions will destabilize the AMPs, leading to dysfunctions.[10-12] The construction of such multicomponent nanoparticulate formulation often requires onerous procedures. Therefore, it is highly imperative to develop simple, yet effective strategies that allow AMPs to be incorporated within a nanostructure in a precisely controlled manner while maintaining their antimicrobial

activity but enhancing membrane selectivity. The establishment of this platform technology may greatly boost the therapeutic index of AMPs, potentiating their use as clinical antimicrobials.

Supramolecular peptide nanofibers based on the self-assembly of β-sheet forming peptides have emerged as an important class of biomaterials having great utility in a variety of biomedical settings.[13-18] These nanofibers, which offer unique templates for controlling the internal order and molecular packing of the therapeutics, define important parameters for effectively interfacing with cells and tissues in a controlled and predictable manner. The design and synthesis of the molecular building blocks can be highly modular by incorporating diverse functional peptides or proteins at the termini of the β-sheet forming peptides. Upon self-assembly, nanofibers presenting multivalent ligands and epitopes can be fabricated with precisely controlled recognition sites, stoichiometry, density and multi-valency to provide desired biological functionality. This strategy has been exquisitely applied for the construction of fibrous tissue scaffolds,[19,20] supramolecular nanofiber vaccines[21-23] and recently angiogenic nanofibers.[24,25] However, their application for antimicrobial nanomaterial design and synthesis has rarely been explored. As most AMPs suffer poor membrane selectivity and severe cytotoxicity against mammalian cells, new approaches to improve their cytocompatibility are highly needed. This study will establish a new method by presenting natural AMPs on a nanofiber scaffold to improve their cytocompatibility. In addition, the self-assembly approach is highly modular with the potential of integrating multiple AMPs with distinct sequences and structures to exert synergistic effects. The preliminary results shown in this study serve as the foundation for new fundamental studies of peptide-membrane interaction in the context of a confined supramolecular framework. These results will also provide a new application direction for these nanofiber scaffolds that can display a combination of various natural AMPs and potentially other biologically active peptides for a range of biomedical applications.

To fabricate these new nanofibers, we capitalized on our recent development of self-assembling antimicrobial nanofibers (SAANs) using synthetic multidomain peptides (MDPs) as the molecular building block.[26] MDPs have a general sequence of $K_x(QL)_zK_y$ (K: lysine; Q: glutamine; L: leucine) in which x, y, z represent the numbers of the repeating units of each domain. MDPs were designed to mimic natural AMPs in which a global amphiphilic β-sheet secondary structure is formed driven by the hydrophobic interaction and hydrogen bonding among the alternating $(QL)_6$ repeating units. Unlike traditional single-chain AMPs, MDPs undergo self-assembly into a sandwich-like nanofiber in which the hydrophobic leucine residues are embedded within the nanofiber. Recently, using transmission electron microscopy (TEM) and solid-state NMR (ssNMR), we demonstrated that partial masking of the hydrophobic surface upon self-assembly is an important factor contributing to the reduction in mammalian cytotoxicity of the MDPs, yet preserving efficacy against broad-spectrum bacteria.[27] Building on the success, we applied this self-assembly strategy to the production of cytocompatible SAANs containing natural AMPs that are known for their potent antimicrobial activity but severe cell/tissue cytotoxicity. Upon self-assembly, the constraints on the hydrophobic residues of melittin limit their hydrophobic interaction with the lipid membrane, which led to a considerably larger reduction of melittin's induced permeability of the mammalian cell membrane than that of the bacterial cell membrane. As a result, an increase of membrane selectivity toward bacteria was achieved. The results provided in the following sections serve to establish – through structural assessments, bioactivity, and biophysical evaluation of membrane response – as the next step, a SAAN-based technology platform that can be applied to a variety of naturally occurring and synthetic AMPs to improve their cytocompatibility for safer and more effective therapeutic administration.

3.2 Results and Discussion

3.2.1 Peptide Design

For the proof-of-concept study, we selected melittin (Mel, 26aa) as a model naturally occurring AMP which is known to have severe cytotoxicity against mammalian cells.[28,29] Mel was conjugated to the C-terminus of an MDP with the sequence of HHHQLQLQLQLQLQL (**Figure 3.1**). The conjugate is named as $(QL)_6$-Mel. Three histidine residues were included at the N-terminus of the $(QL)_6$ domain to increase the solubility of the conjugate at the acidic pH for reverse phase HPLC purification. The histidine residues were not directly conjugated to the Mel domain such that Mel can exert their biological activity without potential interference from this tagging domain. While it is not the primary focus of this study, the inclusion of histidine residues may also allow the fabrication of pH-responsive antimicrobial nanomaterials. For the second peptide, we chose a previously studied MDP (sequence: WKKQLQLQLQLQLQLKK), named as $(QL)_6$-K which can co-assemble with $(QL)_6$-Mel to generate Mel-presenting nanofibers with controlled stoichiometry (**Figure 3.1**).

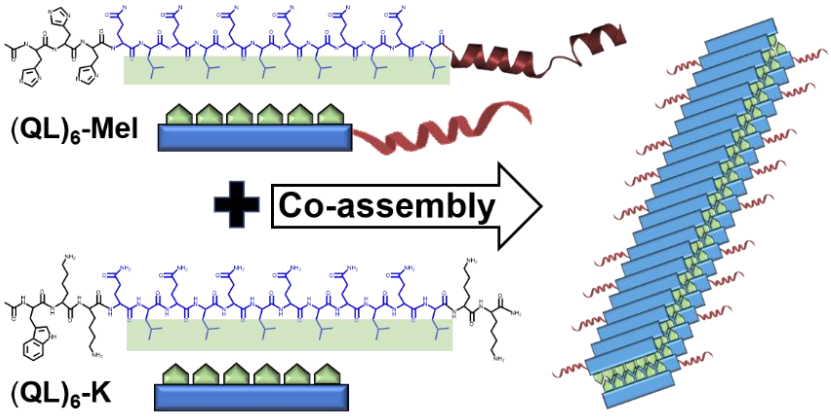

Figure 3.1. Chemical structures of the molecular building blocks for the construction of Mel-integrated SAANs for the investigation of supramolecular structure-dependent membrane selectivity and cytotoxicity.

The selection of $(QL)_6$-K is based on the following considerations. First, the stability of the nanofiber is dictated by the ratio of the repeating units of each domain. Based on our previous studies, $(QL)_6$-K seemed to strike a good balance between self-assembly and disassembly, which led to highly water-soluble nanofibers with good supramolecular stability as demonstrated by the slow subunit exchange through fluorescence self-quenching.[30] Secondly, $(QL)_6$-K showed exceptional hemocompatibility and cytocompatibility upon nanofiber formation by confining the hydrophobic residues within the interior of the nanofiber to minimize their interaction with the cell membrane. This makes it an ideal supramolecular scaffold upon which to construct functional peptide nanostructures with good cytocompatibility. SAANs consisting of 10%, 30% and 50% of Mel were formulated and characterized for their secondary structure, nanostructure, membrane selectivity, cytotoxicity and antimicrobial activity. In the following study, they are referred as SAANs (Mel-10%), SAANs (Mel-30%) and SAANs (Mel-50%).

3.2.2 Structural Characterization

To validate that co-assembly indeed occurred, we measured and compared the fluorescence intensity of three rhodamine (Rho)-labeled Mel-containing formulations (**Figure 3.2A**), (1) Free Rho-Mel, (2) Co-assembly of Rho-$(QL)_6$-Mel with $(QL)_6$-K and (3) Homo-assembly of Rho-$(QL)_6$-Mel. As expected, the co-assembly exhibited fluorescence emission between the free Mel and the homo-assembly of $(QL)_6$-Mel (**Figure 3.2B**), suggesting that Mel was organized within the assembly and "diluted" by $(QL)_6$-K to reduce the fluorescence self-quenching effect. The co-assembly exhibited good supramolecular stability as shown by the minimum change of the fluorescence intensity up to 24 hrs of incubation at room temperature (RT) (**Figure 3.3A**). A mixture consisting of free Mel and $(QL)_6$-K showed comparable fluorescence intensity to that of free Mel (**Figure 3.3B**), suggesting no physical interaction occurred between free Mel and $(QL)_6$-

K and the co-assembly is specifically driven by the $(QL)_6$ domains. More interestingly, we found that the post-assembly product, which is formulated by mixing preformed $(QL)_6$-Mel nanofiber and $(QL)_6$-K nanofiber in the aqueous buffer, exhibited an increase of fluorescence intensity that reached a plateau after 12 hrs (**Figure 3.3C**). This observation further confirmed the presence of a highly specific interaction between $(QL)_6$-Mel and $(QL)_6$-K and the co-assembly is largely driven by the consensus β-sheet forming domain of $(QL)_6$. Notably, the final fluorescence reading of the post-assembly is lower than that of the co-assembly indicative of the presence of $(QL)_6$-Mel clusters that may self-quench, rather than being fully "dissolved" within the $(QL)_6$-K matrix (**Figure 3.3D**).

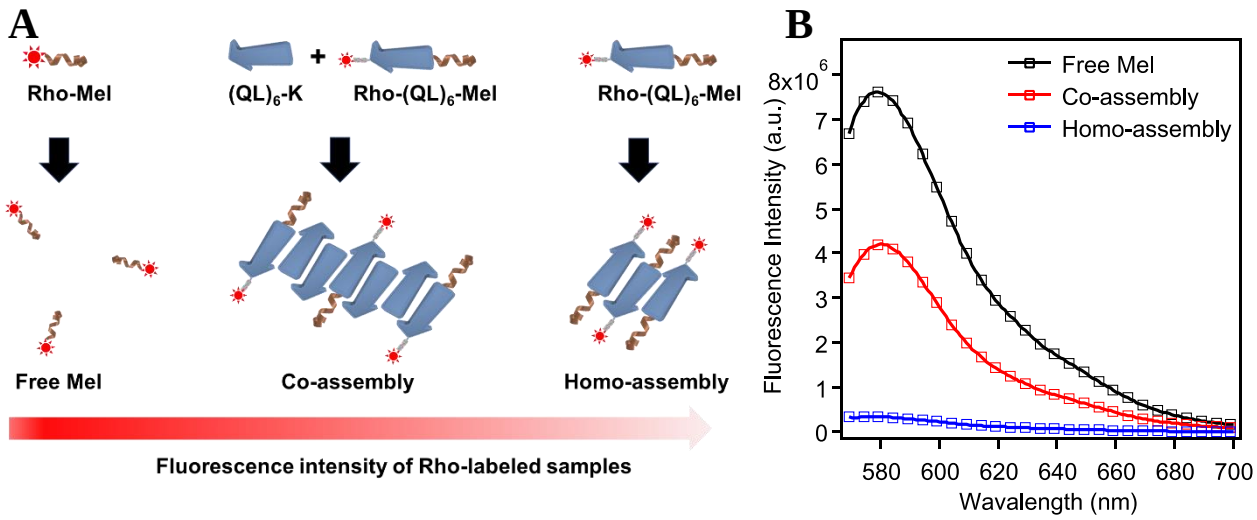

Figure 3.2. (A) Schematic cartoon showing the formation of Mel-integrated SAANs driven by the consensus fiber-forming domain of $(QL)_6$. Rhodamine is used as a fluorescence readout for monitoring and confirming the self-assembly and co-assembly process. **(B)** The fluorescence emission spectra of co-assembled Mel-presenting SAANs in comparison with free Mel and its homo-assembly. Samples were prepared in Tris buffer (pH = 7.4, 20 mM) with a final concentration for free Rho-Mel at 1 μM, homo-assembly of Rho-$(QL)_6$-Mel at 1 μM and co-assembly of Rho-$(QL)_6$-Mel at 1 μM and $(QL)_6$-K at 49 μM. Spectra were acquired after 12 hrs of incubation at room temperature.

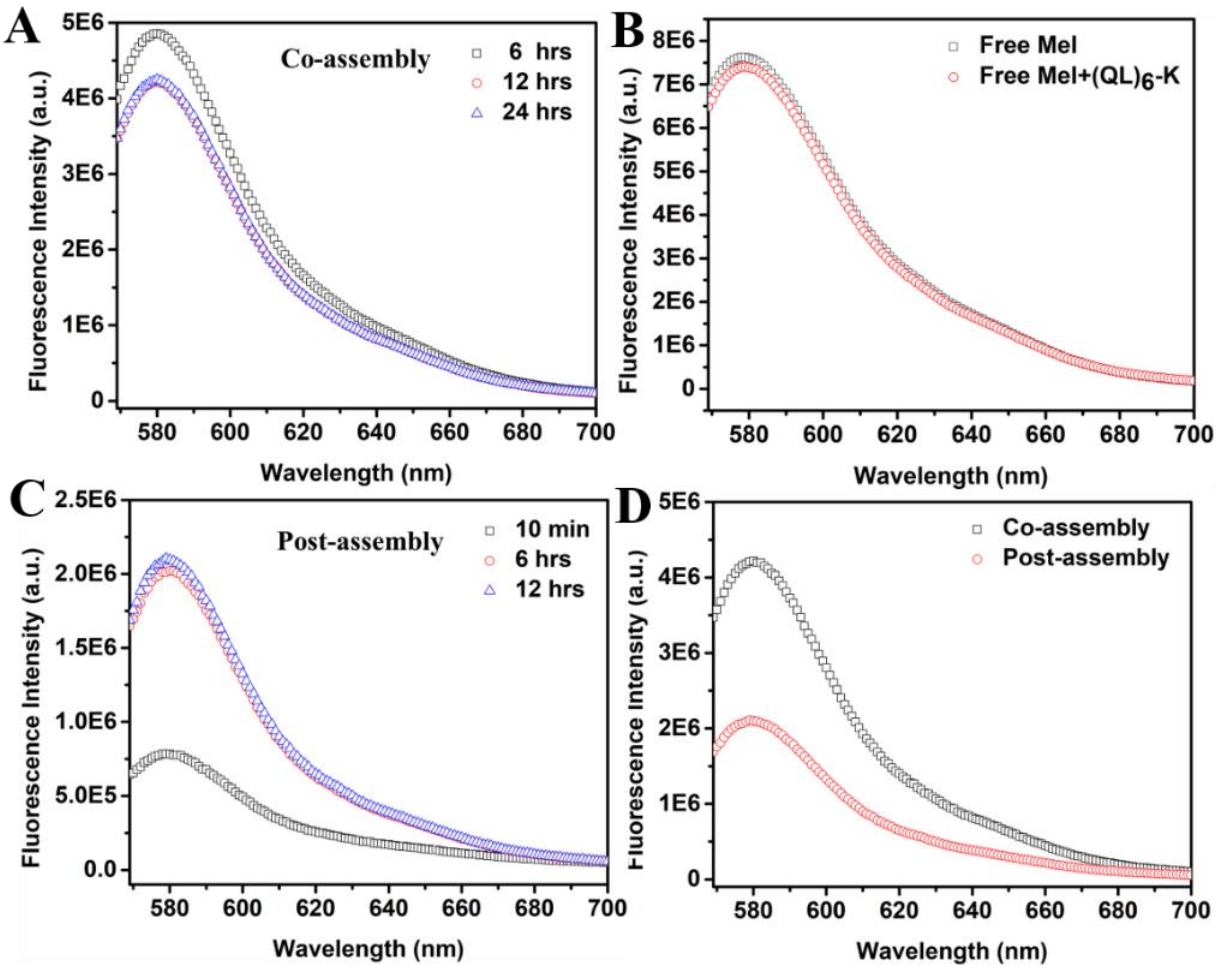

Figure 3.3. (A) The time-dependent fluorescence emission spectra of the Rho-labeled co-assembly exhibits a minimum change of the fluorescence intensity of the co-assembly therefore good supramolecular stability; **(B)** The fluorescence emission spectra of free Mel and a physical mixture of Mel/$(QL)_6$-K shows comparable fluorescence intensity after 12 hrs of incubation suggesting the lack of non-specific physical interaction between Mel and $(QL)_6$-K nanofibers; **(C)** The fluorescence emission spectra of the post-assembly shows time-dependent fluorescence recovery confirming the specific interaction occurs between the preformed $(QL)_6$-Mel and $(QL)_6$-K nanofibers as driven by the β-sheet forming domain of $(QL)_6$; **(D)** Comparison of the fluorescence emission spectra of the co-assembly versus post-assembly further supports that co-assembly can be used to integrate and arrange Rho-labeled $(QL)_6$-Mel more effectively across the entire $(QL)_6$-K nanofiber to minimize the self-quenching effect. All samples were prepared in Tris buffer (pH=7.4, 20 mM) with free Rho-Mel at 1 μM; Mel/$(QL)_6$-K physical mixture at a total concentration of 50 μM consisting of 1 μM of Rho-Mel; Co-assembly at a total concentration of 50 μM consisting of 1 μM of Rho-$(QL)_6$-Mel.

Melittin is known to adopt random coils when standing alone and changes to α-helices upon binding to the cell membrane.[29,31] The structural change was confirmed by the circular

dichroism (CD) spectroscopy for free Mel in the absence and presence of sodium dodecyl sulfate (SDS) micelles which are used to mimic the negatively charged bacterial membrane (**Figure 3.4A**). The formation of a global amphiphilic α-helix is an important factor that allows Mel to effectively interact and disrupt the bacterial cell membrane. However, due to the lack of membrane selectivity, these helical structures pose a significant challenge to the membrane integrity and cell viability of mammalian cells. Upon the formation of SAANs, the secondary structures of Mel changed. The three co-assemblies, namely SAANs (Mel-10%), SAANs (Mel-30%) and SAANs (Mel-50%) exhibited a typical β-sheet secondary structure with one negative absorption peak at around 216 nm in SDS-free solutions (**Figure 3.4B** to **3.4D**). The Collier group reported an exquisite family of immunologically active β-sheet nanofibers which are independent of the size and secondary structural propensity of the terminal peptide/protein antigen epitopes.[17] Inspired by these findings, we postulate that upon self-assembly, the majority of Mel was forced to form β-sheet secondary structures to accommodate the intermolecular packing of the building blocks to form supramolecular nanofibers. The structural confinement of Mel on a supramolecular scaffold was later found to be critical in modulating their membrane selectivity. In the bacterial membrane-mimicking condition (SDS micelles), small fractions of α-helices may be induced as shown by the slight shift and peak broadening toward a lower wavelength for all co-assemblies (**Figure 3.4B** to **3.4D**). We are aware that CD spectroscopy may not provide a more detailed and quantitative analysis of the potential α-helical structure and its percentage. We are currently using ss-NMR spectroscopy to identify the amino acids that are responsible for the helix formation and related findings will be reported separately.

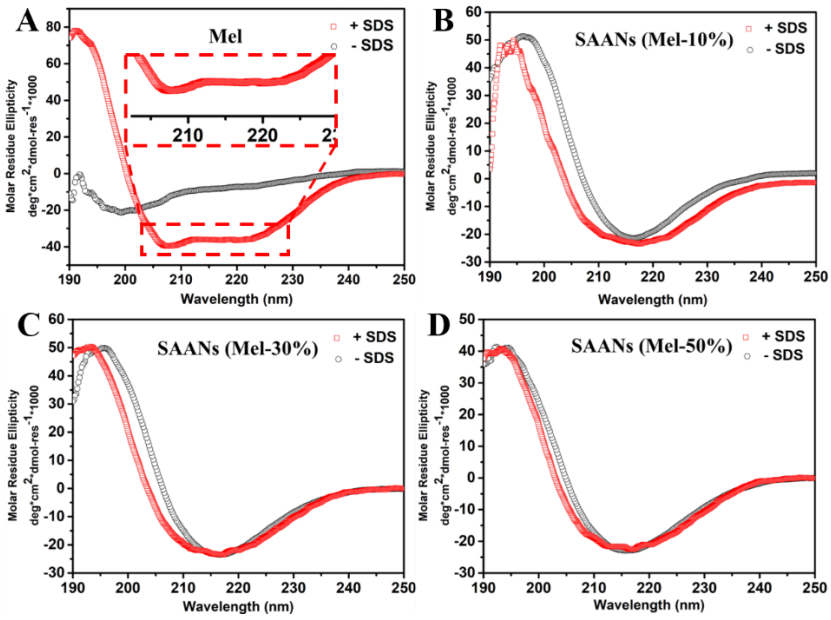

Figure 3.4. Secondary structures of free Mel and Mel-integrated SAANs in the absence and presence of SDS as monitored by CD spectroscopy. **(A)** Free Mel; **(B)** SAANs (Mel-10%); **(C)** SAANs (Mel-30%); **(D)** SAANs (Mel-50%). Peptides were prepared in Tris buffer (pH=7.4, 20 mM) with a final total peptide concentration at 50 μM.

Transmission electron microscopy (TEM) was used to characterize the nanostructures of different SAANs formulations. Like most β-sheet peptide nanofibers,[32,33] all SAANs show a polydisperse fiber length distribution. As shown in **Figure 3.5**, increasing the composition of Mel has a drastic effect on the fiber morphology, broadening the fiber diameter and shortening the fiber length. This is presumably due to the steric hindrance caused by the bulky Mel moieties, which compromised the molecular packing of peptides in the longitudinal direction as Mel composition increases. As a control, simply mixing of free Mel with $(QL)_6$-K did not cause an appreciable change in the fiber morphology formed by $(QL)_6$-K (**Figure 3.6**), which suggests that physical interactions alone between free Mel and $(QL)_6$-K were inadequate for significant association or encapsulation. Integrating Mel and the β-sheet forming $(QL)_6$ peptide is an effective means for the fabrication of Mel-integrated SAANs with tunable physicochemical properties and biological activities. Dynamic light scattering (DLS) provided a semi-quantitative measure of the volume-

weighted distribution of hydrodynamic size of different SAANs (**Figure 3.7A**), further confirming the TEM results in which the increase of Mel composition resulted in SAANs of smaller dimension. The plot of the hydrodynamic diameter by intensity (**Figure 3.7B**), more sensitive to the larger particles, showed the same trend of size reduction with the increase of Mel composition. Notably, the integration of Mel caused a wider size distribution of the nanofibers as shown by both TEM and DLS experimental results. The underlying mechanisms for such changes are of current interest and the focus of continuing systematic investigations.

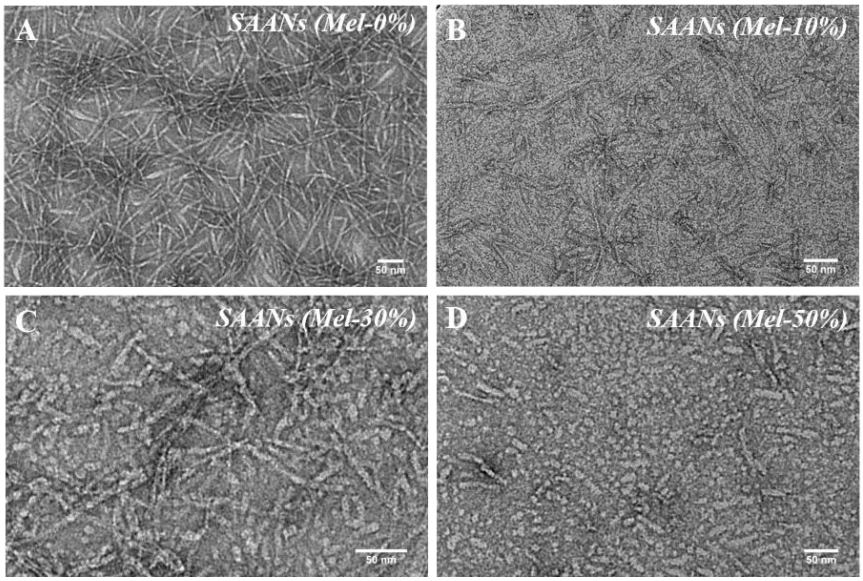

Figure 3.5. TEM images of SAANs containing different Mel contents. **(A)**. SAANs (Mel-0%); **(B)**. SAANs (Mel-10%); **(C)**. SAANs (Mel-30%); **(D)**. SAANs (Mel-50%). The total peptide concentration for TEM sample preparation is at 50 μM.

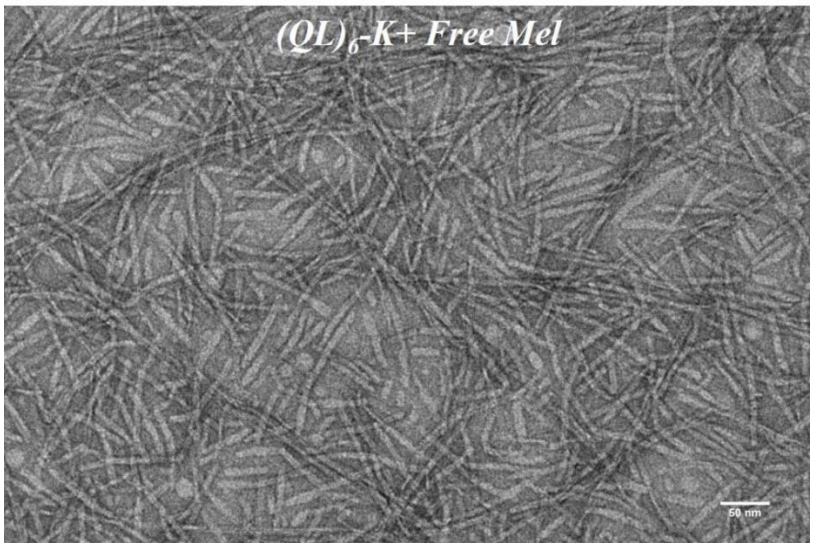

Figure 3.6. The TEM image of physically mixed $(QL)_6$-K with free Mel shows minimum change of the fiber morphology compared to that formed $(QL)_6$-K alone, which suggests a lack of interaction between free Mel and $(QL)_6$-K. The peptides were prepared in Tris buffer with a total concentration at 50 μM and free Mel accounts for 30% (15 μM).

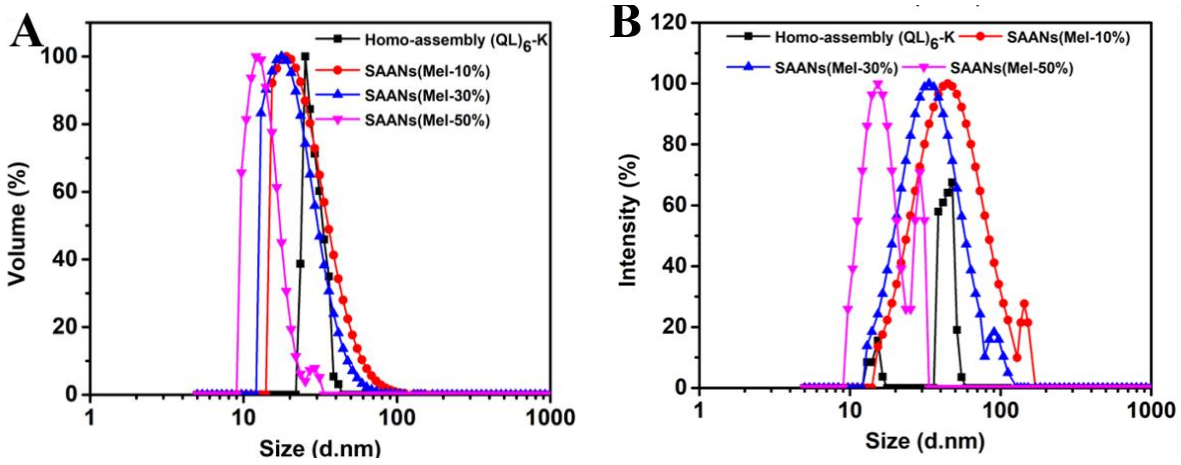

Figure 3.7. Hydrodynamic size characterization of different SAANs by DLS, scattering observed at an angle of 90° and a temperature of 23 °C. The hydrodynamic diameter distributions are weighted by: **(A)** particle volume and **(B)** particle scattering intensity. In these figures the relative fraction is based on amplitudes of scattering from the particle scattering most, a value set to 100. Notably, in both **Figure 3.7A** and **3.7B**, the hydrodynamic diameter of Mel-integrated SAANs decreased with increasing of Mel composition. All samples were prepared in Tris buffer (pH 7.4, 20 mM) with a total peptide concentration at 10 μM.

3.2.3 Biophysical Characterization of the Membrane Activity

Membrane permeation assay was used to investigate the membrane activity of Mel-integrated SAANs. The basic principle of the assay relies upon the depolarization of the cytoplasmic membrane that causes fluorescence intensity change of a membrane potential-dependent probe (diSC3-5) upon membrane disruption. Liposomes with two different compositions were prepared i.e. PC/PG liposomes (1:1 W/W) and PC/Cholesterol liposomes (8:1 W/W) to mimic the bacterial and mammalian cell membranes respectively.[34-36] The addition of Mel-integrated SAANs or free Mel will cause membrane disruption leading to an increase of the fluorescence intensity of diSC3-5 which was pre-encapsulated in the liposome. The fluorescence intensity can be considered as a qualitative measurement of the peptides' ability to disrupt different cell membranes. For any given sample, the bacterial/mammalian cell membrane selectivity can be quantified by the selection index (SI) which is defined and calculated as the ratio of the fluorescence intensity measured in the PC/PG/Cholesterol liposome solution (bacterial membrane mimetics) to that of PC/Cholesterol liposomes (mammalian cell membrane mimetics). As shown in **Figure 3.8**, the fluorescence recovery occurs rapidly after 30 s upon mixing liposomes with various Mel containing samples. After reaching the equilibrium after 4 minutes, Mel exhibited poor membrane selectivity with a SI at 1.06 while the Mel-presenting SAANs dramatically improved the selectivity with SI at 4.76 for SAANs (Mel-10%), 3.34 for SAANs (Mel-30%) and 2.36 for SAANs (Mel-50%).

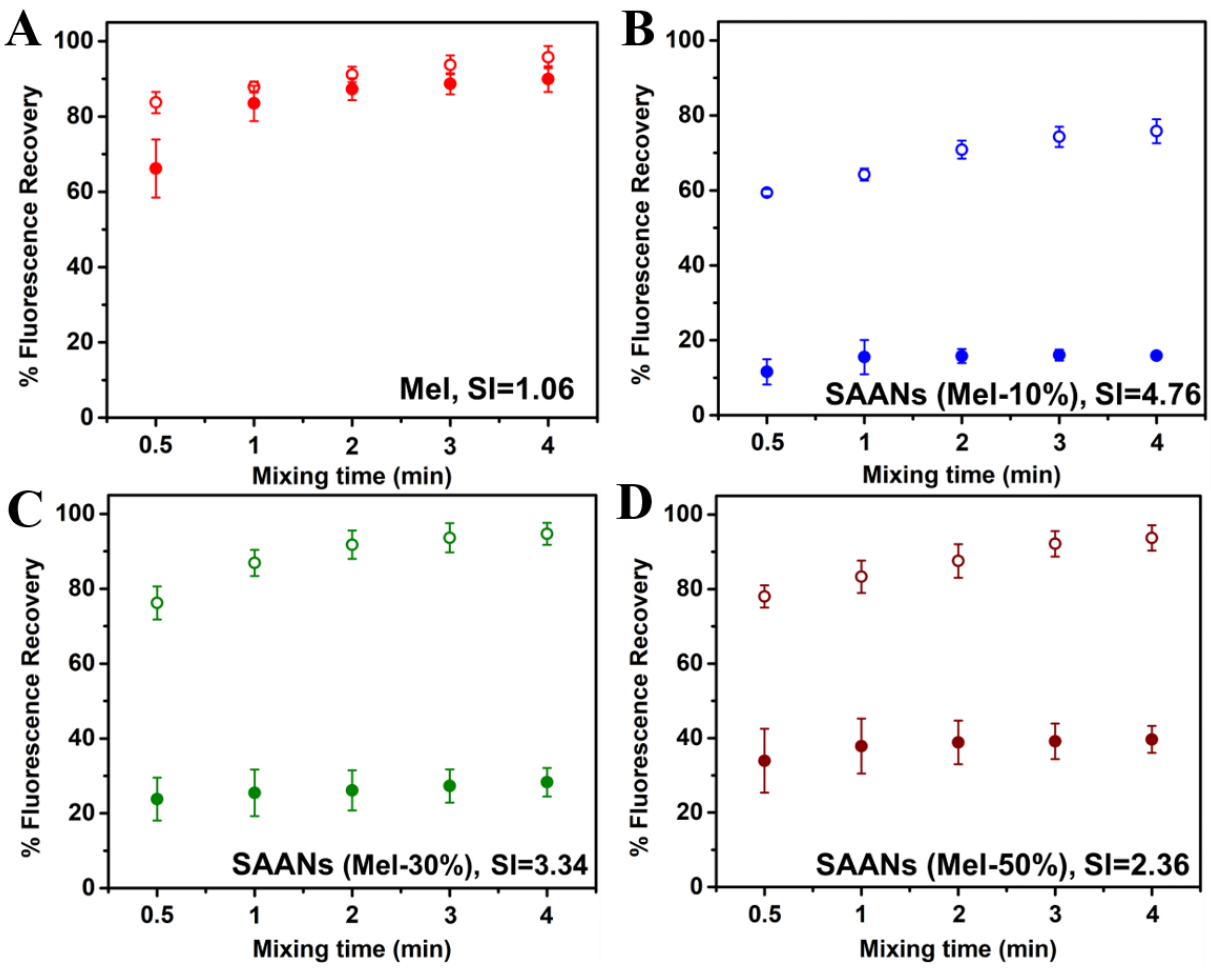

Figure 3.8. Membrane permeability assay by monitoring the fluorescence recovery of a membrane potential-dependent probe (diSC3-5) upon membrane disruption caused by **(A)** free Mel; **(B)** SAANs (Mel-10%); **(C)** SAANs (Mel-30%); **(D)** SAANs (Mel-50%). Open circle: PC/PG (1:1, W/W) liposomes for mimicking the bacterial membrane; Close circle: PC/Cholesterol (8:1, W/W) for mimicking the mammalian cell membrane. The total peptide concentration for SAANs was 20 μM. Free Mel was prepared at 6 μM.

AMPs rely on a combined hydrophobic and electrostatic interaction to cause membrane disruption and lysis. The membrane activity of AMPs toward mammalian cells and bacteria can be adjusted by changing these interactions. The hydrophobic interaction has been considered as a more dominant factor for AMPs to permeabilize the mammalian cell membrane and cause membrane lysis compared to the bacteria.[37-39] Because of this, many studies used site-specific hydrophobic residue mutation to weaken the hydrophobic interactions of AMPs with the lipid

membranes to increase the membrane selectivity.[29,40-43] In the current work, we demonstrated an alternative yet effective route to enhance the membrane selectivity of AMPs by integrating them on a supramolecular nanofiber scaffold on which structurally confined hydrophobic residues of AMPs have limited accessibility to the lipid membrane, leading to reduced hydrophobic effects.

3.2.4 Cytotoxicity and Antimicrobial Activity Evaluation

Cytotoxicity is a primary concern for most natural and synthetic AMPs in clinical applications.[44] Based on the above results from membrane permeation assay, we hypothesized that structural constraint and partial shielding of Mel on SAANs may be effective to alleviate their cytotoxicity towards mammalian cells. To test the hypothesis, we performed an *in vitro* cytotoxicity assay for SAANs with and without Mel and free Mel in NIH/3T3 mouse fibroblasts. For the negative control group, namely SAANs (Mel-0%) more than 80% of cell viability was observed up to 40 μM and 70% at 80 μM, suggesting good cytocompatibility of SAANs (**Figure 3.9A**). For Mel containing SAANs, the samples were prepared to have the same Mel concentrations. Four Mel dosages at 2.5 μM, 5 μM, 10 μM and 15 μM were used for comparison of the toxicity effect from different formulations. After 24 hrs of incubation, MTT assay was performed to quantify the cell viability. As shown in **Figure 3.9B to 3.9E**, all three Mel-integrated SAANs demonstrated greatly reduced cytotoxicity compared to free Mel and the difference was much more dramatic at higher Mel dosages. A more thorough dose-dependent cytotoxicity measurements were also performed (**Figure 3.10**). These results suggest that tuning the structural constraint of natural AMPs such as Mel on the nanofiber surface may be an effective route to modulate and improve their cytocompatibility. As a control experiment, we prepared a mixture consisting of free Mel and $(QL)_6$-K which exhibited much higher cytotoxicity than that of co-

assembled SAANs composed $(QL)_6$-Mel/$(QL)_6$-K (**Figure 3.11**), further supporting the important role of the local structural order and restriction for reduced cytotoxicity of Mel.

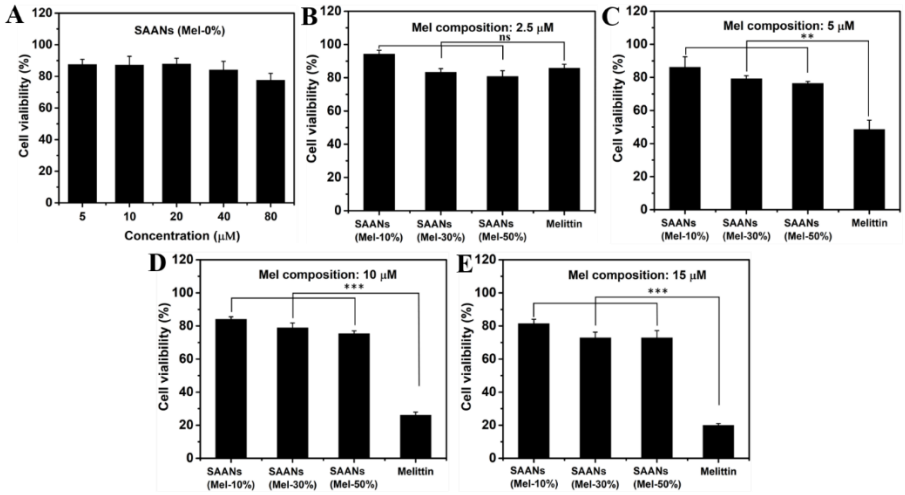

Figure 3.9. Cell viability assay for Mel-free SAANs, Mel-integrated SAANs and free Mel after 24 hrs of incubation of peptides with NIH/3T3 mouse fibroblasts. **(A)** SAANs without Mel, namely SAANs (Mel-0%) at different concentrations; **(B)** Mel-integrated SAANs with Mel composition at 2.5 μM; **(C)** Mel-integrated SAANs with Mel composition at 5 μM; **(D)** Mel-integrated SAANs with Mel composition at 10 μM; **(E)** Mel-integrated SAANs with Mel composition at 15 μM. Statistically significant differences are indicated by **p < 0.01, ***p < 0.001, NS: not significant.

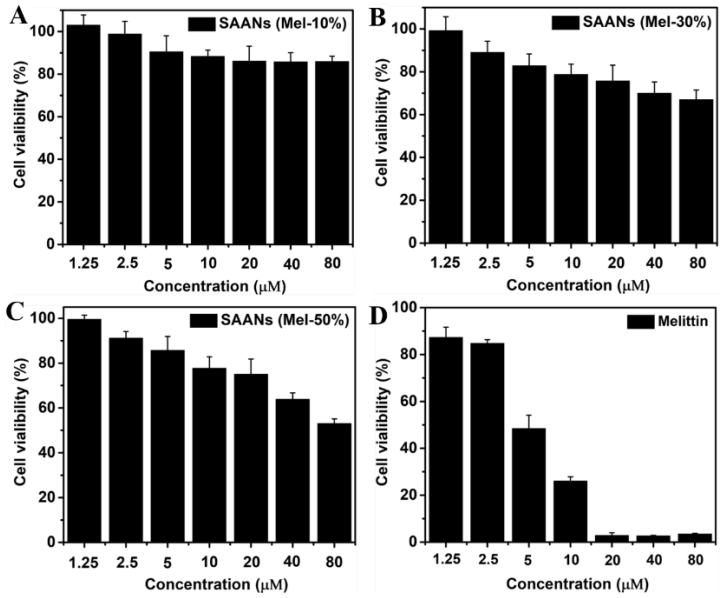

Figure 3.10. Additional cell viability assay of NIH/3T3 mouse fibroblasts upon incubation with different Mel-integrated SAANs, **(A)** SAANs (Mel-10%), **(B)** SAANs (Mel-30%) and **(C)** SAANs (Mel-50%) in comparison with **(D)** free Mel. The assay was performed after 24 hrs of incubation of cells with peptide samples with total peptide concentrations ranging from 1.25 μM to 80 μM.

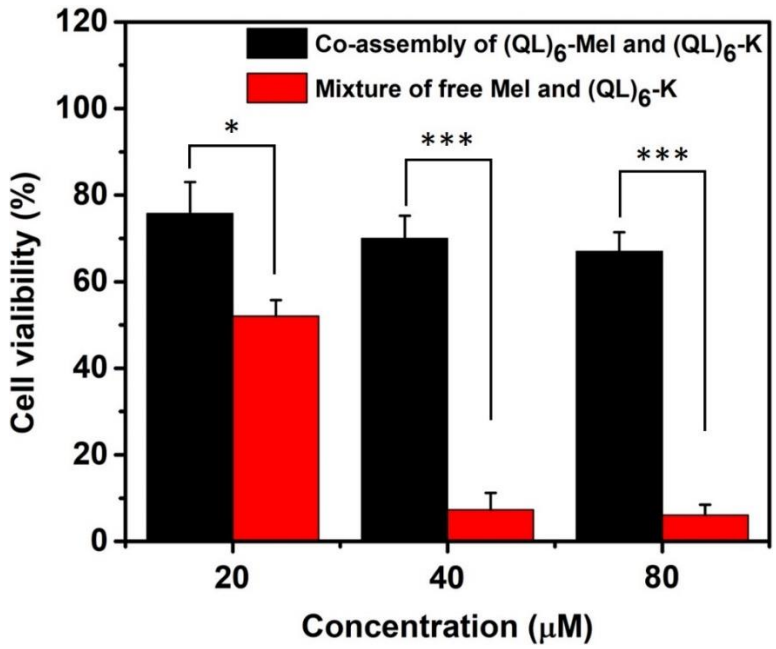

Figure 3.11. Cell viability assay upon 24 hrs of incubation of peptides with NIH/3T3 mouse fibroblasts for SAANs (Mel-30%) and physical mixtures of free Mel (30% of total peptide concentration) and $(QL)_6$-K. The concentrations are the total peptide concentration. The results show greatly reduced cytotoxicity upon assembly. Statistic significant difference are indicated by *$p < 0.05$, ***$p < 0.001$.

The antimicrobial activity of the co-assemblies and free Mel was investigated by the minimum inhibitory concentration (MIC) assay and bacterial killing efficiency assay. The MIC values were presented as both the total peptide concentration and the concentration of Mel in the co-assemblies (**Table 3.1**).

Table 3.1. MICs of free Mel and Mel-integrated SAANs against *E.coli*

Peptides	MIC(μM)
Free Mel	2.5
SAANs (Mel-10%)	>80 (8)
SAANs (Mel-30%)	10 (3.3)
SAANs (Mel-50%)	10 (5)

The value in the parenthesis refers to the concentration of Mel in SAANs

Although SAANs (Mel-10%) did not exhibit antimicrobial activity within the tested concentration range, SAANs (Mel-30%) and SAANs (Mel-50%) had MIC values (3.3 μM and 5 μM, respectively) that are comparable to that of free Mel (2.5 μM). The killing efficiency assay

was further performed to investigate and confirm the antimicrobial activity of Mel upon integration on the nanofiber. After incubation of *E. coli* with SAANs (Mel-30%) and SAANs (Mel-50%) for 24 hrs, the number of bacteria was quantified by counting the colony forming units (CFU) on an agar plate. The CFU was plotted and compared with those from the control *E. coli* culture (without peptides), *E. coli* treated with SAANs (Mel-0%) and *E. coli* treated with free Mel. The results showed both SAANs (Mel-30%) and SAANs (Mel-50%) are effective against *E. coli* growth leading to a significant reduction of bacterial numbers compared to the control *E. coli* while SAANs without Mel conjugation was not effective against *E. coli* growth up to 80 μM (**Figure 3.12)**. It is also not surprising that the activity of SAANs (Mel-30%) and SAANs (Mel-50%) was compromised to some degree compared to free Mel due to the partial restriction of Mel when integrated on SAANs. However, considering the reduced cytotoxicity of SAANs (Mel-30%) and SAANs (Mel-50%) (**Figure 3.9B** and **3.9C**), the cell selectivity toward bacteria was dramatically improved upon the formation of SAANs.

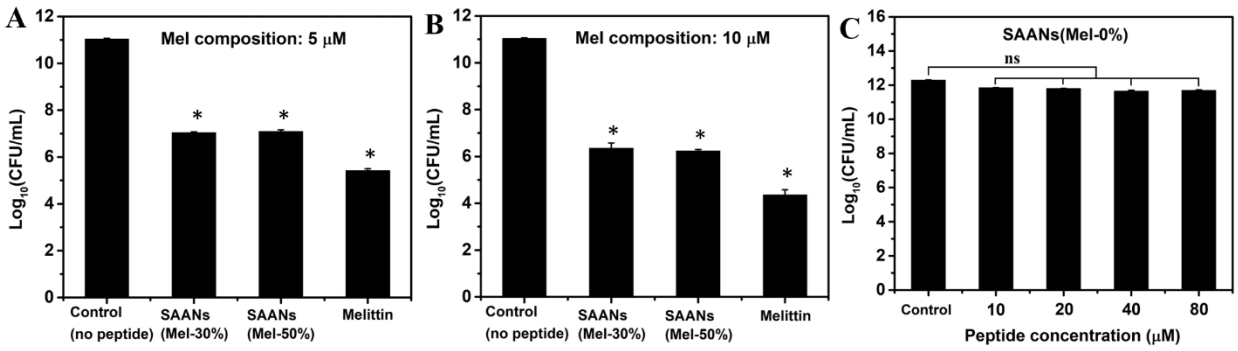

Figure 3.12. The numbers of *E. coli.* upon 24 hrs of incubation of *E. coli* with free Mel and Mel-integrated SAANs at Mel concentrations at **(A)** 5 μM and **(B)** 10 μM and **(C)** with Mel-free SAANs. Statistically significant differences are indicated by *p < 0.05, NS: not significant.

3.2.5 *In vitro* Cell-based Membrane Activity

To identify the mechanisms governing the reduced cytotoxicity of Mel, we investigated the cellular localization of Mel-integrated SAANs upon incubation with NIH/3T3 mouse fibroblast

using epi-fluorescent microscopy. For comparison, free Mel and three physical mixtures of Mel/$(QL)_6$-K containing 10%, 30% and 50% of Mel were prepared and all samples were labeled with Rho for cell localization study. Cells were incubated with different peptide samples for 2 hrs followed by extensive washing to remove non-specific bound peptides. As shown in **Figure 3.13A**, free Mel and all physical mixtures of Mel/$(QL)_6$-K have high membrane permeability and can be found inside the cytoplasm and some even in the nucleus. Within 2 hrs of exposure to free Mel or Mel/$(QL)_6$-K, cells tend to shrink with a clear sign of membrane damage. In contrast, Mel-integrated SAANs were accumulated largely on the surface of cell membrane **(Figure 3.13B)** causing negligible change on the cell membrane and overall morphology.

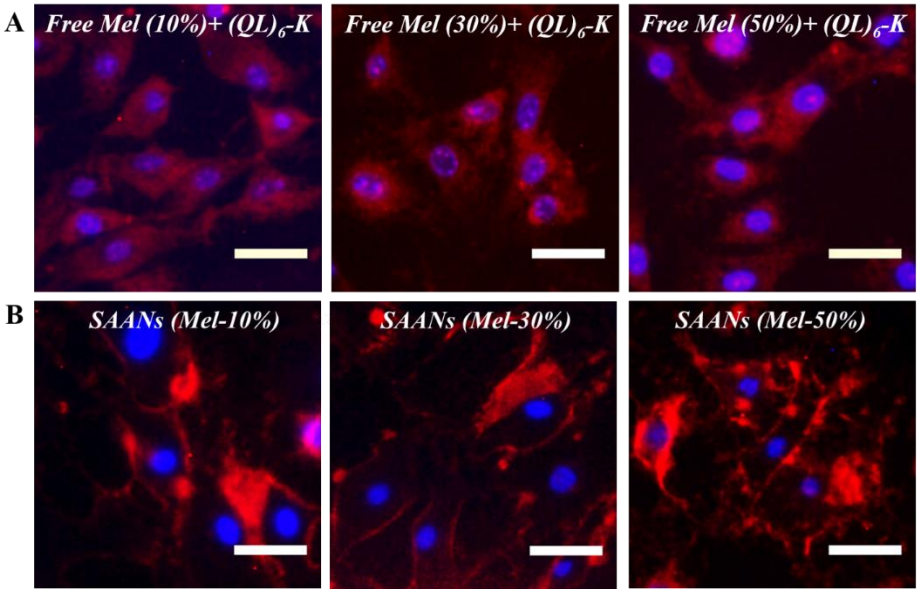

Figure 3.13. Fluorescence images of NIH/3T3 mouse fibroblasts treated with **(A)** Rho-labeled mixture of free Mel and $(QL)_6$-K; **(B)** Mel-integrated SAANs with different Mel composition. The physical mixtures were permeabilized into cells while the co-assemblies accumulated on the membrane after 2 hrs of incubation. The total peptide concentrations were 20 μM. Scale: 50 μm.

The live/dead assay was performed to further confirm the effect of self-assembly on Mel's cytocompatibility and antimicrobial activity. Based on the membrane permeability, MIC and cytotoxicity assay results, we selected SAANs (Mel-30%) to perform the live/dead assay against both *E. coli* and NIH/3T3 fibroblasts. Free Mel was used as a control. As shown in **Figure 3.14A**

and **3.14B**, a large fraction of dead *E. coli* was observed for both SAANs (Mel-30%) and free Mel (top panel) treated bacteria culture as shown by the red staining of propidium iodide (PI). PI was commonly used to evaluate the bacterial cell membrane integrity by penetrating bacteria having damaged membranes.[45,46] This result illustrated free Mel and SAANs (Mel-30%) shared the same antimicrobial mechanism to kill bacteria through punching holes and thus increasing PI's permeability on the bacterial membrane. Using the live/dead fluorescence images, the cell viability was quantified showing comparable killing efficiency between free Mel and SAANs (Mel-30%) (**Figure 3.14E**). For NIH/3T3 mouse fibroblasts, while Mel still caused significant cell death as shown by the red fluorescence (**Figure 3.14C**), SAANs (Mel-30%) had dramatically reduced cytotoxicity as shown by the predominant green fluorescence from the live cells (**Figure 3.14D**). Quantitative analysis of NIH/3T3 cell viability showed much higher cell survival rates upon treatment with SAANs (Mel-30%) than those with free Mel (**Figure 3.14F**).

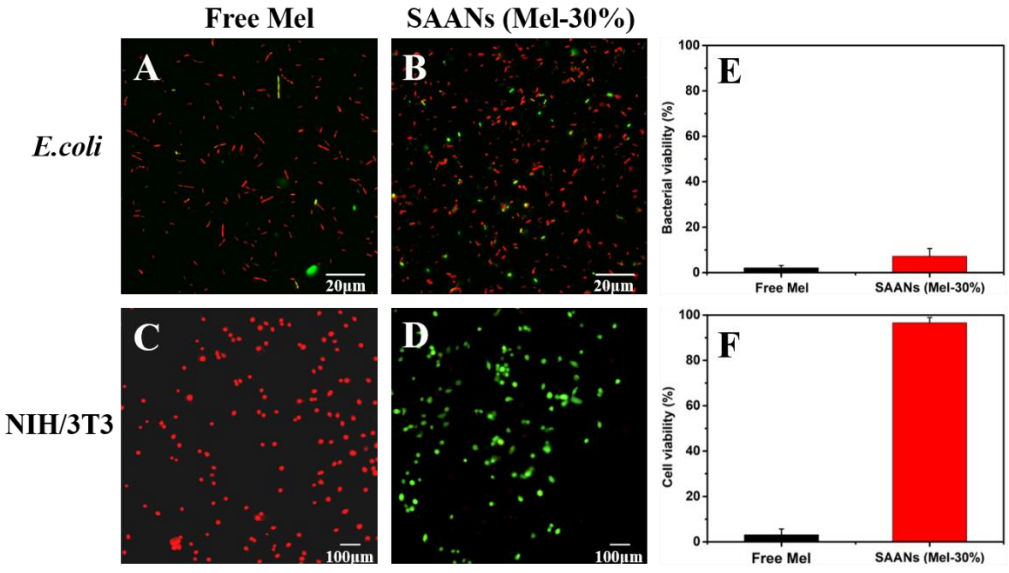

Figure 3.14. Merged fluorescence images of live/dead bacterial and mammalian cell assay for **(A)** free Mel against *E. coli*; **(B)** SAANs (Mel-30%) against *E. coli*; **(C)** free Mel against NIH/3T3 fibroblasts and **(D)** SAANs (Mel-30%) against NIH/3T3 fibroblasts. **(E)** Quantification of *E. coli* viability and (F) NIH/3T3 fibroblast viability upon incubation with free Mel and SAANs (Mel-30%). The total peptide concentration of SAANs (Mel-30%) is 20 μM. The concentration of free Mel: 6 μM.

Although further studies are needed to fully uncover the mechanism of reduced membrane penetration and cytotoxicity, we believe that the structural constraint and partial shielding of natural AMPs play an important role in such reactions. In addition, the difference of the membrane composition and mechanics between bacteria and mammalian cells could play critical roles in mediating their interactions with AMPs that are confined on a rigid supramolecular backbone. Deeper insights are expected through a detailed investigation of various lipid-associated peptide self-assemblies using ss-NMR spectroscopy.

3.3 Conclusions

Mel-integrated SAANs were fabricated to possess greatly improved membrane selectivity and cytocompatibility. By confining AMPs within a conformationally rigid supramolecular polymer scaffold, this new approach is found to limit AMP's flexibility and reduce their cytotoxicity toward mammalian cells. Due to the modularity nature of the MDP assembly, the proposed system could be used to integrate multiple sequences and structurally distinct AMPs in one nanofiber entity to further enhance the antimicrobial activity against resistant bacteria through synergy. This methodology can also serve as a generic strategy for the re-engineering and re-formatting of thousands of natural and synthetic AMPs available in the peptide databank as cytocompatible antimicrobials, thereby greatly boosting their therapeutic potential.

3.4 Experimental Section

Materials. Fmoc-protected amino acids, *N,N,N′,N′*-Tetramethyl-*O*-(1*H*-benzotriazol-1-yl)uronium hexafluorophosphate (HBTU), MBHA rink amide resin, were purchased from Novabiochem. Piperidine, diisopropylethylamine (DIPEA), 5(6)-carboxy-tetramethyl-rhodamine, Mueller Hinton Broth (MHB), MTT assay kit were purchased from Sigma-Aldrich. Solvents for

peptide synthesis and purification including dimethyl formamide (DMF) and acetonitrile, trifluoroacetic acid (TFA), live/dead bacterial and mammalian cell viability kit, Sodium dodecyl sulfate (SDS), valinomycin and Hoechst dye were purchased from Fisher Scientific. Dulbecco's modified Eagle medium (DMEM) culture medium was purchased from Life Technologies. Fetal Bovine Serum (FBS) was purchased from VWR. TEM staining reagent, uranium acetate dihydrate and TEM grid were purchased from TED PELLA, INC. L-α-phosphatidylglycerol (Egg, Chicken) (sodium salt) and L-α-phosphatidylcholine (95%) (Egg, Chicken) were purchased from Avanti Polar Lipids, INC. *Escherichia coli* (ATCC 25922) was purchased from ATCC.

Synthesis and purification of peptides. Peptides were synthesized on a *Prelude*® peptide synthesizer using standard FMOC-solid phase peptide synthesis procedures. Fmoc groups were deprotected in 20% (V/V) piperidine in N, N-dimethylformamide (DMF) for 5 min and repeated 2 times. HBTU was used as the coupling reagent and reacted with Fmoc-protected amino acids in the presence of DIPEA with a molar ratio of 1:1:2.5 (amino acid: HBTU: DIPEA). After the completion of the synthesis, the N-terminus of the peptides were acetylated in the mixed solvents of acetic anhydride and DIPEA in DMF. A mixture of trifluoroacetic acid (TFA) / triisopropanolsilane (TIS) / H_2O (95/2.5/2.5 by volume) was used to cleavage the acetylated peptides from resin for 3 hours. The cleavage solution was collected through filtration and the wash of neat TFA. TFA solution was evaporated under air flow. The residual peptide solution was precipitated in cold diethyl ether, followed by centrifugation and washing with cold diethyl ether for three times. The crude peptide was dried under vacuum overnight for HPLC purification. The peptide was purified using a preparative reversed phase C4 column with a linear gradient of water/acetonitrile containing 0.05% TFA. Elution was monitored at 230 nm and 280 nm. Rhodamine terminated peptides were synthesized as follows. After final deprotection of the

peptide, the N-terminus was coupled with 4 equivalents of 5(6)-carboxy-tetramethyl-rhodamine using a combination of 4 equivalents of HCTU and 8 equivalents of DIPEA in DMF. The reaction mixture was stirred overnight. The completion of the coupling reaction was confirmed by the Kaiser test. The cleavage and purification procedure followed the same procedure as described for the nonlabelled peptides. The molecular mass was confirmed by MALDI. $(QL)_6$-K: expected mass for $[M+H]^+$ and $[M+Na]^+$: 2205.3 and 2228.3 respectively, observed mass for $[M+H]^+$ and $[M+Na]^+$: 2204.9 and 2227.9; Mel: expected $[M+H]^+$: 2887.7, observed $[M+H]^+$: 2887.3; $(QL)_6$-Mel: expected $[M+H]^+$: 4745.8, observed $[M+H]^+$: 4746.3. Rho-Mel: expected $[M+H]^+$: 3258.2, observed $[M+H]^+$: 3258.0; Rho-$(QL)_6$-Mel: expected $[M+H]^+$: 5120.1, observed $[M+H]^+$: 5120.5.

Formulation of Mel-integrated SAANs. Mel-containing SAANs was fabricated through co-assembly of $(QL)_6$-Mel and $(QL)_6$-K (the selection of the peptide sequences will be discussed in the section of peptide design) at various molar ratios. The two individual components were fully dissolved in a mixture of aqueous and organic solvent (typically 1:1 (V/V) water and acetonitrile) to achieve a "molecularly mixed state", followed by lyophilization and rehydration in aqueous buffer to form water-soluble assemblies with various Mel composition.

Circular dichroism (CD) spectroscopy. Samples were prepared with a total peptide concentration, namely, the sum of $(QL)_6$-K and $(QL)_6$-Mel) at 50 μM in Tris buffer (pH 7.4, 20 mM). Data were collected from 250 nm to 190 nm at room temperature (RT) using a 1 mm cuvette, a bandwidth at 1 nm, scan rate at 100 nm/min and a response time of 2 sec. Each spectrum was averaged from three scans. The mDeg of rotation was converted to molar residual ellipticity via the formula $\theta=(mDeg*1000)/(c*n*l)$, where c is the concentration of the peptide solution expressed in μM, n is the number of amino acids in the peptide sequence and l is the path length of the cell used in mm.

Transmission electron microscopy (TEM). Sample preparation was the same as that used in the CD experiment. 10 μL of peptide solution was dropped onto a lacey carbon grid (TED PELLA 01824). After 2 minutes, excess solution was carefully removed with filter paper. 10 μL of 2 wt % uranyl acetate aqueous solution was dropped onto the grid for negative staining. After 2 minutes, excess staining solution was removed and the TEM samples were dried for overnight before imaging.

Dynamic light scattering (DLS) measurement. The light scattering measurements were made using a BI-200SM Research Goniometer System and data processed using Particle Explorer software, capable of doing angle and temperature dependent static and dynamic light scattering (DLS) evaluations, manufactured by Brookhaven Instruments Corporation, Holtsville, NY, a Nova Instruments LLC company, Wakefield, MA. Measurements were made on solutions studied in both and 10 and 25 mm diameter glass cells and at multiple angles, from 45° to 135°. These solutions were equilibrated at room temperature, 23 °C. Typically, the autocorrelation functions for the DLS measurements were acquired over a period of 2 or more minutes, collecting typically a million or more samples.

Minimal inhibitory concentration (MIC) determination. *E.coli* was cultured in MHB media under constant shaking at 100 rpm at 37 ^{o}C to reach the mid-exponential growth phase. The number of bacteria was determined by counting the colony forming unit (CFU) formed on the agar plate. Bacterial suspensions were diluted to approximately $1x10^5$ CFU/mL in MHB media. Peptide solutions at various total peptide concentrations (160, 80, 40, 20, 10, 5, 2.5 μM) were prepared in Tris buffer (pH 7.4, 20 mM). 50 μL of peptide solution was mixed with 50 μL of bacterial suspension in a 96-well plate and the experiments were performed in triplicates. The plates were incubated at 37 ^{o}C under constant shaking at 100 rpm for 18 hrs and the optical density (OD) at

600 nm was measured on a plate reader. The MIC was determined as the peptide concentration in which OD reading is below 0.06 and no cloudiness was visible to naked eyes.

Membrane permeability assay. The preparation of PC/PG (1:1 W/W) and PC/Cholesterol (8:1 W/W) liposomes followed a standard procedure.[47-49] Briefly, a stock liposome suspension in K^+ buffer (50 mM K_2SO_4, 25 mM HEPES-SO_4^{2-}, pH 7.2) was diluted in 1 mL of isotonic K^+ free buffer (50 mM Na_2SO_4, 25 mM HEPES-SO_4^{2-}, pH 7.2) in a glass vial. The potentiometric dye, 3,3'-Dipropylthiadicarbocyanine iodide (diSC3-5) was added to reach a final concentration at 10 μM. Valinomycin was added to the suspension to reach a final concentration of 1 μM that contributes to a negative diffusion potential across the vesicles wall to quench fluorescence. The fluorescence recovery was monitored on a fluorescence spectrometer with an excitation wavelength at 620 nm and emission at 670 nm. The peptide-induced dissipation of diffusion potential was detected by the increased fluorescence intensity. The increased fluorescence intensity was converted into fluorescence recovery (F_t), defined as $F_t = [(I_t - I_0)/(I_f - I_0)] \times 100\%$, where I_t is fluorescence intensity upon the addition of peptides at time t, I_0 is the fluorescence intensity after adding valinomycin, and I_f is the fluorescence intensity prior to the addition of valinomycin.

Mammalian cell membrane localization assay. NIH/3T3 cell suspensions were added to a confocal dish. After 24 hrs of incubation with peptides, the dish was washed with PBS buffer for three times to remove any non-adherent cells. 180 μL of DMEM cell culture media and 20 μL of Rhodamine (Rho)-labeled peptides were added to the dish to reach a total peptide concentration at 20 μM. After 2 hrs of incubation, cells were washed with PBS buffer for three times to remove any non-specific bound peptides. Cells were stained with nuclear-specific dye, Hoechst at room

temperature for 15 min followed by PBS buffer washing for three times. Images were captured using a fluorescence microscope and processed with ImageJ software.

Live and dead bacterial assay. 400 μL of bacterial suspensions (*E.coli*, 10^8 CFU/mL) was added to a confocal dish and incubated at 37 ^oC for 24 hrs. Using pipette to remove bacterial suspensions and PBS buffers was used to wash away any non-adherent bacteria. 100 μL of 40 μM peptide solution in Tris buffer (pH 7.4, 20 mM) and 100 μL of Mueller Hinton Broth (MHB) medium were mixed and added in the confocal dish. After incubation at 37 ^oC for 3 hrs, MHB medium was removed and washed extensively with PBS buffers for three times. Bacteria were stained with the live/dead bacteria assay kit solution at room temperature for 15 min. Finally, bacteria were washed with PBS buffer for three times. Images were captured with epifluorescence and processed with ImageJ software.

Live and dead mammalian cell assay. 400 μL of NIH/3T3 mouse fibroblasts was added to a confocal dish and incubated at 37 ^oC for 24 hrs. Cell suspensions were removed and washed with PBS buffers for three times to remove any non-adherent cell. 180 μL of fresh cell culture DMEM medium and 20 μL of 200 μM peptide solution in Tris buffer (pH 7.4, 20 mM) were mixed and added into the confocal dish. After incubation at 37 ^oC for 3 hrs, the culture medium was removed and washed extensively with PBS buffer for three times. NIH/3T3 cells were stained with live/dead mammalian cell assay kit solution at room temperature for 20 min. Finally, cells were washed with PBS buffer for three times. Images were captured with epifluorescence and processed with ImageJ software.

Cytotoxicity measurement. NIH/3T3 cells were seeded onto a 96-well plate at a density of 10^4 cells/well and incubated for 24 hrs at 37 °C in an incubator with 5% of CO_2. After 24 hrs, the culture medium was removed. 10 μL of peptide solution in Tris buffer (pH 7.4, 20mM) at various

concentrations (800, 400, 200, 100, 50, 25, 12.5 µM) was mixed with 90 µL cell culture medium in a 96-well plate. After 24 hrs of incubation, the MTT assay was performed to quantify the cell viability by monitoring the UV absorbance at 570 nm. The cell without incubation with peptides was used as a control. All the experiments were performed in four replicates.

Statistical analysis. The data for cytotoxicity and antimicrobial activity measurements expressed as means ± standard deviation (SD). The statistical analysis was performed using Student's T-test and one-way analysis of variance (ANOVA) at confidence levels of 95% and above.

3.5 References

(1) Brooks, B. D.; Brooks, A. E. Therapeutic strategies to combat antibiotic resistance. *Adv. Drug Deliv. Rev.* **2014**, *78*, 14-27.

(2) Hancock, R. E. W.; Sahl, H.-G. Antimicrobial and host-defense peptides as new anti-infective therapeutic strategies. *Nat. Biotechnol.* **2006**, *24*, 1551-1557.

(3) Hassan, M.; Kjos, M.; Nes, I.; Diep, D.; Lotfipour, F. Natural antimicrobial peptides from bacteria: characteristics and potential applications to fight against antibiotic resistance. *J. Appl. Microbiol.* **2012**, *113*, 723-736.

(4) Mahlapuu, M.; Håkansson, J.; Ringstad, L.; Björn, C. Antimicrobial Peptides: An Emerging Category of Therapeutic Agents. *Front. Cell. Infect. Microbiol.* **2016**, *6*.

(5) Kang, S.-J.; Park, S. J.; Mishig-Ochir, T.; Lee, B.-J. Antimicrobial peptides: therapeutic potentials. *Expert. Rev. Anti Infect. Ther.* **2014**, *12*, 1477-1486.

(6) Yeung, A. T.; Gellatly, S. L.; Hancock, R. E. Multifunctional cationic host defence peptides and their clinical applications. *Cell. Mol. Life Sci.* **2011**, *68*, 2161-2176.

(7) Marr, A. K.; Gooderham, W. J.; Hancock, R. E. W. Antibacterial peptides for therapeutic use: obstacles and realistic outlook. *Curr. Opin. Pharmacol.* **2006**, *6*, 468-472.

(8) Nordström, R.; Malmsten, M. Delivery systems for antimicrobial peptides. *Adv. Colloid Interface Sci.* **2017**, *242*, 17-34.

(9) Piras, A. M.; Maisetta, G.; Sandreschi, S.; Gazzarri, M.; Bartoli, C.; Grassi, L.; Esin, S.; Chiellini, F.; Batoni, G. Chitosan nanoparticles loaded with the antimicrobial peptide temporin B exert a long-term antibacterial activity in vitro against clinical isolates of Staphylococcus epidermidis. *Front. Microbiol.* **2015**, *6*, 372-372.

(10) Biswaro, L. S.; da Costa Sousa, M. G.; Rezende, T. M. B.; Dias, S. C.; Franco, O. L. Antimicrobial peptides and nanotechnology, recent advances and challenges. *Front. Microbiol.* **2018**, *9*.

(11) Gallarate, M.; Battaglia, L.; Peira, E.; Trotta, M. Peptide-loaded solid lipid nanoparticles prepared through coacervation technique. *Int. J. Chem. Eng.* **2011**, *2011*, 6.

(12) Mohammadi-Samani, S.; Taghipour, B. PLGA micro and nanoparticles in delivery of peptides and proteins; problems and approaches. *Pharm. Dev. Technol.* **2015**, *20*, 385-393.

(13) Moore, A. N.; Hartgerink, J. D. Self-assembling multidomain peptide nanofibers for delivery of bioactive molecules and tissue regeneration. *Acc. Chem. Res.* **2017**, *50*, 714-722.
(14) Acar, H.; Srivastava, S.; Chung, E. J.; Schnorenberg, M. R.; Barrett, J. C.; LaBelle, J. L.; Tirrell, M. Self-assembling peptide-based building blocks in medical applications. *Adv. Drug Deliv. Rev.* **2017**, *110-111*, 65-79.
(15) Cui, H.; Webber, M. J.; Stupp, S. I. Self-assembly of peptide amphiphiles: From molecules to nanostructures to biomaterials. *J. Pept. Sci.* **2010**, *94*, 1-18.
(16) Haines-Butterick, L.; Rajagopal, K.; Branco, M.; Salick, D.; Rughani, R.; Pilarz, M.; Lamm, M. S.; Pochan, D. J.; Schneider, J. P. Controlling hydrogelation kinetics by peptide design for three-dimensional encapsulation and injectable delivery of cells. *Proc. Natl. Acad. Sci. U.S.A.* **2007**, *104*, 7791-7796.
(17) Hudalla, G. A.; Sun, T.; Gasiorowski, J. Z.; Han, H.; Tian, Y. F.; Chong, A. S.; Collier, J. H. Gradated assembly of multiple proteins into supramolecular nanomaterials. *Nat. Mater.* **2014**, *13*, 829-836.
(18) Bowerman, C. J.; Nilsson, B. L. Review self-assembly of amphipathic β-sheet peptides: Insights and applications. *J. Pept. Sci.* **2012**, *98*, 169-184.
(19) Galler, K. M.; Aulisa, L.; Regan, K. R.; D'Souza, R. N.; Hartgerink, J. D. Self-assembling multidomain peptide hydrogels: designed susceptibility to enzymatic cleavage allows enhanced cell migration and spreading. *J. Am. Chem. Soc.* **2010**, *132*, 3217-3223.
(20) Liu, X.; Wang, X.; Horii, A.; Wang, X.; Qiao, L.; Zhang, S.; Cui, F.-Z. In vivo studies on angiogenic activity of two designer self-assembling peptide scaffold hydrogels in the chicken embryo chorioallantoic membrane. *Nanoscale* **2012**, *4*, 2720-2727.
(21) Rudra, J. S.; Tian, Y. F.; Jung, J. P.; Collier, J. H. A self-assembling peptide acting as an immune adjuvant. *Proc. Natl. Acad. Sci. U.S.A.* **2010**, *107*, 622-627.
(22) Hudalla, G. A.; Modica, J. A.; Tian, Y. F.; Rudra, J. S.; Chong, A. S.; Sun, T.; Mrksich, M.; Collier, J. H. A self-adjuvanting supramolecular vaccine carrying a folded protein antigen. *Adv. Healthc. Mater.* **2013**, *2*, 1114-1119.
(23) Wen, Y.; Collier, J. H. Supramolecular peptide vaccines: tuning adaptive immunity. *Curr. Opin. Immunol.* **2015**, *35*, 73-79.
(24) Wickremasinghe, N. C.; Kumar, V. A.; Shi, S.; Hartgerink, J. D. Controlled angiogenesis in peptide nanofiber composite hydrogels. *ACS Biomater. Sci. Eng.* **2015**, *1*, 845-854.
(25) Kumar, V. A.; Taylor, N. L.; Shi, S.; Wang, B. K.; Jalan, A. A.; Kang, M. K.; Wickremasinghe, N. C.; Hartgerink, J. D. Highly angiogenic peptide nanofibers. *ACS Nano* **2015**, *9*, 860-868.
(26) Xu, D.; Jiang, L.; Singh, A.; Dustin, D.; Yang, M.; Liu, L.; Lund, R.; Sellati, T. J.; Dong, H. Designed supramolecular filamentous peptides: balance of nanostructure, cytotoxicity and antimicrobial activity. *Chem. Comm.* **2015**, *51*, 1289-1292.
(27) Xu, D.; Chen, W.; Tobin-Miyaji, Y. J.; Sturge, C. R.; Yang, S.; Elmore, B.; Singh, A.; Pybus, C.; Greenberg, D. E.; Sellati, T. J.; Qiang, W.; Dong, H. Fabrication and microscopic and spectroscopic characterization of cytocompatible self-assembling antimicrobial nanofibers. *ACS Infect. Dis.* **2018**, *4*, 1327-1335.
(28) Terwilliger, T. C.; Weissman, L.; Eisenberg, D. The structure of melittin in the form I crystals and its implication for melittin's lytic and surface activities. *Biophys. J.* **1982**, *37*, 353-361.
(29) Asthana, N.; Yadav, S. P.; Ghosh, J. K. Dissection of antibacterial and toxic activity of Melittin a leucine zipper motif plays a crucial role in determining its hemolytic activity but not antibacterial activity. *J. Biol. Chem.* **2004**, *279*, 55042-55050.

(30) Yang, M.; Xu, D.; Jiang, L.; Zhang, L.; Dustin, D.; Lund, R.; Liu, L.; Dong, H. Filamentous supramolecular peptide–drug conjugates as highly efficient drug delivery vehicles. *Chem. Comm.* **2014**, *50*, 4827-4830.
(31) Sui, S.-F.; Wu, H.; Guo, Y.; Chen, K.-S. Conformational changes of melittin upon insertion into phospholipid monolayer and vesicle1. *J. Biochem.* **1994**, *116*, 482-487.
(32) Cormier, A. R.; Pang, X.; Zimmerman, M. I.; Zhou, H.-X.; Paravastu, A. K. Molecular structure of RADA16-I designer self-assembling peptide nanofibers. *ACS Nano* **2013**, *7*, 7562-7572.
(33) Dong, H.; Paramonov, S. E.; Aulisa, L.; Bakota, E. L.; Hartgerink, J. D. Self-assembly of multidomain peptides: balancing molecular frustration controls conformation and nanostructure. *J. Am. Chem. Soc.* **2007**, *129*, 12468-12472.
(34) Lee, J.; Park, C.; Park, S.-C.; Woo, E.-R.; Park, Y.; Hahm, K. S.; Lee, D. G. Cell selectivity-membrane phospholipids relationship of the antimicrobial effects shown by pleurocidin enantiomeric peptides. *J.Pept.Sci.* **2009**, *15*, 601-606.
(35) Zhang, L.; Rozek, A.; Hancock, R. E. Interaction of cationic antimicrobial peptides with model membranes. *J. Biol. Chem.* **2001**, *276*, 35714-35722.
(36) Oren, Z.; Lerman, J. C.; Gudmundsson, G. H.; Agerberth, B.; Shai, Y. Structure and organization of the human antimicrobial peptide LL-37 in phospholipid membranes: relevance to the molecular basis for its non-cell-selective activity. *Biochem J* **1999**, *341 (Pt 3)*, 501-513.
(37) Oren, Z.; Hong, J.; Shai, Y. A repertoire of novel antibacterial diastereomeric peptides with selective cytolytic activity. *J. Biol. Chem.* **1997**, *272*, 14643-14649.
(38) Toke, O. Antimicrobial peptides: New candidates in the fight against bacterial infections. *J. Pept. Sci.* **2005**, *80*, 717-735.
(39) Glukhov, E.; Stark, M.; Burrows, L. L.; Deber, C. M. Basis for selectivity of cationic antimicrobial peptides for bacterial versus mammalian membranes. *J. Biol. Chem.* **2005**, *280*, 33960-33967.
(40) Kamech, N.; Vukičević, D.; Ladram, A.; Piesse, C.; Vasseur, J.; Bojović, V.; Simunić, J.; Juretić, D. Improving the selectivity of antimicrobial peptides from anuran skin. *J. Chem. Inf. Model.* **2012**, *52*, 3341-3351.
(41) Hollmann, A.; Martínez, M.; Noguera, M. E.; Augusto, M. T.; Disalvo, A.; Santos, N. C.; Semorile, L.; Maffía, P. C. Role of amphipathicity and hydrophobicity in the balance between hemolysis and peptide–membrane interactions of three related antimicrobial peptides. *Colloids Surf. B Biointerfaces* **2016**, *141*, 528-536.
(42) Blondelle, S. E.; Houghten, R. A. Hemolytic and antimicrobial activities of the twenty-four individual omission analogs of melittin. *Biochemistry* **1991**, *30*, 4671-4678.
(43) Meng, H.; Kumar, K. Antimicrobial activity and protease stability of peptides containing fluorinated amino acids. *J. Am. Chem. Soc.* **2007**, *129*, 15615-15622.
(44) Aoki, W.; Kuroda, K.; Ueda, M. Next generation of antimicrobial peptides as molecular targeted medicines. *J. Biosci. Bioeng.* **2012**, *114*, 365-370.
(45) Gabriel, G. J.; Madkour, A. E.; Dabkowski, J. M.; Nelson, C. F.; Nüsslein, K.; Tew, G. N. Synthetic mimic of antimicrobial peptide with nonmembrane-disrupting antibacterial properties. *Biomacromolecules* **2008**, *9*, 2980-2983.
(46) Lv, Y.; Wang, J.; Gao, H.; Wang, Z.; Dong, N.; Ma, Q.; Shan, A. Antimicrobial properties and membrane-active mechanism of a potential α-helical antimicrobial derived from cathelicidin PMAP-36. *PLOS ONE* **2014**, *9*, e86364.

(47) Loew, L. M.; Rosenberg, I.; Bridge, M.; Gitler, C. Diffusion potential cascade. Convenient detection of transferable membrane pores. *Biochemistry* **1983**, *22*, 837-844.
(48) Sims, P. J.; Waggoner, A. S.; Wang, C.-H.; Hoffman, J. F. Mechanism by which cyanine dyes measure membrane potential in red blood cells and phosphatidylcholine vesicles. *Biochemistry* **1974**, *13*, 3315-3330.
(49) Ghosh, J. K.; Ovadia, M.; Shai, Y. A leucine zipper motif in the ectodomain of sendai virus fusion protein assembles in solution and in membranes and specifically binds biologically-active peptides and the virus. *Biochemistry* **1997**, *36*, 15451-15462.

Chapter 4: Design of Acid-responsive Peptide Self-assembly for Targeted Bacterial Therapy*

4.1 Introduction

Stimuli-responsive nanomaterials have tremendous promise for targeted therapeutic delivery strategies that improve the treatment of a variety of diseases.[1-6] Among various approaches, self-assembly has been proven as an effective bottom-up approach to construct functional nanomaterials. A wide range of molecular building blocks, including amphiphilic polymers, lipids, proteins and peptides can be custom-designed and assembled into "smart" nanomaterials that can sense various disease-specific microenvironmental conditions.[7-9] Self-assembled nanomaterials can easily change their physicochemical properties in response to the environmental change and lead to local release of therapeutics with enhanced drug potency and reduced side effects on healthy tissues and cells. In recent years, great levels of success have been achieved for nanomaterials designed for targeted cancer therapy.[10-13] However, the development of self-assembled nanomaterials for targeted antimicrobial delivery is just getting underway for infectious disease treatment.[14-17]

Similar to some of the tumor tissues, certain bacteria can reduce the local pH of the infection tissues through low oxygen-triggered anaerobic fermentation.[18,19] Host immune response can further lower the local pH where bacteria reside through mechanisms of production of lactic acids during phagocytosis.[20-23] While the acidic pH is considered as an undesirable factor causing the reduction of the antimicrobial activity of several classes of antibiotics,[24] it can be utilized as a natural physiological cue for the design of antimicrobial nanomaterials for targeted antimicrobial

* This chapter is based on Weike Chen, Shuxin Li, Paul Renick, Su Yang, Nikhil Pandy, Cara Boutte, Kytai T. Nguyen, Liping Tang, He Dong. Bacterial acidity-triggered antimicrobial activity of self-assembling peptide nanofibers. *J. Mater. Chem. B*, **2019**, *7*, 2915-2919. Some sections were rearranged for continuity.

delivery. Recent reports have demonstrated advances in the design of acid-sensitive nanoparticles for targeting the bacterial membrane and delivery of small molecule antibiotics to treat bacterial infections in acidic conditions.[14] Acid-dependent helical polypeptides were also reported to selectively target and eradicate pathogenic *H. pylori* without affecting commensal bacteria in the stomach.[17] These successful examples provide inspiration and highlight the feasibility of using pH as a physiological trigger to achieve targeted antimicrobial therapy.

4.2 Results and Discussion

4.2.1 Design of Acid-activatable Peptide Self-assembly

In this work, we sought to develop a novel acid-activatable antimicrobial therapy by capitalizing on our recent development of self-assembling nanofibers (SANs) for bacterial acidity-triggered antimicrobial delivery. SANs are supramolecular assemblies of *de novo* designed multidomain peptides (MDPs) that have been explored as highly cytocompatible antimicrobial and cell penetrating nanomaterials.[25,26] The first generation of MDPs has a general formula of $K_x(QL)_yK_z$ (amino acid single code letter K: Lysine, Q: Glutamine, L: Leucine) to mimic natural cationic antimicrobial peptides (AMPs). Unlike most conventional AMPs that exist as monomers in solution, MDPs can form supramolecular β-sheet nanofibers in which the hydrophobic residues and non-polar surface are partially masked between the two sheets, which has been proven as an important factor to minimize the cytotoxicity of MDPs toward mammalian cells.[27] As shown in our previous work, the cytocompatibility was greatly enhanced for SANs compared to that of traditional monomeric AMPs. However, on the negative side, the confinement of the hydrophobic moiety within the assembly can also reduce their antimicrobial activity while monomeric AMPs are more potent to kill bacteria. As such, the current study by developing SANs that undergo pH-

responsive disassembly combines the advantages of both self-assembled peptides in terms of their cytocompatibility and monomeric AMPs in terms of their antimicrobial activity to treat acidity-associated bacterial infection. The central hypothesis is SANs under the physiological condition are bio-inert because the membrane-interacting hydrophobic moieties of SANs are buried inside the assembly and not accessible to the cell membrane. At the bacterial colonization site with an acidic pH, MDPs become charged and the increased charge density triggers SANs disassembly and subsequent release of activated peptides to effectively interact with the cell membrane and kill bacteria (**Figure 4.1**).

Three MDPs with the sequences of $WH_5(QL)_6K_2$, $WH_7(QL)_6K_2$, and $WH_9(QL)_6K_2$ were abbreviated as WH_5, WH_7 and WH_9 (H: Histidine, W: Tryptophan) were initially explored as the building units to fabricate SANs. The sequences were chosen based on the following considerations. First, the central repeating (QL) domain provides the driving force for SANs formation under the neutral physiological condition as discussed in our previous studies.8b Second, oligo-histidine of different lengths was incorporated at the N-terminus to endow pH-responsiveness to SANs. At a pH below the pKa of histidine, peptides become charged. The electrostatic repulsion among the positively charged MDPs will destabilize SANs and lead to the release of activated MDPs that can effectively eradicate bacteria. Third, the numbers of histidine residues are varied in order to integrate and achieve a good balance between self-assembly under the neutral condition and disassembly upon acidification. MDPs with different numbers of histidine would render a small library to explore the effect of charge on SANs stability, disassembly efficiency and their resulting biological activities. Lastly, two lysine residues were appended at the C-terminus to ensure sufficient solubility of SANs and minimize lateral fiber

aggregation through electrostatic repulsion. All peptides contain a tryptophan residue for accurate determination of the peptide concentration by UV spectroscopy.

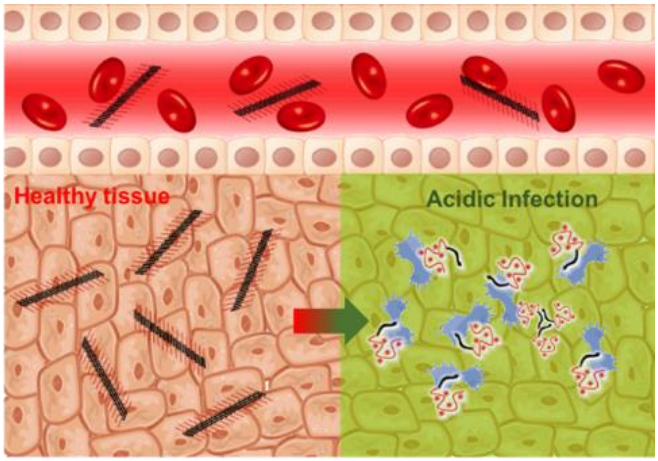

Figure 4.1. Cartoon representation of cytocompatible and hemocompatible SANs formed by pH-responsive MDPs and their disassembly triggered by local bacterial acidity for the delivery of activated MDPs to eradicate bacteria.

4.2.2 pH-dependent Structural Characterization

Elucidating the physicochemical properties of MDPs as a function of pH is critical to tailoring their biological activities. Critical assembly concentration (CAC) measurements were first conducted to investigate their ability to assemble under different pH conditions. As shown in **Figure 4.2**, a non-linear relationship was observed for all three MDPs at pH 7.4 (Tris buffer, 20 mM) suggesting the formation of higher ordered assemblies as the concentration increased. At an acidic pH (MES buffer, pH 5.7, 20 mM), a linear correlation was found between the fluorescence intensity and peptide concentrations, suggesting the majority of peptides do not self-assemble and rather remain isolated. It is worth noting that we choose pH 5.7 as the acidic condition for this study, considering the balance between the protonation degree of histidine (pKa=~6) and bacterial growth under the acidic condition. The pH-dependent self-assembly and disassembly were further investigated and confirmed by circular dichroism (CD) spectroscopy. At pH 7.4, all three peptides

exhibited predominant β-sheet structures as characterized by a minimum peak between 210-220 nm (**Figure 4.3A**) indicating the formation of SANs. When the pH is reduced to 5.7, which is below the pKa point of histidine, the presumed increase in positive charges and electrostatic repulsion triggered disassembly and unfolding of β-sheets to random coils and/or weak helices. As shown in **Figure 4.3B**, all three MDPs unfolded upon pH reduction, but to different degrees. WH_7 and WH_9 exhibited more disordered structures than WH_5 given the larger blue shifts of the minimum absorption down to ~ 203 nm indicating a greater tendency to disassemble. To quantitatively determine the extent of SANs disassembly, spin dialysis was used to estimate the amounts of disassembled MDPs upon pH reduction. Centrifugal filters with molecular weight (MW) cutoff at 10 kDa and 30 kDa were used to separate the monomeric MDP and any potential non-specific aggregates (up to 9 mers) (due to their amphiphilic nature) from the residual higher ordered assemblies, respectively. As shown in **Table 4.1**, no materials were detected in the filtrate for all three MDPs through spin dialysis suggesting the stability and integrity of SANs at the neutral pH. At the acidic pH, disassembly occurs as shown by the increased concentrations of MDPs in the filtrate using both filters. It was estimated that 24.60% of WH_5, 34.70% of WH_7 and 41.00% of WH_9 were disassembled to monomers based on the dialysis result using the filter with a MW cutoff at 10 kDa. Using a 30 kDa filter, the percentage of MDPs in the filtrate increased to 37.77%, 62.56% and 71.46% for WH_5, WH_7 and WH_9, respectively.

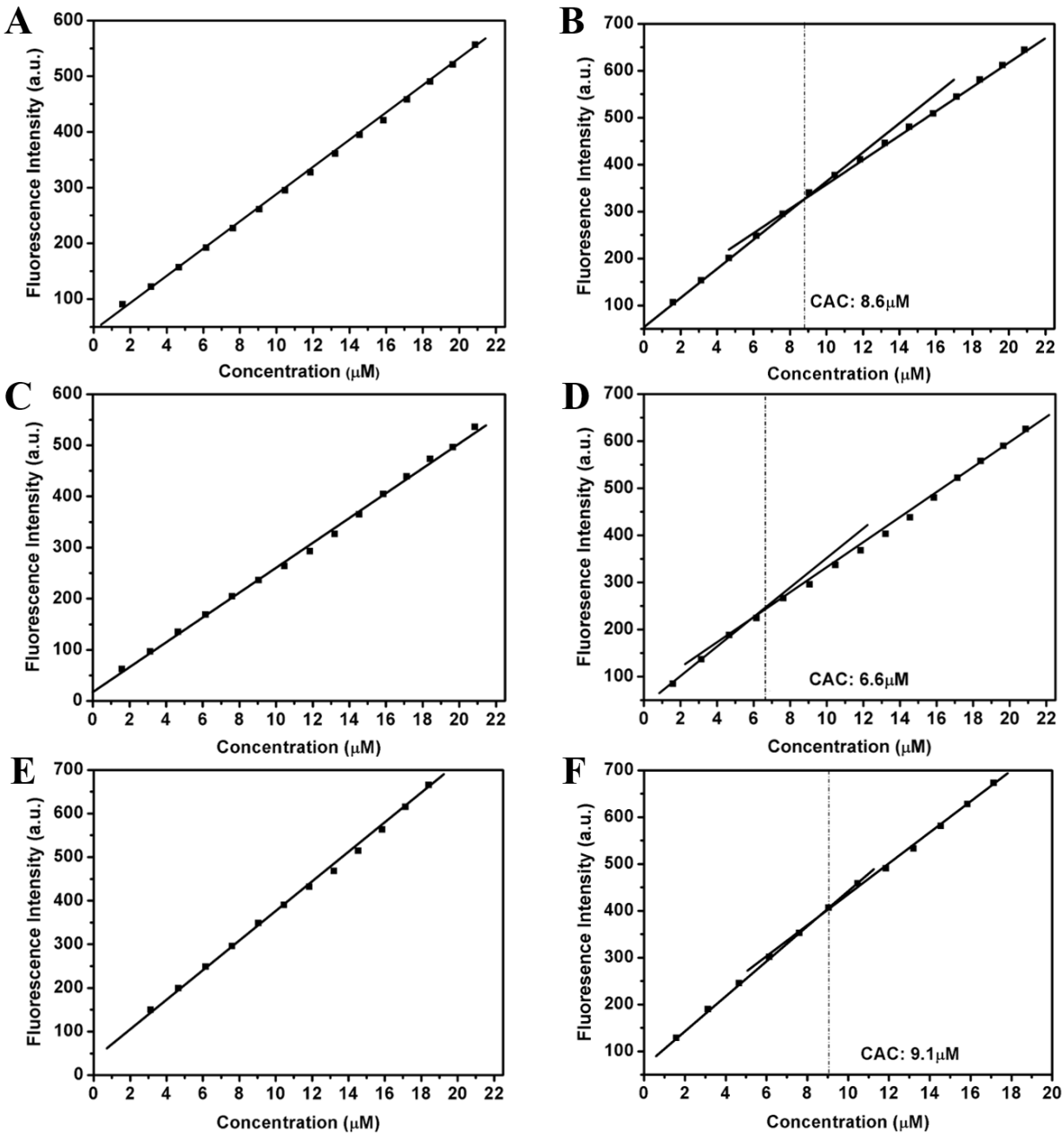

Figure 4.2. CAC determination by monitoring the tryptophan fluorescence at various peptide concentrations at pH 7.4 and pH 5.7. WH_5 at **(A)** pH 5.7 and **(B)** pH 7.4; WH_7 at **(C)** pH 5.7 and **(D)** pH 7.4; WH_9 at **(E)** pH 5.7 and **(F)** pH 7.4.

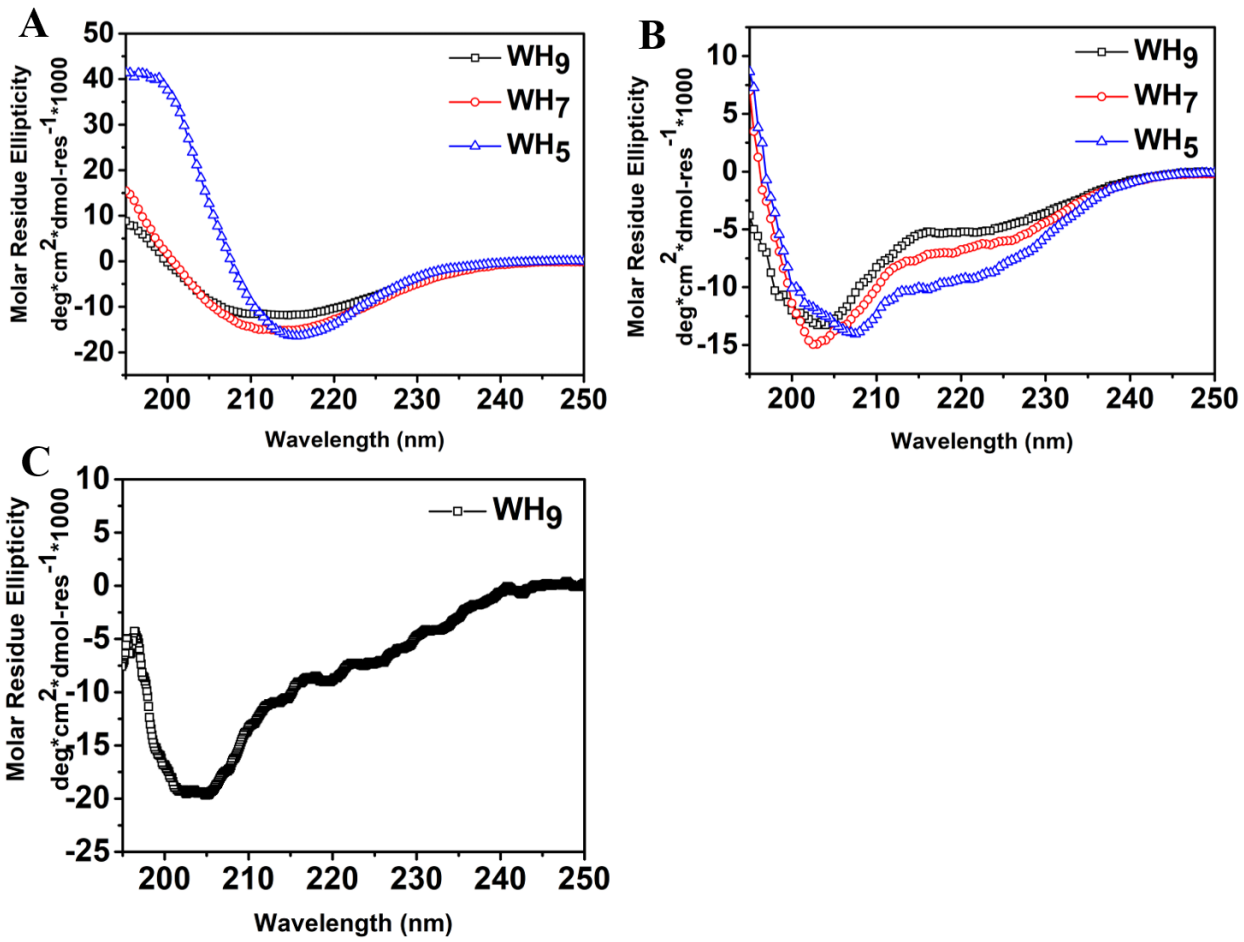

Figure 4.3. pH-dependent peptide secondary structures by CD spectroscopy at RT. **(A)** CD spectra of peptides shows predominant β-sheet secondary structures in Tris buffer (pH 7.4, 20 mM); **(B)** CD spectra of peptides in MES buffer (pH 5.7, 20 mM) showing weak helices/random coils; **(C)** CD spectra of the filtrate of WH_9 in MES buffer (pH 5.7, 20 mM) shows a random coiled structure. Peptide concentration: 50 μM.

Table 4.1. Quantification of disassembled MDPs

Peptides	10 kDa filter		30 kDa filter	
	pH 7.4	pH 5.7	pH 7.4	pH 5.7
WH_5	0	24.60 ± 0.08%	0	37.77 ± 0.56%
WH_7	0	34.70 ± 0.08%	0	62.56 ± 3.55 %
WH_9	0	41.00 ± 0.49%	0	71.64 ± 0.27%

Standard deviation is calculated based on 3 measurements for each sample

The filtrate of WH_9 at pH 5.7 was analyzed by CD spectroscopy showing highly disordered random coil structures (**Figure 4.3C**), thus excluding the possibility of the presence of β-sheet oligomers in the filtrate. The oligomeric species present in the filtrate is likely due to the non-specific aggregation between the amphiphilic MDPs. Transmission electron microscopy (TEM) reveals the morphological change of MDPs under different pH treatments. For TEM characterization and the following biological evaluation, we primarily focused on WH_9 because it is the most sensitive to pH change giving a higher extent of disassembly upon solution acidification. At pH 7.4, WH_9 spontaneously self-assembled to form elongated fibers (**Figure 4.4A**). Reducing the pH to 5.7 led to a significant reduction of the fiber density and the formation of non-specific spherical aggregates (**Figure 4.4B**). We suspect that these spherical aggregates were formed from disassembled MDPs due to the drying effect during TEM sample preparation process. The disassembly of SANs was verified by dynamic light scattering (DLS) measurements showing a

dramatically reduced particle size to below 2 nm when pH was reduced (**Figure 4.4C** and **Figure 4.5**). Although the number mean of the hydrodynamic diameter generated by DLS does not represent the actual size of these nanofibers due to their non-spherical shapes, the dramatic size reduction suggests the effectiveness of solution acidity to trigger the disassembly of SANs.

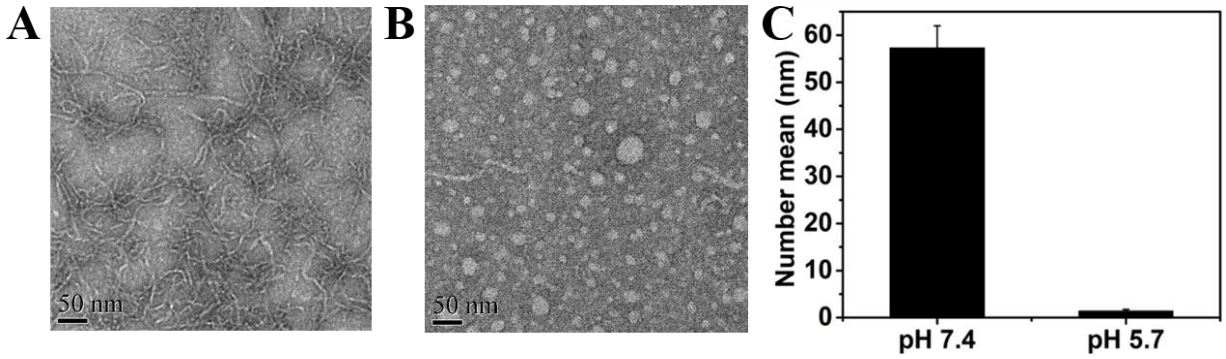

Figure 4.4. Negatively stained TEM images of WH_9 at **(A)** pH 7.4 shows SANs formation and **(B)** at pH 5.7 shows SANs disassembly. **(C)** pH-dependent hydrodynamic size measurement by DLS. Peptide concentration: 100 μM in Tris buffer (pH 7.4, 20 mM) and MES buffer (pH 5.7, 20 mM)

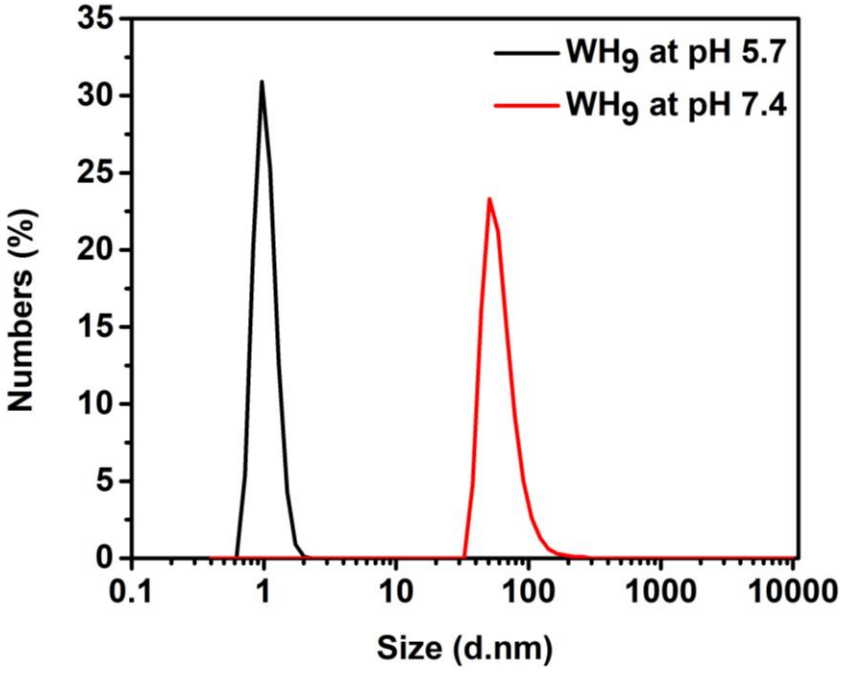

Figure 4.5. Particle size distribution by numbers (%) of WH_9 at neutral and acidic condition.

4.2.3 Fluorescence Imaging of pH-dependent Self-assembly/Disassembly

Acidity-triggered SANs disassembly was further studied in the context of bacterial inoculation on an agar plate. We chose Bacteroides fragilis as a model bacterium that undergoes anaerobic growth leading to the acidification of the surrounding environment. We first determined whether the growth of *B. fragilis* would influence the pH immediately adjacent to the bacterial colony. Using a pH ratiometric near infrared probe developed recently,10 we measured the change of fluorescent intensity of the probe with time using an in vivo Kodak imager. The results allow us to calculate the pH nearby the colony on an agar plate at 0.5, 2.5, 7, and 22.5 hrs upon bacterial inoculation. Interestingly, we find that the growth of B. fragilis releases metabolites that can cause the surrounding environment to become acidic (from pH 7.5 to pH 6.3 in less than 24 hrs) (**Figure 4.6**). To test whether the in-situ low pH can induce SANs disassembly, we synthesized and prepared rhodamine (Rho)-labeled WH_9. Rho-WH_9 has very low fluorescent intensity due to fluorescent quenching upon self-assembly. By reducing the local pH, WH_9 disassembles leading to the recovery of rhodamine fluorescence. Therefore, the fluorescence intensity of the peptide reflects the degree of peptide disassembly and can be used to correlate with the microenvironmental pH change associated with bacterial growth. To determine whether the acidic environment nearby bacterial colonies cause SANs to disassemble, Rho-WH_9 was applied on both the bacterial colonies and non-inoculated agars as controls after 24 hrs of bacterial inoculation. The fluorescence intensity was monitored immediately using an *in vivo* Kodak imager. The results showed an average of 88% increase of the fluorescence intensity for peptides deposited on the bacteria colonies than those on the agar media without bacteria (**Figure 4.7A**), suggesting a local acidic pH can trigger the disassembly of SANs, leading to the recovery of self-quenched fluorescence. The fluorescence intensity of the peptide across the bacterial colony was further

plotted as a function of imaging pixels (~ 0.1 mm/per pixel) starting from the outermost of a colony (shown as 0 on the x-axis of **Figure 4.7B**) while moving toward the center (shown as 10 on the x-axis of **Figure 4.7B**). The local bacterial pH change across a single colony was measured by the ratiometric fluorescence probe described above and plotted in the same manner. A good correlation was observed between the reduced pH and the increased fluorescence of Rho-WH_9, further confirming local bacterial acidity can trigger SANs disassembly.

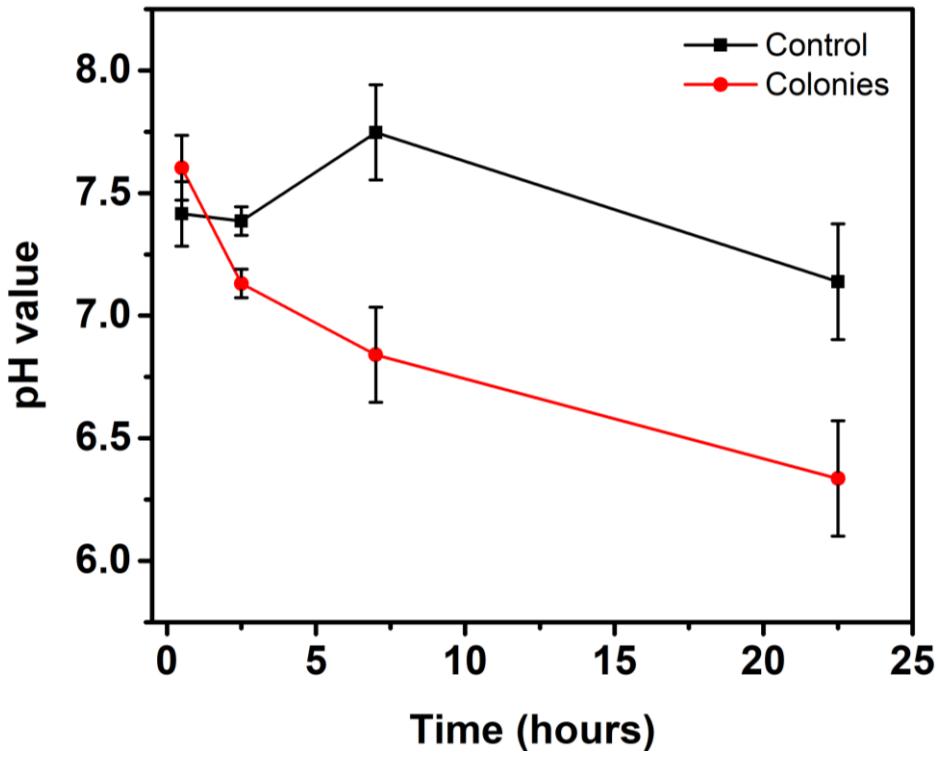

Figure 4.6. Time-dependent local pH of *B. fragilis* on the agar plate.

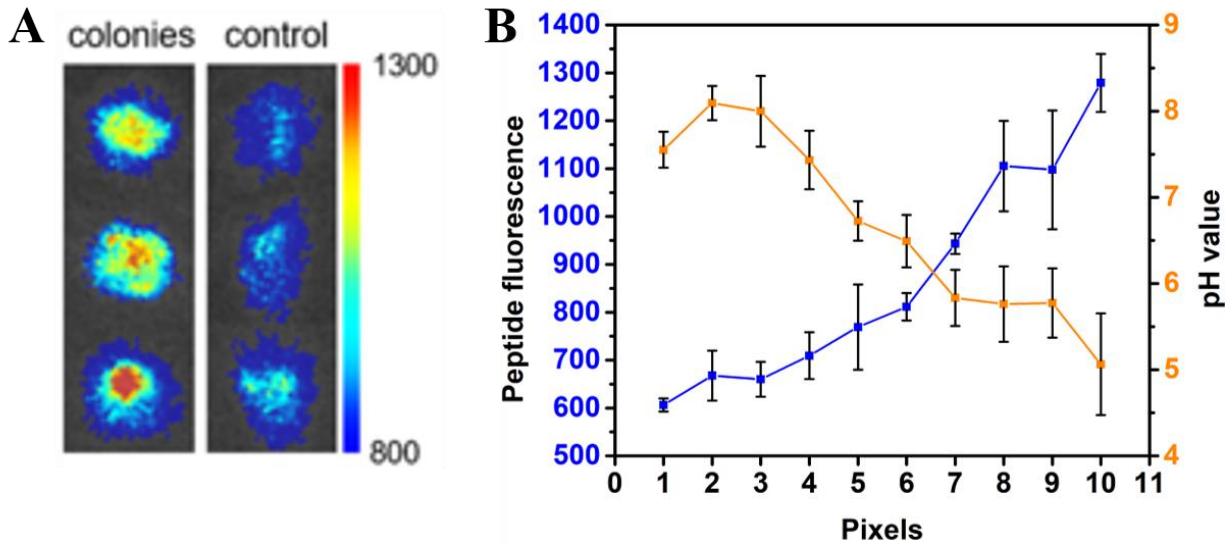

Figure 4.7. Local bacterial acidity triggered peptide disassembly as determined by in situ fluorescence microscopy. **(A)** Fluorescence intensity of Rho-labelled WH_9 deposited on 3 bacterial colonies (3 spots on the left panel) compared to those on agar media (right panel) without bacteria showing that the acidic bacterial environment can induce SANs disassembly that led to a recovery of the self-quenched rhodamine fluorescence. **(B)** Correlation of the local bacterial pH (orange line) with the fluorescence intensity of Rho-labelled WH_9 (blue lines) applied on bacterial colonies. The inset pictures are fluorescent microscopic images of bacterial colonies upon Rho-labelled peptide treatment (right) and colonies containing the near infrared pH probe (left).

4.2.4 Evaluation of pH-dependent Antimicrobial Activity

The antimicrobial activities of WH_9 were tested against both Gram-negative bacteria, *Escherichia coli* and *B. fragilis* and Gram-positive bacteria, *Staphylococcus aureus* under the anaerobic condition where bacterial cultures became acidic over time Peptides were co-incubated with *E. coli*, *B. fragilis* and *S. aureus* for 48 hrs and the UV absorbance at 600 nm was measured for the estimation of the minimum inhibitory concentration (MIC) values. As shown in **Table 4.2**, WH_9 was effective against all three bacterial strains in the anaerobic condition where the bacterial culture gradually became acidic to pH 6.4. The MIC values of WH_9 were determined at 10 μM against *E. coli*, 5 μM against *B. fragilis* and 5 μM against *S. aureus*. In contrast, the MIC of WH_9 was estimated at 40 μM against *E. coli* in the aerobic condition where the culture pH remained

neutral (pH was between 7.2 and 7.5 during culture). For aerobic bacterial cultures with a starting pH of 5.7, the MIC was determined as 10 μM comparable to that determined in the anaerobic condition. In comparison, the MICs of WH_5 and WH_7 were determined at 40 μM and 20 μM in the acidic aerobic *E. coli* cultures showing less potency to inhibit the growth of bacteria. The antimicrobial activity also correlates well with the peptide's ability to dissemble as detailed in the spin dialysis experiment (**Table 4.1**).

Table 4.2. Antimicrobial activity, cytotoxicity and hemolytic activity

Peptides	MIC (μM)					IC_{50} μM	HC_{10} μM
	Anaerobic			Aerobic			
	E.coli	*B. fragilis*	*S.aureus*	*E.coli*			
				pH 7.4	pH 5.7		
WH_9	10	5	5	>40	10	>80	>160

The mode of antimicrobial action was investigated by epifluorescence microscopy. WH_9 was co-incubated with *E. coli* aerobically so that the culture pH can be adjusted and maintained at either acidic or neutral during the entire culture. A live-dead assay was performed wherein *E. coli* was incubated with WH_9 for 3 hrs, followed by staining with SYTO9 and Propidium Iodide (PI). As shown in (**Figure 4.8A**), a much higher fraction of *E. coli* cells fluoresced red at the acidic pH due to pH-triggered disassembly and release of peptides that can increase the membrane

permeability of PI. At the neutral pH (**Figure 4.8B**), the peptide was confined within the SANs and does not have sufficient freedom to access and further permeate the bacterial cell membrane. The live-dead assay was also performed in Gram-positive *S. aureus* culture showing the same trend of pH-dependent antimicrobial activity (**Figure 4.9**).

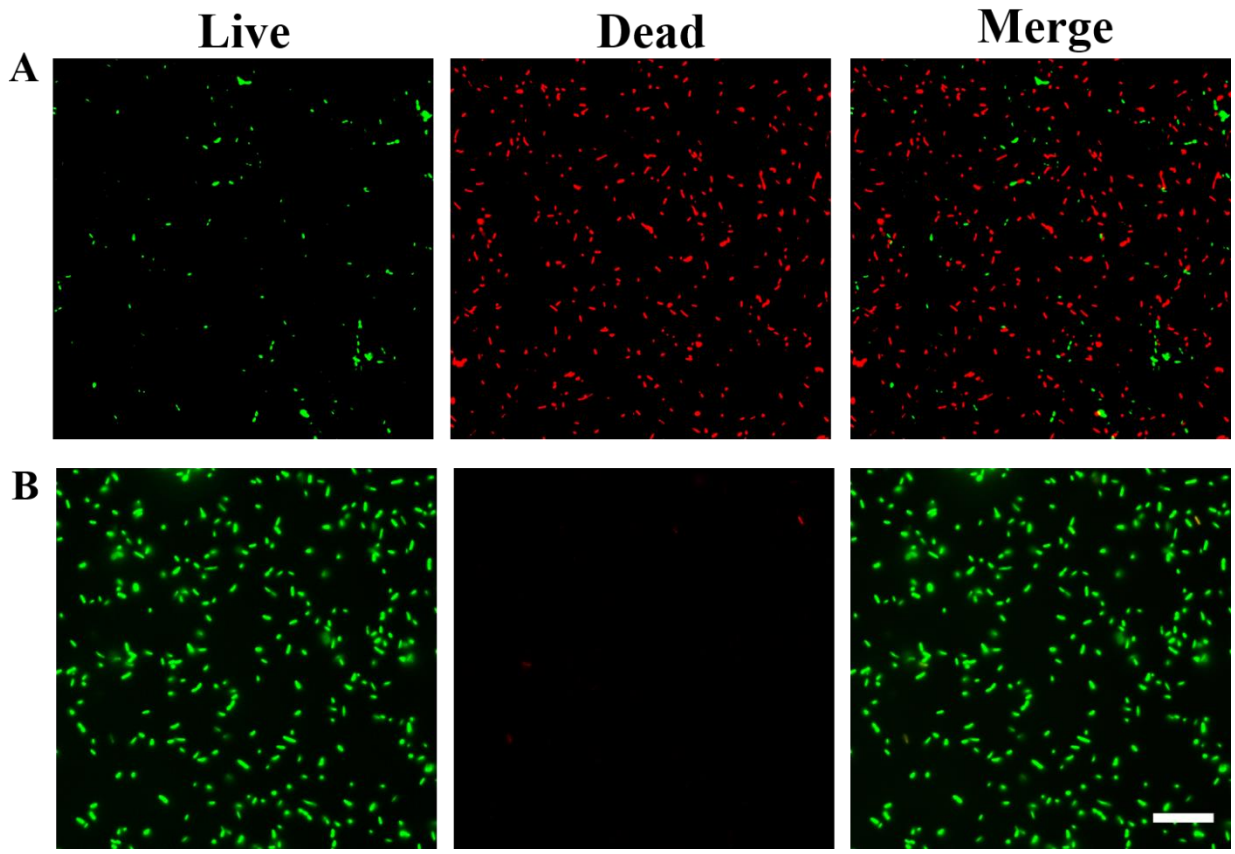

Figure 4.8. Fluorescence images of Live/dead bacterial assay results. Top panel: *E.coli* treated with 20 µM WH_9 at **(A)** pH 5.7 and **(B)** pH 7.4 for 3 hrs. Live bacteria were stained with SYTO9 (green) and dead bacteria were stained with PI (red). Scale bar: 20 µm.

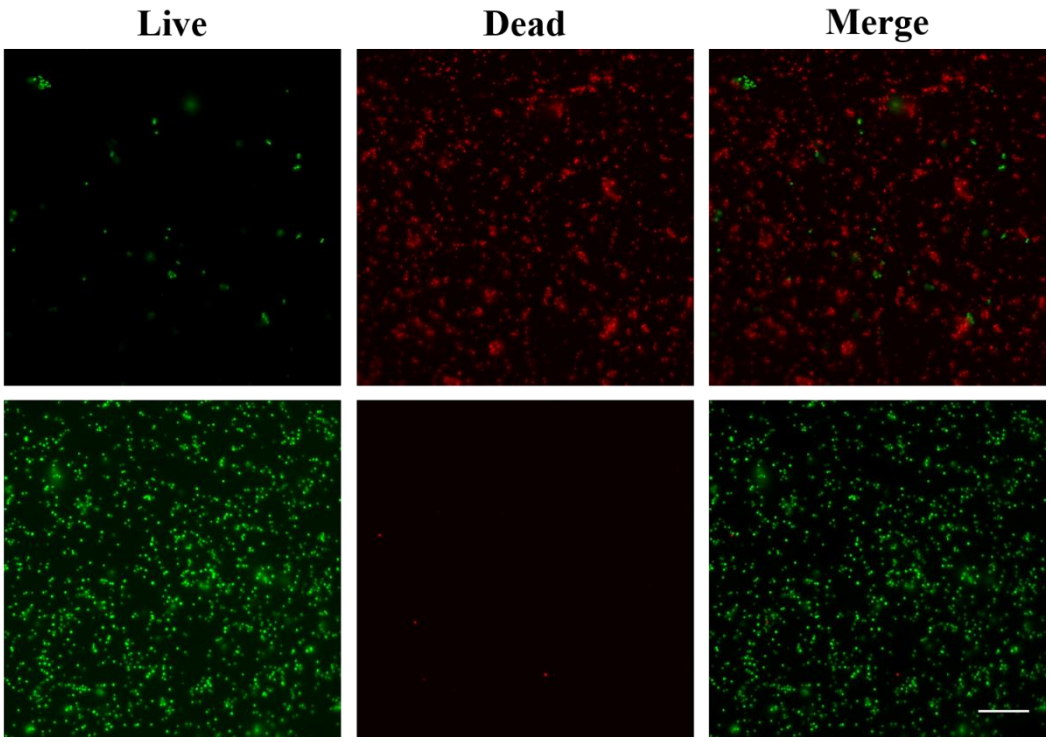

Figure 4.9. Fluorescence images of live/dead bacterial assay results. Top panel: *S.aureus* treated with 10 μM WH_9 at **(A)** pH 5.7 and **(B)** pH 7.4 for 3hrs. Live bacteria were stained with SYTO9 (green) and dead bacteria were stained with PI (red). Scale bar: 20 μm.

The physical interaction between WH_9 and bacteria was also studied by fluorescence microscopy upon incubation of FITC-labelled WH_9 with *E. coli* followed by PI staining. The binding affinity of WH_9 toward bacteria was greatly improved upon acidification as demonstrated by the numbers of bacterial cells that are attached by peptides showing green fluorescence on the cell membrane (**Figure 4.10A**) while at the neutral condition much less binding occurs between the peptides and bacteria (**Figure 4.10B**). Scan electron microscopy (SEM) was used to visualize any morphological change induced in bacteria by exposure to WH_9 under the acidic condition. As compared to control bacteria without peptide treatment (**Figure 4.11A**), *E. coli* incubated with WH_9 under the acidic culture condition showed significant membrane damage (**Figure 4.11B**), suggesting the mode of action is through bacterial membrane disruption by the disassembled peptides.

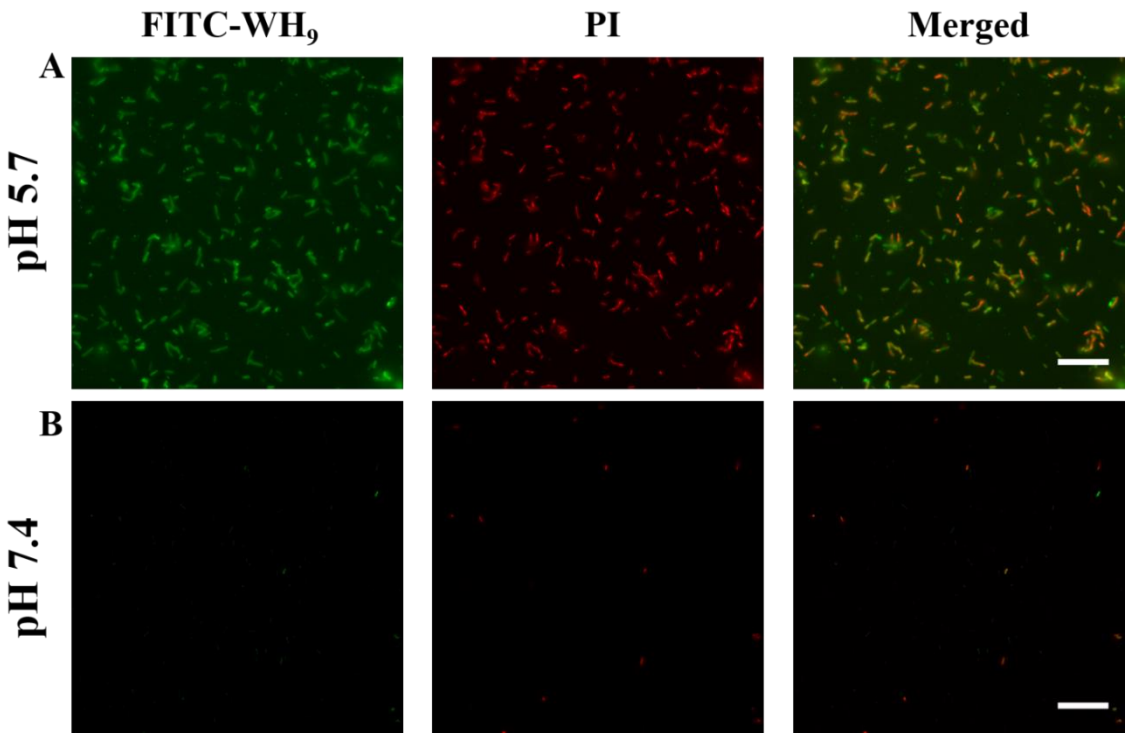

Figure 4.10. Fluorescence images of *E.coli* treated with FITC-WH_9 followed by PI staining in **(A)** acidic (pH 5.7) and **(B)** neutral culture conditions (pH 7.4). FITC-WH_9 was found to attach to the bacterial membrane in the acidic condition, causing membrane disruption and bacterial death as stained by PI. Scale: 20 µm.

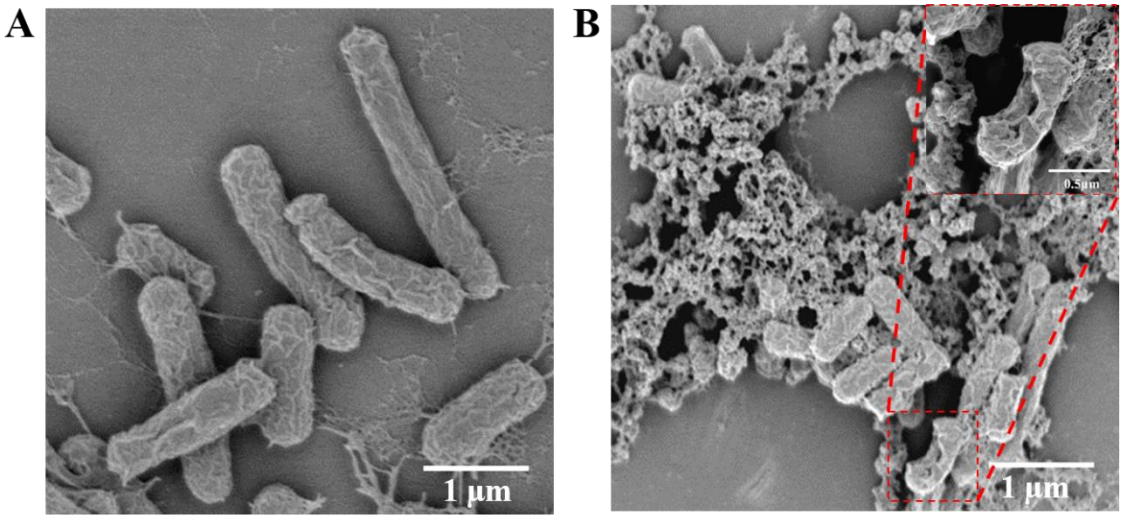

Figure 4.11. SEM images showing the morphological change of *E. coli* with and without peptide treatment in the acidic condition. **(A)** *E. coli* without peptide treatment at pH 5.7. **(B)** *E. coli* upon WH_9 incubation (2 x MIC) for 1 hr at pH 5.7. The inset picture shows the damage of bacterial membrane upon peptide treatment.

4.2.5 Evaluation of Cytotoxicity and Hemocompatibility

A critical challenge associated with conventional AMPs is their moderate to severe cytotoxicity and hemolytic activity.[28] We have recently demonstrated that self-assembly can be an effective approach to reduce the non-polar membrane-contact area of AMPs leading to greatly improved cytocompatibility and bacterial cell selectivity.[27] To evaluate the cytotoxicity of the newly designed WH_9 toward mammalian cells during blood circulation, NIH/3T3 fibroblasts were incubated with peptides at various concentrations and the cell viability was quantified by the MTT assay. 80 μM was selected as the upper concentration threshold to avoid potential precipitate formation as the peptide concentration increases in the mammalian culture media. As shown in **Figure 4.12**, dose-dependent cell viability was measured showing > 80% of cell viability up to 40 μM and 72% of cells were still alive upon incubation with peptides at 80 μM. The hemocompatiblity was evaluated by incubating human red blood cells (RBCs) with WH_9 at different concentrations for 1 hr and released haemoglobin was measured by UV spectroscopy (**Figure 4.13**). Within the tested peptide concentrations up to 160 μM (16 times of the MIC) less than 5% of hemolysis was observed with peptide-treated RBCs compared to the positive control group of RBCs treated with Triton-100. Taken together, the pH-triggered antimicrobial activity and excellent cytocompatibility and hemocompatibility of self-assembled WH_9 highlight their great potential as a new antimicrobial strategy to effectively treat bacterial infections associated with acidity.

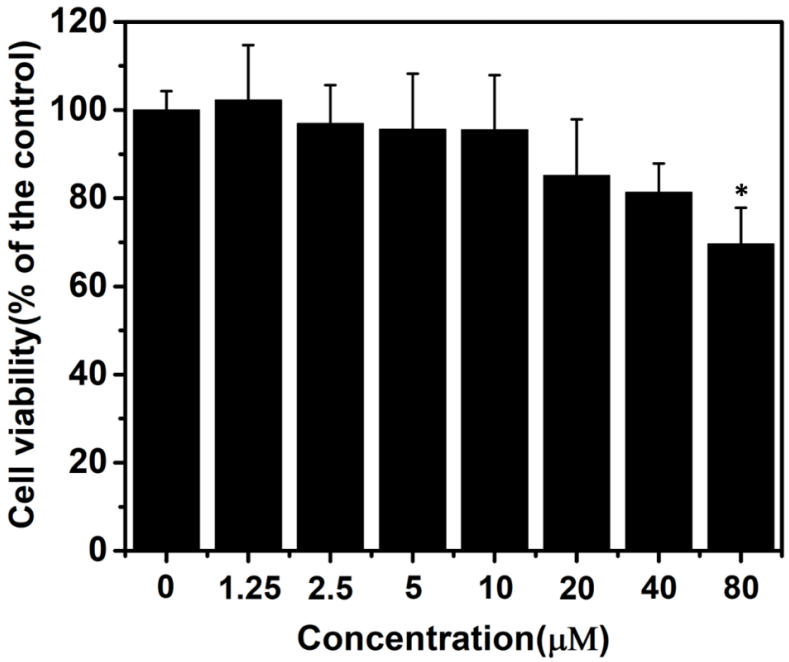

Figure 4.12. NIH/3T3 cell viability of peptide-treated cells in relative to the control group without peptides after 24 hrs of incubation with WH_9 at various concentrations. Statistic significant differences are indicated by $*p < 0.05$.

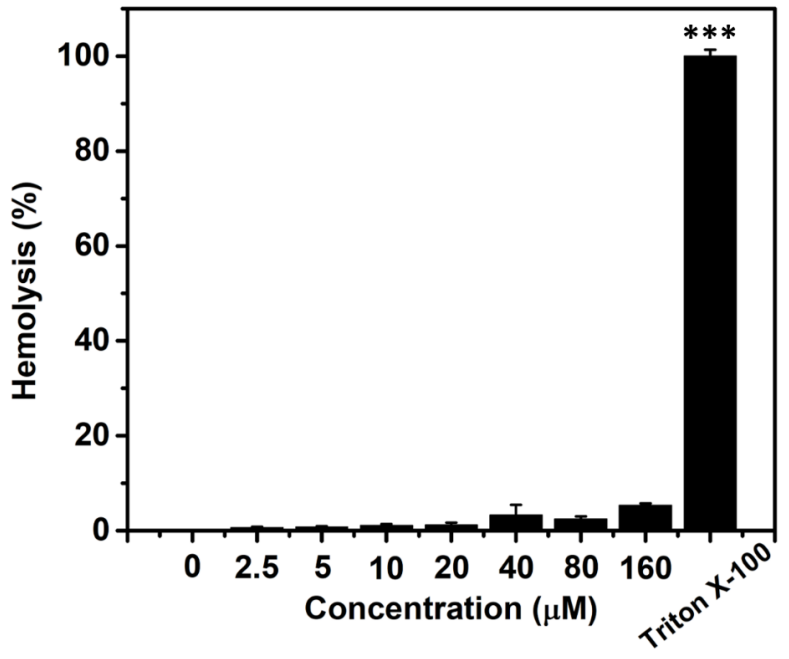

Figure 4.13. The percentage of hemolysis induced by WH_9 at various peptide concentrations. Statistic significant difference are indicated by $***p < 0.001$.

4.3 Conclusions

In summary, we have demonstrated a new pH-responsive antimicrobial nanomaterial based on the self-assembly of de novo designed MDPs for acid-responsive antimicrobial delivery at the site of infection associated with bacterial acidity. The MDP can be designed to form stable nanofibrous structures in neutral pH with excellent cytocompatibility and hemocompatibility. The pH-triggered disassembly was demonstrated in both the aqueous solution and on a bacteria-inoculated agar plate and shown to be an important factor for their antimicrobial activity. This new antimicrobial strategy while awaiting more extensive *in vitro* evaluation and in vivo studies holds great promise to treat bacterial infections in which acidity plays an important role in bacterial pathogenesis. For future studies, SANs based on custom-designed non-natural amino acids may offer diverse chemical functionality and broader pH-tunability to suit various clinical needs in the combat of infectious diseases.

4.4 Experimental Section

Materials. Fmoc-protected amino acids, 2-(6-Chloro-1-H-benzotriazole-1-yl)-1,1,3,3-tetramethylaminium hexafluorophosphate (HCTU), MBHA rink amide resin, were purchased from Novabiochem. Piperidine, diisopropylethylamine (DIPEA) 5(6)-Carboxyfluorescein (FAM), 5(6)-carboxy-tetramethyl-rhodamine, Mueller Hinton Broth (MHB), MTT assay kit were purchased from Sigma-Aldrich. LIVE/DEAD^{TM} BacLight^{TM} Bacterial Viability Kit, Centrifugation filters with molecular weight cutoff at 10 kDa and 30 kDa, Agar, Triton^{TM} X-100, Blood agar (TSA with 5% sheep blood) were purchased from Fisher Scientific. Dulbecco's modified Eagle medium (DMEM) culture medium was purchased from Life Technologies. Fetal Bovine Serum (FBS) was purchased from VWR. TEM staining reagent, uranium acetate dihydrate and TEM grid were purchased from TED PELLA, INC. *Escherichia coli* (ATCC 25922), *Bacteroides fragilis* (ATCC

25285) and *Staphylococcus aureus* (ATCC 29213) were purchased from ATCC.

Synthesis and purification of peptides. Multidomain peptides were synthesized on a *Prelude*® peptide synthesizer using standard FMOC-solid phase peptide synthesis procedures. Fmoc groups were deprotected by 20% (V/V) piperidine in N, N-dimethylformamide (DMF) for 5 min (2 times). HCTU was used as the coupling reagent and mixed Fmoc protected amino acids in the presence of DIPEA with a molar ratio of 1:1:2.5 (amino acid: HCTU: DIPEA). Upon the completion of the synthesis, the N-terminus of the peptides were acetylated in the presence acetic anhydride and DIPEA in DMF. The acetylated peptides were cleaved from the resin using a mixture of trifluoroacetic acid (TFA) / triisopropanolsilane (TIS) / H_2O (95/2.5/2.5 by volume) for 3 hours. The cleavage solution was collected through filtration and neat TFA was used to wash the resin twice. TFA solution was evaporated under moderate air flow. The residual peptide solution was precipitated in cold diethyl ether, followed by centrifugation and washing with cold diethyl ether for four times. The crude peptide was dried under vacuum overnight for HPLC purification. The peptide was purified using a preparative reversed phase C4 column with a linear gradient of water/acetonitrile containing 0.05% TFA. Elution was monitored at 230 nm and 280 nm. The mass of the three peptides were confirmed by MALDI. WH_5: expected $[M+H]^+$: 2634, observed $[M+H]^+$: 2634; WH_7: expected $[M+H]^+$: 2908, observed $[M+H]^+$: 2908; WH_9: expected $[M+H]^+$: 3182, observed $[M+H]^+$: 3182. Fluorescein and rhodamine terminated peptides were synthesized as follows. After final deprotection of the peptide, the N-terminus was coupled with 4 equivalents of 5(6)-carboxyl fluorescein or 5(6)-carboxy-tetramethyl-rhodamine using a combination of 4 equivalents of HCTU and 8 equivalents of DIPEA in DMF. The reaction mixture was stirred overnight. The completion of the coupling reaction was confirmed by the Kaiser test. If necessary, the coupling of 5-(6)-carboxyl-fluorescein or 5(6)-carboxy-tetramethyl-rhodamine was repeated

once. The cleavage and purification procedure followed the same procedure as described for the nonlabelled peptides. The molecular weight was confirmed by MALDI. FITC-WH_9: expected $[M+H]^+$: 3499, observed $[M+H]^+$: 3500; Rho-WH_9: expected $[M+H]^+$: 3553, observed $[M+H]^+$: 3554.

The purified MDP solutions that were collected from HPLC machine were lyophilized for 48 hrs to remove any solvents. Then the powder of MDPs was dissolved in sterile Tris buffer or MES buffer for further bacterial and cell assay.

Circular dichroism (CD) spectroscopy. Samples were prepared by dilution from the peptide stock solution to a concentration at 50 μM in either Tris buffer (pH 7.4, 20 mM) or MES buffer (pH 5.7, 20 mM). The samples were incubated at 4°C overnight. Data were collected from 250 nm to 190 nm at room temperature (RT) using a 1 mm cuvette, a bandwidth at 1 nm, scan rate at 100 nm/min and a response time of 2 sec. Each spectrum was averaged from three scans. The mDeg of rotation was converted to molar residual ellipticity via the formula θ=(mDeg*1000)/(c*n*l), where c is the concentration of the peptide solution expressed in mM, n is the number of amino acids in the peptide sequence and l is the path length of the cell used in mm.

Transmission electron microscopy (TEM). Sample preparation was the same as that used in the CD experiment. Peptide solution (10 μL) was dropped onto a holey carbon grid (TED PELLA 01824). After 2 minutes, excess solution was carefully removed with filter paper. 10 μL of 2 wt % uranyl acetate aqueous solution was dropped onto the grid for negative staining. After 2 minutes, excess staining solution was removed and the TEM samples were dried for overnight before imaging.

Critical aggregation concentration (CAC) measurement. Peptide solution (160 μM) was added in either 200 μL Tris buffer (20 mM, pH 7.4) or 200 μL MES buffer (20 mM, pH 5.7) with an

increment of 2 μL each time. Fluorescence spectra were acquired after each peptide addition by monitoring the emission of peptides from 295 nm to 440 nm using an excitation wavelength at 280 nm. Fluorescence intensity at 350 nm was plotted as a function of the peptide concentrations. The CAC was determined to be the concentration at which nonlinearity started to develop as shown in

Minimum inhibitory concentration (MIC) determination. For the MIC test in the aerobic condition*, E.coli* was cultured in MHB media under constant shaking at 100 rpm at 37 ºC to reach the mid-exponential growth phase. The bacterial solution was plated on an agar plate for colony forming unit (CFU) counting. Bacterial suspensions were diluted to approximately $2x10^5$ CFU/mL in MHB media at either pH 7.4 or 5.7. Peptide solutions at various concentration (80, 40, 20, 10, 5, 2.5 μM) were prepared in either Tris buffer (pH 7.4, 20 mM) or MES buffer (pH 5.7, 20 mM). 50 μL of each peptide solution was mixed with 50 μL of bacterial solution in a 96-well plate and the experiments were performed in triplicates. The plates were incubated at 37 ºC under constant shaking at 100 rpm for 18 hrs and the optical density (OD) at 600 nm was measured on a plate reader. The MIC was determined at the peptide concentration in which OD reading is below 0.06 and no cloudiness was visible to naked eyes.

For the MIC test in the anaerobic condition, *E. coli* (ATCC 25922), *B. fragilis* (ATCC 25285) and *S. aureus* (ATCC 29213) inocula were prepared using the BBL Prompt Inoculation System to generate an approximate 1.5 x 10^8 CFU/mL that was further diluted to generate an inoculum at 1.0 x 10^6 CFU/mL in MHB media at pH 7.4. Peptide solutions with various concentration (80, 40, 20, 10, 5, 2.5 μM) were prepared in Tris buffer (pH 7.4, 20 mM). All the reagents for the anaerobic test were reduced under anaerobic conditions for at least 2 hrs prior to the initiation of testing and care was taken to minimize all bacterial strains to oxygen exposure. 50 μL of each peptide solution was mixed with 50 μL of bacterial solution in a 96-well plate and the experiments were performed

in triplicates. The plates were incubated 48 hrs under constant shaking at 100 rpm. The MIC was determined at the peptide concentration in which OD reading is below 0.06 and no cloudiness was visible to naked eyes. For all MIC tests, bacterial culture without peptides was used as a negative control. Gentamicin was used as the positive control that helps validate the MIC assay. Gentamicin is efficacious against *E.coli* and *S. aureus* although the MIC is shifted higher in anaerobic versus aerobic conditions.

Bacterial culture without peptides were used as a negative control. Gentamicin was used as the positive control that helps validate the MIC assay. Gentamicin is efficacious against *E.coli* and *S. aureus* although the MIC is shifted higher in anaerobic versus aerobic conditions.[29,30]

Scanning electron microscopy to examine the morphology of the bacterial membrane. 400 μL bacterial suspensions (*E.coli*, 10^8 CFU/mL) were added to a 24-well plate with a cover glass (d=12 mm) placed on the bottom of each well. After 24 hrs of incubation, bacterial suspension was removed and the plates were washed with PBS buffer (pH 7.4) to remove any non-adherent bacteria. 100 μL of fresh MHB media (pH 5.7) and 100 μL of 40 μM peptide solution in MES buffer (pH 5.7, 20 mM) were mixed and added in each well and incubated at 37 ºC for 1 hr. The media were removed and the cover glasses were washed with Tris buffer for three times. Bacteria were fixed using 4% glutaraldehyde solution for overnight. The cover glasses were further dehydrated using a series of graded ethanol solutions from 35, 50, 75, 90, 95 and 100% (contents of ethanol volume). Samples were placed on a carbon tape and further coated with a 5 nm-thick gold layer. The morphology of the bacteria with and without peptide treatments were observed using a field emission scanning electron microscope operated at an accelerating voltage of 1.0 kV and a working distance of 5.8 mm.

Live and dead bacterial assay. 400 μL of bacterial suspensions (*E.coli*, 10^8 CFU/mL) was added

to confocal dish and incubated at 37 ºC for 24 hrs. Bacterial suspensions were removed from the confocal dish and washed with PBS buffer (pH 7.4) for three times to remove any non-adherent bacteria. 100 μL of fresh MHB media and 100 μL of 40 μM peptide solution in either Tris buffer (pH 7.4, 20 mM) or MES buffer (pH 5.7, 20 mM) was added sequentially in the confocal dish. After incubation at 37 ºC for 3 hrs, the culture media were removed and washed with PBS buffer (pH 7.4) for three times. Bacteria were stained with live/dead bacteria assay kit solution at room temperature for 15 min. Finally, bacteria were washed with PBS buffer (pH 7.4) for three times. Images were captured with epifluorescence and processed with ImageJ software.

Membrane localization assay. Bacterial suspensions (*E.coli*, 10^8 CFU/mL) were added to a confocal dish. After 24 hrs of incubation, bacterial suspensions were removed and confocal dish was washed with PBS buffer (pH 7.4) for three times to remove any non-adherent bacteria. Next, 100 μL of MHB media and 100 μL of 7% FITC-labeled peptides were added to confocal dish to reach a concentration at 40 μM. After 3 hrs of incubation, bacteria were washed with PBS (pH 7.4) for three times. Bacteria were stained with PI at room temperature for 15 min. Finally, bacteria were washed with PBS buffer (pH 7.4) for three times. Images were captured using a fluorescence microscope and processed with ImageJ software.

Hemolytic activity test. Human red blood cells (RBCs) were donated from a volunteer and 4% of human RBCs were prepared in PBS buffer (pH 7.4). 20 μL of peptide solution at various concentrations (1600, 800, 400, 200, 100, 50, and 25 μM) were prepared in PBS buffer (pH 7.4). Peptides were mixed with 180 μL of RBC suspensions in a 1.5 mL Eppendorf tube. The mixtures were incubated at 37 ºC for 1 hr, followed by centrifugation at 3000 g for 5 mins. 100 μL of the supernatant was taken out and transferred to a 96-well plate. Hemoglobin release was determined by measuring the absorbance of the supernatant at 540 nm on a microplate reader (Vitor2 1420

Multilabel Counter, PerkinElmer). RBCs treated with 1% Triton-X served as positive controls and untreated RBCs served as a negative control group. Each sample was tested in three replicates. The percentage of hemolysis remained is calculated using the following equation

$$\% \text{ hemolysis} = (A_{\text{peptide}} - A_{\text{negative control}}) / (A_{\text{Triton X}} - A_{\text{negative control}}) \times 100$$

in which the negative control group contains RBC suspension mixed with PBS buffer without peptides.

Cytotoxicity measurement. NIH/3T3 cells were seeded onto a 96-well plate at a density of 10^4 cells/well and incubated for 24 hrs at 37 °C in an incubator with 5% of CO_2. After 24 hrs, the culture medium was removed. 10 μL of peptide solution at various concentrations (800, 400, 200, 100, 50, 25, 12.5 μM) was mixed with 90 μL fresh culture medium in a 96-well plate. After 24 hrs of incubation, the MTT assay was performed to quantify the cell viability by monitoring the UV absorbance at 490 nm. Cell culture without peptides were used as a negative control. All the experiments were performed in four replicates.

Measurement of the microenvironmental pH in bacterial colonies. The pH value of the *B. fragilis* living milieu was measured using a pH ratiometric fluorescence imaging probe based on our previous publication with minor modification.[31] First, probes in PBS (0.5mg/mL) with different pH values were dropped on surface of the blank TSAB (Trptic Soy Agar with 5% sheep blood) plate, imaged with an *in vivo* Kodak imager (Ex 630nm, Em 700 nm, Exposure time 10 s; Ex 760nm, Em 830 nm, Exposure time 10 s). The results were analyzed to acquire a correlation curve between fluorescence ratio and indicated pH value and further plotted as a standard curve. Secondly, probes suspended in DI water (0.5 mg/mL) were dropped on individual *B. fragilis* colonies on a TSAB plate and the plate without bacteria (as a control) and were imaged with the same protocol. The pH around bacterial colonies was determined based on the standard curve

established above.

Statistical analysis. All data were expressed as means ± standard deviation (SD). The statistical analysis was performed using Student's T-test and one-way analysis of variance (ANOVA) at confidence levels of 95%.

4.5 References

(1) Torchilin, V. P. Multifunctional, stimuli-sensitive nanoparticulate systems for drug delivery. *Nat. Rev. Drug Discov.* **2014**, *13*, 813.
(2) Veiseh, O.; Tang, B. C.; Whitehead, K. A.; Anderson, D. G.; Langer, R. Managing diabetes with nanomedicine: challenges and opportunities. *Nat. Rev. Drug Discov.* **2014**, *14*, 45.
(3) Chung, E. J.; Mlinar, L. B.; Nord, K.; Sugimoto, M. J.; Wonder, E.; Alenghat, F. J.; Fang, Y.; Tirrell, M. Monocyte-targeting supramolecular micellar assemblies: a molecular diagnostic tool for atherosclerosis. *Adv. Healthc. Mater.* **2015**, *4*, 367-376.
(4) Lock, L. L.; Tang, Z.; Keith, D.; Reyes, C.; Cui, H. Enzyme-specific doxorubicin drug beacon as drug-resistant theranostic molecular probes. *ACS Macro Lett.* **2015**, *4*, 552-555.
(5) Wang, Y.; Kohane, D. S. External triggering and triggered targeting strategies for drug delivery. *Nat. Rev. Mater.* **2017**, *2*, 17020.
(6) Rosenblum, D.; Joshi, N.; Tao, W.; Karp, J. M.; Peer, D. Progress and challenges towards targeted delivery of cancer therapeutics. *Nat. Commun.* **2018**, *9*, 1410.
(7) Chung, H. J.; Park, T. G. Self-assembled and nanostructured hydrogels for drug delivery and tissue engineering. *Nano Today* **2009**, *4*, 429-437.
(8) Hosseinkhani, H.; Hong, P.-D.; Yu, D.-S. Self-assembled proteins and peptides for regenerative medicine. *Chem. Rev.* **2013**, *113*, 4837-4861.
(9) Zhang, L.; Chan, J. M.; Gu, F. X.; Rhee, J.-W.; Wang, A. Z.; Radovic-Moreno, A. F.; Alexis, F.; Langer, R.; Farokhzad, O. C. Self-assembled lipid−polymer hybrid nanoparticles: a robust drug delivery platform. *ACS Nano.* **2008**, *2*, 1696-1702.
(10) Gu, L.; Mooney, D. J. Biomaterials and emerging anticancer therapeutics: engineering the microenvironment. *Nat. Rev. Cancer.* **2015**, *16*, 56.
(11) Scheinberg, D. A.; Villa, C. H.; Escorcia, F. E.; McDevitt, M. R. Conscripts of the infinite armada: systemic cancer therapy using nanomaterials. *Nat. Rev. Clin. Oncol.* **2010**, *7*, 266.
(12) Barreto, J. A.; O'Malley, W.; Kubeil, M.; Graham, B.; Stephan, H.; Spiccia, L. Nanomaterials: applications in cancer Imaging and therapy. *Adv. Mater.* **2011**, *23*, H18-H40.
(13) Sun, Q.; Zhou, Z.; Qiu, N.; Shen, Y. Rational design of cancer nanomedicine: nanoproperty integration and synchronization. *Adv. Mater.* **2017**, *29*, 1606628.
(14) Radovic-Moreno, A. F.; Lu, T. K.; Puscasu, V. A.; Yoon, C. J.; Langer, R.; Farokhzad, O. C. Surface charge-switching polymeric nanoparticles for bacterial cell wall-targeted delivery of antibiotics. *ACS Nano.* **2012**, *6*, 4279-4287.
(15) Hughes, M.; Debnath, S.; Knapp, C. W.; Ulijn, R. V. Antimicrobial properties of enzymatically triggered self-assembling aromatic peptide amphiphiles. *Biomater. Sci.* **2013**, *1*, 1138-1142.

(16) Horev, B.; Klein, M. I.; Hwang, G.; Li, Y.; Kim, D.; Koo, H.; Benoit, D. S. W. pH-activated nanoparticles for controlled topical delivery of farnesol to disrupt oral biofilm virulence. *ACS Nano.* **2015**, *9*, 2390-2404.
(17) Xiong, M.; Bao, Y.; Xu, X.; Wang, H.; Han, Z.; Wang, Z.; Liu, Y.; Huang, S.; Song, Z.; Chen, J.; Peek, R. M.; Yin, L.; Chen, L.-F.; Cheng, J. Selective killing of *helicobacter pylori* with pH-responsive helix–coil conformation transitionable antimicrobial polypeptides. *Proc. Natl. Acad. Sci. U.S.A.* **2017**, *114*, 12675-12680.
(18) Fuchs, S.; Pané-Farré, J.; Kohler, C.; Hecker, M.; Engelmann, S. Anaerobic gene expression in staphylococcus aureus. *J. Bacteriol.* **2007**, *189*, 4275-4289.
(19) Marteyn, B.; Scorza, F. B.; Sansonetti, P. J.; Tang, C. Breathing life into pathogens: the influence of oxygen on bacterial virulence and host responses in the gastrointestinal tract. *Cell. Microbiol.* **2011**, *13*, 171-176.
(20) Dubos, R. The micro-environment of information or metchnikoff revisited. *Lancet* **1955**, *266*, xxiv-5.
(21) Trevani, A. S.; Andonegui, G.; Giordano, M.; López, D. H.; Gamberale, R.; Minucci, F.; Geffner, J. R. Extracellular acidification induces human neutrophil activation. *J. Immunol.* **1999**, *162*, 4849-4857.
(22) Marsland, B. J.; Gollwitzer, E. S. Host–microorganism interactions in lung diseases. *Nat. Rev. Immunol.* **2014**, *14*, 827.
(23) Kilian, M.; Chapple, I. L. C.; Hannig, M.; Marsh, P. D.; Meuric, V.; Pedersen, A. M. L.; Tonetti, M. S.; Wade, W. G.; Zaura, E. The oral microbiome – an update for oral healthcare professionals. *Bdj* **2016**, *221*, 657.
(24) Mercier, R.-C.; Stumpo, C.; Rybak, M. J. Effect of growth phase and pH on the in vitro activity of a new glycopeptide, oritavancin (LY333328), against Staphylococcus aureus and Enterococcus faecium. *J. Antimicrob. Chemother.* **2002**, *50*, 19-24.
(25) Xu, D.; Dustin, D.; Jiang, L.; Samways, D. S. K.; Dong, H. Designed filamentous cell penetrating peptides: probing supramolecular structure-dependent membrane activity and transfection efficiency. *Chem. Comm.* **2015**, *51*, 11757-11760.
(26) Xu, D.; Jiang, L.; Singh, A.; Dustin, D.; Yang, M.; Liu, L.; Lund, R.; Sellati, T. J.; Dong, H. Designed supramolecular filamentous peptides: balance of nanostructure, cytotoxicity and antimicrobial activity. *Chem. Comm.* **2015**, *51*, 1289-1292.
(27) Xu, D.; Chen, W.; Tobin-Miyaji, Y. J.; Sturge, C. R.; Yang, S.; Elmore, B.; Singh, A.; Pybus, C.; Greenberg, D. E.; Sellati, T. J.; Qiang, W.; Dong, H. Fabrication and microscopic and spectroscopic characterization of cytocompatible self-assembling antimicrobial nanofibers. *ACS Infect. Dis.* **2018**, *4*, 1327-1335.
(28) Aoki, W.; Kuroda, K.; Ueda, M. Next generation of antimicrobial peptides as molecular targeted medicines. *J. Biosci. Bioeng.* **2012**, *114*, 365-370.
(29) DeMars, Z.; Biswas, S.; Amachawadi, R. G.; Renter, D. G.; Volkova, V. V. Antimicrobial susceptibility of enteric gram negative facultative anaerobe bacilli in aerobic versus anaerobic conditions. *PLOS ONE* **2016**, *11*, e0155599.
(30) Harrell, L. J.; Evans, J. B. Anaerobic resistance of clinical isolates of Staphylococcus aureus to aminoglycosides. *Antimicrob. Agents Chemother.* **1978**, *14*, 927-929.
(31) Tsai, Y.-T.; Zhou, J.; Weng, H.; Shen, J.; Tang, L.; Hu, W.-J. Real-time noninvasive monitoring of in vivo inflammatory responses using a pH ratiometric fluorescence imaging probe. *Adv. Healthc. Mater.* **2014**, *3*, 221-229.

Chapter 5: Design of Alkaline-responsive Polydiacetylene-Peptide (PDA-Pep) Assembly for Bacterial Sensing and Antimicrobial Therapy*

5.1 Introduction

Given the ever-growing public health problem posed by antibiotic resistance, there is an urgent need to advance novel antimicrobial strategies to combat drug-resistant infectious diseases. Stimuli-responsive drug delivery has the potential to provide effective treatments through releasing antibiotics at the infection sites to maximize therapeutic efficacy and minimize drug resistance. [1-3] Among various stimuli, pH has been considered as an important endogenous stimulus for the design and synthesis of pH-responsive materials to selectively deliver antibiotics at the site of infection. [4,5] In the past several decades, acid-responsive materials have been extensively explored to treat infections caused by lactic acid-producing bacteria. [6-8] However, materials that can respond to an alkaline bacterial microenvironment, for example diseases involving chronic wound infections (pH 7.2-8.9), [9,10] pancreas infections (pH 7.5-8.5) [11,12] and catheter-associated urinary tract infections (pH 7.0-8.5) [13] are still under-developed. From the viewpoint of both fundamental and practical materials research, there is a need to explore novel stimuli-responsive materials that can target bacterial infections associated with local pH increase. It is more beneficial to develop a system capable of both sensing/signaling and on-demand antimicrobial delivery. Such systems would greatly benefit clinical research on real-time bacterial imaging and antimicrobial therapy.

* This chapter is based on Weike Chen, Shan Hazoor, Ryan Madigan, Ashley A. Adones, Uday K. Chintapula, Kytai T. Nguyen, Liping Tang, Frank W. Foss Jr., He Dong. Alkaline-responsive polydiacetylene-peptide hydrogel for pH-sensing and on-demand antimicrobial release. *Mater. Today Adv.*, **2022**, Submitted. Some sections were rearranged for continuity.

Inspired by the recent advances in polydiacetylene (PDA)-based biosensor design, [14-19] we aim to establish a new class of alkaline-responsive hydrogels based on PDA-peptide (PDA-Pep) conjugates for colorimetric pH-sensing and antimicrobial properties. PDA-Pep is a new family of nanomaterials that are constructed through the self-assembly of diacetylene-peptide (DA-Pep) to form supramolecular nanofibers or micelles. [20-24] In particular, when nanofibers are formed, the DA components are aligned internally along the long fiber axis of the nanofiber while the peptide moieties are flanking at the fiber-solvent interface. Upon UV irradiation, DA undergoes polymerization to form PDA with conformation-dependent chromic properties. Compared with other PDA-based materials, PDA-Pep has unique advantages regarding the control over the internal order of each molecular and macromolecular components within the nanofibers. The use of peptides provides an efficient method to tune not only the intermolecular packing within a single fiber, but also the macroscopic packing of these nanofibers to form higher-ordered dynamic assemblies. In this work, we will take advantages of the dynamic nature of PDA-Pep to design and synthesize a new family of alkaline-responsive hydrogels for monitoring and signaling the alkaline microenvironment upon bacterial infection and consequently control antimicrobial characteristics.

5.2 Results and Discussion

5.2.1 Design of Alkaline-responsive PDA-Pep Assembly

Figure 5.1 shows the chemical structure of DA-Pep and its dynamic self-assembly and disassembly process with pH. DA-Pep contains an internal aromatic diphenyldiacetylene linker which is attached to a glutamic acid-containing oligopeptide bearing a bacterial targeting ligand at both ends (**Figure 5.1A**). Based on the design principle, self-assembly of DA-Pep occurs under an acidic condition when the charge on the oligopeptide is neutralized, leading to supramolecular nanofibers with internally aligned DA groups (**Figure 5.1B**). At a high concentration of DA-Pep,

macroscopic hydrogels, which consist of physically crosslinked supramolecular nanofibers can be formulated. Upon UV irradiation, DA is polymerized to form PDA showing a characteristic blue color. As the local pH increases, glutamic acids are deprotonated and therefore electrostatic repulsion is generated among the oligopeptides. There are two levels of structural control with pH increase. On the molecular level, the electrostatic repulsion among the peptide domains will change the packing and conformation of PDA within a single nanofiber. The conformational change of PDA is known to induce a colorimetric transition from blue to red or purple and therefore can provide a visual and spectroscopic read-out for the local pH change (**Figure 5.1B**). On the macroscopic level, the hydrogel is likely to be disrupted as a result of the repulsive interaction between individual fibers upon pH increase. A gel-to-sol transition is expected as the solution becomes alkaline. It is worth noting that small molecule antibiotics and/or antimicrobial peptides (AMPs) can be readily incorporated into the hydrogels during the formulation process and are subject to release upon gel-to-sol transition as the local pH increases.

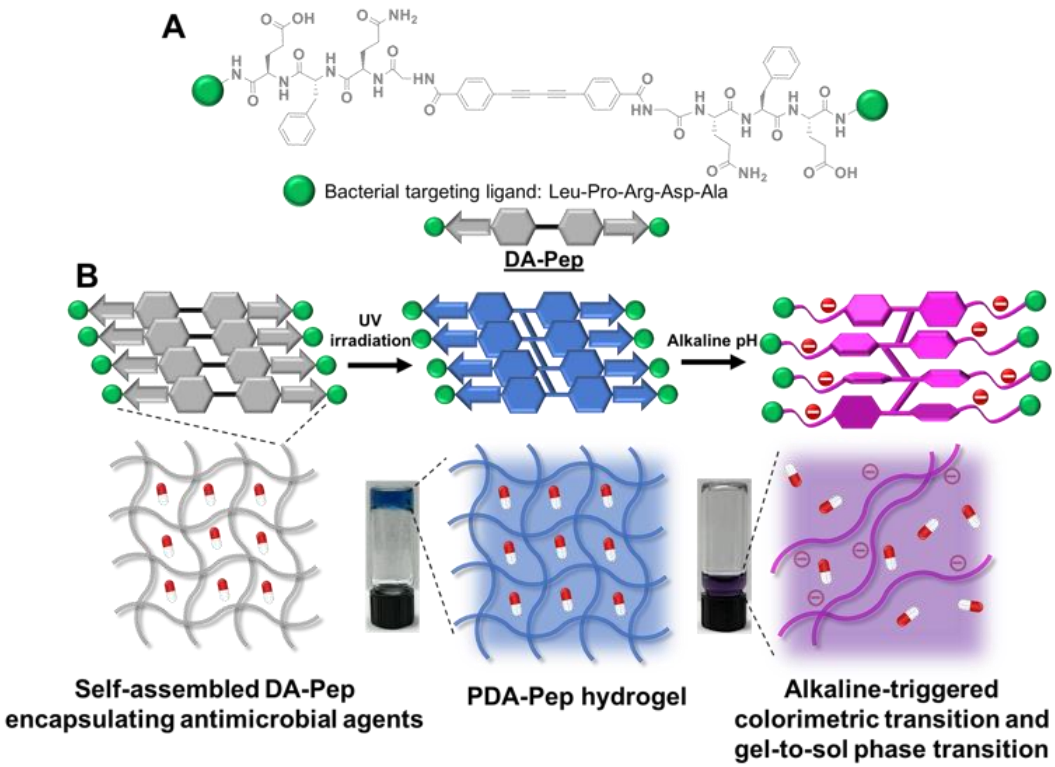

Figure 5.1. Illustration of the chemical design of PDA-Pep hydrogels that undergo alkaline-triggered blue-to-purple colorimetric transition with simultaneous gel-to-sol phase transition for antibiotic release. **(A)** Chemical structure of DA-Pep conjugate. **(B)** Illustration of self-assembled DA-Pep (in grey) that forms an elongated nanofiber and the formation of PDA-Pep hydrogel that appear in blue upon UV irradiation. The PDA-Pep became charged under the alkaline condition, which led to a conformational change of the PDA domain and a blue-to-purple colorimetric transition. The electrostatic repulsion induces a gel-to-sol transition and consequently antimicrobial release.

5.2.2 pH-dependent Molecular and Macromolecular Structural Characterization

The synthetic procedures and purification steps for the DA-linker and DA-Pep were shown in the **Experimental Section** (**Scheme-1)** and **Appendix D** (**Figure D-S1-1** to **D-S1-9** and **Figure D-S2**). A small library of DA-Pep was synthesized and tested for their gelation capability under the acidic condition (pH 5.5) by the tube inversion method (**Figure 5.2**). Initially, we started with a sequence containing a binary hydrophilic-hydrophobic residue repeating unit of QFQF in the peptide domain (Q: glutamine, F: phenylalanine), which is known to drive β-sheet packing. [25,26]

However, as shown in **Figure 5.2A**, this construct failed to form gels, nor did it polymerize. Further increasing the number of QF repeating units was ineffective to promote gelation, rather it caused precipitates due to phase separation upon self-assembly (data not shown). On the contrary, DA-Pep containing a single QF motif was found to gel which can be further polymerized as shown by the appearance of a blue color upon UV irradiation (**Figure 5.2B**). The results suggest an unstructured oligopeptide is more favorable for the self-assembly process in which a delicate balance can be achieved between the π-π stacking among the DA domains and the intermolecular hydrogen packing among the peptide domains. Peptides with an intrinsic secondary structural propensity are likely to compromise the internal alignment of the DA domain needed to form ordered supramolecular nanofibers and further macroscopic hydrogelation. It was also found that substitution of glutamine with serine completely inhibited gelation although polymerization still occurred (**Figure 5.2C**). Substitution of phenylalanine with aliphatic isoleucine did not affect gelation (**Figure 5.2D**); however, the color transition upon pH increase is less sensitive compared to that of DA-Pep with a QF sequence (**Figure 5.2E**). Given the initial screening result, we selected DA-Pep with the sequence of QF to construct alkaline-responsive hydrogels and investigate its alkaline-triggered colorimetric transition and antibiotic release.

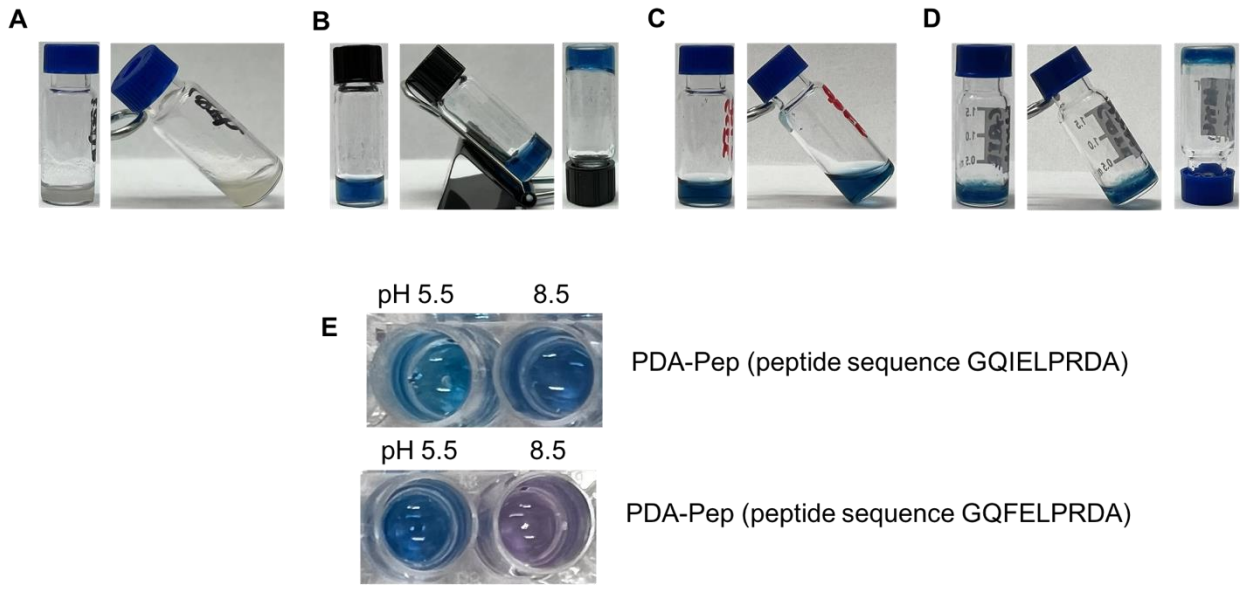

Figure 5.2. Comparison of gelation capability of PDA-Pep conjugates. **(A)** DA-Pep with GQFQFE, **(B)** PDA-Pep with GQFE, **(C)** PDA-Pep with GSFE, and **(D)** PDA-Pep with GQIE under acidic condition (pH 5.5). **(E)** Alkaline-triggered colorimetric transition of PDA-Pep conjugates. PDA-Pep concentration: 10 mg/mL

We are primarily interested in the pH range from 5.5 to 8.5 due to their implication for bacterial infections in several diseases. Gels were first prepared in a MES buffer at pH 5.5 and the pH was adjusted using sodium hydroxide to the desired values at 6.5, 7.5 and 8.5. As shown in **Figure 5.3A**, at pH 5.5, DA-Pep formed a stable self-supporting hydrogel which appeared blue upon UV-initiated polymerization. With the increase of pH, glutamic acids became deprotonated, and a net negative charge was built on each fibril to induce electrostatic repulsion between individual fibrils. The inter-fibril repulsion eventually disrupted the physical crosslinking in the hydrogel and a gel-to-sol transition was observed accordingly. This macroscopic structural change upon gel-to-sol transition was confirmed by transmission electron microscopy (TEM) showing a densely packed fibrous network at pH 5.5 and gradually reduced to dispersed fibers at pH 8.5 (**Figure 5.4**). Notably, the gel-to-sol phase transition was accompanied by a blue-to-purple color transition, which was presumably caused by the conformational change of the PDA moieties within a single nanofiber. To further quantify the colorimetric transition, which can be potentially

used as a diagnostic tool for monitoring the alkalinity of bacterial microenvironment, UV-vis spectroscopy was used to examine the conformation-dependent absorption at various pH values. As shown in **Figure 5.5**, PDA-Pep showed a major absorption peak at 652 nm with a vibronic shoulder at 596 nm at all pHs up to 6.8. Consistent with many literature reports [27-29], the peak at 652 nm is a signature absorption for PDA conformation that results in a visible blue color. As the solution became alkaline and a blue-to-purple colorimetric transition occurred, the absorption at 652 nm was dramatically reduced and a single broad peak at 566 nm was predominant, suggesting a conformational change of PDA. The ratio of the absorption at 566 nm and 652 nm represents the relative contribution of each chromatic solution component that is associated with different PDA conformation. Fitting the ratio of (A_{566}/A_{652}) to a modified Boltzmann sigmoidal function allows the estimation of the transition pH, i.e. the first derivative of the sigmoidal curve, which is at 7.3 (**Figure 5.3B**). The sensitivity of the colorimetric assay was further quantified based on the ratio of the UV-Vis absorption at 566 nm and the overall absorption values at both 566 nm and 652 nm, i.e. $A_{566}/(A_{566}+A_{652})$. The results showed that PDA-Pep is highly sensitive to pH change with 81 % colorimetric response at pH 8.5 and 70 % at pH 7.5 versus 35 % at pH 6.5 and 30 % at pH 5.5 (**Figure 5.3C).**

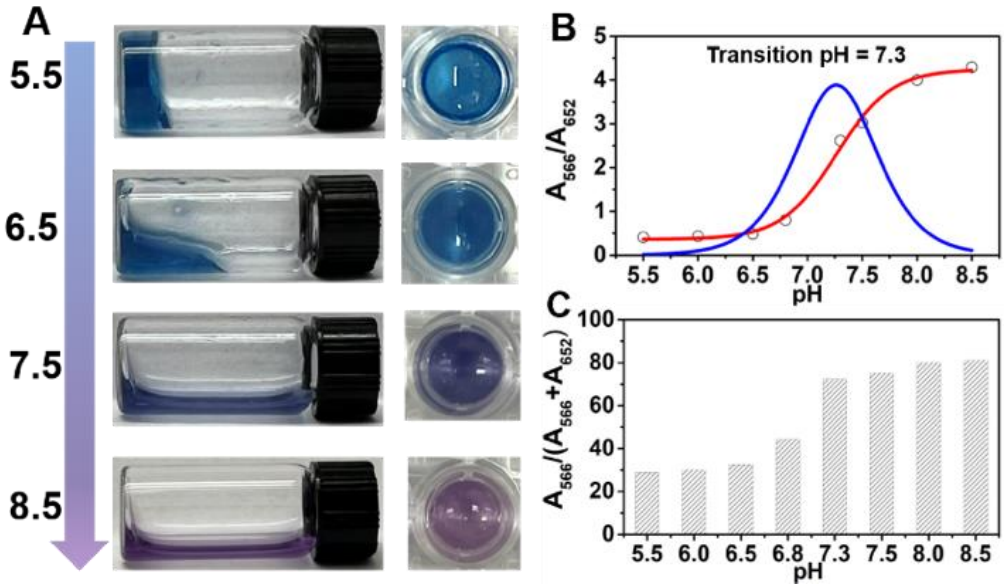

Figure 5.3. (A) pH-dependent gel and sol phase of PDA-Pep and their optical images showing an alkaline triggered blue-to-purple colorimetric transition. PDA-Pep concentration: 10 mg/mL. **(B)** Boltzmann sigmoidal fitting and first derivative of the absorbance ratio of A_{566}/A_{652} as a function of pH to determine the colorimetric transition pH. **(C)** Colorimetric response of PDA-Pep at various pH values. PDA-Pep concentration: 100 μM.

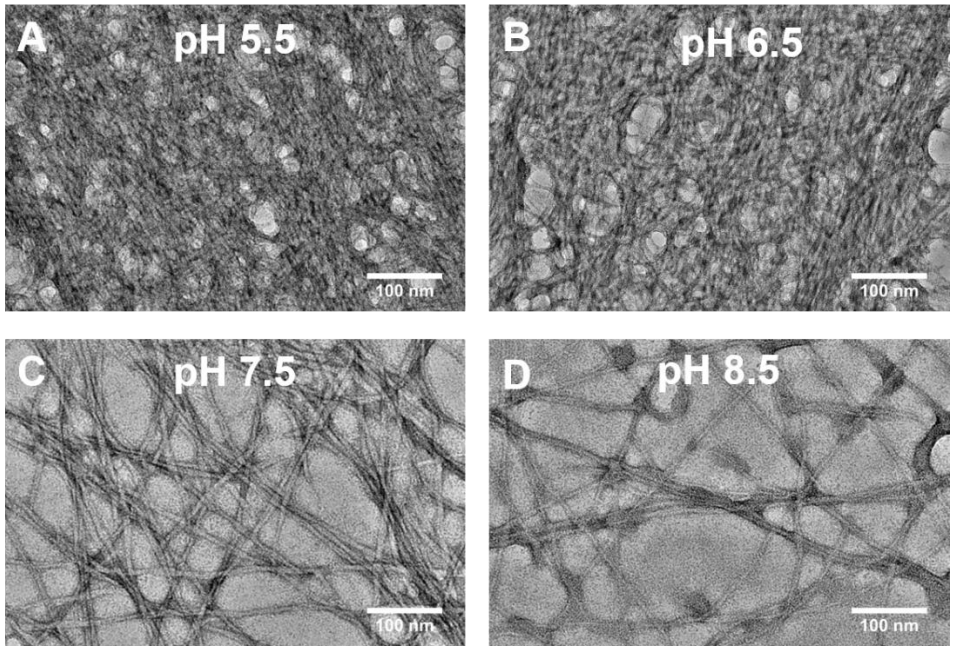

Figure 5.4. Alkaline-triggered macroscopic nanostructure transition of PDA-Pep at pH **(A)** 5.5, **(B)** 6.5, **(C)** 7.5, **(D)** 8.5. PDA-Pep concentration: 10 mg/mL

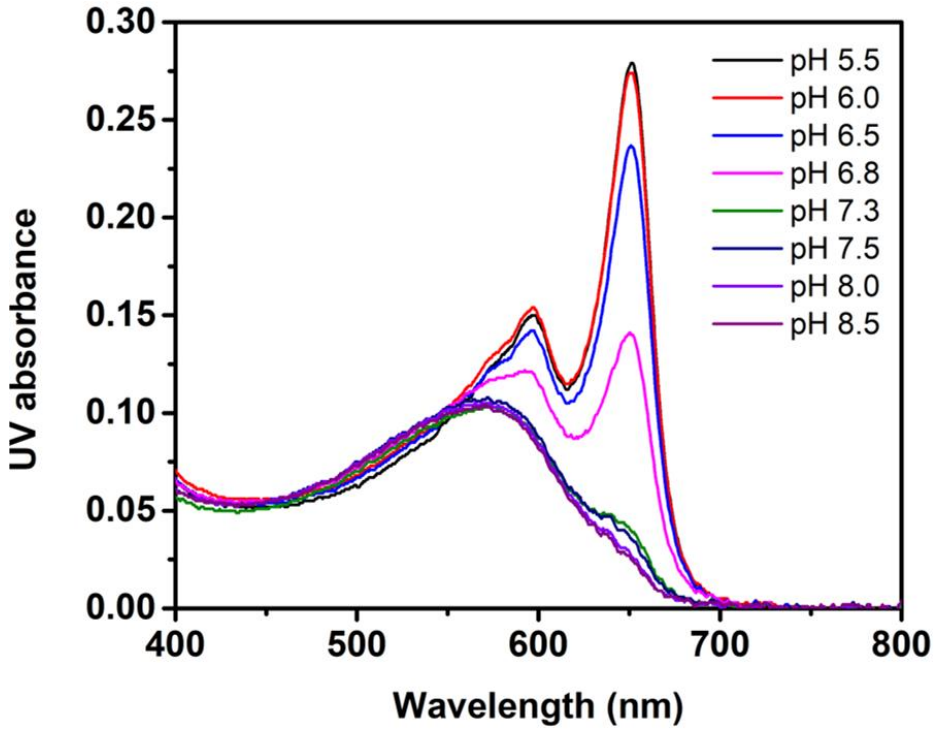

Figure 5.5. UV-vis spectra of PDA-Pep at different pHs. PDA-pep concentration: 100 μM

To gain deeper insights into the molecular mechanism for the gel-to-sol transition and in particular colorimetric transition of PDA-Pep, we performed circular dichroism (CD) spectroscopic measurement, which provides information about molecular conformation of both peptides and PDA at different pH values. There are two distinct chiral absorption regions on the CD spectrum. As shown in **Figure 5.6**, in the far UV region (200 nm to 280 nm), a peak shift was observed from 214 nm to ~200 nm as the solution became basic. The result suggests that the peptide moiety adopted a predominant β-sheet structure under the acidic condition and unfolded to a random coil at a neutral or alkaline condition. Notably, the peptide alone without DA conjugation formed a random coil structure across all pH ranges (**Figure 5.7**) and TEM did not reveal defined structures (**Figure 5.8**). These results suggest the important role of the DA in promoting the molecular and supramolecular packing of DA-Pep to form supramolecular nanofibers in which the peptides form an ordered molecular secondary structure through

intermolecular hydrogen bonding. In the middle and near UV region (280 nm to 400 nm), a strong chiral absorption was observed under the acidic condition (**Figure 5.6**). It has been reported that macromolecular self-assembly could facilitate supramolecular chirality transfer from the chiral groups to an achiral moiety [30,31]. For the PDA-Pep, the Cotton effect shown between 300 nm to 380 nm is presumably attributed to such chirality transfer from the peptide domain to the PDA that are both organized within the supramolecular nanofiber. The chiral absorption wavelengths on the CD spectrum match well with UV-vis absorption of the PDA moiety (**Figure 5.5**), further confirming the supramolecular chiral packing of the PDA upon self-assembly. As pH increases, the Cotton effect in the near UV region was diminished, suggesting a change of molecular conformation, and packing of the PDA domain. As discussed above, this conformation change is likely caused by the electrostatic repulsion among peptides that are deprotonated upon pH increase. The electrostatic repulsion disrupts ideal hydrophobic and π-π interactions within the PDA domain, and eventually drives a conformational change of PDA as charges continue to build up on the peptides, yielding a red-shifted, less conjugated PDA chromophore.

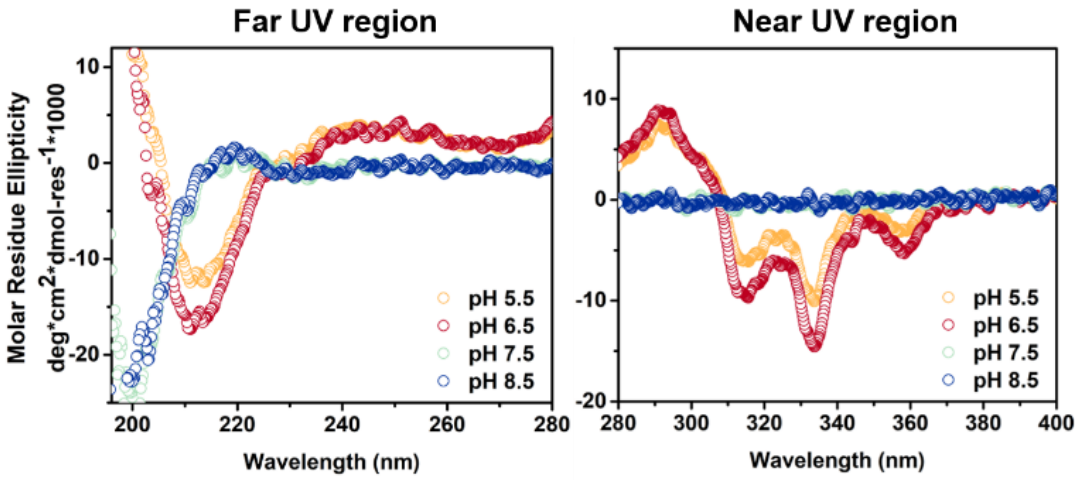

Figure 5.6. CD spectra of PDA-Pep at different pH values. The far UV region (left) shows the secondary structure of the peptide domain and the middle and near UV region (right) shows the chiral absorption of the PDA domain. PDA-Pep concentration: 10 mg/mL.

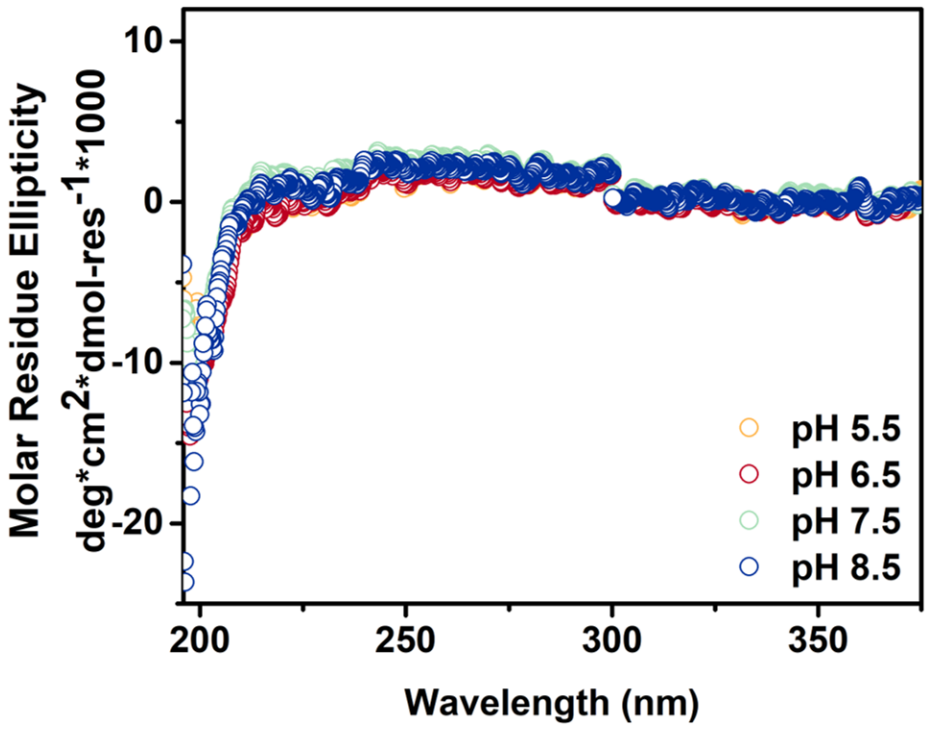

Figure 5.7. CD spectroscopy of GQFEG$_3$LPRDA at various pHs. Peptide concentration: 100 µM

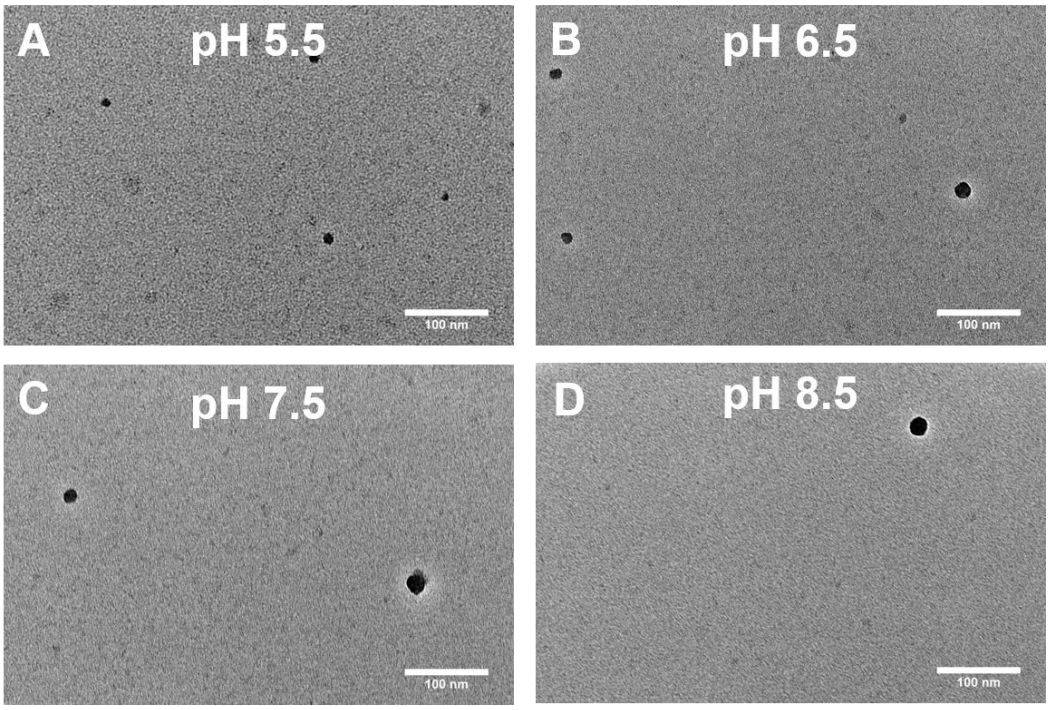

Figure 5.8. TEM images of GQFEG$_3$LPRDA at pH **(A)** 5.5, **(B)** 6.5, **(C)** 7.5, and **(D)** 8.5. Peptide concentration: 10 mg/mL

Antimicrobial agents, such as vancomycin or synthetic AMPs can be readily encapsulated in PDA-Pep hydrogels and released upon gel-to-sol transition to achieve controlled antimicrobial release. Notably, we used a custom-designed cationic AMP with the sequence of $K_8(QF)_6K_8$ in which the subscript indicates the number of the repeating units for lysine and the binary QF motif. MES buffer (pH 5.5) containing vancomycin or AMP was used to dissolve DA-Pep powder. Gelation immediately occurred and was subject to UV polymerization to form PDA-Pep hydrogels that appeared blue. We monitored the release of vancomycin and AMPs from the hydrogels to the aqueous buffer which was placed on top of the gels over time. As shown in **Figure 5.9**, upon treatment with alkaline solutions at pH 8.5, PDA-Pep (Van) and PDA-Pep (AMP) showed a time-dependent release profile with nearly 100% of antimicrobials released over a 4 h incubation period. At pH 5.5, less than 10% of antimicrobial agents were released from gels. The results suggest the great potential of these PDA-Pep hydrogels as smart antimicrobial materials capable of on-demand antimicrobial release upon an increase of local microenvironment pH.

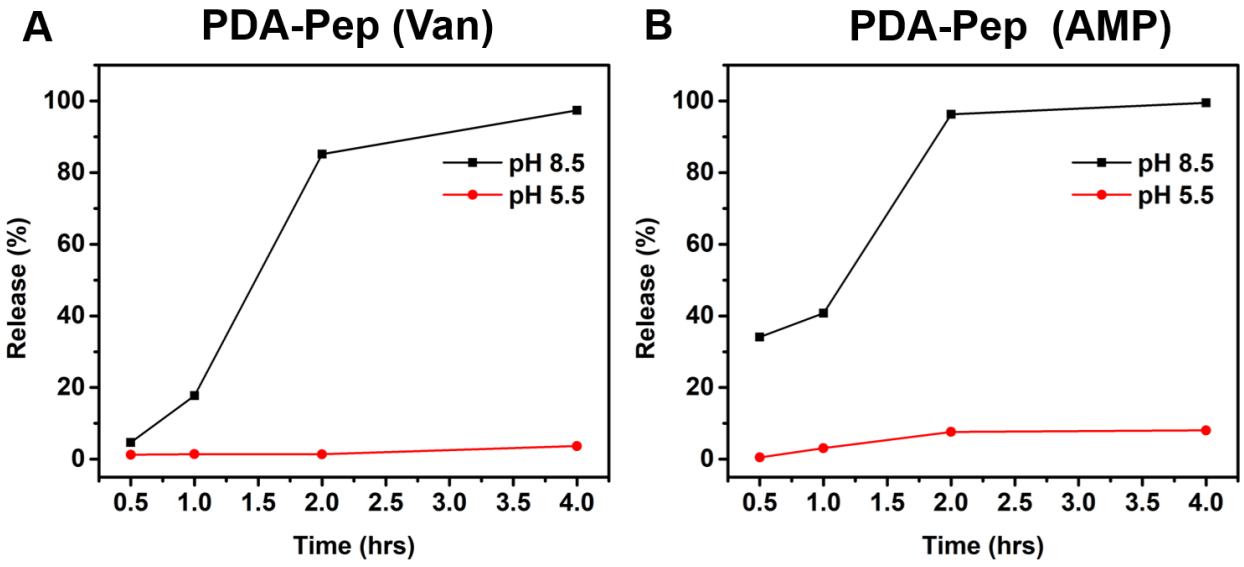

Figure 5.9. Time-dependent release profile of **(A)** PDA-Pep (Van) and **(B)** PDA-Pep (AMP) at pH 5.5 and 8.5. PDA-Pep concentration: 10 mg/mL. Van concentration: 100 µM. AMP concentration: 100 µM.

5.2.3 Evaluation of Alkaline-triggered Antimicrobial Activity

The ability of PDA-Pep to undergo on-demand, alkaline-triggered antimicrobial delivery to kill or inhibit the growth of bacteria was further evaluated. Methicillin-resistant staphylococcus aureus (*MRSA*) was selected for bacterial killing assay study. *MRSA* has a high expression of sortase receptors on its bacterial cell membrane. [32] Therefore, we added an additional oligopeptide ligand (with the sequence of LPRDA) that can recognize the sortase receptors on *MRSA*. [33] A general experimental set-up for the antimicrobial assay is shown in **Figure 5.10A**. MES buffer (pH 5.5) containing vancomycin or AMP was used to dissolve DA-Pep powder to form hydrogels. The gels were subject to UV polymerization to form PDA-Pep hydrogels that appeared in blue color (**step 1**). The gels were prepared with a final concentration of 10 mg/mL and used for all the following studies. *MRSA* culture at varying pH values was loaded on top of the PDA-Pep gels (**step 2**). Visual inspection of the color change was followed during the incubation time (**step 3**) and bacterial killing efficiency was determined through plate counting at the end of 4 h of incubation period (**step 4**). **Figure 5.10B** and **5.10C** shows the optical images of vancomycin-encapsulated PDA-Pep gels, denoted as PDA-Pep (Van) and AMP encapsulated PDA-Pep denoted as PDA-Pep (AMP) incubated with acidic or alkaline bacterial culture at 5 min and 4 h time point. It was found that PDA-Pep (Van) and PDA-Pep (AMP) hydrogels incubated with an acidic bacterial culture maintained the original blue color after 4 h of incubation. On the contrary, the PDA-Pep (Van) and PDA-Pep (AMP) hydrogels exhibited a blue-to-violet colorimetric transition upon incubation with bacterial cultures at pH 7.5 and further changed to purple at pH 8.5. As shown earlier, the pH-dependent colorimetric transition occurs synergistically with a gel-to-sol phase transition which provides an opportunity for on-demand delivery of antimicrobials at the site of bacterial infection under the alkaline conditions. Bacterial killing efficiency of PDA-Pep

(Van) and PDA-Pep (AMP) hydrogels against *MRSA* at different pH values was determined by plate counting of the viable bacteria that remained in the culture. Based on the plate counting results, PDA-Pep (Van) exhibited potent antimicrobial activity towards *MRSA* at pH 7.5 and 8.5 with ~ 70% and ~ 99% bacterial killing efficiency, respectively (**Figure 5.10D**). In contrast, the antimicrobial activity of PDA-Pep (Van) was much lower against the acidic bacterial culture, with a killing efficiency at ~20% and ~25% at pH 5.5 and pH 6.5, respectively. A similar trend of pH-dependent antimicrobial activity against *MRSA* was observed for PDA-Pep (AMP) (**Figure 5.10E**). PDA-Pep (AMP) showed the highest killing efficiency at ~ 90% against *MRSA* at pH 8.5 while it exhibited a moderate to weak antimicrobial activity at a neutral or acidic culture.

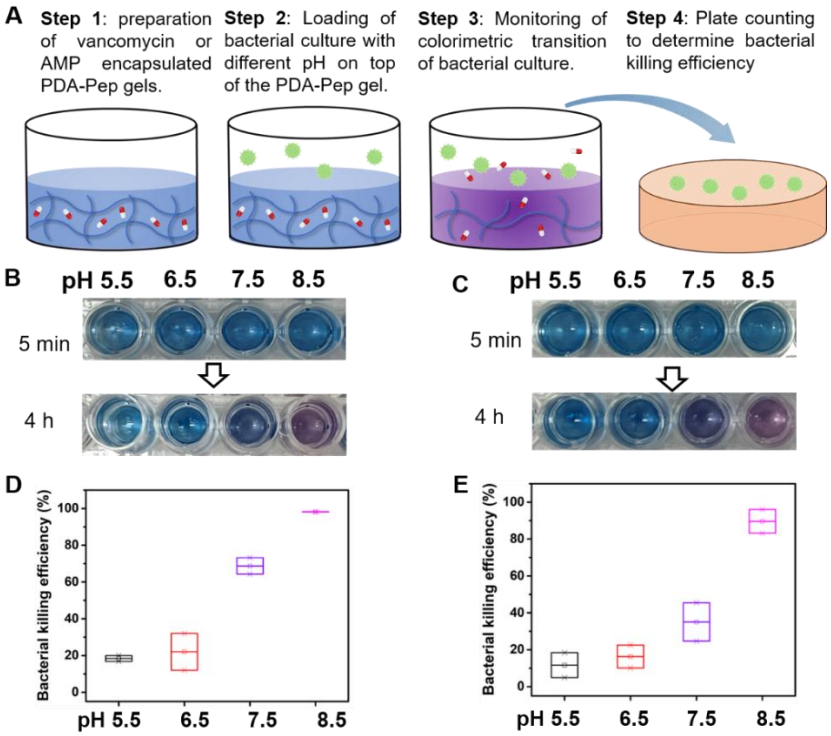

Figure 5.10. (A) Experimental setup for the evaluation of alkaline-triggered antimicrobial release and their killing efficiency. Colorimetric transition of **(B)** PDA-Pep (Van) and **(C)** PDA-Pep (AMP) upon incubation with bacterial culture at different pH (acidic versus basic). Bacterial killing efficiency of **(D)** PDA-Pep (Van) and **(E)** PDA-Pep (AMP) at different pH (acidic versus basic). PDA-Pep concentration: 10 mg/mL. The concentration of vancomycin and AMP encapsulated in the gel are 10 μM and 20 μM, respectively.

Fluorescence live/dead assay was performed to further confirm alkaline-triggered antibacterial activity. Bacteria were seeded on a glass slide overnight followed by deposition of hydrogels on top of the bacterial colonies. Upon incubation for 4 hrs, bacteria were stained with live/dead assay kit for fluorescence imaging. Live bacteria show green fluorescence and dead bacteria exhibit red fluorescence. As shown in **Figure 5.11**, PDA-Pep alone did not exhibit antimicrobial activity against *MRSA* at all pH conditions. PDA-Pep (Van) and PDA-Pep (AMP) exhibited pH-dependent antimicrobial activity with predominant dead bacteria shown in red under the alkaline condition. While most bacteria were viable in the acidic culture, the majority of bacteria were killed in the alkaline culture upon hydrogel treatment.

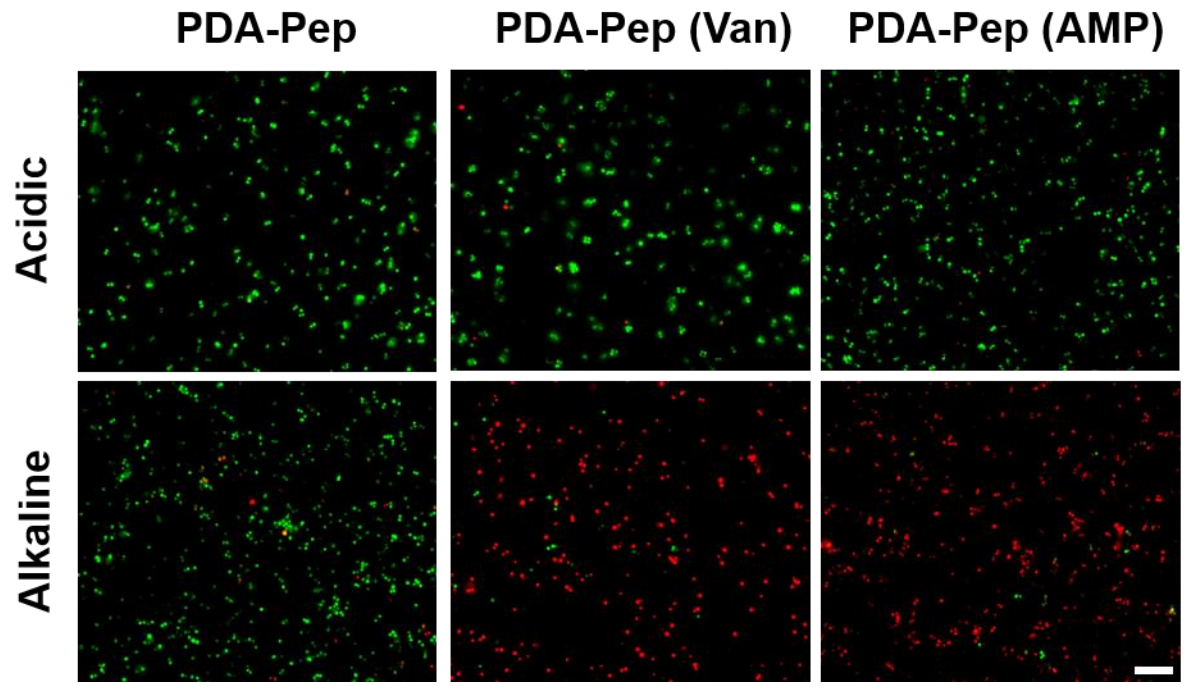

Figure 5.11. Fluorescence live/dead assay images of *MRSA* treated with PDA-Pep, PDA-Pep (Van) and PDA-Pep (AMP) at the acidic condition (pH 5.5) and alkaline condition (pH 8.5). PDA-Pep concentration: 10 mg/mL. The concentration of vancomycin and AMP encapsulated in the gel are 10 μM and 20 μM, respectively. Scale bar: 20 μm.

5.2.4 Investigation of Hemocompatibility

The hemocompatibility of PDA-Pep with and without antimicrobials was also evaluated. PDA-Pep, PDA-Pep (Van) and PDA-Pep (AMP) hydrogels prepared at 1 wt% were incubated with human red blood cells (HRBCs) at three different pH for 4 hrs and the released hemoglobin was quantified by UV-Vis spectroscopy. As shown in **Figure 5.12**, all gels under all pH conditions demonstrated good hemocompatibility with less than 10 % of hemolysis using Triton-100 as the positive control. Taken together, the alkaline-triggered antimicrobial activity, good hemocompatibility along with sensitive colorimetric transition of these PDA-Pep hydrogels highlight their great potential as new theranostic materials for real-time monitoring and on-demand treatment of bacterial infections with an alkaline bacterial microenvironment.

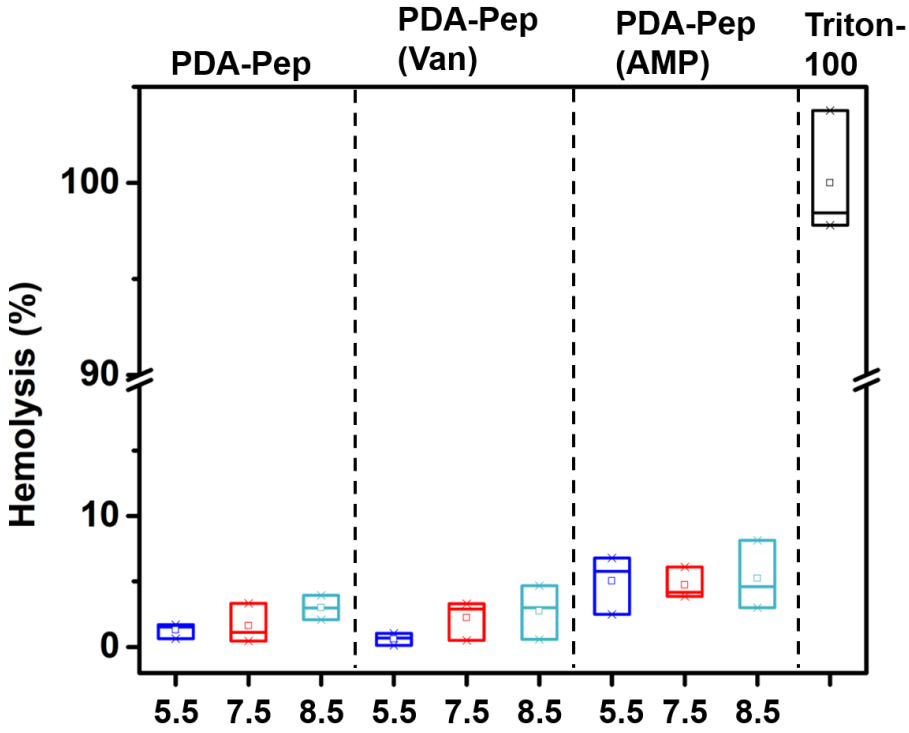

Figure 5.12. Hemocompatibility assay of DA-Pep, DA-Pep (Van), DA-Pep (AMP) at various pHs. PDA-Pep concentration: 10 mg/mL, Van concentration: 10 μM, AMP concentration: 20 μM

5.2.5 Evaluation of Translational Potential on Inoculated Pig Skins

As a preliminary effort to assess the translational potential of the PDA-Pep hydrogels, we tested the antimicrobial activity and colorimetric response of the gels toward bacteria that are cultured under different pH conditions and later inoculated on pig skins. PDA-Pep (Van) hydrogels were applied on top of the inoculation sites and incubated at 37 °C for qualitative, real-time monitoring of the color change of gels and bacterial killing efficiency. As shown in **Figure 5.13A**, gels that are deposited on acidic bacteria at pH 5.5 and 6.5 largely remained blue within the 2 hrs testing time window. A blue-to-purple colorimetric transition was observed for gels in contact with bacteria at increased pH values. Based on the visual inspection, such transition occurred in ~ 1 hr at a pH of 7.5 and less than 0.5 h at a pH of 8.5. The residual bacteria on the pig skins were thoroughly washed off into culture media which were then subject to a serial dilution for plate counting of the viable *MRSA* bacteria upon hydrogel treatment at different pH conditions. Bacterial killing efficiency was calculated as the ratio of the CFU of bacteria treated with PDA-Pep (Van) to that of PDA-Pep hydrogels without antibiotics. As shown in **Figure 5.13B**, a substantially higher bacterial killing efficiency (73.71%) was observed for gels at a pH of 8.5 followed by 63.90% at pH 7.5 while gels in the acidic condition have minimal antimicrobial activity with 1.21% (pH 5.5) and 4.50% (pH 6.5) killing efficiency. Taken together, the PDA-Pep (Van) hydrogels showed potent alkaline-triggered antimicrobial activity, easy-to-read colorimetric transition and good hemocompatibility. These properties highlight their great potential as theranostic materials for real-time monitoring and on-demand treatment of bacterial infections with increased alkalinity.

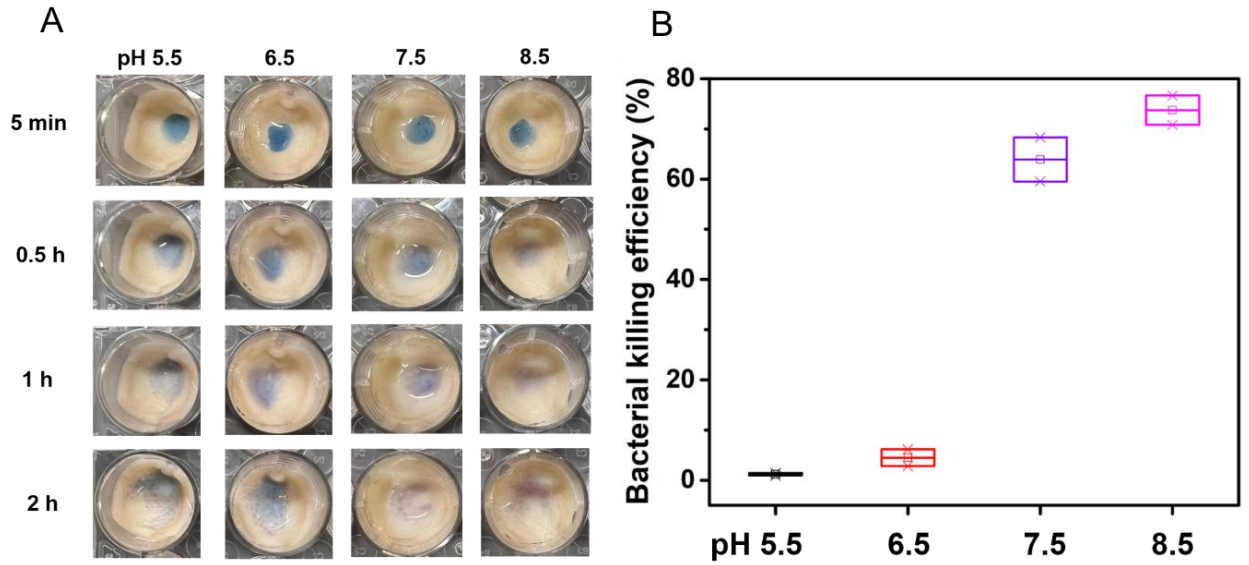

Figure 5.13. (A) Real-time monitoring of the colorimetric transition of the PDA-Pep (Van) hydrogel that are applied on top of the inoculated bacteria on pig skins. **(B)** Bacterial killing efficiency of PDA-Pep (Van) hydrogels at different pH conditions toward inoculated bacteria on pig skins. PDA-Pep concentration: 10 mg/mL. The concentration of vancomycin encapsulated in the gel is 10 μM.

5.3 Conclusions

In summary, we demonstrated the design, synthesis and alkalinity-induced antimicrobial activity of PDA-Pep hydrogels. The increase of the local bacterial pH triggers a conformational change of the PDA domain leading to a blue-to-purple colorimetric transition. Simultaneously, a gel-to-sol phase transition occurs causing the release of antibiotics or antimicrobial peptides into the site of infection. It should be noted that although PDA-Pep has been studied, it is the first time that they were explored as functional antimicrobial hydrogels which is capable of real-time monitoring the local alkaline pH change in bacterial cultures. The work shown here represents our initial efforts in building this material framework. Future studies are focused on the application of these materials toward infection treatment associated with an alkaline bacterial microenvironment, for example diseases involving chronic wound infections and others.

5.4 Experimental Section

Materials. Fmoc-protected amino acids, *N,N,N′,N′*-Tetramethyl-*O*-(1*H*-benzotriazol-1-yl) uronium hexafluorophosphate (HBTU), and MBHA rink amide resin, piperidine, diisopropylethylamine (DIPEA), Tetrakis(triphenylphosphine)palladium, triethyl amine, copper(I) iodide, dimethylformamide, copper(II) acetate hydrate, pyridine, Mueller Hinton Broth (MHB), and Agar were purchased from Sigma-Aldrich. Reagents and solvents for peptide synthesis and purification including dimethyl formamide (DMF), acetonitrile (ACN), trifluoroacetic acid (TFA), triisopropylsilane (TIS), vancomycin, live/dead bacterial viability kit were purchased from Fisher Scientific. TEM staining reagent, uranium acetate dihydrate and TEM grid were purchased from TED PELLA, INC. Trimethylsilylacetylene, 4-Bromobenzoate, potassium carbonate, sodium hydroxide, tetrahydrofuran, and ethanol were purchased from Alfa Aesar. Methicillin-resistant *staphylococcus aureus* (ATCC 33592) was purchased from ATCC. Pig skins were purchased from supermarket.

NMR spectroscopy. ^{1}H NMRs were recorded on 500 MHz spectrometers and referenced to the internal solvents (7.26 ppm in $CDCl_3$ or 2.5 ppm DMSO-d_6). ^{13}C ^{34} NMRs were recorded on 125 MHz spectrometers and referenced to the internal solvent signals (central peak 77.00 ppm $CDCl_3$ or 39.5 DMSO-d_6). NMR data are reported as: chemical shift (in ppm, δ), integration, multiplicity (s = singlet, d = doublet, t = triplet, q = quartet, m = multiplet, br = broad), coupling constant (in Hz, J).

Diphenyldiacetylene linker (DA) synthesis. DA linker (**6**) was synthesized as depicted in **Scheme 1**. Sonogashira cross coupling was carried out between ethyl 4-bromobezoate and trimethylsilylacetylene to acquired 67% of compound **3**. Deprotection of trimethylsilyl group (TMS) was performed with K_2CO_3 with ethanol as solvent to get product (**4**) with 62% yield.

Glaser coupling enabled the diacetylene functional group of DA linker. Copper acetate monohydrate $Cu(OAc)_2 \cdot H_2O$ was used to get diacetylene compound (**5**) as 80% yield. Hydrolysis of esters were accomplished with NaOH using mixture of solvents to get final product as off-white solid with 73% yield (**6**).

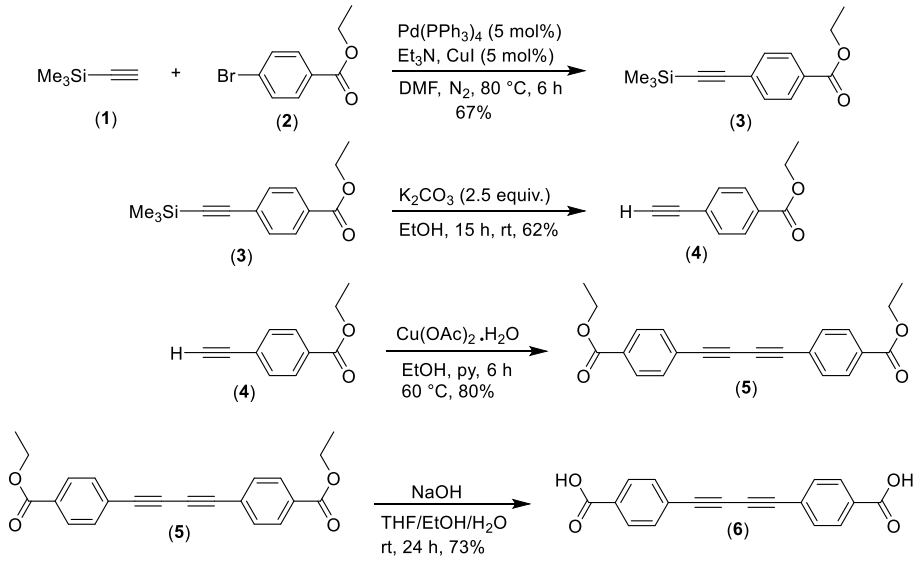

Scheme 1. Synthetic routs for the synthesis of diphenyldiacetylene linker

Synthesis of Ethyl 4-((trimethylsilyl)ethynyl)benzoate (3)[1]. In an oven dried round bottom flask (RBF), 15 mL of anhydrous DMF and 8.0 mL of triethylamine were put together and nitrogen was bubbled through it for 30 min. Then, 5 mol% of $Pd(PPh_3)_4$ and CuI were added in the purged solvent followed by the addition of reagent 0.37 mL (2.6 mmol) of **1** and 0.5 g (2.2 mmol) of **2**. The mixture was heated to 80 ˚C for 6 h. The solvent was concentrated on rotary evaporation and oily mixture was taken up in 50 mL of ethyl acetate. The organic layer was washed three times with NH_4Cl, brine and water and dried over anhydrous $MgSO_4$. Organic layer was evaporated, and flash chromatography was performed with 5% EtOAc in hexane to get pure product. 0.3 g yellow oily product was obtained with 67% yield. ^{1}H NMR (500 MHz, CHLOROFORM-*D*) δ 7.98 – 7.93 (m, 2H), 7.52 – 7.47 (m, 2H), 4.35 (q, *J* = 7.1 Hz, 2H), 1.37 (t, *J* = 7.1 Hz, 3H), 0.25 (s, 9H). ^{13}C

NMR (126 MHz, CHLOROFORM-*D*) δ 166.2, 131.9, 130.1, 129.4, 127.7, 104.2, 97.6, 61.2, 14.4, -0.08.

Synthesis of Ethyl 4-ethynylbenzoate (4)[1]. In a RBF 0.1 g (0.4 mmol) of **3** was dissolved in anhydrous ethanol, 0.17 g of (1.2 mmol; 3 equiv.) of K_2CO_3 were added in the solution and the mixture was stirred for 18 h at room temperature under nitrogen environment. It was filtered off and solvent was evaporated in vacuo. The residues were taken up into 40 mL of 1:1 ethyl acetate and 1 M HCl solution. The organic layer was separated and washed with brine and DI water twice before rotary evaporated to get yellow precipitates. Flash chromatography was performed with 2% EtOAc in hexane to get 44 mg of product with 62% yield. The product was yellow solid. ^{1}H NMR (500 MHz, CHLOROFORM-*D*) δ 8.03 – 7.96 (m, 2H), 7.58 – 7.51 (m, 2H), 4.37 (q, *J* = 7.1 Hz, 2H), 3.23 (s, 1H), 1.39 (t, *J* = 7.1 Hz, 3H). ^{13}C NMR (126 MHz, CHLOROFORM-*D*) δ 165.8, 131.9, 130.4, 129.3, 126.5, 82.7, 79.8, 61.1, 14.2.

Synthesis of Diethyl 4,4'-(buta-1,3-diyne-1,4-diyl)dibenzoate (5)[2]. 1.0 g (5.8 mmol) of compound **4** was added into the RBF equipped with stirrer bar containing solution of 2 g (10 mmol) copper acetate monohydrate ($Cu(OAc)_2.H_2O$) in 10 mL methanol and pyridine solvents (1:1). The reaction mixture was stirred for 6 h at 60 °C. The mixture was brought to room temperature followed by addition of 50 mL ice cold water in it. Solid precipitation was observed and filtered off. The precipitated were collected after filtration and were washed many times with water. The solid was suspended in hexane and filtered off, it was washed multiple times with hexane to get rid of impurities and let it air dry overnight. The obtained product was off white solid 1.6 g as 80% yield. ^{1}H NMR (500 MHz, CHLOROFORM-*D*) δ 8.02 (dt, *J* = 7.8, 0.9 Hz, 4H), 7.61 – 7.50 (m, 4H), 4.39 (qd, *J* = 7.2, 0.9 Hz, 4H), 1.40 (td, *J* = 7.2, 0.9 Hz, 6H). ^{13}C NMR (126 MHz, CHLOROFORM-*D*) δ 165.9, 132.6, 131.1, 129.7, 126.1, 82.0, 76.3, 61.5, 14.4.

Synthesis of 4,4'-(buta-1,3-diyne-1,4-diyl)dibenzoic acid (6)[2]. In a 250 mL RBF 0.80 g (20 mmol) of NaOH were dissolved in solvent system THF/EtOH/H_2O (25/25/25 mL) solvent system followed by 0.85 g (2.5 mmol) of **5** was added. The mixture was stirred for 24 h, the solvent was evaporated in vacuo. The solid obtained was dissolved in 50 mL water and the pH was brought to 2 with 1 M HCl. Solid was filtered and washed with water; it was set to air dry overnight on a running high vacuum. 0.52 g of final product was collected as white solid with 73% yield. ^{1}H NMR (500 MHz, DMSO-D_6) δ 7.97 (d, J = 8.0 Hz, 4H), 7.75 (d, J = 8.0 Hz, 4H). Due to insufficient solubility of product in DMSO the Carbon NMR was not practicable, addition of few drops of base (DIPEA) solubilize the compound.

NMR with DIPEA: ^{1}H NMR (500 MHz, DMSO-D_6) δ 7.88 (d, J = 7.9 Hz, 4H), 7.54 (d, J = 7.9 Hz, 4H). ^{13}C NMR (126 MHz, DMSO-D_6) δ 168.5, 140.7, 131.9, 129.6, 121.2, 82.6, 74.4.

Synthesis and purification of peptides. Peptides were synthesized on a *Prelude*® peptide synthesizer using standard Fmoc-solid phase peptide synthesis procedures. Fmoc groups were deprotected in 20% (V/V) piperidine in DMF for 5 min and repeated 2 times. HBTU was used as the coupling reagent and reacted with Fmoc-protected amino acids in the presence of DIPEA with a molar ratio of 1:1:2 (amino acid: HBTU: DIPEA). After final Fmoc-deprotection of the peptide, the resin was transferred into rotary reaction vessel. The coupling reaction of peptide resin with DA linker was carried out in the presence of DA linker, HBTU, DIPEA with a molar ratio of 1:2:4 with respect to the number of amino groups on resin in DMF. The reaction mixture was rotated for 48 h. The completion of the coupling reaction was confirmed by the Kaiser test. A mixture of TFA/TIS/H_2O (95/2.5/2.5 by volume) was used to cleavage the peptide from resin for 3 h. The cleavage solution was filtered, and filtrates were collected. The resin was washed three times with neat TFA, and all filtrate solutions were combined and evaporated under airflow. The residual

peptide solution was precipitated in cold diethyl ether, followed by centrifugation and washing with cold diethyl ether for three times. The crude peptide was dried under vacuum overnight for HPLC purification. The peptide was purified using a semi-preparative reversed phase C4 column with a linear gradient of water/acetonitrile (5% to 95% of acetonitrile in 30 mins) containing 0.05% TFA. Elution was monitored at 230 nm and 280 nm. The molecular mass was confirmed by electrospray ionization mass spectrometry. Calculated mass $[M+2H]^{2+}$ for DA-Pep (peptide sequence: GQFQFEGGGLPRDA): 1605.10 and experimental mass $[M+2H]^{2+}$: 1605.40. Calculated mass $[M+2H]^{2+}$ for DA-Pep (peptide sequence: GQFEGGGLPRDA): 1329.30 and experimental mass $[M+2H]^{2+}$: 1329.55. Calculated mass $[M+2H]^{2+}$ for DA-Pep (peptide sequence: GSFEGGGLPRDA): 1288.24 and experimental mass $[M+2H]^{2+}$: 1288.80. Calculated mass $[M+2H]^{2+}$ for DA-Pep (peptide sequence: GQIEGGGLPRDA): 1295.28 and experimental mass $[M+2H]^{2+}$: 1295.50. Calculated mass $[M+2H]^{2+}$ for peptide without DA (peptide sequence: GQFEGGGLPRDA): 622.17 and experimental mass $[M+2H]^{2+}$: 622.38. Calculated mass $[M+3H]^{3+}$for $K_8(QF)_6K_8$: 1254.00 and experimental mass $[M+3H]^{3+}$: 1255.00.

UV-Vis spectroscopy. UV-Vis spectroscopy was performed on a Thermo Scientific NanoDrop. The PDA-Pep hydrogel was prepared dissolving lyophilized powder directly in MES buffer (pH 5.5) to reach a final concentration at 10 mg/mL. The hydrogel was polymerized to form PDA-Pep through UV irradiation with a hand-held UV lamp (254 nm, 6 watt) for 1 hr with a distance of approximately 1 cm. Samples for UV-vis analysis were prepared by dilution of the stock PDA-Pep hydrogel (10 mg/mL) to a concentration at 150 μM in various Britton–Robinson buffer (20 mM) with pH of 5.5, 6.0, 6.5, 6.8, 7.3, 7.5, 8.0 and 8.5. The UV-Vis spectra were collected from 400-800 nm at room temperature (RT) using a 1 mm cuvette. The absorbance ratio of A_{566}/A_{652} was fitted into the sigmoidal Boltzmann equation implemented in OriginPro 9.0.

Preparation of PDA-Pep hydrogels. The DA-Pep hydrogel was first prepared by dissolving lyophilized powder directly in MES buffer (pH 5.5) to reach a final concentration at 10 mg/mL. The hydrogel was polymerized to form PDA-Pep through UV irradiation with a hand-held UV lamp (254 nm, 6 watt) for 1 hr with a distance of approximately 1 cm. PDA-Pep (Van) hydrogels were prepared with the same procedure but using MES buffer (pH 5.5) containing pre-dissolved vancomycin at 10 μM. PDA-Pep (AMP) PDA-Pep (AMP) hydrogels were prepared with the same procedure but using MES buffer (pH 5.5) containing pre-dissolved AMP at 20 μM.

UV-Vis spectroscopy. UV-Vis spectroscopy was performed on a Thermo Scientific NanoDrop. The PDA-pep hydrogel was prepared in MES buffer (pH 5.5) with a final concentration of 10mg/mL. The DA-pep hydrogel was polymerized upon UV irradiation for 1h to form PDA-pep hydrogel. The samples were prepared by dilution of the PDA-pep hydrogel to a concentration at 150 μM in various Britton–Robinson buffer (20mM) with pH of 5.5, 6.0, 6.5, 6.8, 7.3, 7.5, 8.0 and 8.5. The UV-Vis spectra were collected from 400-800 nm at room temperature (RT) using a 1 mm cuvette. The absorbance ratio data of A_{566}/A_{652} was fitted by the sigmoidal Boltzmann equation implemented in OriginPro 9.0.

Circular dichroism (CD) spectroscopy. CD spectroscopy was performed on a Jasco 710 CD spectrometer. The preparation of PDA-pep hydrogel was same with procedures in UV-Vis spectroscopy. The CD samples were prepared by dilution of the PDA-pep hydrogel to a concentration at 100 μM in various Britton–Robinson buffer buffer (20mM) with pH of 5.5, 6.5, 7.5, and 8.5. The CD spectra were collected from 400 nm to 190 nm at room temperature (RT) using a 1 mm cuvette, a bandwidth at 0.1 nm, scan rate at 100 nm/min and a response time of 2 sec. Each spectrum was averaged from three scans. The mDeg of rotation was converted to molar residual ellipticity via the formula $\theta = \frac{1000 \times mDeg}{c * n * l}$ where c is the concentration of the PDA-pep

solution expressed in μM, n is the number of amino acids in the PDA-pep sequence and l is the path length of the cell used in the unit of millimeter.

Transmission electron microscopy (TEM). PDA-pep hydrogels were prepared in MES buffer (pH 5.5, 6.5, 7.5, and 8.5) with a final concentration of 10mg/mL (1% wt). 10 μL of PDA-pep sample was pipetted onto a lacey carbon grid (TED PELLA 01824). After 1 min, excess solution was carefully removed with filter paper. 10 μL of 2 wt % uranyl acetate aqueous solution was pipetted onto the grid for negative staining. After 1 min, excess staining solution was removed and the TEM samples were dried for overnight before imaging on a Hitachi H-9500 high-resolution TEM.

Bacterial killing efficiency in culture. *MRSA* was cultured in MHB media under constant shaking at 100 rpm at 37 ºC to reach the mid-exponential growth phase. The bacterial solution was plated on an agar plate for colony forming unit (CFU) counting. Bacterial suspensions were diluted to approximately $1x10^5$ CFU/mL in various MHB media at pH 5.5, 6.5, 7.5, and 8.5. PDA-Pep, PDA-Pep (Van) and PDA-Pep (AMP) hydrogels were prepared in MES buffer (pH 5.5) by UV irradiation with a concentration of 10 mg/mL. 50 μL of bacterial suspensions at different pHs were loaded on top of the hydrogels (50 μL) and each sample was prepared in duplicates. Upon 4 h of incubation, both the gels and bacterial suspensions were quickly transferred to a MHB medium followed by 10-fold serial dilution of for plating counting of viable bacteria. Bacterial killing efficiency was determined as the ratio of the viable bacteria in cultures treated with PDA-Pep (Van) or PDA-Pep (AMP) gels to that of the PDA-Pep gel group.

Live and dead bacterial assay. 400 μL of bacterial suspensions (*MRSA*, 10^8 CFU/mL) was added to a confocal dish and incubated at 37 ºC for 24 hrs. Using pipette to remove bacterial suspensions and PBS buffers was used to wash away any non-adherent bacteria. PDA-pep, PDA-pep (Van)

and PDA-pep (AMP) hydrogel was prepared in MES buffer (pH 5.5) by UV irradiation with a concentration of 10mg/mL (1% wt). 50 μL of MHB medium at pH 5.5 or 8.5 was added in the confocal dish followed by the addition of 50 μL of either PDA-pep, PDA-pep (Van) or PDA-pep (AMP). After incubation at 37 ºC for 4 hrs, PDA-pep and MHB medium was removed and washed extensively with PBS buffers for three times. Bacteria were stained with the live/dead bacteria assay kit solution at 37 ºC for 15 min. Finally, bacteria were washed with PBS buffer for three times. Images were captured with epifluorescence (ECHO REVOLVE) and processed with ImageJ software.

pH-dependent kinetic release. PDA-pep (100 μM Van) and PDA-pep (100 μM AMP) hydrogels were prepared in MES buffer (pH 5.5) by UV irradiation with a concentration of 10mg/mL (1% wt). 50 μL of MES buffer (20 mM, pH 5.5) or Tris buffer (20 mM, pH 8.5) was loaded on the top of 50 μL of either PDA-pep (Van) or PDA-pep (AMP) hydrogel in a 96-well plate and the experiments were performed in two replicates. After 4 h-incubation, 50 μL of the supernatant was taken out and injected onto the analytical C18 column. The area of the elution peaks of Van or AMP corresponding to total amount and the released fraction were integrated and used to calculate the release%.

Hemolytic activity test. Human red blood cells (RBCs) were donated from a volunteer and 4% of human RBCs were prepared in PBS buffer (pH 5.5, 7.5, 8.5). PDA-pep, PDA-pep (Van) and PDA-pep (AMP) hydrogel was prepared in MES buffer (pH 5.5) by UV irradiation with a concentration of 10mg/mL (1% wt). 100 μL of 4% human RBCs was added on the top of 100 μL of either PDA-pep, PDA-pep (Van) or PDA-pep (AMP) hydrogel in a 1.5 mL Eppendorf tube. The mixtures were incubated at room temperature for 4 hr. 100 μL of the supernatant was taken out and transferred to a 96-well plate. Hemoglobin release was determined by measuring the absorbance of the

supernatant at 540 nm on a microplate reader (Vitor2 1420 Multilabel Counter, PerkinElmer). RBCs treated with 1% Triton-X served as positive controls and untreated RBCs served as a negative control group. Each sample was tested in three replicates. The percentage of hemolysis remained is calculated using the following equation

$$\%hemolysis = \frac{A_{PDA-Pep} - A_{untreated\ RBCs}}{A_{triton} - A_{untreated\ RBCs}} \times 100$$

Bacterial killing efficiency on pig skins. *MRSA* cultures were prepared in MHB media at pH 5.5, 6.5, 7.5, and 8.5. Pig skins were treated with 70% of ethanol solution before inoculation with the above bacteria suspensions (30 uL bacterial suspensions with $1x10^5$ CFU/mL). 30 μL of PDA-Pep and PDA-Pep (Van) hydrogels were applied on top of the inoculation sites and incubated at 37 °C for up to 2 h. Visual color changes were recorded at 5 min, 0.5 h, 1 hr, and 2 hrs showing alkalinity-responsive blue-to-purple color change. After 2 h, pig skins were thoroughly washed with MHB media and the solutions were collected and subject to serial dilution and plate counting. The killing efficiency was calculated as the ratio of the viable bacteria on pig skins treated with PDA-Pep (Van) gels to that of the PDA-Pep gel group. Each sample was prepared in duplicates.

5.5 References

(1) Li, L.-L.; Ma, H.-L.; Qi, G.-B.; Zhang, D.; Yu, F.; Hu, Z.; Wang, H. Pathological-condition-driven construction of supramolecular nanoassemblies for bacterial infection detection. *Adv. Mater.* **2016**, *28*, 254-262.

(2) Sikder, A.; Chaudhuri, A.; Mondal, S.; Singh, N. D. P. Recent advances on stimuli-responsive combination therapy against multidrug-resistant bacteria and biofilm. *ACS Appl. Bio Mater.* **2021**, *4*, 4667-4683.

(3) Wang, X.; Shan, M.; Zhang, S.; Chen, X.; Liu, W.; Chen, J.; Liu, X. Stimuli-responsive antibacterial materials: molecular structures, design principles, and biomedical applications. *Adv. Sci.* **2022**, *9*, 2104843.

(4) Lin, Q.; Pilewski, J. M.; Di, Y. P. Acidic microenvironment determines antibiotic susceptibility and biofilm formation of *pseudomonas aeruginosa*. *Front. Microbiol.* **2021**, *12*.

(5) Vu, H.; Nair, A.; Tran, L.; Pal, S.; Senkowsky, J.; Hu, W.; Tang, L. A device to predict short-term healing outcome of chronic wounds. *Adv. Wound Care* **2019**, *9*, 312-324.

(6) Li, M.; Ning, Y.; Chen, J.; Duan, X.; Song, N.; Ding, D.; Su, X.; Yu, Z. Proline isomerization-regulated tumor microenvironment-adaptable self-assembly of peptides for enhanced therapeutic efficacy. *Nano Lett.* **2019**, *19*, 7965-7976.
(7) Radovic-Moreno, A. F.; Lu, T. K.; Puscasu, V. A.; Yoon, C. J.; Langer, R.; Farokhzad, O. C. Surface charge-switching polymeric nanoparticles for bacterial cell wall-targeted delivery of antibiotics. *ACS Nano.* **2012**, *6*, 4279-4287.
(8) Xiong, M.; Bao, Y.; Xu, X.; Wang, H.; Han, Z.; Wang, Z.; Liu, Y.; Huang, S.; Song, Z.; Chen, J.; Peek, R. M.; Yin, L.; Chen, L.-F.; Cheng, J. Selective killing of *Helicobacter pylori* with pH-responsive helix-coil conformation transitionable antimicrobial polypeptides. *Proc. Natl. Acad. Sci. U.S.A.* **2017**, *114*, 12675-12680.
(9) Kathawala, M. H.; Ng, W. L.; Liu, D.; Naing, M. W.; Yeong, W. Y.; Spiller, K. L.; Van Dyke, M.; Ng, K. W. Healing of chronic wounds: an update of recent developments and future possibilities. *Tissue Eng. Part B Rev.* **2019**, *25*, 429-444.
(10) Schneider, L. A.; Korber, A.; Grabbe, S.; Dissemond, J. Influence of pH on wound-healing: a new perspective for wound-therapy? *Arch. Dermatol. Res.* **2007**, *298*, 413-420.
(11) Itoyama, S.; Noda, E.; Takamatsu, S.; Kondo, J.; Kawaguchi, R.; Shimosaka, M.; Fukuoka, T.; Motooka, D.; Nakamura, S.; Tanemura, M. Enterococcus spp. have higher fitness for survival, in a pH-dependent manner, in pancreatic juice among duodenal bacterial flora. *JGH Open* **2022**, *6*, 85-90.
(12) Melamed, P.; Melamed, F. Chronic metabolic acidosis destroys pancreas. *J. Pancreas* **2014**, *15*, 552-560.
(13) Milo, S.; Thet, N. T.; Liu, D.; Nzakizwanayo, J.; Jones, B. V.; Jenkins, A. T. A. An in-situ infection detection sensor coating for urinary catheters. *Biosens. Bioelectron.* **2016**, *81*, 166-172.
(14) Hussain, S.; Deb, R.; Suklabaidya, S.; Bhattacharjee, D.; Arshad Hussain, S. Polydiacetylene a unique material to design biosensors. *Mater. Today: Proc.* **2022**.
(15) Kim, C.; Lee, K. Polydiacetylene (PDA) liposome-based immunosensor for the detection of exosomes. *Biomacromolecules* **2019**, *20*, 3392-3398.
(16) Kumar, A.; Sivagnanam, S.; Ghosh, S.; Das, P. Polydiacetylene (PDA) liposome-based colorimetric sensor for the detection of ATP in aqueous medium. *Mater. Today: Proc.* **2021**, *40*, S230-S235.
(17) Park, J.; Ku, S. K.; Seo, D.; Hur, K.; Jeon, H.; Shvartsman, D.; Seok, H.-K.; Mooney, D. J.; Lee, K. Label-free bacterial detection using polydiacetylene liposomes. *Chem. Commun.* **2016**, *52*, 10346-10349.
(18) Yapor, J. P.; Alharby, A.; Gentry-Weeks, C.; Reynolds, M. M.; Alam, A. K. M. M.; Li, Y. V. Polydiacetylene nanofiber composites as a colorimetric sensor responding to *escherichia coli* and pH. *ACS Omega* **2017**, *2*, 7334-7342.
(19) Zhou, J.; Duan, M.; Huang, D.; Shao, H.; Zhou, Y.; Fan, Y. Label-free visible colorimetric biosensor for detection of multiple pathogenic bacteria based on engineered polydiacetylene liposomes. *J. Colloid Interface Sci.* **2022**, *606*, 1684-1694.
(20) Ardoña, H. A. M.; Tovar, J. D. Peptide π-electron conjugates: organic electronics for biology? *Bioconjug. Chem.* **2015**, *26*, 2290-2302.
(21) Diegelmann, S. R.; Hartman, N.; Markovic, N.; Tovar, J. D. Synthesis and alignment of discrete polydiacetylene-peptide nanostructures. *J. Am. Chem. Soc.* **2012**, *134*, 2028-2031.
(22) Hsu, L.; Cvetanovich, G. L.; Stupp, S. I. Peptide amphiphile nanofibers with conjugated polydiacetylene backbones in their core. *J. Am. Chem. Soc.* **2008**, *130*, 3892-3899.

(23) Jaworski, J.; Yokoyama, K.; Zueger, C.; Chung, W.-J.; Lee, S.-W.; Majumdar, A. Polydiacetylene incorporated with peptide receptors for the detection of trinitrotoluene explosives. *Langmuir* **2011**, *27*, 3180-3187.
(24) Tran, N.; Shiveshwarkar, P.; Jaworski, J. Peptide linked diacetylene amphiphiles for detection of epitope specific antibodies. *Chemosensors* **2022**, *10*, 62.
(25) Bakota, E. L.; Sensoy, O.; Ozgur, B.; Sayar, M.; Hartgerink, J. D. Self-assembling multidomain peptide fibers with aromatic cores. *Biomacromolecules* **2013**, *14*, 1370-1378.
(26) Dong, H.; Paramonov, S. E.; Aulisa, L.; Bakota, E. L.; Hartgerink, J. D. Self-assembly of multidomain peptides: balancing molecular frustration controls conformation and nanostructure. *J. Am. Chem. Soc.* **2007**, *129*, 12468-12472.
(27) Chae, S.; Lee, J. P.; Kim, J. M. Mechanically drawable thermochromic and mechanothermochromic polydiacetylene sensors. *Adv. Funct. Mater.* **2016**, *26*, 1769-1776.
(28) Kuo, S.-Y.; Li, H.-H.; Wu, P.-J.; Chen, C.-P.; Huang, Y.-C.; Chan, Y.-H. Dual colorimetric and fluorescent sensor based on semiconducting polymer dots for ratiometric detection of lead ions in living cells. *Anal. Chem.* **2015**, *87*, 4765-4771.
(29) Park, I. S.; Park, H. J.; Kim, J.-M. A soluble, low-temperature thermochromic and chemically reactive polydiacetylene. *ACS Appl. Mater. Interfaces* **2013**, *5*, 8805-8812.
(30) Duan, P.; Cao, H.; Zhang, L.; Liu, M. Gelation induced supramolecular chirality: chirality transfer, amplification and application. *Soft Matter* **2014**, *10*, 5428-5448.
(31) Huang, S.; Yu, H.; Li, Q. Supramolecular chirality transfer toward chiral aggregation: asymmetric hierarchical self-assembly. *Adv. Sci.* **2021**, *8*, 2002132.
(32) Volynets, G. P.; Barthels, F.; Hammerschmidt, S. J.; Moshynets, O. V.; Lukashov, S. S.; Starosyla, S. A.; Vyshniakova, H. V.; Iungin, O. S.; Bdzhola, V. G.; Prykhod'ko, A. O. Identification of novel small-molecular inhibitors of Staphylococcus aureus sortase A using hybrid virtual screening. *J. Antibiot.* **2022**, *75*, 321-332.
(33) Wang, J.; Li, H.; Pan, J.; Dong, J.; Zhou, X.; Niu, X.; Deng, X. Oligopeptide targeting sortase a as potential anti-infective therapy for Staphylococcus aureus. *Front. Microbiol.* **2018**, *9*, 245.
(34) Hosseinkhani, H.; Hong, P.-D.; Yu, D.-S. Self-assembled proteins and peptides for regenerative medicine. *Chem. Rev.* **2013**, *113*, 4837-4861.

Chapter 6: Summary

In **Chapter 2**, a series of tumor microenvironment-responsive peptide nanofibers with enhanced tumor targeting sensitivity and specificity were developed. The chemical characterizations showed that self-assembling monomer precursor (SAM-P) can undergo chemical and physical transformation to form nanostructures with various geometry, including short nanofibers, long nanofibers, and spherical nanoparticles under a reductive condition. The *in vitro* fluorescence cell imaging demonstrated the resultant long nanofibers bearing multivalent targeting ligands showed selective binding and highest targeting efficiency to U87mg tumor cells with overexpression of integrin receptors, compared to NIH/3T3 normal cells under a non-reductive condition.

In **Chapter 3**, to overcome the clinical limitations of natural antimicrobial peptides (AMPs) in terms of their high cytotoxicity and low hemocompatibility, a library of AMP-integrated self-assembling antimicrobial nanofibers (SAANs) was constructed via co-assembly strategy. The chemical and physical characterizations revealed that the secondary structure and nanostructure morphology of AMP-integrated SAANs can be tuned by modifying the molar ratio of AMP and SAANs, which affected both their antimicrobial activity and cytotoxicity. The *in vitro* antimicrobial assay and cell viability assay illustrated that SAANs (Mel-30%) showed an optimized balance of antimicrobial efficiency and cell toxicity, meaning SAANs (Mel-30%) exhibited lower cytotoxicity but retained potent antimicrobial activity. We envision that these co-assembled systems can be employed in other natural AMPs to overcome their clinical barriers.

In **Chapter 4**, to advance the antimicrobial delivery of self-assembling peptides for targeted bacterial therapy, a series of bacterial acidity-responsive assembling peptides (SANs), $WH_x(QL)_6K_2$ (x =5, 7, 9) were developed. The CD and TEM results showed these acid-sensitive

SANs had a propensity to form β-sheet forming nanofibers under neutral conditions whereas disassembled into monomers or oligomers exposed to acidic conditions. The *in vitro* antimicrobial test and hemocompatibility assay suggested that acidity-activatable SAN nanofibers were nearly nontoxic toward human blood cells under neural conditions and can selectively kill both Gram-positive and Gram-negative bacteria under acidic conditions.

In **Chapter 5**, we introduced the current research of bacteria-triggered hydrogel for alkaline bacterial environment sensing and on-demand drug delivery. A polydiacetylene-peptide (PDA-Pep) hydrogel was synthesized and prepared by the on-resin coupling reaction. Upon the increase of pH, the deprotonation of glutamic acid residues interrupted the π-π packing of PDA motifs to induce a colorimetric transition of PDA-Pep hydrogel from blue to purple. Simultaneously, the deprotonated glutamic acids generated electrostatic repulsion among individual nanofibers triggering a gel-to-sol phase transition, resulting in the controlled release of antimicrobial drugs. Notably, the alkaline-triggered blue-to-purple color transition and gel-to-sol transformation of PDA-Pep hydrogel were confirmed on inoculated pig skins. The bacterial plate counting results showed that PDA-Pep hydrogel can kill ~70% of *MRSA* under basic conditions.

Appendix A

Supporting Data for Chapter 2

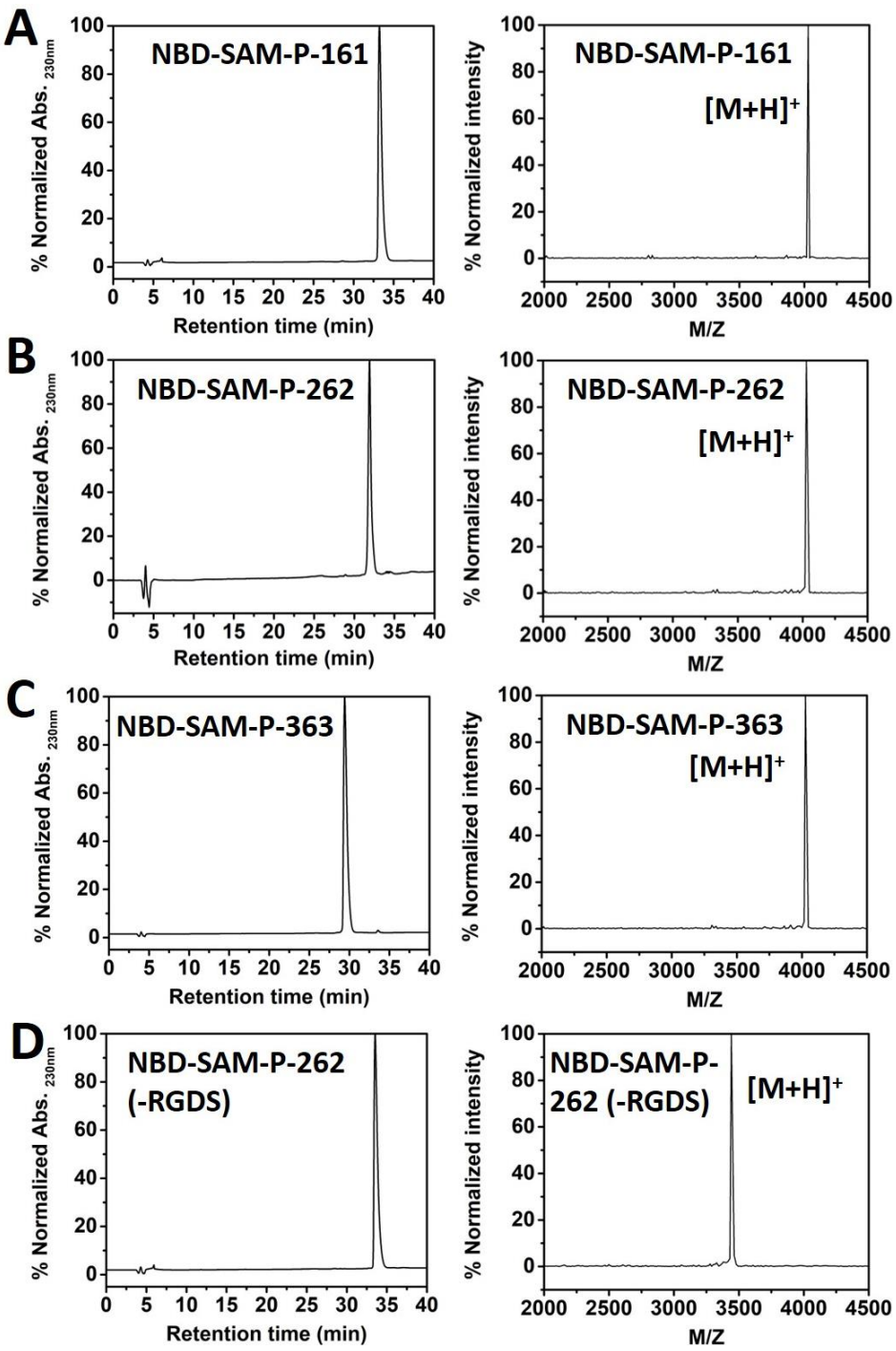

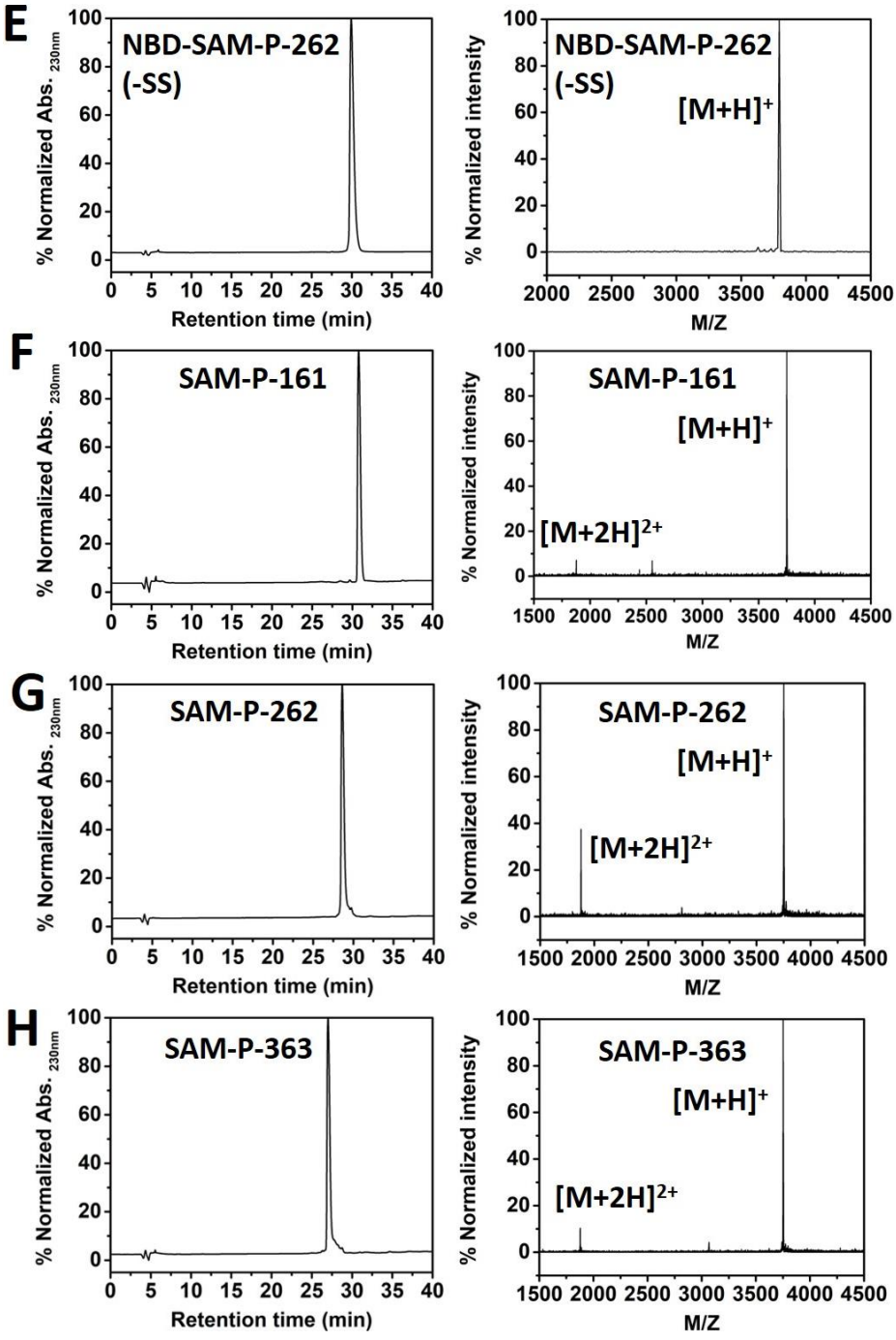
E
NBD-SAM-P-262
(-SS)
% Normalized Abs. 230nm
Retention time (min)
NBD-SAM-P-262
(-SS)
[M+H]+
% Normalized intensity
M/Z
F
SAM-P-161
% Normalized Abs. 230nm
Retention time (min)
SAM-P-161
[M+H]+
[M+2H]2+
% Normalized intensity
M/Z
G
SAM-P-262
% Normalized Abs. 230nm
Retention time (min)
SAM-P-262
[M+H]+
[M+2H]2+
% Normalized intensity
M/Z
H
SAM-P-363
% Normalized Abs. 230nm
Retention time (min)
SAM-P-363
[M+H]+
[M+2H]2+
% Normalized intensity
M/Z

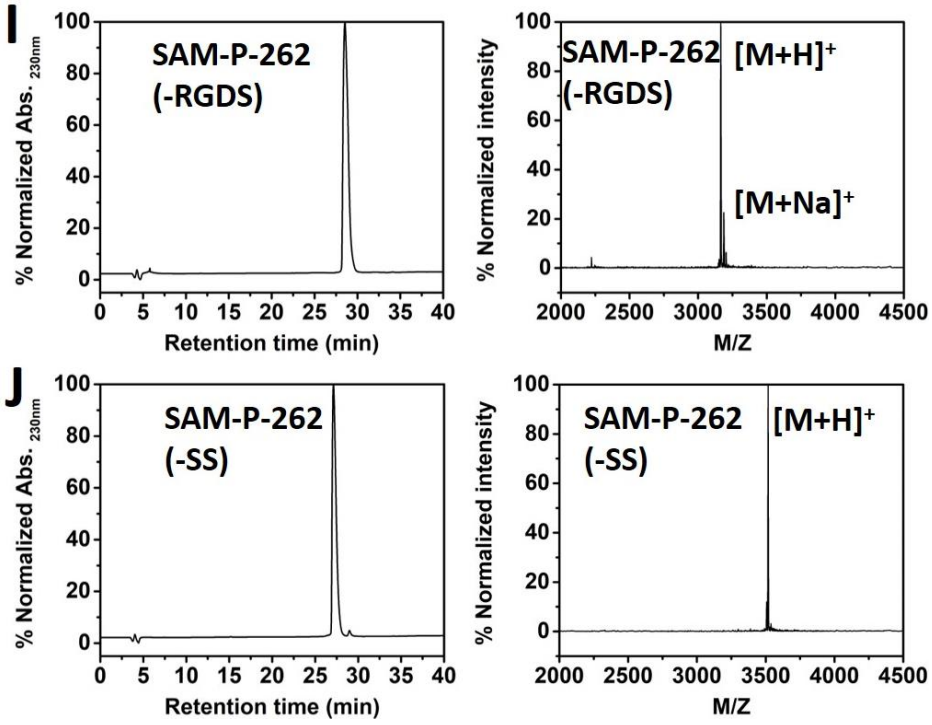

Figure A-S1. HPLC and MALDI of **(A)** NBD-SAM-P-161; **(B)** NBD-SAM-P-262; **(C)** NBD-SAM-P-363; **(D)** NBD-SAM-P-262 (-RGDS); **(E)** NBD-SAM-P-262 (-SS); **(F)** SAM-P-161; **(G)** SAM-P-262; **(H)** SAM-P-363; **(I)** SAM-P-262 (-RGDS); **(J)** SAM-P-262 (-SS).

Appendix B

Supporting Data for Chapter 3

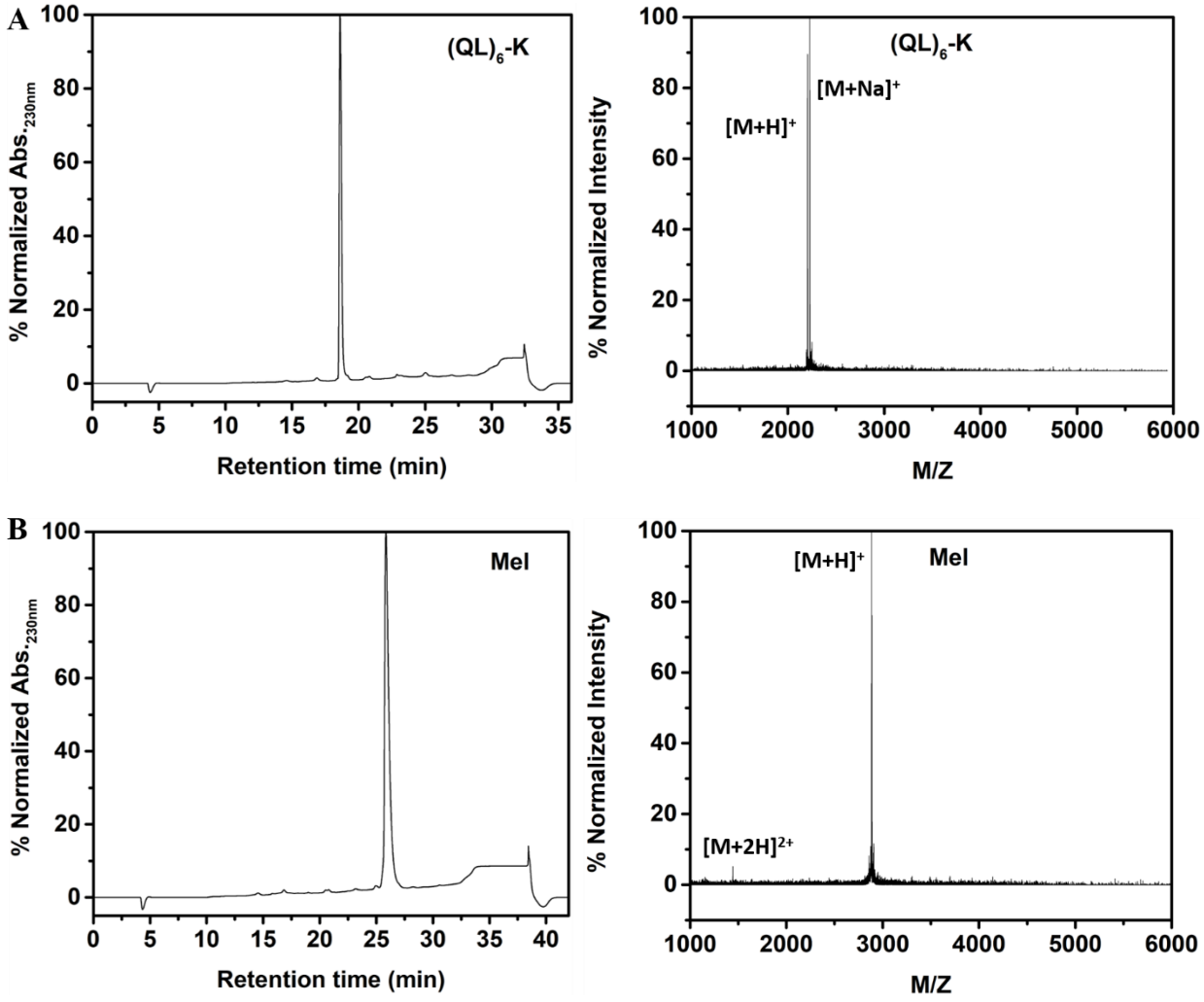

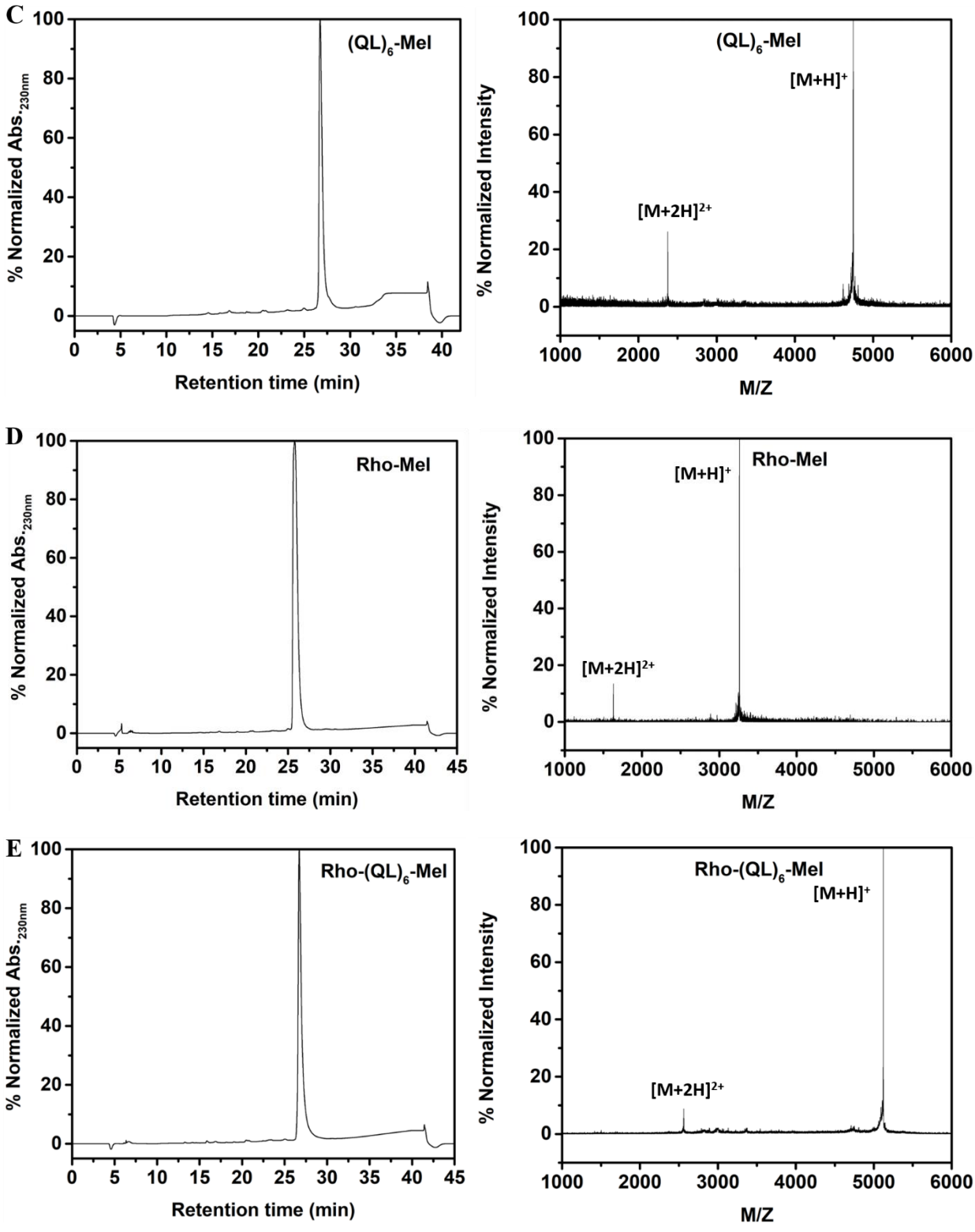

Figure B-S1. HPLC and MALDI spectra of (A) $(QL)_6$-K; (B) Mel; (C) $(QL)_6$-Mel; (D) Rho-Mel; (E) Rho-$(QL)_6$-Mel

Appendix C

Supporting Data for Chapter 4

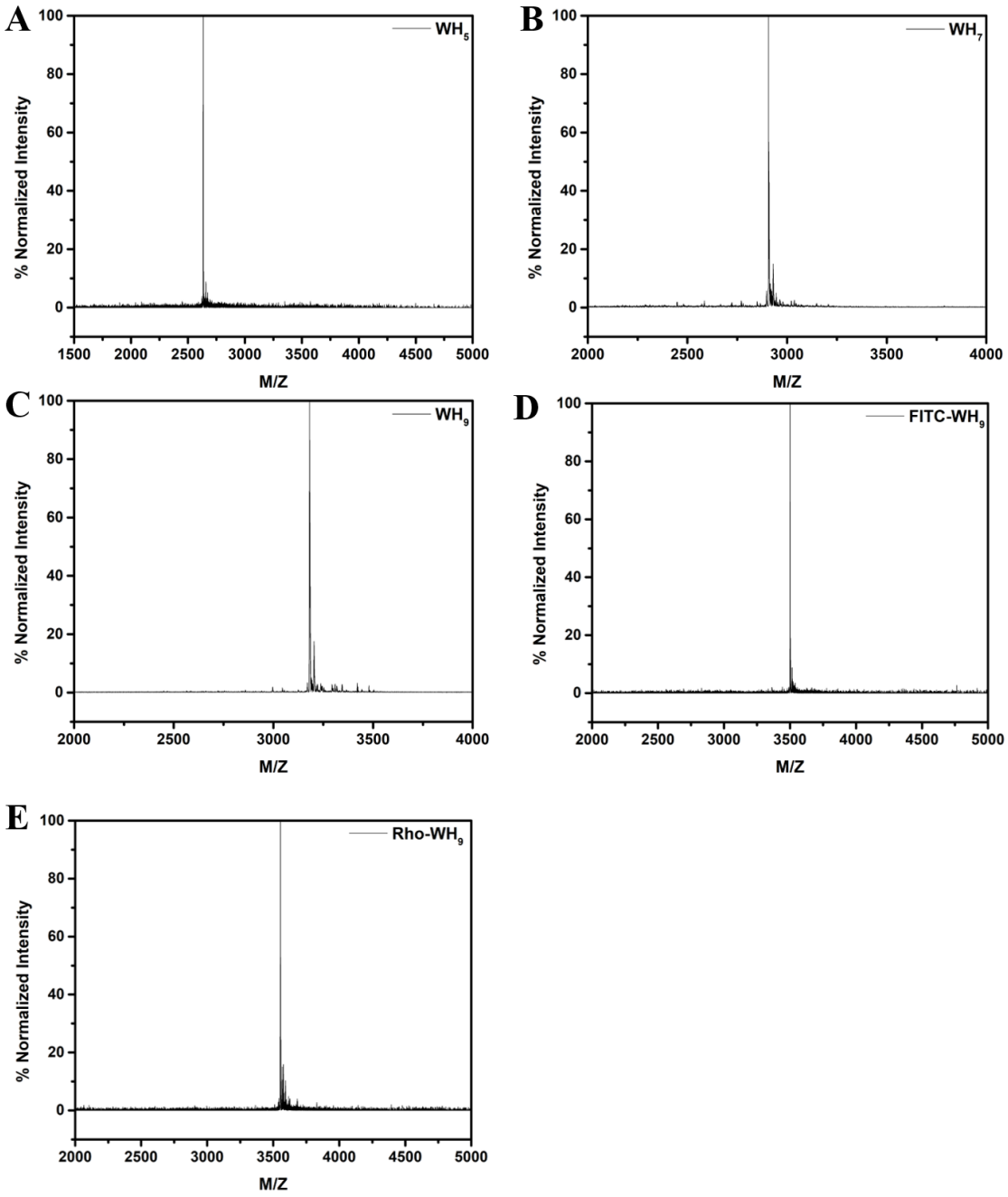

Figure C-S1. MALDI spectra of WH_5 **(A)**, WH_7 **(B)**, WH_9 **(C)**, FITC-WH_9 **(D)** and Rho-WH_9 **(E)**.

Appendix D

Supporting Data for Chapter 5

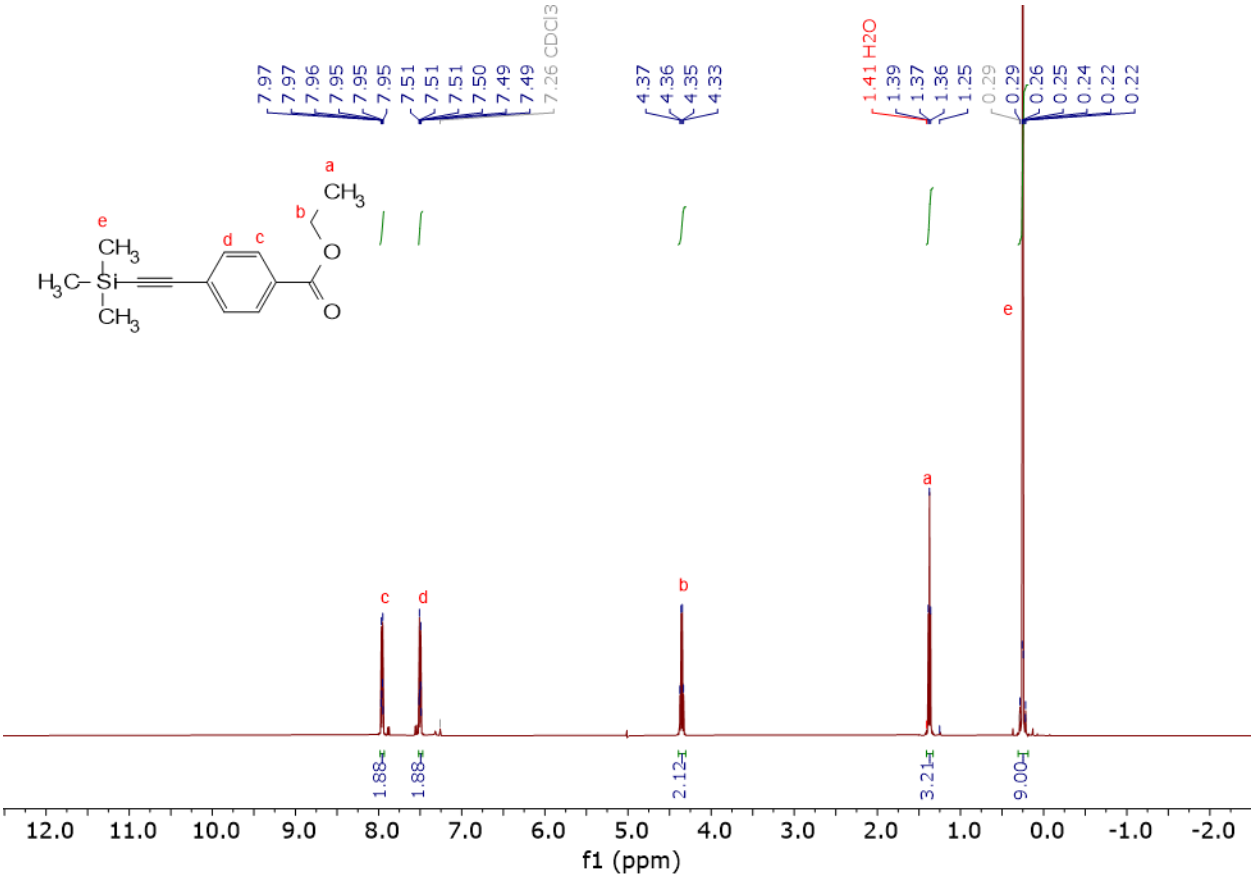

Figure D-S1-1. NMR spectra of compound 3 in $CDCl_3$

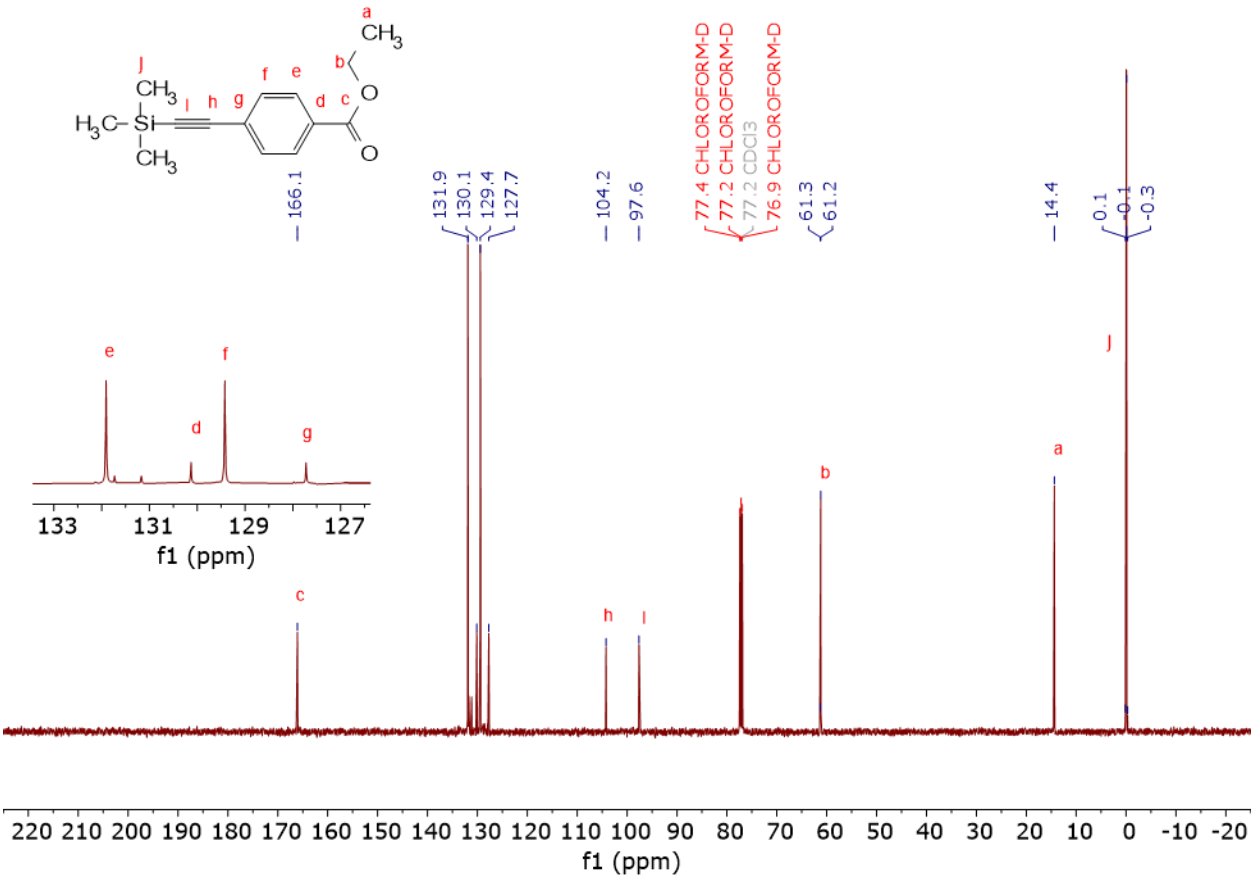

Figure D-S1-2. NMR spectra of compound 3 in $CDCl_3$

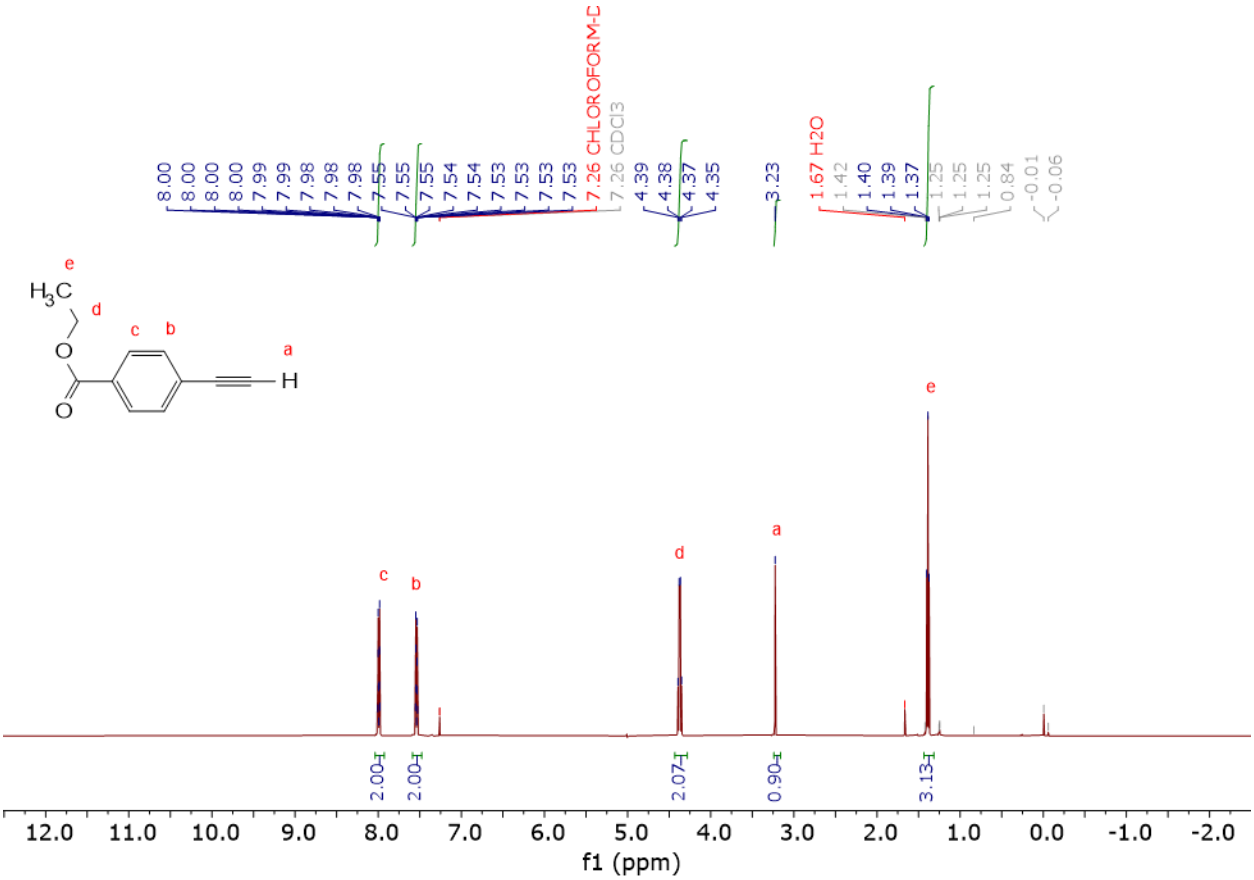

Figure D-S1-3. NMR spectra of compound 4 in $CDCl_3$

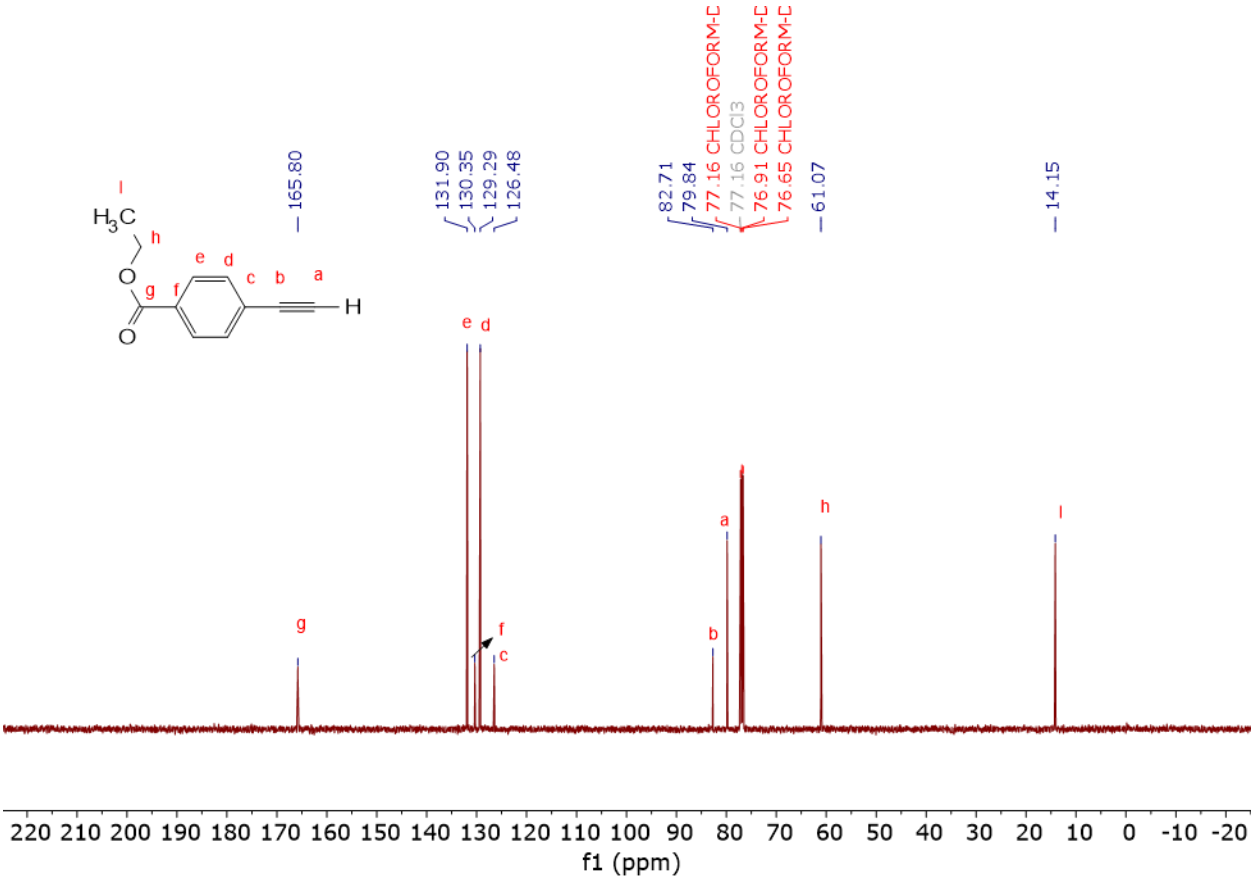

Figure D-S1-4. NMR spectra of compound 4 in $CDCl_3$

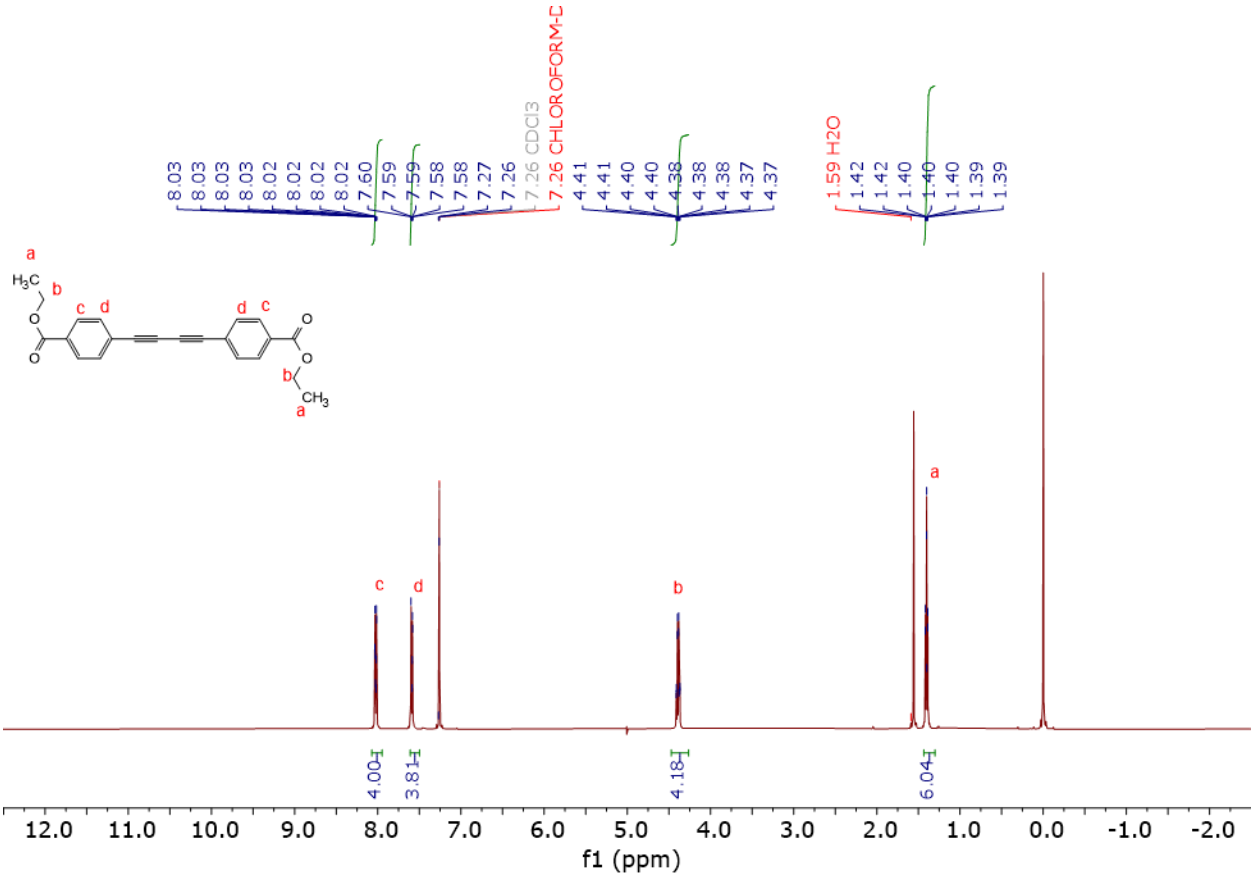

Figure D-S1-5. NMR spectra of compound 5 in $CDCl_3$

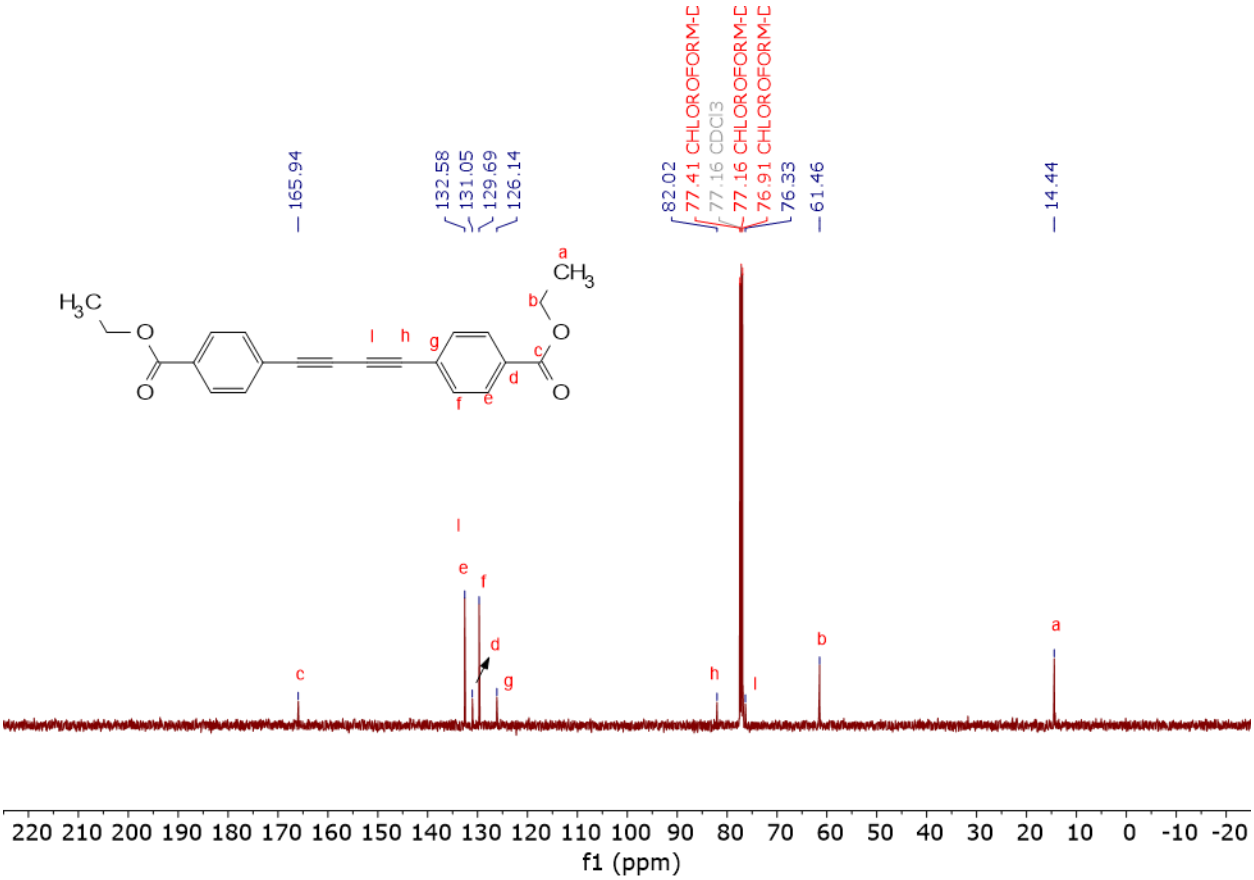

Figure D-S1-6. NMR spectra of compound 5 in $CDCl_3$

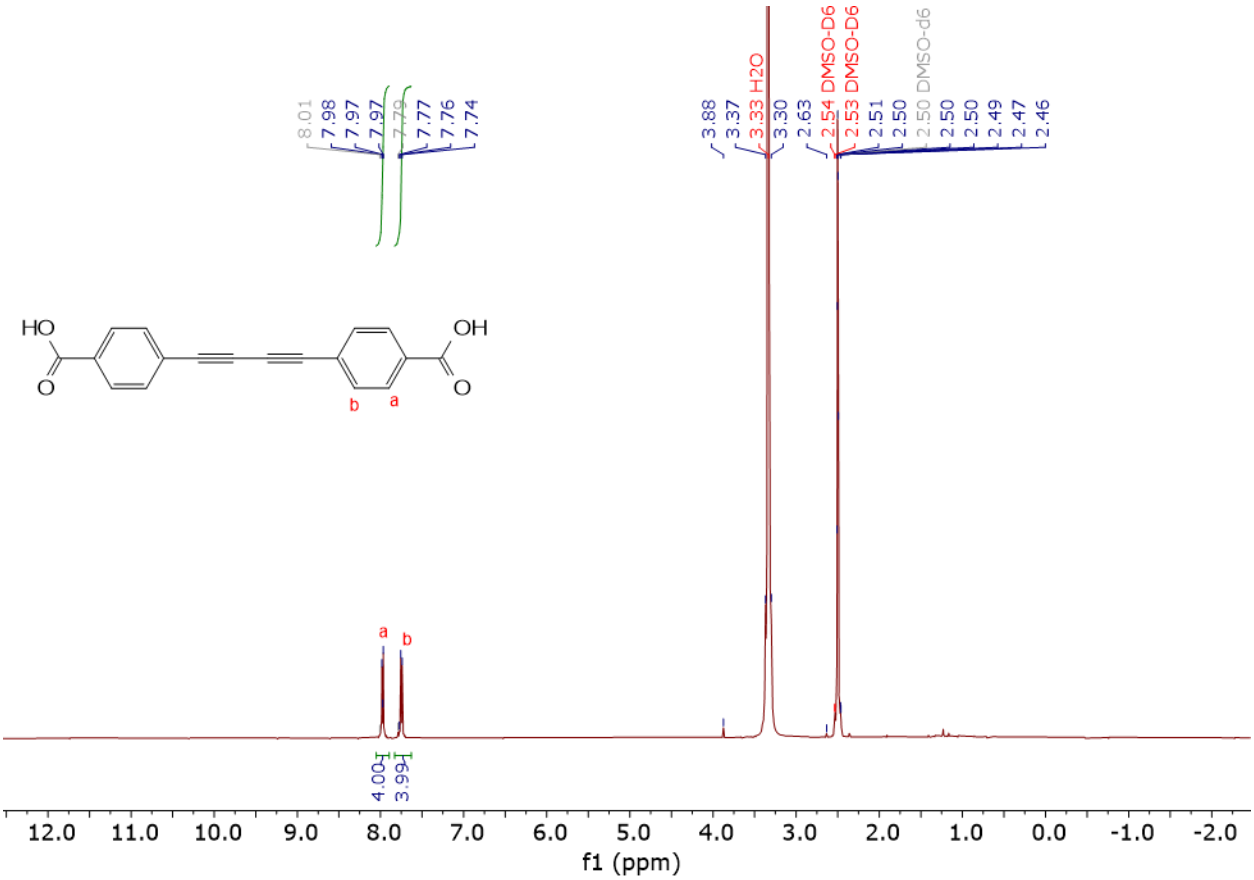

Figure D-S1-7. NMR spectra of compound 6 in DMSO-d_6

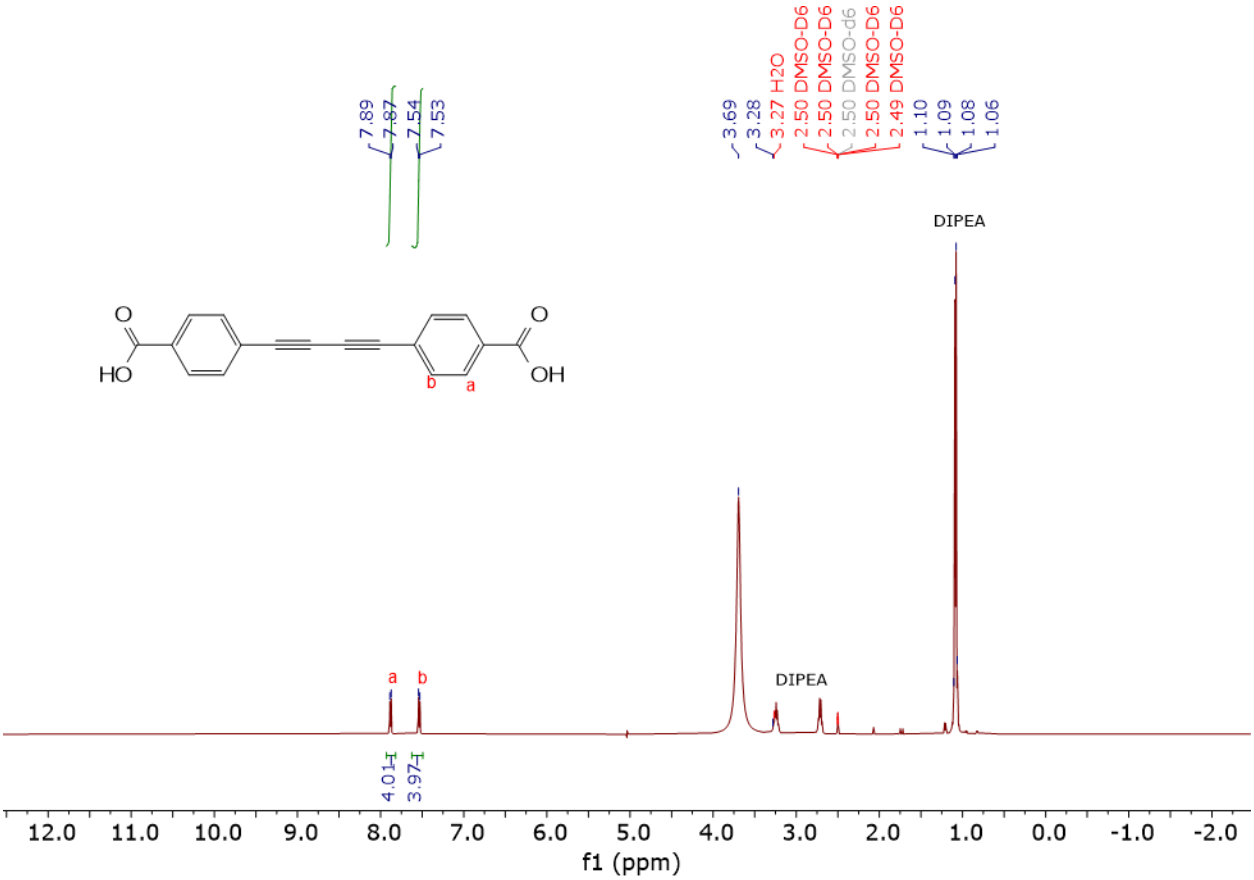

Figure D-S1-8. NMR spectra of compound 6 with DIPEA in DMSO-d_6

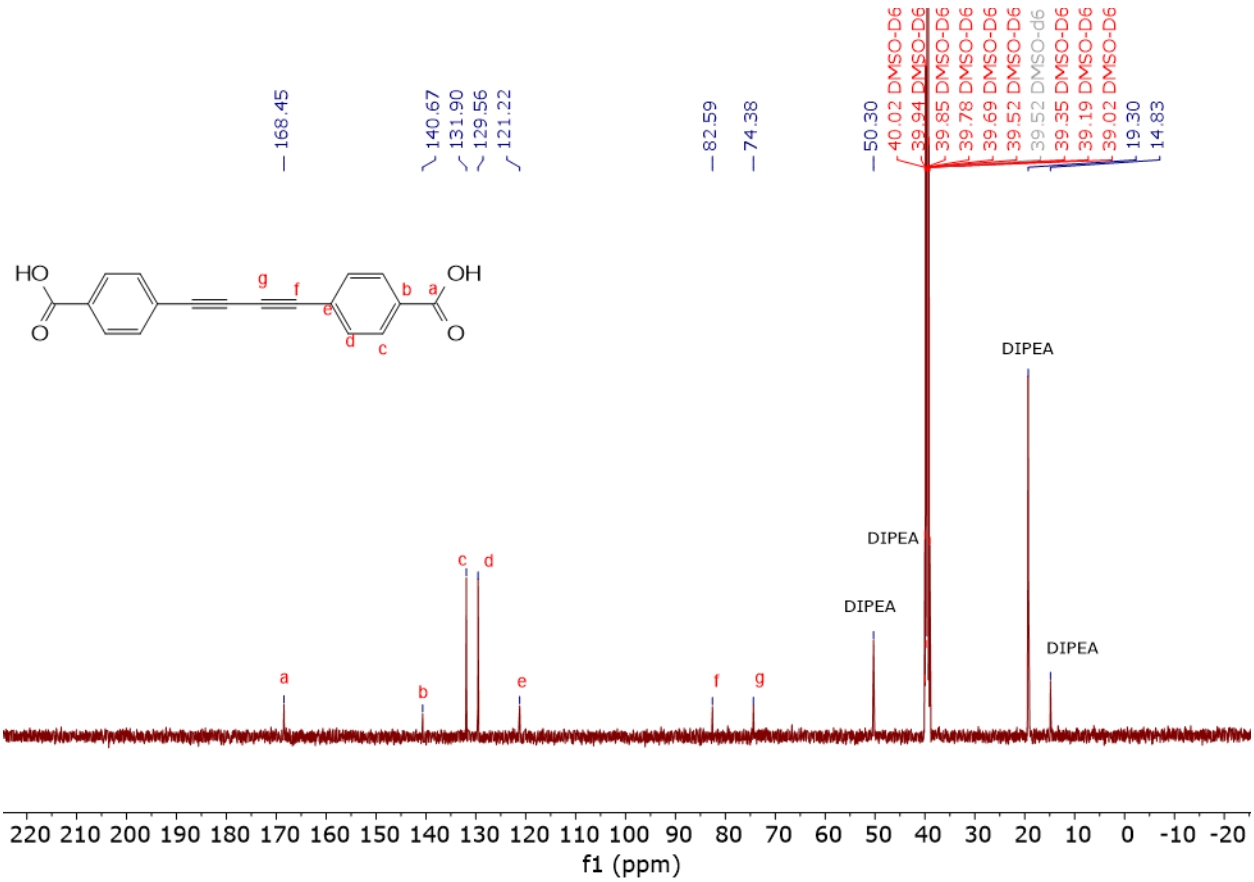

Figure D-S1-9. NMR spectra of compound 6 with DIPEA in DMSO-d_6

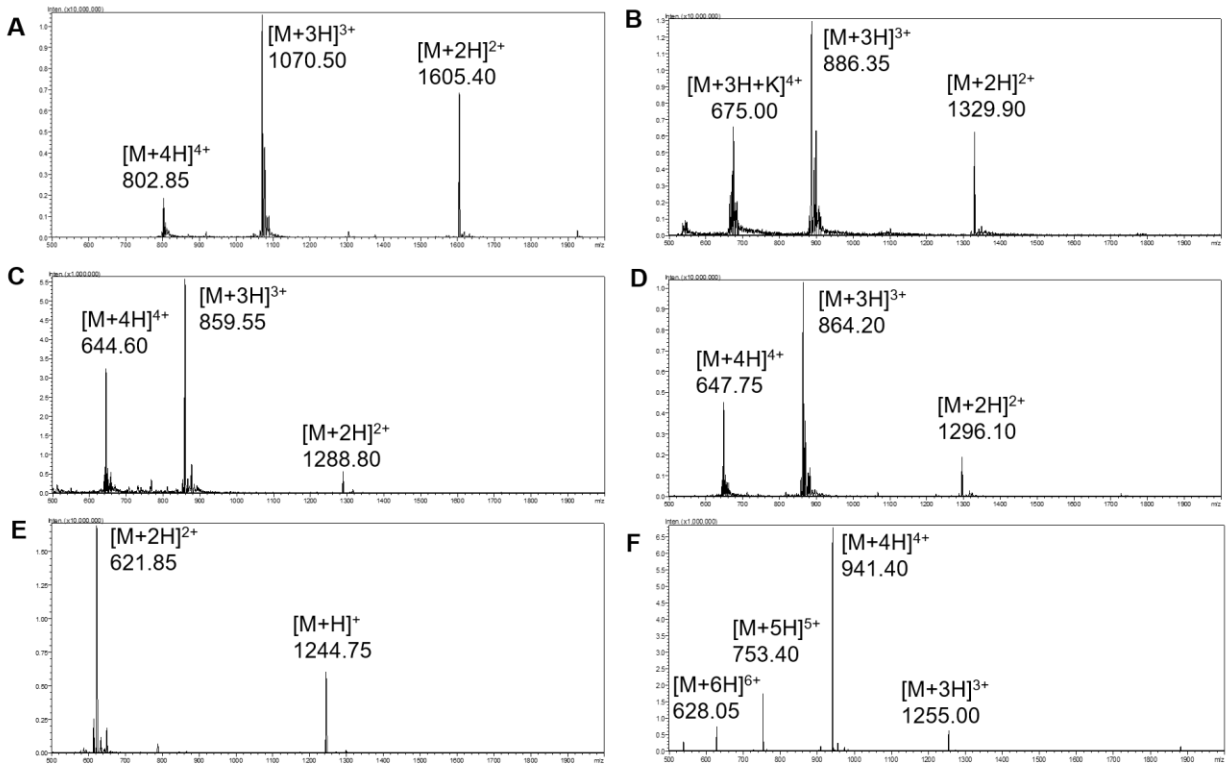

Figure D-S2. ESI/MS of **(A)** DA-Pep (peptide sequence: GQFQFEGGGLPRDA) **(B)** DA-Pep (peptide sequence: GQFEGGGLPRDA) **(C)** DA-Pep (peptide sequence: GSFEGGGLPRDA) **(D)** DA-Pep (peptide sequence: GQIEGGGLPRDA) and **(E)** Peptide without DA (peptide sequence: GQFEGGGLPRDA). **(F)** $K_8(QF)_6K_8$

References

(1) Bertrand, H.C., Schaap, M., Baird, L., Georgakopoulos, N.D., Fowkes, A., Thiollier, C., Kachi, H., Dinkova-Kostova, A.T., Wells, G., Design, synthesis, and evaluation of triazole derivatives that induce Nrf2 dependent gene products and inhibit the Keap1–Nrf2 protein–protein interaction. *J. Med. Chem.* **2015**, *58*, 7186–7194

(2) Stewart, L., Lu, W., Wei. Z.W., IIa, D., Padilla, C., Zhou, H.C. A Zirconium metal-organic framework with an exceptionally high volumetric surface area. *Dalton Trans.,* **2017**, *46*, 14270-14276